

Abstract

BONINO, CHRISTOPHER ADAM. Functional Nanofibers and Hydrogels: From Energy Storage to Biomedical Applications. (Under the direction of Dr. Saad A. Khan).

Electrospun nanofibers and hydrogels have received considerable research attention from their ability to be used in a variety of applications, including battery electrodes and tissue engineering scaffolds. These polymer-based nanomaterials have structures and properties that can be tailored to meet the demands of the specific application. The present study can be essentially divided into three parts. The first part investigates the parameters that affect composite electrospun (nano)fibers prepared by electrospinning. Specifically, we use polyacrylonitrile (PAN), a precursor to carbon fibers. (Nano)particles are incorporated within PAN nanofibers by various approaches. We evaluate the distribution of (nano)particles within the (nano)fibers, as well as the effects on the fiber morphology. We also demonstrate the use of composite nanofibers as anodes in lithium ion batteries.

The second part of this work focuses on parameters that affect electrospun polymer blends. Specifically, we relate the solution properties of sodium alginate, polymer that cannot be electrospun independently, and compare these to blended solutions capable of being electrospun. Nonionic surfactants that enhance the blended nanofiber morphologies are also investigated. In addition, we demonstrate that the alginate blends can be electrospun into unique three-dimensional structures, which can be tailored by solution (i.e., pH) and process (i.e., relative humidity) parameters. Since these nanofibrous materials have potential uses as tissue scaffolds, we evaluate biocompatible and FDA-approved materials that minimize cytotoxicity.

In the last part of this work, we investigate sodium alginate in hydrogels. By using an *in-situ* rheology technique, we characterize the crosslinking reaction of photocrosslinkable alginate. We evaluate the effects of solution (i.e., crosslink density) and process (i.e., UV exposure) parameters on the formation dynamics and final properties of the hydrogels. By tailoring the mechanical properties, we demonstrate the potential applications of alginate hydrogels as scaffolds for different tissue types. We also characterize the onset of gelation by various rheological techniques, including a new approach related to the sample strain.

Functional Nanofibers and Hydrogels: From Energy Storage to Biomedical Applications

by
Christopher Adam Bonino

A dissertation submitted to the Graduate Faculty of
North Carolina State University
in partial fulfillment of the
requirements for the degree of
Doctor of Philosophy

Chemical Engineering

Raleigh, North Carolina

2011

APPROVED BY:

Saad A. Khan
Committee Chair

Peter S. Fedkiw

Xiangwu Zhang

Jan Genzer

Dedication

I dedicate this thesis to my grandfather, Guiseppe (Joseph) Bonino. As a young child, Guiseppe immigrated with his family to the United States from Sicily in 1910. His early life experiences took place in a coal mining town, where his family members worked for the company mine. He later learned the electrical trade and worked as an electrician for more than 45 years. Despite not having the opportunity to attend college, Guiseppe recognized the importance of higher education. He and his wife, Grazia (Grace), worked diligently to ensure that their two sons had this opportunity. Their desire for education and perseverance to make it a reality was a value instilled on my father, and in turn on me. As a result of the fortitude and sacrifices of Guiseppe and his family, I have had the opportunity to achieve this degree.

Biography

Christopher Adam Bonino grew up in Ontario, NY, outside of Rochester. He was educated in the Wayne Central School District, and then enrolled in the University of Rochester in the fall of 1998. At Rochester, he studied chemical engineering, with a minor in chemistry. He was also active in the student chapter of the American Institute of Chemical Engineers (AIChE) and served as co-president for two years. During his junior year, he was accepted into the chemical engineering department's 3-2 Bachelors-Masters (thesis) program. As part of this program, Bonino incorporated graduate-level courses and research while completing his Bachelor's degree (B.S. May 2002). Bonino's interests in polymers and supercritical carbon dioxide led him to join Professor Matthew Yates' research group. In May 2003, he successfully defended his Master's thesis entitled *Microencapsulation of Cadmium Selenide and Lead Selenide Quantum Dots*.

Upon completion of his Master's program, Bonino accepted a position in industry with Lexmark International (Lexington, KY) as an applied research engineer. While at Lexmark, Bonino helped to develop elastomer-based cartridge components for monochrome laser printers. In 2006, Bonino began the Ph.D. program in North Carolina State University's Department of Chemical and Biomolecular Engineering. His interests in polymers and energy-related research led him to join Professor Saad Khan's research group.

Acknowledgements

I begin by acknowledging my advisor, Professor Saad Khan. Your flexibility gave me the opportunities to explore fascinating areas of research and allowed for me to develop creative problem solving skills.

I would also like to thank the other members of my committee. I am grateful to Professor Peter Fedkiw for his willingness to field technical questions throughout my program. I also thank Professor Xiangwu Zhang for helpful discussions and feedback of my research. To Professor Jan Genzer, I am especially appreciative of our many planned and impromptu discussions, which ranged from the intricacies of polymer physics to life philosophies, and some topics in-between. Special thanks for Professor Kirill Efimenko for helpful research talks, especially those related to the 3D electrospinning work.

To our Case Western collaborators, I thank you for your willingness to maintain a long distance relationship. I am grateful to Professor Eben Alsberg for involving me in your group's research projects. I especially thank Melissa Krebs for initiating our collaborative work and showing me that 'bio' research *can* be really interesting. What started as a trivial side conversation, developed into a productive research alliance. Thanks also to Julia Samorezov for helpful discussions related to the UV crosslinking project, and exchanging lessons on tissue engineering for rheology. In addition, I am grateful to Sung In Jeong and Oju Jeon for technical discussions and feedback.

My acknowledgements to Liwen Ji and Andrew Loebel for laboratory assistance and helpful discussions related to our nanofiber battery project. Thanks also to Zhan Lin and Ozan Toprakci for the help with the tin manuscript work. I am grateful to Jairus Kleinart and Randy Erb for many technical and non-technical conversations along the way. In addition, I appreciate all of the members of the Khan group, past and present, who helped to make my Ph.D. experience memorable. I would also like to acknowledge the undergraduate students that I had the privilege to mentor: Douglas Hartley and Kimberly Shearer.

Finally, I am entirely grateful for my wife, Angela, and her support throughout yet another ‘marathon’ project. I also thank my daughter, Eleanor, for giving me some new perspectives on life, and offering me much-needed distractions. I am also appreciative for my parents, Angela’s parents, and my brothers and their families, and their many forms of encouragement, from Skype conversations to being members of my ‘pit crew’ during my final ‘surge’ in February 2011.

Table of Contents

List of Tables	xi
List of Figures	xii
CHAPTER 1. Motivation, Goals, and Background.....	1
1.1.1. Thesis Goals for Composite and Blended Electrospun Nanofibers.....	3
1.1.2. Composite Electrospun Nanofibers	5
1.1.3. Blended Electrospun Nanofibers	8
1.1.4. Thesis Goal for Polymer Hydrogels	11
1.1.5. Motivation for Diverse Research Areas.....	12
1.2. Background	13
1.2.1. Electrospinning	13
1.2.2. Polyacrylonitrile Nanofibers <i>via</i> Electrospinning.....	16
1.2.3. Polyacrylonitrile as a Precursor to Carbon Fibers	17
1.2.4. Nanofibers Containing Nanoparticles <i>via</i> Electrospinning.....	18
1.2.5. Applications for Electrospun Nanofibers: Li-ion Battery Electrodes.....	26
1.2.6. Alginate Nanofibers <i>via</i> Electrospinning.....	27
1.2.7. Applications for Electrospun Nanofibers: Tissue Engineering Scaffolds	28
1.2.8. Hydrogels.....	29
1.2.9. Rheological Methods to Study Gelation.....	29
1.2.10. Alginate Hydrogels.....	32
1.3. Organization of Dissertation	33
1.3.1. References.....	34

CHAPTER 2. Electrospun Fiber Composites Containing Fumed Silica: From Solution Rheology to Materials with Tunable Wetting.....	52
2.1. Introduction.....	55
2.2. Experimental Section.....	59
2.3. Results and Discussions.....	62
2.3.1. Nanocomposites of PAN and FS with Different Surface Chemistries.....	62
2.3.2. Films of PAN/FS.....	64
2.3.3. Electrospun Fibers of PAN/FS.....	65
2.3.4. Electrospun PEO and PVA Solutions Containing Fumed Silica.....	68
2.3.5. Wet Spun PAN fibers.....	69
2.3.6. Tailored Hydrophobic Surfaces of Electrospun PAN Fibers with Fumed Silica.....	70
2.3.7. Carbonization of PAN/FS Composite Fibers.....	71
2.4. Conclusion.....	72
2.5. Acknowledgements.....	73
2.6. References.....	74
CHAPTER 3. Electrospun Carbon-Tin Oxide Composite Nanofibers for Use as Lithium Ion Battery Anodes.....	90
3.1. Introduction.....	93
3.2. Experimental Section.....	96
3.3. Results and Discussions.....	98
3.3.1. Carbon-SnO ₂ Nanofibers by <i>In-situ</i> Electrospinning.....	98
3.3.2. Characterization of Stabilized & Carbonized Nanofibers.....	99
3.3.3. Performance of C-SnO ₂ Nanofiber Mats as Li-Ion Battery Anodes.....	102

3.3.4. Nanofibers Surface-loaded with SnO ₂ Nanoparticles <i>via</i> Soak Treatment	103
3.3.5. Characterization of Stabilized, and Salt-Soaked, & Carbonized Nanofibers	104
3.3.6. Performance of Soaked Carbon-SnO ₂ Nanofiber Mats as Lithium Ion Battery Anodes	106
3.4. Conclusions	108
3.5. Acknowledgements	109
3.6. References	110
CHAPTER 4. Electrospinning alginate-based nanofibers: From blends to crosslinked low molecular weight alginate-only systems.....	126
4.1. Introduction	129
4.2. Materials and Methods	133
Materials.....	133
4.3. Results and Discussion.....	136
4.3.1. Solution rheology and electrospinning alginate.....	136
4.3.2. Effect of Triton X-100 surfactant on alginate/PEO blends.....	139
4.3.3. Role of biocompatible F127 nonionic surfactant.....	141
4.3.4. Electrospinning low MW alginate	142
4.3.5. Crosslinked alginate-only nanofibers	144
4.4. Conclusions	146
4.5. Acknowledgments	147
4.6. References	148
CHAPTER 5. Three Dimensional Electrospun Alginate Mats <i>via</i> Tailored Charge Repulsions.....	165

5.1. Introduction	168
5.2. Experimental Section	173
5.3. Results and Discussions.	175
5.3.1. Formation of Three-Dimensional Electrospun Mats	175
5.3.2. Effects of Relative Humidity on 3D Electrospun Mat Formation	179
5.3.3. Effects of Solution pH on 3D Electrospun Mat Formation	182
5.3.4. Effects of Surface Tension on 3D Electrospun Mat Formation.....	183
5.3.5. 3D Mat Formation in Solutions Without Alginate	184
5.4. Conclusion.....	186
5.5. Acknowledgements.....	187
5.6. References.....	188
CHAPTER 6. Real-time <i>in-situ</i> Rheology of Alginate Hydrogel Photocrosslinking.....	210
Abstract.....	210
6.1. Introduction.....	212
6.2. Experimental Section	217
6.3. Results and Discussions.	218
6.3.1. Evolution of Crosslinking Reaction.....	218
6.3.2. Gel Point.	220
6.3.3. Varying UV Intensity.....	222
6.3.4. Varying Degree of Methacrylation.....	224
6.4. Conclusion.....	227
6.5. Acknowledgements.....	228

6.6. References	229
CHAPTER 7. Conclusions and Recommendations	248
7.2. Recommendations	252
7.2.1. Distribution of nanoparticles and/or other solution components within composite/blended nanofibers by manipulating particle conductivity, charged components, and electrical field.	252
7.2.2. Composite graphitic carbon nanofibers containing nanoparticles by infiltration methods.....	254
7.2.3. 3D Electrospun <i>In situ</i> Crosslinked Nanofibers	256
7.2.4. Rheology of alginate hydrogels containing cells	257
7.3. References	258

List of Tables

Table 3.1. Properties of Electrospun Solutions.....	113
Table 4.1. Properties of electrospun solutions and observations of nanofiber morphology	155
Table 4.2. Properties of electrospun solutions containing Pluronic F127 and observations of nanofiber morphology	156
Table 5.1. Surface atomic composition measured by XPS	193
Table 5.2. Observations of electrospun formations at various relative humidities.....	194
Table 5.3. Observations of electrospun formations at different solution pH.....	195
Table 5.4. Surface atomic composition measured by XPS, with Pluronic F127 surfactant.....	196
Table 5.5. Properties of electrospinning solutions evaluated for 3D mats	197
Table 6.1. Properties of Alginate Hydrogel with Different UV Irradiation Levels.....	233
Table 6.2. Properties of Alginate Hydrogels with Varying Degree of Methacrylation.....	234

List of Figures

Figure 1.1. Diagram depicting chemical structure of sodium alginate.	47
Figure 1.2. Diagram depicting electrospinning setup and resulting nanofibers.	48
Figure 1.3. SEM micrographs of PEO nanofibers electrospun in 10 and 50% relative humidity conditions. Scale bar is 2 μm	49
Figure 1.4. Diagram depicting the change in the chemical structure of PAN as a result of stabilization and carbonization heat treatments.	50
Figure 1.5. Diagram depicting formation of hydrogel, from polymer solution to crosslinked 3D solid-like structure.	51
Figure 2.1. Solution rheology of PAN (7.9 %)/DMF with R805 (2.2 %, hydrophobic, \blacktriangle , \triangle) or A200 (2.2 %, hydrophilic, \blacksquare , \square) fumed silica; (a) dynamic frequency sweep, (b) steady shear viscosity, and (c) shear stress/rate plots.	80
Figure 2.2. Solution rheology of PAN (7.9 %, \diamond , 10 %, \circ) and PAN with R805 (5.5 %, hydrophobic, \blacktriangle) or A200 (5.5 %, hydrophilic, \blacksquare) fumed silica; (a) steady shear viscosity and (b) shear stress/rate plots.	81
Figure 2.3. Solution rheology of R805 (9 %, hydrophobic, \blacktriangle , \triangle) or A200 (9 %, hydrophilic, \blacksquare , \square) fumed silica; (a) dynamic frequency sweep, (b) steady shear viscosity, and (c) shear stress/rate plots.	82
Figure 2.4. Transmission electron micrographs of PAN/R805 (a) and PAN/A200 (b) spun-cast films.	83
Figure 2.5. Scanning electron micrographs of PAN (a, b), PAN/A200 (c, d), and PAN/R805 (e, f) electrospun fibers.	84

Figure 2.6. Scanning and transmission electron micrographs of PAN with R805 fumed silica (a, c, d) and PAN only (b) electrospun fibers. Fiber cross section (a) was prepared by freeze fracture.	85
Figure 2.7. Scanning electron micrographs of composite polymer/fumed silica electrospun fibers: PEO/R805 FS (a) and PEO/A200 FS (b).	86
Figure 2.8. SEM images of PAN fiber (a), top surface (c), cross section (e); and PAN/R805 fiber (b), top surface (d), cross section (f) prepared by wet spinning.....	87
Figure 2.9. Representative contact angle profiles of water on PAN and fumed silica fiber mats. PAN with R805, the hydrophobic FS, has an average contact angle of 128 ^o (a), whereas water spreads across PAN with A200, the hydrophilic FS (b). (The arrow indicates the top surface of spreading droplet.).....	88
Figure 2.10. SEM images of carbon/fumed silica fibers after carbonization heat treatment.	89
Figure 3.1. Electron micrographs of electrospun PAN nanofibers with (a, c, e) and without (b, d, f) tin sulfate. Figures a-d were captured with SEM and e, f with TEM. Average fiber diameters were 293±67 and 298±57 nm, respectively.	114
Figure 3.2. Scanning electron micrographs of carbonized nanofibers with (a, c) and without (b, d) tin oxide. Average fibers diameters were 176±36 and 223±38 nm, respectively.....	115
Figure 3.3. Transmission electron micrographs of composite fibers after stabilization (a) and carbonization (c) heat treatments, and corresponding energy dispersive spectra (b, d, respectively). The presence of Sn and S in spectrum (b) indicates that tin sulfate has not been converted to tin oxide during the stabilization. In comparison, the absence of S in spectrum (d)	

	indicates that SnO ₂ has formed. The peak near 2.7 eV is an artifact of the strong Si peak from the TEM grid.	116
Figure 3.4.	X-ray diffraction patterns of fibers after (a) stabilization heat treatment and (b) carbonization heat treatments. Fibers containing the tin salt show a change in crystal structure from SnSO ₄ (JCPDS no. 16-0252) to SnO ₂ (JCPDS no. 41-1445).	117
Figure 3.5.	Raman spectra of stabilized PAN/SnSO ₄ (a), stabilized PAN (b), carbonized PAN/SnSO ₄ (c) and carbonized PAN (d) fiber mats. The disordered (D) and graphitic (G) peaks centered at ~1340 and ~1580 cm ⁻¹ were fit to the spectra using Lorentzian distributions. Height ratios, <i>I(D)/I(G)</i> are 2.1±0.1, 2.1±0.1, 1.6±0.1 and 1.5±0.2, respectively.	118
Figure 3.6.	Performance of composite and carbon nanofiber mats as anodes in lithium ion battery half cells. Charge-discharge curves for C-SnO ₂ (a) and carbon (b) nanofiber anodes cycled between 0.05 and 2.80 V (vs Li/Li ⁺) at the rate of 50 mA/g. Curves at 1 st , 2 nd , 20 th , and 40 th cycles are shown. Cycle performance at 50 mA g ⁻¹ current density (c) and rate capability at 10 th cycles (d) for C-SnO ₂ composite anodes in Li-ion battery half cells.	119
Figure 3.7.	Micrographs of C-SnO ₂ (a) and carbon (b) fiber anodes after 40 cycles, verifying the mats maintain their structure during lithium de/insertion.	120
Figure 3.8.	Scanning and Transmission Electron Micrographs of PAN/SnSO ₄ (a, b, e, f) nanofibers that have been stabilized, soaked in aqueous tin sulfate, and then carbonized to form C-SnO ₂ composites. Micrograph (c) is PAN nanofibers that have been stabilized, soaked in water, and then carbonized. The corresponding elemental composition of the anode mats as measured by EDS is shown in (d).	121
Figure 3.9.	X-ray diffraction patterns (a) of fibers after soak and carbonization heat treatments. Peaks in the composite fiber mats correspond to SnO ₂	

(JCPDS no. 41-1445). Raman spectra of soaked and carbonized PAN/SnSO₄ (b) and PAN (c) nanofiber mats. Height ratios I(D)/I(G) are 1.9±0.1 and 1.5±0.1, respectively. The formation of the tin oxide nanoparticles during the heat treatment may disrupt the carbon microstructure, causing more disorder as indicated by the peak ratio. 122

Figure 3.10. Charge-discharge curves for (a) pure carbon nanofibers, soaked in water prior to carbonization, and (b) SnO₂-carbon nanofibers, soaked in salt solution prior to carbonization. Cycle life (c) of carbon-tin oxide and carbon nanofiber mats with solution soak treatments. The anodes were cycled with a constant 50 mA g⁻¹ current density. 123

Figure 3.11. Thermal gravimetric analysis (TGA) of tin sulfate decomposition during stabilization and carbonization heat treatments. SnSO₄ was heated in air at 2°C/min up until 280°C, held constant for 6 hours, and then it was heated in nitrogen up to 600°C. The remaining 37 wt % is SnO₂. Mass loss is attributed to the conversion of tin sulfate to tin oxide and the release of sulfur dioxide. 125

Figure 4.1. Scanning electron micrographs of electrospun droplets of alginate (a) and alginate/Triton X-100 (b), both without PEO. Fibers were not seen with all aqueous alginate solutions investigated, regardless of the addition of a surfactant. 157

Figure 4.2. Dependence of specific viscosity (η_{sp}) on concentration for (a) 196 kDa and (b) 37 kDa aqueous sodium alginate solutions. The entanglement concentrations (C_e) are 0.6 and 4 wt%, respectively. 158

Figure 4.3. Scanning electron micrographs of electrospun droplets of alginate-PEG blended (2.0:20.0 wt%) solution (a, b). PEG (35 kDa) is not an effective carrier polymer for alginate, due to its low MW and inability to be electrospun. Also shown are blended nanofibers prepared from alginate-PEO (600 kDa) (70:30 by wt) solutions. Beaded fibers (c) and (d) were

made without surfactant, whereas uniform fibers (e) and (f) contained 1 wt% Triton X-100.....	159
Figure 4.4. Elastic (G') and viscous (G'') moduli as a function of frequency for 2.8 wt% (∇, ∇) and 4.0 wt% alginate ($\blacktriangle, \triangle$), and blends containing alginate/PEO/Triton X-100 (2.8:1.2:1.0 wt%) (\blacklozenge, \lozenge) and alginate/PEO (2.8:1.2 wt%) (\bullet, \circ).....	160
Figure 4.5. Scanning electron micrographs of nanofibers composed of alginate and PEO (2.4:1.6 wt% or 60:40) without (a, b) and with Pluronic F127 (2 wt%) (c, d).	161
Figure 4.6. Steady shear viscosity curves for electrospun solutions containing blends of PEO with 196 kDa alginate (\blacksquare) and 37 kDa alginate (\bullet).....	162
Figure 4.7. Scanning electron micrographs of nanofibers containing 37 kDa alginate/PEO/Pluronic F127 (8.0:1.6:2.0 wt%) (a, b) prior to crosslinking. Nanofibers composed of 196 kDa (c, d) and 37 kDa (e, f) alginate after crosslinking with calcium and soaking in water for 4 days to remove PEO.....	163
Figure 4.8. Fiber diameters (a) of alginate(196kDa)/PEO/Triton X-100 (2.8:1.2:1.0), alginate(196kDa)/PEO/F127 (2.4:1.6:2.0), and alginate (37kDa)/PEO/F127 (8.0:1.6:2.0) before and after crosslinking and soaking in water. (Error bars = 1 standard deviation.) FTIR spectrographs (b) of nanofibers containing 37 or 196 kDa MW alginate and PEO before (37 kDa (1)) and after (37 kDa (2), 196 kDa (3)) soaking. PEO peaks at 844, 1102, and 1342 cm^{-1} disappear after soaking.....	164
Figure 5.1. Electrospinning setup with controlled humidity environment	198
Figure 5.2. Photograph (a) and SEM micrographs (b, c, d) of electrospun cone formation, composed of layers of nanofibers. The electrospinning	

solution contained: alginate – PEO – F127 (10.6:0.8:1.5 wt %) in water (30% RH).....	199
Figure 5.3. Photographs and SEM micrographs of formation of 3D mat structure after 9 (a, d, g, j), 15 (b, e, h, k), and 25 min (c, f, i, l) of electrospinning an aqueous alginate – PEO – F127 (10.6:0.8:1.5 wt %) solution (40% RH).....	200
Figure 5.4. Diagrams depicting fiber-to-fiber repulsions that lead to the formation of 3D structures (a) and the effects of the electric field on negatively-charged species (i.e., alginate) in solution within the Taylor cone (b).	201
Figure 5.5. Representative high resolution XPS scans of oxygen (a) and carbon (b) spectra on electrospun alginate – PEO (10.6-0.8 wt %) 3D mats.....	202
Figure 5.6. Photographs (a, c, e, g, i, k) and SEM micrographs (b, d, f, h, j, l) of electrospun mat structures and nanofibers, respectively, prepared at six different relative humidity conditions by electrospinning an alginate – PEO – F127 (10.6:0.8:1.5 wt %) solution. Scale bars on photographs are 2 cm.....	203
Figure 5.7. SEM micrograph of section of horizontal ‘strand’ on 3D electrospun mat (from Figure 5.4g), prepared by electrospinning alginate – PEO – F127 (10.6:0.8:1.5 wt %) at 40% RH. Arrows indicate the direction of the applied electric field.....	204
Figure 5.8 Photographs and SEM micrographs of mat and fibers electrospun from solutions containing alginate – PEO – F127 (10.6:0.8:1.5 wt %) at pH 7.0 (a, c) and pH 7.9 (b, d). (20% RH)	205
Figure 5.9. Photograph (a) of electrospun mat with 2D visual appearance prepared from surfactant-free solution containing alginate – PEO (10.6:0.8 wt %) at 40% RH. SEM micrographs of peaks on mat surface (b) and beaded nanofibers (c) prepared from the surfactant-free solution. SEM	

micrograph of nanofibers (d) prepared from the alginate – PEO solution containing Pluronic F127 surfactant (1.5 wt %).	206
Figure 5.10. Photographs and SEM micrographs of web-like mat and fibers electrospun from PEO – NaCl – F127 solutions (5.0:1.0:1.5 wt %).	207
Figure 5.11. Diagram depicting distribution of negatively-charged polymers (alginate) and salts (Cl) below surface of electrospun nanofibers.	208
Figure 6.1. Scheme for photocrosslinking reaction of methacrylated alginate.	235
Figure 6.2. Steady shear viscosity profile of alginate solution prior to UV exposure. Zero shear viscosity is 0.007 ± 0.0004 Pa·s, obtained from averaging the first 10 data points in the Newtonian region.	236
Figure 6.3. Elastic (G') and viscous (G'') moduli of photocrosslinkable alginate (11% methacrylation) as a function of frequency plotted after different exposure times with 5 mW/cm^2 UV radiation. At 900 s the solution is a pregel, with G'' is greater than G' at low frequencies and both moduli are frequency dependent. At 1200 s G' and G'' are parallel and have similar values across most frequencies, indicating the material is a postgel. After 1800 s G' is frequency independent and more than two orders of magnitude greater than G'' , indicating a highly crosslinked sample.	237
Figure 6.4. Dynamic viscosity of photocrosslinkable alginate as a function of frequency plotted after 900 (\square), 1200 (\circ), and 1800 (Δ) s of UV exposure with 5 mW/cm^2 UV radiation. Slopes at low frequencies decrease from 0 to -1, indicating the evolution of sol to gel.	238
Figure 6.5. Time dependent rheology of alginate with 11% methacrylation. Beginning at $t=0$, sample was exposed to UV radiation with 5 mW/cm^2 intensity and 1 rad/s oscillation with 0.05 Pa stress. The elastic (G' , \blacksquare) and viscous (G'' , \square) moduli are plotted as a function of time. The gel point time (t_c) is $1080.8 \pm 32.2 \text{ s}$, estimated by the G'/G'' crossover, and	

	the corresponding modulus is 11.2 ± 4.0 Pa. (Means \pm standard deviations are reported, sample size = 6.).....	239
Figure 6.6.	Evolution of tan delta for 11% methacrylated alginate solution with 5 mW/cm^2 UV irradiation using 1 (■), 5 (○), and 10 rad/s (▲) frequencies. The intersection point of the curves at ~ 1100 s indicates the gel point.	240
Figure 6.7.	(a) Strain on MAALG-11 throughout the crosslinking reaction, shown at 1 (■), 5 (○), and 10 rad/s (▲) and a 0.05 Pa constant stress. Strain reduces at onset of gelation. (b) Strain (●) and derivative of log strain (▲) at 1 rad/s plotted as functions of time. The dashed line marks the inflection point of the strain curve, the minimum of the derivative, and corresponds to the gel point.	241
Figure 6.8.	(a) Evolution of elastic and viscous moduli of alginate with 25% methacrylation at 3 (■□), 5(▲Δ), 10(●○), and 15 (◆◇) mW/cm^2 doses of UV irradiation. Dashed lines indicate G' , G'' crossover and gel points. Inset graph: the elastic moduli collapse when the dependent variable is scaled by the crossover time, as t/t_c . (b) Crossover times plotted versus UV intensity. The line is a power law curve fit.	242
Figure 6.9.	Sample strain as a function of time for 3(■), 5(▲), 10(●), and 15(◆) mW/cm^2 intensities. Dashed lines indicate gel points, which match with the inflection points of the experimental data.....	243
Figure 6.10.	(a) Elastic and viscous moduli as a function of time for photocrosslinkable alginate with 5(■□), 7(▲Δ), 11(●○), 19(◆◇), and 25% (▼, ▼) degrees of methacrylation. UV irradiation with 10 mW/cm^2 intensity was applied for $t \geq 0$. Dashed lines mark crossover times, which are approximately the gel points. (b) Time sweeps scaled with crossover times and fitted. Solid red lines are curve fits from: $G' = G'_\infty (1 - \exp[-\alpha(t/t_c - 1)^\beta])$. For 5, 7, 11, 19, and 25% degrees of methacrylation, $G'_\infty = 7.3, 410, 846, 4859, 6860$ Pa; $\alpha = 8.1, 1.0, 0.8,$	

0.8, 0.6; $\beta = 2.0, 1.5, 1.4, 2.2, 1.9$, respectively. (c) Crossover times and plateau moduli for alginate hydrogels with different degrees of methacrylation. Plateau modulus was estimated from curve fit. 244

Figure 6.11. Strain as a function of time for photocrosslinkable alginate with 5 (■), 7 (▲), 11 (●), 19 (◆), and 25% (▼) degree of methacrylation. Dashed lines indicate gel points, which match the inflection points for 7, 11, 19, and 25%. 247

Figure 7.1. Diagram depicting appearance of charge-discharge curves for graphite-like (a) and disordered carbon-like (b) anodes. 263

CHAPTER 1

Motivation, Goals, and Background

Motivation, Goals, and Background

In this chapter we highlight the motivation and goals for this thesis. We also provide a brief background on electrospun nanofibers and hydrogels. Finally, we present an overview of the thesis. Each subsequent chapter, however, is self-contained and can be read independently.

1.1. Motivation and Goals

Functional polymer-based nanomaterials have broad impacts in energy storage and biomedical applications. This thesis investigates two such materials: electrospun nanofibers and hydrogels. This work is motivated by two underlying themes and each chapter attempts to address both themes, which are:

- (1) To examine the interactions between the polymers and (nano)particles, surfactants, or salts.
- (2) To identify possible underlying mechanisms responsible for changes in the functional material when solution properties and/or process conditions are manipulated during fabrication.

1.1.1. Thesis Goals for Composite and Blended Electrospun Nanofibers

Electrospinning technology offers a powerful yet simple method to develop nonwoven materials for a wide range of applications including antimicrobial fabrics, gas sensors, tissue scaffolds, and lithium ion (Li-ion) battery electrodes.¹ Several polymer nanofibers have been fabricated from single polymer solutions (*e.g.*, polyacrylonitrile (PAN) in dimethylformamide (DMF)). However, the capabilities of electrospun nanofibers extend beyond single component materials. In many cases, polymers can be combined with nanoparticles to create composites.² When this combination is used to fabricate electrospun nanofibers, their properties can be enhanced. For example, it has been shown nanoparticles (*e.g.*, silicon or tin) can improve the performance of nanofibers when used as Li-ion battery electrodes.³⁻⁵ Another way to expand the capabilities of electrospun fibers are from blends. Blending polymers is a technique to prepare nanofibers that contain a polymer that is not able to be electrospun independently. One example of such material is sodium alginate. This biopolymer has shown promise in regenerative medicine as a tissue scaffold material.⁶ While its inherent material properties have prevented it from being electrospun independently, a few recent studies have demonstrated alginate-based nanofibers can be created from blends containing polyethylene oxide (PEO) and surfactants.⁷⁻⁹

While incorporating more than one material into electrospun nanofibers has potential benefits, many variables need to be considered. One variable is the effect of the second material (be it nano(particles), salts, surfactants, or polymers) on fiber morphology due to

changes in solution properties. For example, changes to the solution rheology (*i.e.*, increasing zero shear viscosity and relaxation time) have been associated with increases in fiber diameter and the suppression of bead defects.^{10, 11} Another variable that can be altered by the introduction of a second component is the ionic conductivity of the electrospinning solution. For example, adding a salt (which may be precursors to nanoparticles), typically increases ionic conductivity, which may result in the suppression of bead defects or the formation of branches between fibers.^{10, 12} Throughout this thesis, solution properties are examined to better understand how particular properties influence the electrospinning of polymer composites and blends. This is accomplished by characterizing solution properties and relating them to the structure and morphology in the electrospun fibers. For example, for each system, the solution rheology (*e.g.*, zero shear viscosity, relaxation time, entanglement concentration), ionic conductivity, and/or surface tensions are evaluated, and related to the colloidal/polymer interactions between the solution components. A fundamental understanding of the effects of solution parameters on electrospun composites and blends is important because it provides insight to the fabrication of other polymer systems.

In addition to solution-dependent variables, variables in the electrospinning setup can affect the formation of nanofibers. For example, the distribution of nanoparticles¹³ or copolymers¹⁴ within a composite fiber can be influenced by the applied electric field. In addition to the electrospinning apparatus, the ambient conditions appear to have a significant role in the electrospinning process. Specifically, the relative humidity can affect the formation or suppression of bead defects¹⁵, as well as the electrospun fiber surface

appearance.^{16, 17} Due to their important roles in the formation of composite and blended nanofibers, these variables are discussed and manipulated throughout this thesis. Moreover, we examine the relationships between the solution properties and their individual (or combined) effects on the electrospinning process dynamics and the resulting fibers.

1.1.2. Composite Electrospun Nanofibers

One technique to enhance the properties of electrospun fibers is by incorporating (nano)particles or (nano)fillers on or underneath the fiber surfaces. For example, carbon nanotubes inside of nanofibers increase the tensile strength of the fiber mat,¹⁸ whereas iron particles on the fibers surfaces are reactive sites that allow carbon nanotubes to grow from the fibers.¹⁹ In order to add nanoparticles into electrospun fibers there are two common approaches: *ex situ* and *in situ*.

In the *ex situ* method, nanoparticles are added to the polymer solution and electrospun. In the *in situ* approach, a nanoparticle precursor is added to the polymer solution and nanoparticles are formed by conversion in solution or in the electrospun fiber. For this approach, variability in nanoparticle distribution has been observed. Differences in the distribution of nanoparticles, ranging from aggregates on the fiber surfaces to individual particles embedded being within the fiber,²⁰ are a result of the chosen preparation approach and materials. Although limited, previous research suggests that for the *ex situ* approach,

nanoparticle distribution can be affected by three factors: (1) particle conductivity, (2) particle surface chemistry, and (3) particle stability in solution. Specifically, it has been observed that metal nanoparticles align along the fiber axis;¹³ chemical incompatibilities between the fiber polymer and particles result in un-encapsulated particles;²¹ and non-stabilized nanoparticles form aggregates in the electrospun fiber.²⁰ However, it is unknown if these three factors universally contribute to the distribution of nanoparticles within electrospun fibers. In this project, we attempt to better understand the role of these factors on particle distribution in electrospun fibers.

Our interest in composite nanofibers and the underlying mechanism controlling such formation stems from the importance of nanoparticle distribution in Li-ion battery technology. In this application, carbonized composite nanofibers can be directly used as anodes for Li-ion batteries. One challenge for the development of a composite Li-ion anode, however, is that the nanoparticles need to be uniformly distributed within the fiber and spatially-separated. A homogenous distribution prevents the nanoparticles from aggregating into larger particles during lithium insertion, thereby improving the anode capacity. Separate studies suggest that tin oxide nanocomposites²² and carbonized PAN nanofibers²³ are promising materials for Li-ion battery anodes. Additionally, a few recent studies have shown the potential benefits of tin/tin oxide on the performance of carbon nanofiber anodes.^{3, 4} Thus, combining the complementary properties of tin oxide (*i.e.*, high specific capacity) with carbon (*i.e.*, good cycle life), and the high surface energy of electrospun nanofibers yields a promising material for lithium ion batteries.

The goals of the composite fiber research entail examining fundamental and technological issues pertaining to (nano)particle-filled (nano)fibers and its relevance to lithium ion batteries. These goals are:

Goal 1 (Chapter 2): To evaluate parameters that affect composite electrospun fibers prepared by *ex-situ* electrospinning. These parameters include the compatibility between particle surface groups and the polymer. Of particular interest is to test the hypothesis that fumed silica particles with hydrophobic surface functionalities could be incorporated within a hydrophobic polymer fiber (*i.e.*, PAN) because of their chemical compatibility. Composite solutions are characterized with solution rheology to reveal information about the dominate particle-particle and polymer-particle interactions.

Goal 2 (Chapter 3): To investigate the distribution and the loading of a tin salt (*i.e.*, tin sulfate) within PAN nanofibers by two different fabrication schemes: (a) *in-situ* electrospinning within PAN/DMF solutions and (b) a soak treatment of nanofibers in aqueous salt solutions. The salt-polymer nanofibers are subsequently converted to tin oxide-carbon composites and evaluated as anodes in Li-ion batteries. We test the hypothesis that the soak treatment will raise the tin loading within the nanofibers, due to tin sulfate's higher solubility in water than DMF. Thus, we expected that the composite fiber mats would have enhanced performances, relative to single component, carbon fibers when evaluated as Li-ion battery anodes.

1.1.3. Blended Electrospun Nanofibers

Up to this point, we have discussed the effects of salt or particles on a polymer that is capable of being electrospun in its pure state with a solvent. However, not all polymers can be electrospun independently due to inherent properties of the polymer. For example, electrospinning low molecular weight polymers (typically <100 kDa) can result in beads or beaded fibers because of the polymer's poor chain entanglements.^{24, 25} Attempts to electrospin polymers that contain charged groups (*e.g.*, polyelectrolytes) may also be limited by the charge repulsions between polymer chains.²⁶ Researchers have compensated for the inherent shortcomings of these polymers by incorporating other polymers, surfactants, and salts into the electrospinning solutions. As a result, the blended solutions have been successfully electrospun into fibers. In order to enhance electrospinning of the primary polymer, PEO can be blended with chitosan,²⁷ and sodium chloride can be added to poly(2-(dimethylamino) ethyl methacrylate hydrochloride) (PDMAEMA HCl)²⁶, for example. In essence, the second component mitigated the underlying property of the polymer that is responsible for the electrospinning limitation. However these strategies are not universal for every polymer solution. Moreover, the addition of the second component may result in undesirable fiber characteristics or morphology, as discussed earlier. Adding salts to aqueous polymer solutions may cause branched fibers as a result of high ionic conductivities¹², for example. Thus, an investigation of the solution parameters that affect the electrospinning of blends is presented in this thesis.

One material of particular interest for the work presented here is sodium alginate, a polyelectrolyte. (Figure 1.1.) As a biopolymer derived from seaweed, alginate's benign nature has several promising applications, including in the biomedical field. While alginate has shown tremendous potential as a tissue scaffold material in a hydrogel form⁶, it is not capable of being electrospun in its pure state from aqueous solutions. It has been suggested that alginate does not electrospin because of its poor chain entanglements, which are a result of charge repulsions between the polymer chains when in solution.²⁸ Recently, a few researchers have shown that alginate can be electrospun when combined with another polymer or co-solvent.^{7, 9, 28} However, it is not known how solution properties of the alginate blends affect fiber morphology. This leads to our third goal:

Goal 3 (Chapter 4): To characterize the solution properties (*e.g.*, relaxation time, surface tension) and the resulting electrospinning formation when sodium alginate is blended with a polymer (*i.e.*, PEO) and a nonionic surfactant. Since alginate-based nanofibers have potential biomedical applications, we evaluate materials that have low toxicity to cells. For this goal, we test the hypothesis that the addition of an FDA-approved nonionic surfactant (*i.e.*, Pluronic F127) to alginate-PEO solution blends suppresses the formation of bead defects as a result of reduced surface tension.

While working on Goal 3, it was observed that some alginate solutions resulted in three-dimensional (3D) electrospun mat structures. This unexpected finding appeared to be associated with the relative humidity of the electrospinning atmosphere. A few studies have

reported 3D mat formations from other polyelectrolyte solutions. For example, solutions containing poly(p-xylenetetrahydrothiophenium chloride)²⁹ and hyaluronic acid³⁰ formed yarn-like and cotton-like structures, respectively, which extended from the surface of the collector plate in the direction of the electric field. In the former study, it was also reported that relative humidity affected the 3D structure.²⁹ While it has been suggested that observed structures were related to the electrical discharge from the ionically-conductive fibers, no systematic investigation has been conducted to determine the underlying mechanism. Furthermore, although the electric field has been previously shown to distribute charged components near the surface of electrospun jet,¹⁴ its role in the formation of 3D structures containing polyelectrolyte has not been addressed.

Being able to generate 3D structures is of interest because of their potential applications, such as in regenerative medicine. Recent studies in tissue engineering have shown the advantages of scaffolds with 3D structures over traditional 2D (*e.g.*, Petri dish).³¹ This is because the extracellular matrix (ECM), the structure in the body that promotes cell spreading, attachment, and proliferation,³² allows for tissue growth in three dimensions. Thus, a 3D mat nanofiber structure composed of a biocompatible material, such as alginate, would have exciting implications in tissue engineering.

Even though alginate is a polyelectrolyte in solution, 3D alginate mat structures have not been reported in the literature. Moreover, understanding the solution and process

parameters that influence the 3D formation provides a means to control its structure. This leads to our fourth goal:

Goal 4 (Chapter 5): To evaluate solution and process parameters which contribute to the formation of 3D mat structures of alginate-based electrospun nanofibers. We test the hypothesis that alginate is preferentially distributed on the surface of the electrospun nanofibers by the electric field, due to its charges in solution. We also parametrically manipulate the relative humidity during the electrospinning procedure to determine its effect on alginate surface charges within the electrospun nanofibers and the morphology of the 3D mat structure.

1.1.4. Thesis Goal for Polymer Hydrogels

Hydrogels are 3D solid-like structures composed of crosslinked, water-soluble polymers, and have applications in regenerative medicine and microfluidics.³³ As with electrospun nanofibers, hydrogels are another material in which the solution properties and the dynamics of formation affect the final structure. The mechanical properties (*e.g.*, porosity and modulus) of hydrogels can be tailored to the specific application by manipulating the hydrogel fabrication scheme. In general, increasing the concentration of crosslinking agent raises the modulus by increasing the crosslinking density within the hydrogel (as reviewed by Anseth *et al*³⁴). Furthermore, the crosslinking dynamics can play a

critical role in the structure of the formed hydrogel and its resulting mechanical properties.³⁵

This leads to our fifth goal:

Goal 5 (Chapter 6): To characterize the crosslinking reaction in a hydrogel by rheological methods. Specifically, the reaction of a photocurable alginate is monitored *in-situ* and manipulated through solution (*i.e.*, concentration of crosslinking group) and process parameters (*i.e.*, UV intensity). We relate the properties of the hydrogel to its internal structure of the solution.

1.1.5. Motivation for Diverse Research Areas

The works described in this thesis include a variety of materials and fabrication methodologies. However the underlying themes of the characterization approaches and techniques to breakdown key parameters remains consistent throughout each study. One advantage of investigating materials with different applications is the ability to test the robustness of the fundamental approach to problem solving. For example, characterization of the solution properties by rheological methods is an effective way to gain insight on a vast spectrum of solution behaviors, and how these properties relate to the final material. In addition, one can form a new perspective on a work, by solving problems associated with a second area. Specific to this dissertation research, the effects of the ambient conditions (*i.e.*,

humidity) were realized during alginate electrospinning, and helped to explain some of the observations during the composite fiber experiments.

1.2. Background

1.2.1. Electrospinning

Electrospinning is a process to make submicron nonwoven fibers from polymer solutions using an electric field. Fibers prepared by electrospinning have high surface area and porosity, which are important for applications including gas sensors, energy-related materials, and tissue scaffolds. This novel process has advanced the development of nano-scale materials, yet has existed long before “nanotechnology” was popular.

The electrospinning technique was developed several decades before it was widely adopted by the scientific community. The concept dates back to 1934 when Formhals was issued a patent for preparing “artificial threads” from solutions passed through an electric field.³⁶ However, this process was underutilized until the work of Reneker and colleagues in the 1990s.^{37,38} Since then, it has been widely used as evident by the ever-growing number of publications. Furthermore, electrospinning applications have expanded. While initial work focused on identifying polymers that could be electrospun, it has now expanded to include functional materials for energy and tissue engineering applications, for example.

One reason for the popularity of electrospinning is its relative ease of use. The standard electrospinning setups include a syringe, syringe pump, voltage supply, and a collector plate. (Figure 1.2.) In basic terms, electrospinning involves the injection of a polymer solution into an applied electric field, which results in the deposition of non-woven fibers with diameters as small as 50-100 nm onto a collector plate. However, this simplified overview fails to recognize the complexity of the electrospinning process. The competitive interactions between the intrinsic properties of the electrospun solution and process variables create a complex sequence of events, while the solution is converted into solid fibers.

The first step in the electrospinning process begins with the drop of polymer solution that exits a needle at a controlled flow rate. An electric field is applied (typically of positive polarity) between the needle and collector plate. As the intensity of the field is increased, the electrostatic forces on the droplet dominate the surface tension and cause it to stretch into a conical shape, known as a Taylor cone.³⁹ The polymer solution forms a jet at an electric field threshold and ejects it from the syringe tip to the collector plate.

The surface of the jet is charged as a result of excess ions in the solution (which can be created by the flow of electric in/out from the metallic needle in neutral solutions).⁴⁰ As the jet is stretched toward the plate, the forces of the electric field compete with the surface tension and viscoelastic properties of the solution, in addition to the Columbic repulsions from the surface charges.⁴¹ Within a 1-5 cm from the needle, the jet experiences bending instabilities from an imbalance of the forces.²⁵ The bend is quickly exacerbated by repulsive

charges at the jet surface, which create a coil directed nearly perpendicular to the jet axis. At the same time, the jet was elongated, which causes the diameter to shrink and the solvent to evaporate.⁴⁰

During the whipping instability, segments of the coiled jet experience forces in two predominant directions: an outward component from like-charge repulsion in the jet and a component toward the collector plate from the electric field.⁴² These forces cause the jet to continue to elongate with increasingly larger path perimeters. Additional bending instabilities lead to the formation of higher order coils, which eventually terminate when the jet solidifies. This sequence of events determines the diameter and morphology of the electrospun fibers, which can be altered by manipulating solution properties (*e.g.*, viscosity, relaxation time, surface tension, ionic conductivity) and process variables (*e.g.*, flow rate, electric field strength, relative humidity).⁴¹

Two process parameters that are commonly overlooked, but can have profound consequences on the electrospun fiber are *electric field* and *relative humidity*. The electric field can attract polarizable species in the solution to the surfaces of the Taylor cone and jet, resulting in a preferential surface-loading of a component in electrospun fibers.⁴³ For example, a peptide-polymer conjugate was present at the surface, while PEO remained in the interior of a blended electrospun fiber, due to electric field.^{14, 43}

In addition to the electric field, the humidity influences the electrospun fiber morphology in different capacities, depending on the type of polymer. For water-soluble

polymers, such as PEO, the predominant effect of humidity is related to the rate of solidification of the jet. In dry environments (<20% RH), water evaporates more quickly than in more humid conditions (>40% RH), resulting in the solidification of the jet closer to the needle. Thus, the jet is elongated less in the dry condition, resulting in larger diameter fibers.¹⁵ Moreover, the jet in the humid conditions are more susceptible to higher order whipping instabilities, which can lead to beaded fibers. (Figure 1.3.) The effects of humidity are more complicated for water-insoluble polymers, such as polystyrene and PAN. The water vapor can lead to localized phase separations at the jet surface, resulting in pores on the fiber surfaces.^{16, 17} Thus, controlling the electrospinning environment is crucial for consistency in electrospinning fiber morphology.

1.2.2. Polyacrylonitrile Nanofibers *via* Electrospinning

The structure of polyacrylonitrile and its solubility in solvents make it an ideal material for fiber applications. PAN is soluble in aprotic solvents, including DMF and dimethylsulfoxide (DMSO). Shown in Figure 1.4, the chemical structure of PAN consists of a carbon backbone with a nitrile side pendant group. It forms a stable solution in DMF due to the interactions between the nitrile group in PAN and the nitrogen group in DMF.⁴⁴ Although PAN's ability to dissolve in aprotic solvents is attractive for many applications, its *poor solubility* in many solvents has also been utilized. The textiles industry has produced polyacrylonitrile fibers in a wet spinning process, which are formed as they pass into a water

coagulation bath.⁴⁵ In summary, the interactions between PAN and various solvents are important; these can be a deterrent, or an exploit.

When used as a stable solution in DMF, PAN can be easily electrospun into nanofibers. Researchers have prepared solutions containing PAN with molecular weight 80,000 or 150,000 g/mol and concentrations 7-15% in DMF that were electrospun into fibers with diameters ranging from a few hundred nanometers to micron-sized.^{46, 47} Other researchers reported PAN nanofibers with diameters as low as 65 nm when the polymer solution was heated to 90°C prior to electrospinning.⁴⁸ Methods to electrospun polyacrylonitrile nanofibers are well-documented in the literature. For this reason, PAN was selected as the polymer to prepare composite nanofibers containing nanoparticles in this thesis work.

1.2.3. Polyacrylonitrile as a Precursor to Carbon Fibers

The ability of PAN to be carbonized is one of its most useful properties. PAN is the precursor for 90% of all carbon and graphite fibers produced commercially.⁴⁹ The process of converting PAN to carbon is achieved by chemically-modifying its structure through a series of heat treatments. (Figure 1.4) The first heat treatment is done at 250-300°C in air. During this step, PAN becomes crosslinked from dehydrogenation and cyclization reactions. The resulting crosslinked structure prevents chain scissions during the subsequent heat

treatments.⁵⁰ The next thermal treatment is performed in an inert atmosphere, such as nitrogen or argon. The oxidized fibers become carbonized as they are heated up to 700-1100°C. During this process, the non-carbon elements are released in the forms of methane, hydrogen, hydrogen cyanide, water, carbon dioxide, and ammonia.⁴⁹ The carbonized fiber has a higher density, reduced diameter, and is 40-50% of its weight compared to the original material.^{23, 51} The carbon fibers can be used in this state, or can undergo additional heat treatments up to 3000°C to yield graphitic structures.⁵² The carbon and graphite fibers are conductive and have a stable structure, which have many important applications. For example, carbonized PAN nanofibers prepared by electrospinning have been used as anodes in lithium ion batteries.²³

1.2.4. Nanofibers Containing Nanoparticles *via* Electrospinning

In addition to carbon fibers, nanocomposite materials formed by electrospinning have many novel properties. The combination of the two unlike materials, particle and nanoparticles have many uses, including antimicrobial fabrics and gas sensors.^{1, 53, 54} The methods to prepare composite nanofibers add a level of complexity to the facile electrospinning process. We will discuss two approaches, *ex situ* and *in situ*. The distribution of the nanoparticles within the nanofiber is affected by both methods.

1.2.4.1. Ex Situ Preparation of Nanofibers Containing Nanoparticles

The *ex situ* method is the first of the two approaches to prepare composite nanofibers. In this method nanoparticles are added directly to the polymer solution and then electrospun. More specifically, the nanoparticles are synthesized separately, prior to being combined with the polymer solution. The distribution of nanoparticles within fibers prepared by the *ex situ* method is affected by nanoparticle (1) conductivity, (2) stability in solution, and (3) surface chemistry of polymers.

The distribution of nano-materials within electrospun nanofiber by *ex situ* preparation is dependent on their stability and conductivity. For example, carbon nanotubes are a common additive, based on their ability to improve the conductive and mechanical properties of electrospun fibers.⁵⁵ McCullen *et al.* and Hou *et al.* reported composites of carbon nanotubes within polyethylene oxide and polyacrylonitrile fibers.^{18, 56} Prior to electrospinning, the surfaces of the carbon nanotubes were modified by gum arabic or nitric acid to prevent aggregation in water or DMF, respectively. After electrospinning homogenous solutions, analysis by transmission electron microscopy (TEM) revealed that nanotubes aligned along the axis of the fibers. A similar observation was made when metal and metal oxide nanoparticles were added to polymer solutions for electrospinning. Gold nanoparticles stabilized by thiol groups were electrospun with PEO in chloroform.¹³ The authors reported “chainlike” structures of gold nanoparticles aligned axially inside the PEO fibers. Rutledge and co-workers also reported a similar appearance of iron oxide (Fe₃O₄) particles aligned within PEO and polyvinyl alcohol (PVA).⁵⁷ In each of these examples, the

stability of the nanotubes/particles in solution and conductivity contributed to their distribution within the fiber.

Just like in the previous examples with conductive nano-materials, particles that are insulators can be encapsulated within electrospun fibers. However, in contrast to the previous studies, the distribution of the particles was determined by the chemical compatibility between their surface groups and the polymer. Researchers varied this compatibility by changing the electrospun polymer. Lim *et al.* combined silica particles, stabilized in solution, with polyacrylamide (PAM), PEO, and PAN and electrospun composite fibers.²¹ They found that the hydrophobicity of the polymer affected the silica particle distribution in the fiber. PAM and PEO are more hydrophilic than PAN, and encapsulated the hydrophilic silica. By comparison, silica particles were present on the outer surfaces of the PAN. This study is important because it showed that particles that can be stabilized in a solution may not be embedded within the electrospun fiber. Thus, the compatibility between the surface groups on silica particles and the polymer chemistry was a crucial factor. Despite the implications of this work to future studies that prepare composite fibers, the results may not be universal for all particles. This is because all of the particles tested were greater than 100 nm. Particles that are the same size as (or larger than) the polymer fibers will affect the electrospinning dynamics differently than particles much smaller than the fiber. As the polymer solution is stretched within the electric field, its ability to cover the surfaces of large particles is determined by its “wettability.”²¹ In contrast, the polymer can effectively cover particles that are much smaller than final fiber diameter. As a

result, they can be incorporated within the fibers, as shown with conductive nanoparticles in the previous section.¹³ However, little or no work is available that investigates how non-conductive nanoparticles are distributed within electrospun nanofibers, or how the compatibility of the surface groups on nanoparticles with the polymer affects their distribution. Thus, a study that systematically tests the conductivity of nanoparticles and surface functionality would be crucial for developing composite nanofibers with specific distributions.

The composite fibers that have been discussed up to this point have been prepared using nanomaterials stabilized in solution by surface groups. In these cases, the nanoparticles were spatially-separated throughout, or on the surface of electrospun fibers. In contrast, the distribution of nanoparticles that are not well stabilized in solution prior to electrospinning is more limited. Instead of having well-dispersed individual nanoparticles, aggregates of nanoparticles may form on the fibers. To show this, researchers have electrospun nanoparticles with varying degrees of stabilization in solution. For example, Andrew *et al.* prepared polymer solutions for electrospinning with either Ni-Zn ferrite nanoparticles stabilized with silica surface groups or titanium dioxide nanoparticles dispersed in solution.⁵⁸ The ferrite particles were spatially-separated within the fiber, whereas the TiO₂ particles were present as surface aggregates. Kedem *et al.* observed a similar result when they combined TiO₂ and carbon nanotubes with PAN.²⁰ The carbon nanotubes were present within the fiber, whereas the titania nanoparticles were present near/on the surface. In both of these examples, the limited stability of the nanoparticles prior to electrospinning caused

the formation of aggregates. The location of the aggregates on the surface on the fibers may be the result of incompatibilities between the surface chemistries of the polymer and particle, or the effects of charging induced by the electric field.²¹ One aspect that these works did not address was to change the stability of the same material. For example, electrospinning TiO₂ particles with and without surface groups would be a systematic approach to investigate particle distribution in electrospun fibers.

In summary, composite nanofibers containing nanoparticles and nanotubes have been prepared by electrospinning, using an *ex situ* method. The stability of the nanoparticles in solution, conductivity, and surface compatibility with the polymer contributed to their distribution within the electrospun fiber. Despite the publications using the *ex situ* method, the literature lacks a fundamental study that investigates these factors, in detail. The work described in this thesis (Chapters 2) attempts to understand the roles of particle stability, surface functionality, and polymer chemistry on the particle distribution in composite fibers.

1.2.4.2. In Situ Preparation of Nanofibers Containing Nanoparticles

In contrast to *ex situ* which uses pre-synthesized nanoparticles, the *in situ* method involves the synthesis of nanoparticles in the polymer media of interest. Metal salts are combined with the polymer solution and reduced prior to electrospinning, or in the electrospun fiber. Additionally, the nanoparticles can be synthesized while the polymer is also converted to a new structure, such as during a carbonization process. One advantage of

the *in situ* method over the *ex situ* is that the distribution of the spatially-separated nanoparticles within the fiber can be controlled with the conversion step. Fibers can be prepared with nanoparticles distributed throughout the interior, as well as predominately near the surface. Thus, depending on your application needs, you may tailor the distribution of the particles within the fiber by using different reduction approaches.

Reducing metal salts prior to electrospinning can yield electrospun fibers with conductive nanoparticles distributed throughout the interiors, as well as on the surface; this is a different distribution from composite nanofibers by *ex situ*. Several nano-composites have been prepared by the *in situ* approach, including some that use a facile one-step procedure. For example, Youk and co-workers prepared silver nanoparticles from a salt, with PAN or polyvinylpyrrolidone (PVP) in two separate studies.^{59, 60} In both cases, DMF was the solvent and the reducing agent of silver nitrate. Nanoparticles formed within the PAN polymer solutions within a few hours after introducing the salt. The solutions were subsequently electrospun into composite fibers. Analysis by TEM revealed that the nanoparticles were distributed within the fibers, as well as on the surface. Unlike the *ex situ* methods, the nanoparticles in these studies did not align along the axis of the fiber. This can be attributed to the role of PVP and PAN during the nanoparticle synthesis. The polymers stabilized the nanoparticles during the nucleation.⁶⁰ As a result, the nanoparticles were part of the polymer matrix during electrospinning, and the effects of the electric field on individual particles were reduced. Nanoparticles that are distributed throughout the fiber and not packed together in aligned chains are preferred for applications where a maximum separation distance is needed

between the nanoparticles. For example, metal particles that are hosts for lithium in battery anodes can expand when forming an alloy.⁶¹ Nanoparticles that are closely aligned may combine during the lithium insertion and volume change, which would reduce the number of host sites in the anode. Thus, metal nanoparticles distributed evenly throughout fibers prepared by *in situ* would be more appropriate for battery applications.

Nanoparticles that are predominately on the surface of the fibers can also be prepared using another *in situ* approach. Unlike the last method, metal salts can be reduced *after* electrospinning. For example, PVP nanofibers containing lead acetate were exposed to H₂S gas, resulting in lead sulfide particles.⁶² In another study, PAN nanofibers containing silver salt were soaked in a solution of N₂H₅OH, a reducing agent.⁶³ This resulted in silver nanoparticles of different sizes that were location dependent; the largest particles were on the fiber surfaces. The diffusion of the reducing agent within the fibers most likely contributed to the size discrepancy. Thus, a nanocomposite materials prepared by this *in situ* method would be appropriate for applications where nanoparticles are used as surface active sites, such as gas sensors.⁵⁴

The final *in situ* approach involves converting two different materials in one step. Two topics that have been discussed previously are the carbonization of a polymer by heat treatments, and the reduction of metal salts into nanoparticles. These two steps can be used in PAN nanofibers containing metal salts, which make PAN an attractive material for composite carbon nanofibers. Researchers have used an additional heat step during the

carbonization to activate the nanoparticles. For example, electrospun PAN nanofibers containing ruthenium(III) acetylacetonate, underwent a series of three heat treatments.⁶⁴ The composite fibers were (1) stabilized in air to crosslink the PAN, (2) heated to 800°C under nitrogen to carbonize the fibers, and then (3) activated in a nitrogen/steam atmosphere to convert the ruthenium complex. The resulting carbon fibers had ruthenium particles dispersed on and below the outer surfaces. Other researchers prepared carbon nanofibers containing iron nanoparticles by a similar method; in place of a third heat treatment, they used a reducing agent gas. Reneker and co-workers reduced iron acetylacetonate inside PAN fibers in an argon/hydrogen atmosphere at 550°C, after stabilization in air.¹⁹ The fibers were subsequently carbonized at 1100°C in argon. Iron nanoparticles were predominately on the fiber surface, due to the diffusion-limiting reaction. In another study Fe₃O₄ nanoparticles were prepared using the same iron precursor.⁶⁵ The formation of the iron oxide nanoparticles occurred during the stabilization and carbonization steps, without additional activation. Thus, the ability of PAN to be carbonized can be exploited as part of an *in situ* approach to make nanoparticles. Composite carbon nanofibers containing nanoparticles have many applications, including materials in Li-ion batteries.⁶⁶

In summary, the *in situ* method for preparing nanoparticles within nanofibers can be performed before or after electrospinning. One advantage of this approach compared to *ex situ* is the polymer matrix acts as the stabilizing group on the nanoparticles. Thus, nanoparticles can be embedded within the polymer fiber without additional surface modifying groups, which may not be compatible with the solvent or polymer. However,

nanoparticles formed in the electrospun fiber may be polydisperse and concentrated near the outer surfaces as a result of diffusion-limited reactions. The *ex situ* method is more appropriate when stabilized nanoparticles are readily available, eliminating a reduction step.

While previous work has prepared and characterized composite nanofibers by *ex situ* and *in situ* methods, these studies do not directly assess the nanoparticle distribution. The nanoparticle distribution can be affected by the particle stability in solution and chemical compatibility between surface groups. However, these factors have not been tested systematically. This is an important research direction because the applications for composite fibers may require a certain distribution. For example, a particle that is a catalyst for a surface reaction would need a different distribution than a particle that reinforces the fiber structure.^{18, 19} Thus, the work in this thesis attempts to understand the solution and process parameters that affect the (nano)particle distribution within electrospun fibers. (Chapters 2, 3)

1.2.5. Applications for Electrospun Nanofibers: Li-ion Battery Electrodes

We live in a world that is “power hungry.” Technology users expect to be able to use portable electronics, such as cell phones, computers, and transmitters, on a regular basis; however, battery life is a major limitation of current devices. For example, soldiers in the field for more than 48 hours may have to carry 30 pounds of batteries to power their signal

transmitters.⁶⁷ Thus, there is a great need for lighter, more powerful batteries. New generations of Li-ion battery can meet these requirements with advances in nanotechnology.⁶⁸ One way to utilize nanotechnology with Li-ion batteries is to use composite nanofibers. Nanofibers have high surface area and porosity, and nanoparticles within the fibers can be used as host sites for electrochemical reactions. Recent studies have shown the potential benefits of composite nanofibers used as electrodes in Li-ion batteries.(*e.g.*,^{5, 66}) Work in this thesis investigates the effects of composite carbon nanofibers filled with nanoparticles (*i.e.*, tin oxide) on their performance as Li-ion anodes.

1.2.6. Alginate Nanofibers *via* Electrospinning

Like PAN, sodium alginate is another polymeric material with a range of applications, including wound healing.⁶⁹ Alginate is a biocompatible, water-soluble polysaccharide, derived from the seaweed. The structure of alginate is composed of blocks of α -D-mannuronic acid (M) and α -L-guluronic acid (G), which can dissociate in solution. As a polyelectrolyte, the tendency for alginate chains to be negatively-charged in solution may have consequences on its ability to be fabricated into functional materials, such as electrospun nanofibers.

A few researchers have reported on the inability of alginate to be electrospun in a pure state from aqueous solutions.^{7, 9, 28} Possible explanations have included the gel-like

behavior of alginate⁷ and the lack of chain entanglements due to its rigid, charged structure.²⁸ However, the inherent challenges of alginate have been overcome by combining it with a second polymer. In one case, chitosan and alginate formed a gel, which was subsequently electrospun into nanofibers.⁷⁰ In the most commonly used approach, another water-soluble polymer (*e.g.*, PEO or PVA) was blended with alginate and electrospun.^{8, 9, 71, 72} PEO and PVA can be electrospun by themselves, and serve as “carrier” polymers for alginate. Hydrogen bonding between the blended polymers may aid in electrospinning.^{28, 73}

1.2.7. Applications for Electrospun Nanofibers: Tissue Engineering Scaffolds

Alginate nanofibers offer exciting possibilities for use as tissue scaffolds. Previous studies with alginate hydrogels have shown its capabilities in regenerative medicine.⁶ Furthermore, electrospun nanofiber mats have the potential to mimic the structure of the extracellular matrix, as well as promote cell adhesion, spreading, and proliferation.³² As discussed above, alginate can be electrospun into nanofibers when blended with another polymer. In one of the first studies to evaluate the alginate-based nanofiber mats as scaffolds, researchers showed their cell viability.⁷ Cell adhesion and spreading was improved by electrospinning alginate modified by the RGD peptide, as compared to unmodified alginate nanofibers.⁷⁴ While these early studies have identified alginate nanofibers as potential scaffolds, further work is needed to broaden the capabilities of the material (*e.g.*, M_w appropriate for *in vivo* use). Work in this thesis examines the preparation

of electrospun alginate nanofibers, including those composed of a low molecular weight (*i.e.*, 37 kDa) alginate. (Chapters 4, 5)

1.2.8. Hydrogels

Similar to electrospun nanofibers, hydrogels are another polymer-based functional material that can be relatively facile to fabricate. These insoluble, 3D network-materials with customizable shapes can be prepared by dissolving a polymer (*e.g.*, alginate) in water with an appropriate amount of crosslinking agent (*e.g.*, calcium chloride).⁷⁵ (Figure 1.5.) Despite their potential ease of fabrication, the applications of hydrogels can be complex, ranging from microfluidic devices to regenerative medicine.³³ The variety of uses for hydrogels is a testament to the versatility of the material, since its properties (*e.g.*, porosity, stiffness) can be customized by manipulating concentrations and crosslinking conditions.⁷⁶ These properties are related to the connectivity of the molecular structure inside the hydrogel.

1.2.9. Rheological Methods to Study Gelation

Knowledge of the formation of the molecular structure within the hydrogel, including the polymerization kinetics, is important when tailoring its material properties.⁷⁶ One technique to characterize the crosslinking reaction dynamics is by using solution rheology,

since changes in the rheological properties of the material reflect the formation and density of crosslinks.⁷⁷ In particular, dynamic, small amplitude oscillatory shear (SAOS) measurements can be used to monitor the gelation reaction with minimal disruptions to the forming network, compared to other rheological techniques (*e.g.*, steady-state shear).⁷⁸ The rheological properties of the forming hydrogel can be monitored in-situ with a reaction that is initiated at start of the rheological experiment, either by self initiation, or by external conditions (*e.g.*, light, heat).

Some important material properties of gels measured by dynamic rheology include the storage (G') and loss (G'') moduli, which correspond to the behavior of the material as an elastic solid and viscous liquid, respectively. In a strain-controlled rheometer, these properties can be represented as:⁷⁹

$$\tau(t) = \gamma_0 [G'(\omega) \sin(\omega t) + G''(\omega) \cos(\omega t)] \quad (1.1)$$

In the above expression, ω is the frequency of oscillation, γ is the strain amplitude, t is time, and τ is measured stress on the sample. The ratio of the two moduli can be expressed as:

$$\tan \delta = \frac{G''}{G'} \quad (1.2)$$

The value of the tangent of the phase angle (δ), or the loss tangent, is >1 for liquid-like materials, and <1 for solid-like materials. This parameter is of particular interest to (hydro)gel reactions, since it can be used to determine the gel point.⁸⁰ Another important property is the complex or dynamic viscosity (η^*), which may be related to the viscosity ($\eta(\tau)$) measured in steady shear experiments,⁸¹ is represented as:

$$\eta^*(\omega) = \left[\left(\frac{G''}{\omega} \right)^2 + \left(\frac{G'}{\omega} \right)^2 \right]^{1/2} \quad (1.3)$$

The formation of (hydro)gels can be also be represented by the initial and final states, which can help to explain the transition region from pregel to gel. During gelation a fluid transitions into a solid; the material properties of each state are expressed as:⁸²

$$\eta_0 = \frac{\tau}{\dot{\gamma}} \text{ for fluids, where } \eta_0 \text{ is the zero shear viscosity, and } \dot{\gamma} \text{ is the strain rate}$$

$$G_e = \frac{\tau}{\gamma} \text{ for solids, where } G_e \text{ is the equilibrium modulus}$$

The fluid-to-solid transition can be characterized by rheological material properties as functions of time, which also relate to the zero shear viscosity and equilibrium modulus. In addition, insight on the structure within the hydrogel can be obtained from changes in the material properties. In the early stages of gelation $G'' > G'$ and corresponds to a fluid having limited connectivity between its forming networks. When the values of $G'' \sim G'$, the sol-to-gel transition connectivity of crosslinked structures begin to approach the size scale of the distance between the rheometer's plates. The critical gel is the state at which the network of crosslinked polymer chains spans the distance between the plates. The time at the critical gel, known as the gel point, relates to interesting changes in rheological properties. At the gel point, the zero shear viscosity and equilibrium modulus approaches positive and zero, respectively.⁷⁷ In addition the relaxation time of the gel reaches a maximum. For linear, flexible polymers, the G'/G'' crossover time (t_c) can correspond to the gel point.⁸³ The

intersection of loss tangent at different oscillatory frequencies has also been shown to predict the gel point.⁸⁴ Beyond the gel point, $G' > G''$, the crosslinking network becomes dense, and the material behaves like an elastic solid. Essentially, the G' curve will reach a plateau, or the terminal modulus, corresponding to the maximum modulus of the crosslinked gel.

1.2.10. Alginate Hydrogels

Of the many polymers that can form hydrogels, sodium alginate can be crosslinked by a variety of methods, as a result of its chemical structure. As shown in Figure 1.1, alginate is a polysaccharide that contains hydroxyl and carboxylic acid functional groups. These groups can become the sites for alginate's crosslinking reactions, depending on the method.

Alginate is capable of being crosslinked ionically, chemicallly, and/or photochemically. The first involves a physical association between a divalent salt (*e.g.*, Ca^{2+}) and alginate's G blocks.⁷⁵ Alginate chains can be chemical crosslinked at the site of the hydroxyl groups (*e.g.*, glutaldehyde) or the carboxylic acid groups (*e.g.*, adipic acid).⁷¹ Finally, the third crosslinking reaction type, involves a chemical modification of alginate's carboxylic acid groups, which subsequently can form crosslinks by a UV-curable reaction in the presence of a photoinitiator.⁸⁵

This final crosslinking type has potential for *in vivo* biomedical uses. Photocrosslinkable hydrogels have the capabilities to be gelled *in situ*, allowing the polymer

to match the shape of an implantation site, or to entrap cells that are uniformly distributed within the gelled structure.⁷⁶ Work in this thesis investigates the crosslinking reaction of photocrosslinkable alginate. (Chapter 6)

1.3. Organization of Dissertation

Chapter 2 focuses on the role of particle surface groups in *ex-situ* electrospinning. In Chapter 3, the factors affecting the incorporation of salts within electrospun nanofibers are investigated in two approaches: *in-situ* electrospinning and a post-electrospinning soak treatment. The role of surfactants and a co-polymer on the ability to electrospin a polymer (*i.e.*, alginate) which cannot be prepared into nanofibers in its pure form in water is investigated in Chapter 4. Chapter 5 describes the effects of solution properties and process parameters on the dynamics of electrospinning mats with 3D architectures. Chapter 6 focuses on the rheological behaviors within a photocrosslinkable hydrogel during its formation. The key findings of this work are summarized in Chapter 7, and future studies are proposed.

1.3.1. References

1. Huang, Z. M.; Zhang, Y. Z.; Kotaki, M.; Ramakrishna, S., A review on polymer nanofibers by electrospinning and their applications in nanocomposites. *Composites Science and Technology* **2003**, 63, (15), 2223-2253.
2. Winey, K. I.; Vaia, R. A., Polymer nanocomposites. *Mrs Bulletin* **2007**, 32, (4), 314-319.
3. Yu, Y.; Gu, L.; Wang, C. L.; Dhanabalan, A.; van Aken, P. A.; Maier, J., Encapsulation of Sn@carbon Nanoparticles in Bamboo-like Hollow Carbon Nanofibers as an Anode Material in Lithium-Based Batteries. *Angewandte Chemie-International Edition* **2009**, 48, (35), 6485-6489.
4. Zou, L.; Gan, L.; Kang, F.; Wang, M.; Shen, W.; Huang, Z., Sn/C non-woven film prepared by electrospinning as anode materials for lithium ion batteries. *Journal of Power Sources* **2010**, 195, 1216-1210.
5. Ji, L. W.; Zhang, X. W., Fabrication of porous carbon/Si composite nanofibers as high-capacity battery electrodes. *Electrochemistry Communications* **2009**, 11, (6), 1146-1149.
6. Alsberg, E.; Anderson, K. W.; Albeiruti, A.; Rowley, J. A.; Mooney, D. J., Engineering growing tissues. *Proceedings of the National Academy of Sciences of the United States of America* **2002**, 99, (19), 12025-12030.

7. Bhattarai, N.; Li, Z. S.; Edmondson, D.; Zhang, M. Q., Alginate-based nanofibrous scaffolds: Structural, mechanical, and biological properties. *Advanced Materials* **2006**, 18, (11), 1463-1467.
8. Nie, H. R.; He, A. H.; Wu, W. L.; Zheng, J. F.; Xu, S. S.; Li, J. X.; Han, C. C., Effect of poly(ethylene oxide) with different molecular weights on the electrospinnability of sodium alginate. *Polymer* **2009**, 50, (20), 4926-4934.
9. Safi, S.; Morshed, M.; Ravandi, S. A. H.; Ghiaci, M., Study of electrospinning of sodium alginate, blended solutions of sodium alginate/poly(vinyl alcohol) and sodium alginate/poly(ethylene oxide). *Journal of Applied Polymer Science* **2007**, 104, (5), 3245-3255.
10. Fong, H.; Chun, I.; Reneker, D. H., Beaded nanofibers formed during electrospinning. *Polymer* **1999**, 40, (16), 4585-4592.
11. Fridrikh, S. V.; Yu, J. H.; Brenner, M. P.; Rutledge, G. C., Controlling the fiber diameter during electrospinning. *Physical Review Letters* **2003**, 90, (14).
12. Barakat, N. A. M.; Kanjwal, M. A.; Sheikh, F. A.; Kim, H. Y., Spider-net within the N6, PVA and PU electrospun nanofiber mats using salt addition: Novel strategy in the electrospinning process. *Polymer* **2009**, 50, (18), 4389-4396.

13. Kim, G.; Wutzler, A.; Radusch, H.; Michler, G.; Simon, P.; Sperling, R.; Parak, W., One-Dimensional Arrangement of Gold Nanoparticles by Electrospinning. *Chemistry of Materials* **2005**, *17*, (20), 4949-4957.
14. Sun, X. Y.; Shankar, R.; Borner, H. G.; Ghosh, T. K.; Spontak, R. J., Field-driven biofunctionalization of polymer fiber surfaces during electrospinning. *Advanced Materials* **2007**, *19*, (1), 87-+.
15. Tripatanasuwan, S.; Zhong, Z. X.; Reneker, D. H., Effect of evaporation and solidification of the charged jet in electrospinning of poly(ethylene oxide) aqueous solution. *Polymer* **2007**, *48*, (19), 5742-5746.
16. Casper, C. L.; Stephens, J. S.; Tassi, N. G.; Chase, D. B.; Rabolt, J. F., Controlling surface morphology of electrospun polystyrene fibers: Effect of humidity and molecular weight in the electrospinning process. *Macromolecules* **2004**, *37*, (2), 573-578.
17. Pai, C. L.; Boyce, M. C.; Rutledge, G. C., Morphology of Porous and Wrinkled Fibers of Polystyrene Electrospun from Dimethylformamide. *Macromolecules* **2009**, *42*, (6), 2102-2114.
18. Hou, H. Q.; Ge, J. J.; Zeng, J.; Li, Q.; Reneker, D. H.; Greiner, A.; Cheng, S. Z. D., Electrospun polyacrylonitrile nanofibers containing a high concentration of well-aligned multiwall carbon nanotubes. *Chemistry of Materials* **2005**, *17*, (5), 967-973.

19. Hou, H.; Reneker, D. H., Carbon Nanotubes on Carbon Nanofibers: A Novel Structure Based on Electrospun Polymer Nanofibers. *Advanced Materials* **2004**, 16, (1), 69-73.
20. Kedem, S.; Schmidt, J.; Paz, Y.; Cohen, Y., Composite polymer nanofibers with carbon nanotubes and titanium dioxide particles. *Langmuir* **2005**, 21, (12), 5600-5604.
21. Lim, J.-M.; Moon, J. H.; Yi, G.-R.; Heo, C.-J.; Yang, S.-M., Fabrication of One-Dimensional Colloidal Assemblies from Electrospun Nanofibers. *Langmuir* **2006**, 22, (8), 3445-3449.
22. Li, N.; Martin, C. R., A High-Rate, High-Capacity, Nanostructured Sn-Based Anode Prepared Using Sol-Gel Template Synthesis. *Journal of the Electrochemical Society* **2001**, 148, (2), A164-A170.
23. Kim, C.; Yang, K. S.; Kojima, M.; Yoshida, K.; Kim, Y. J.; Kim, Y. A.; Endo, M., Fabrication of electrospinning-derived carbon nanofiber webs for the anode material of lithium-ion secondary batteries. *Advanced Functional Materials* **2006**, 16, (18), 2393-2397.
24. Shenoy, S. L.; Bates, W. D.; Frisch, H. L.; Wnek, G. E., Role of chain entanglements on fiber formation during electrospinning of polymer solutions: good solvent, non-specific polymer-polymer interaction limit. *Polymer* **2005**, 46, (10), 3372-3384.

25. Yu, J. H.; Fridrikh, S. V.; Rutledge, G. C., The role of elasticity in the formation of electrospun fibers. *Polymer* **2006**, 47, (13), 4789-4797.
26. McKee, M. G.; Hunley, M. T.; Layman, J. M.; Long, T. E., Solution rheological behavior and electrospinning of cationic polyelectrolytes. *Macromolecules* **2006**, 39, (2), 575-583.
27. Klossner, R. R.; Queen, H. A.; Coughlin, A. J.; Krause, W. E., Correlation of Chitosan's Rheological Properties and Its Ability to Electrospin. *Biomacromolecules* **2008**, 9, (10), 2947-2953.
28. Nie, H.; He, A.; Zheng, J.; Xu, S.; Li, J.; Han, C. C., Effects of Chain Conformation and Entanglement on the Electrospinning of Pure Alginate. *Biomacromolecules* **2008**, 9, 1362-1365.
29. Okuzaki, H.; Takahashi, T.; Miyajima, N.; Suzuki, Y.; Kuwabara, T., Spontaneous formation of poly(p-phenylenevinylene) nanofiber yarns through electrospinning of a precursor. *Macromolecules* **2006**, 39, (13), 4276-4278.
30. Kim, T. G.; Chung, H. J.; Park, T. G., Macroporous and nanofibrous hyaluronic acid/collagen hybrid scaffold fabricated by concurrent electrospinning and deposition/leaching of salt particles. *Acta Biomaterialia* **2008**, 4, (6), 1611-1619.
31. Lee, J.; Cuddihy, M. J.; Kotov, N. A., Three-dimensional cell culture matrices: State of the art. *Tissue Engineering Part B-Reviews* **2008**, 14, (1), 61-86.

32. Liang, D.; Hsiao, B. S.; Chu, B., Functional electrospun nanofibrous scaffolds for biomedical applications. *Advanced Drug Delivery Reviews* **2007**, 59, (14), 1392-1412.
33. Jagur-Grodzinski, J., Polymeric gels and hydrogels for biomedical and pharmaceutical applications. *Polymers for Advanced Technologies* **2009**, 21, (1), 27-47.
34. Anseth, K. S.; Bowman, C. N.; BrannonPeppas, L., Mechanical properties of hydrogels and their experimental determination. *Biomaterials* **1996**, 17, (17), 1647-1657.
35. Bowman, C. N.; Kloxin, C. J., Toward an Enhanced Understanding and Implementation of Photopolymerization Reactions. *Aiche Journal* **2008**, 54, (11), 2775-2795.
36. Formhals, A. Process and Apparatus for Preparing Artificial Threads. October 2, 1934, 1934.
37. Reneker, D. H.; Chun, I., Nanometre diameter fibres of polymer, produced by electrospinning. *Nanotechnology* **1996**, 7, (3), 216-223.
38. Doshi, J.; Reneker, D. H., Electrospinning Process and Applications. *Journal of Electrostatics* **1995**, 35, 151-160.

39. Taylor, G., Disintegration of Water Drops in Electric Field. *Proceedings of the Royal Society of London Series a-Mathematical and Physical Sciences* **1964**, 280, (138), 383-&.
40. Reneker, D. H.; Yarin, A. L., Electrospinning jets and polymer nanofibers. *Polymer* **2008**, 49, (10), 2387-2425.
41. Li, D.; Xia, Y. N., Electrospinning of nanofibers: Reinventing the wheel? *Advanced Materials* **2004**, 16, (14), 1151-1170.
42. Yarin, A. L.; Koombhongse, S.; Reneker, D. H., Bending instability in electrospinning of nanofibers. *Journal of Applied Physics* **2001**, 89, (5), 3018-3026.
43. Sun, X.-Y. Concurrent and Sequential Surface Modification of Electrospun Polymer Micro/Nano-Fibers. North Carolina State University, Raleigh, 2008.
44. Phadke, M. A.; Musale, D. A.; Kulkarni, S. S.; Karode, S. K., Poly(acrylonitrile) ultrafiltration membranes. I. Polymer-salt-solvent interactions. *Journal of Polymer Science Part B-Polymer Physics* **2005**, 43, (15), 2061-2073.
45. Paul, D. R., Diffusion During the Coagulation Step of Wet-Spinning. *Journal of Applied Polymer Science* **1968**, 12, 383-402.
46. Wang, T.; Kumar, S., Electrospinning of Polyacrylonitrile Nanofibers. *Journal of Applied Polymer Science* **2006**, 102, 1023–1029.

47. Chun, I.; Reneker, D. H.; Fong, H.; Fang, X. Y.; Dietzel, J.; Tan, N. B.; Kearns, K., Carbon nanofibers from polyacrylonitrile and mesophase pitch. *Journal of Advanced Materials* **1999**, 31, (1), 36-41.
48. Wang, C.; Chien, H. S.; Hsu, C. H.; Wang, Y. C.; Wang, C. T.; Lu, H. A., Electrospinning of polyacrylonitrile solutions at elevated temperatures. *Macromolecules* **2007**, 40, (22), 7973-7983.
49. Rahaman, M. S. A.; Ismail, A. F.; Mustafa, A., A review of heat treatment on polyacrylonitrile fiber. *Polymer Degradation and Stability* **2007**, 92, (8), 1421-1432.
50. Edie, D. D., The Effect of Processing on the Structure and Properties of Carbon Fibers. *Carbon* **1998**, 36, (4), 345-362.
51. Mittal, J.; Bahl, O. P.; Mathur, R. B., Single step carbonization and graphitization of highly stabilized PAN fibers. *Carbon* **1997**, 35, (8), 1196-1197.
52. Sittig, M., *Carbon and Graphite Fibers Manufacture and Applications*. Noyes Data Corporation: Park Ridge, NJ, 1980; p 422.
53. Lala, N. L.; Ramaseshan, R.; Li, B. J.; Sundarrajan, S.; Barhate, R. S.; Liu, Y. J.; Ramakrishna, S., Fabrication of nanofibers with antimicrobial functionality used as filters: Protection against bacterial contaminants. *Biotechnology and Bioengineering* **2007**, 97, (6), 1357-1365.

54. Luoh, R.; Hahn, H. T., Electrospun nanocomposite fiber mats as gas sensors. *Composites Science and Technology* **2006**, 66, (14), 2436-2441.
55. Chronakis, I. S., Novel Nanocomposites and Nanoceramics Based on Polymer Nanofibers Using Electrospinning Process--A Review. *Journal of Materials Processing Technology* **2005**, 167, 283-293.
56. McCullen, S. D.; Stevens, D. R.; Roberts, W. A.; Ojha, S. S.; Clarke, L. I.; Gorga, R. E., Morphological, Electrical, and Mechanical Characterization of Electrospun Nanofiber Mats Containing Multiwalled Carbon Nanotubes. *Macromolecules* **2007**, 40, 997-1003.
57. Wang, M.; Singh, H.; Hatton, T. A.; Rutledge, G. C., Field-responsive superparamagnetic composite nanofibers by electrospinning. *Polymer* **2004**, 45, 5505-5514.
58. Andrew, J. S.; Mack, J. J.; Clarke, D. R., Electrospinning of polyvinylidene difluoride-based nanocomposite fibers. *Journal of Materials Research* **2008**, 23, (1), 105-114.
59. Lee, H. K.; Jeong, E. H.; Baek, C. K.; Youk, J. H., One-step preparation of ultrafine poly(acrylonitrile) fibers containing silver nanoparticles. *Materials Letters* **2005**, 59, (23), 2977-2980.

60. Jin, W. J.; Lee, H. K.; Jeong, E. H.; Park, W. H.; Youk, J. H., Preparation of polymer nanofibers containing silver nanoparticles by using poly (N-vinylpyrrolidone). *Macromolecular Rapid Communications* **2005**, 26, (24), 1903-1907.
61. Winter, M.; Besenhard, J. O.; Spahr, M. E.; Novak, P., Insertion electrode materials for rechargeable lithium batteries. *Advanced Materials* **1998**, 10, (10), 725-763.
62. Lu, X. F.; Zhao, Y. Y.; Wang, C., Fabrication of PbS nanoparticles in polymer-fiber matrices by electrospinning. *Advanced Materials* **2005**, 17, (20), 2485-+.
63. Wang, Y. Z.; Yang, Q. B.; Shan, G. Y.; Wang, C.; Du, J. S.; Wang, S. G.; Li, Y. X.; Chen, X. S.; Jing, X. B.; Wei, Y., Preparation of silver nanoparticles dispersed in polyacrylonitrile nanofiber film spun by electrospinning. *Materials Letters* **2005**, 59, (24-25), 3046-3049.
64. Ju, Y. W.; Choi, G. R.; Jung, H. R.; Kim, C.; Yang, K. S.; Lee, W. J., A hydrous ruthenium oxide-carbon nanofibers composite electrodes prepared by electrospinning. *Journal of the Electrochemical Society* **2007**, 154, (3), A192-A197.
65. Panels, J. E.; Lee, J.; Park, K. Y.; Kang, S. Y.; Marquez, M.; Wiesner, U.; Joo, Y. L., Synthesis and characterization of magnetically active carbon nanofiber/iron oxide composites with hierarchical pore structures. *Nanotechnology* **2008**, 19, (45).

66. Wang, L.; Yu, Y.; Chen, P. C.; Zhang, D. W.; Chen, C. H., Electrospinning synthesis of C/Fe₃O₄ composite nanofibers and their application for high performance lithium-ion batteries. *Journal of Power Sources* **2008**, 183, 717-723.
67. Systems, C. o. S. P. E., Meeting the Energy Needs of Future Warriors. In Board on Amy Science and Technology, N. R. C., Ed. The National Academies Press: 2004.
68. Reisch, M. S., Thirst for Power. *Chemical and Engineering News* **2007**, 85, (28), 24-25.
69. Hashimoto, T.; Suzuki, Y.; Tanihara, M.; Kakimaru, Y.; Suzuki, K., Development of alginate wound dressings linked with hybrid peptides derived from laminin and elastin. *Biomaterials* **2004**, 25, (7-8), 1407-1414.
70. Jeong, S. I.; Krebs, M. D.; Bonino, C. A.; Samorezov, J. E.; Khan, S. A.; Alsberg, E., Electrospun Chitosan–Alginate Nanofibers with In Situ Polyelectrolyte Complexation for Use as Tissue Engineering Scaffolds. *TISSUE ENGINEERING: Part A* **2011**, 17, (1&2), 59-70.
71. Bhattarai, N.; Zhang, M., Controlled Synthesis and Structural Stability of Alginate-based Nanofibers. *Nanotechnology* **2007**, 18, 10.
72. Bhattarai, N.; Zhang, M. Q., Controlled synthesis and structural stability of alginate-based nanofibers. *Nanotechnology* **2007**, 18, (45).

73. Caykara, T.; Demirci, S.; Eroglu, M. S.; Guven, O., Poly(ethylene oxide) and its blends with sodium alginate. *Polymer* **2005**, 46, (24), 10750-10757.
74. Jeong, S. I.; Krebs, M. D.; Bonino, C. A.; Khan, S. A.; Alsberg, E., Electrospun alginate nanofibers with controlled cell adhesion for tissue engineering. *Macromolecular Bioscience* **2010**, (10), 934-943.
75. Smidsrod, O.; Skjakbraek, G., Alginate as Immobilization Matrix for Cells. *Trends in Biotechnology* **1990**, 8, (3), 71-78.
76. Peppas, N. A.; Hilt, J. Z.; Khademhosseini, A.; Langer, R., Hydrogels in biology and medicine: From molecular principles to bionanotechnology. *Advanced Materials* **2006**, 18, (11), 1345-1360.
77. Winter, H. H., *Physical and Chemical Gelation*. Elsevier: New York, 2001; Vol. 5, p 6991-6999.
78. Chambon, F.; Winter, H. H., Stopping of Crosslinking Reaction in a Pdms Polymer at the Gel Point. *Polymer Bulletin* **1985**, 13, (6), 499-503.
79. Macosko, C. W., *Rheology Principles, Measurements, and Applications*. Wiley-VCH: New York, 1994.
80. Winter, H. H., Transient Networks: Evolution of rheology during chemical gelation. *Progress in Colloid & Polymer Science* **1987**, 75, 104-110.

81. Cox, W. P.; Merz, E. H., Correlation of Dynamic and Steady Flow Viscosities. *Journal of Polymer Science* **1958**, 28, (118), 619-622.
82. Larson, R. G., *The structure and rheology of complex fluids*. Oxford University Press: New York, 1999.
83. Winter, H. H., Can the Gel Point of a Cross-Linking Polymer Be Detected by the G' - G'' Crossover. *Polymer Engineering and Science* **1987**, 27, (22), 1698-1702.
84. Winter, H. H.; Chambon, F., Analysis of Linear Viscoelasticity of a Cross-Linking Polymer at the Gel Point. *Journal of Rheology* **1986**, 30, (2), 367-382.
85. Jeon, O.; Bouhadir, K. H.; Mansour, J. M.; Alsberg, E., Photocrosslinked alginate hydrogels with tunable biodegradation rates and mechanical properties. *Biomaterials* **2009**, 30, (14), 2724-2734.

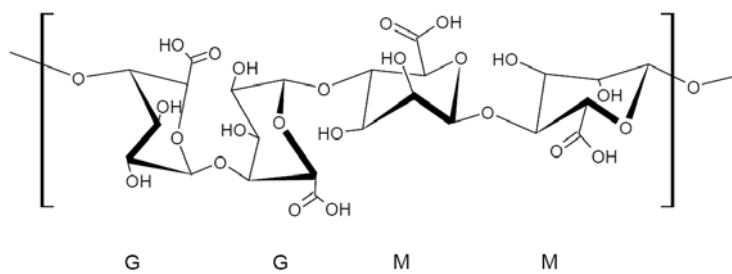


Figure 1.1. Diagram depicting chemical structure of sodium alginate.

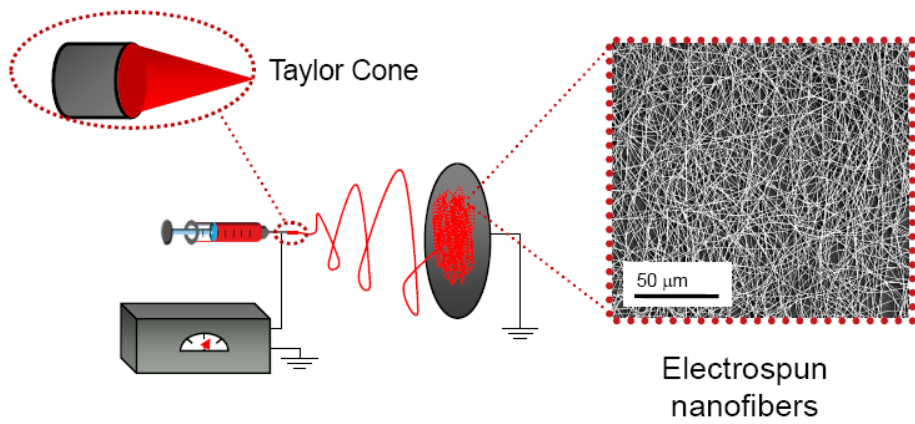


Figure 1.2. Diagram depicting electrospinning setup and resulting nanofibers.

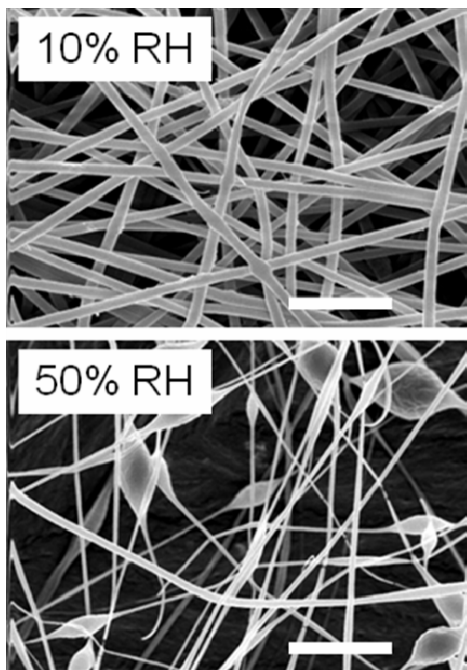


Figure 1.3. SEM micrographs of PEO nanofibers electrospun in 10 and 50% relative humidity conditions. Scale bar is 2 μm .

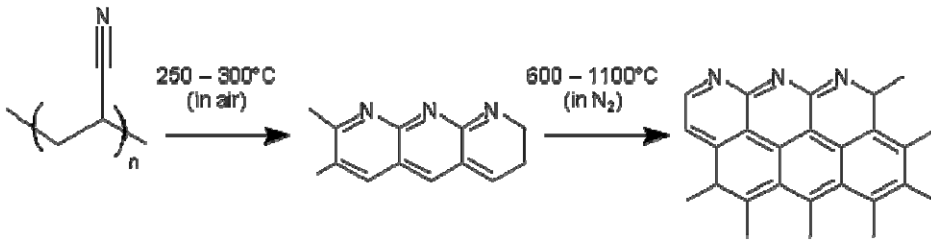


Figure 1.4. Diagram depicting the change in the chemical structure of PAN as a result of stabilization and carbonization heat treatments.

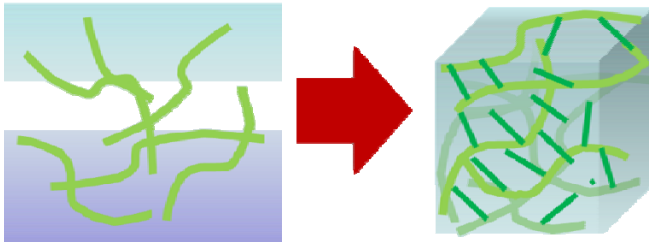


Figure 1.5. Diagram depicting formation of hydrogel, from polymer solution to crosslinked 3D solid-like structure.

CHAPTER 2

Electrospun Fiber Composites Containing Fumed Silica: From Solution Rheology to Materials with Tunable Wetting

Chapter 2 is essentially a manuscript by Christopher A. Bonino and Saad A. Khan prepared for submission to *Nanotechnology*.

Electrospun Fiber Composites Containing Fumed Silica: From Solution Rheology to Materials with Tunable Wetting

Christopher A. Bonino and Saad A. Khan^{1*}

Department of Chemical and Biomolecular Engineering, North Carolina State University,
Raleigh, NC 27695-7905

Abstract

Fumed silica (FS) particles with hydrophobic (R805) and hydrophilic (A200) surface functionalities are incorporated on/within polyacrylonitrile (PAN) fibers by electrospinning. Fumed silica particles are ideal for evaluating the effects of colloidal interactions between polar and non-polar groups on the composite fiber morphology and particle distribution, since the FS particle fillers form associative networks within the electrospun solution that do not sediment. Solution dynamic and steady shear rheology is employed to elucidate the particle-particle and particle-polymer interactions within the PAN/FS solutions. The rheological differences with the two PAN/FS solutions are compared with the resulting electrospun fibers. Furthermore, PAN/FS fiber morphology and particle distribution is compared to fumed silica composites with more hydrophilic polymers, polyethylene oxide

* corresponding author: khan@eos.ncsu.edu (email); 919-515-4519 (ph)

(PEO) and polyvinyl alcohol (PVA). The FS distribution is also evaluated in the absence of an electric field, by wet spinning PAN. In addition, the PAN/FS are evaluated in two potential applications: fabrics with adjustable wettability and carbon-silica composite. In the former, the R805 and A200 FS on the surface of the PAN fibers alter the contact angle of water droplet, from surface-repelling to surface-wetting, respectively. Finally, the conversion of PAN to carbon through a series of heat treatments, and silica as a model material for a more reactive species (*i.e.*, silicon), reveal another potential use for this composite, such as battery electrodes.

2.1. Introduction

Polyacrylonitrile (PAN) fiber technologies have evolved over the past half-century, from traditional textile processing (*i.e.*, wet spinning¹) to nanofibers prepared by electrospinning.² The continued use of PAN is related to its ability to be converted to carbon, as it is the precursor of 90% of carbon and graphite fibers produced commercially.³ The well-established carbonization, which typically involves two sequential heat treatments in air and inert atmospheres, has also been exploited in electrospun fibers.⁴ PAN-based carbon (nano)fibers have shown promising futures in applications, such as next generation battery components.⁵

The capabilities of electrospun PAN (nano)fibers have been expanded by the incorporation of particle fillers. Composite fibers may have increased tensile strength, such as with multi-walled carbon nanotubes loaded into PAN⁶, or higher storage capacity for lithium, such as tin oxide nanoparticles in carbon used as battery anodes⁷, as compared to the pure polymer/carbon alternatives. In addition to the selection of the polymer and (nano)filler, the preparation approach is another technique to tailor composite electrospun fibers.

The fabrication of composite electrospun fibers is typically done by two approaches: *in situ* and *ex situ*. The former involves electrospinning a precursor of particle fillers, which is subsequently converted into the particle following a heat treatment or reducing step.

While the *in-situ* approach is a convenient way to incorporate (nano)particles within the polymer matrix, the ability to modify the particle diameter and distribution may be limited by the conversion step. For example, the soaking treatment of PAN fibers containing silver nitrate resulted in a skewed size distribution of silver particle sizes (average 10 nm), the largest at the outer surfaces, which may be attributed to the penetration of the reducing agent.⁸

The *ex-situ* approach involves adding particles, which have already been synthesized, directly to the polymer solution prior to electrospinning. This approach can be advantageous when embedding particles with specific diameters and size distributions within the fiber. For example, Kim *et al* synthesized 4 nm diameter gold nanoparticles, capped with dodecane-thiol, and subsequently electrospun the particles within PEO nanofibers.⁹ The thiol surface groups prevented aggregation and or sedimentation of the gold nanoparticles prior to electrospinning.

The formation of particle aggregates within the solution (and resulting fiber) can be limited by functional groups on the particle surfaces by electrostatic or steric stabilization.¹⁰ However, many functional groups and/or solvent used to stabilize the particles are not compatible with the electrospinning polymer solution. For example, colloidal silica particles are commonly stabilized (and commercially available) in water and/or ethanol,^{11, 12} which are anti-solvents for PAN. Thus, additional process steps (*e.g.*, dialysis¹³) may be required to transfer the particles into an appropriate solvent for electrospinning solution (*i.e.*, dimethyl formamide (DMF)). Furthermore, particles that are poorly stabilized or temporarily

dispersed in the electrospinning solutions may aggregate in the process times required to achieve thick (*e.g.*, 10 hrs for $\sim 50 \mu\text{m}^7$) electrospun mats, resulting in low loading within the composite fibers.

Fumed silica (FS) particles offer an alternative in *ex-situ* electrospinning to solutions of stabilized particles. Fumed silica is commercially available as powders with a range of hydrophilic and hydrophobic surface functionalities, which are capable of being incorporated into a variety of solvents (*e.g.*, polyethylene glycol)¹⁴ with relatively high loading, well beyond those limited by traditional silica particle solutions. The versatility of fumed silica has led to its use in polymer composites with various applications, including gel electrolytes¹⁵ and flame retardant materials.¹⁶

The large scope of uses for fumed silica led to thorough examinations of its complex behaviors in solution. Solution rheology is one method to characterize the colloidal interactions within fumed silica solutions, which can elucidate vital information on the nano- and micro-structures within fumed silica-polymer composites. FS particles (individual diameter ~ 12 nm) can form self-supporting networks that prevent the particles from losing stability within the solution. The ability of FS to form networks and their effects on the solution rheology, are related to the (in)compatibilities between the FS surface groups and other the components in the solution. For example, FS particles with non-polar surface groups in a polar solvent formed networks of particles, which increased the solution modulus, as compared to hydrophilic particles.¹⁷ In this case, the particle-solvent incompatibility caused FS to form associations of particles, and yet maintain stability in

solution. The colloidal interactions between FS particles can be further complicated with the addition a polymer. The combination of a hydrophilic polymer (*i.e.*, polyethylene oxide) with hydrophilic fumed silica, led to solutions with greater moduli than with hydrophobic fumed silica.¹⁸ On the other hand, the addition of a hydrophobic polymer (*i.e.*, polystyrene) to solution containing hydrophilic fumed silica reduced the solution moduli, by breaking down the associated fumed silica network.¹⁹ Thus, the polymer-particle and particle-particle interactions in polymer solutions containing fumed silica can have significant consequences on their rheological properties.

In turn, solution rheology has profound implications on electrospun fiber morphology. Several studies have shown increases in solution viscosity and relaxation times can increase fiber diameters and suppress bead defects.^{20, 21} While these properties have been well-established in polymer solutions, electrospinning literature is lacking in studies that relate the rheological properties of polymer fillers, such as fumed silica, with fiber morphology. Furthermore, previous works have fabricated and characterized electrospun composites containing silica particles, including PAN and FS.²²⁻²⁴ In particular, Lim *et al* identified the importance of polymer-particle compatibility on the silica particle distribution within the electrospun fiber.²² Silica particles (average diameter ~300 nm) with hydrophilic surface groups were more effectively incorporated with electrospun polymer fibers that were also hydrophilic (*i.e.*, polyacrylamide, PEO), as compared by a hydrophobic polymer (*i.e.*, PAN). Despite this finding, previous studies have failed to fully characterize the particle-polymer-solvent interactions within electrospinning solutions using rheological methods.

With the wide-spread growth of electrospun composite (nano)fibers and their use as functional materials (*e.g.*, battery electrodes), it is essential to examine the roles of particle fillers.

In this study, we investigate the effects of particle fillers on morphology of PAN fibers. Fumed silica particles with two different surface functionalities (hydrophobic vs. hydrophilic) are used to evaluate the role of particle-polymer chemical compatibility on the particle distributions within the electrospun fibers. We explore rheological methods to characterize differences in the PAN solutions with each type of fumed silica, comparing with electrospun fiber morphology. In order to decouple the effects the surface chemistry of PAN from the applied electric field on fumed silica particle distribution, composite fibers are prepared by electrospinning more hydrophilic polymers (*i.e.*, PVA, PEO), as well as wet spinning PAN fibers (without an electric field). Finally, we explore some potential uses of the PAN/FS composites, as fabrics with control wettability, as well as carbon-silica fibers.

2.2. Experimental Section

Materials Polyacrylonitrile (PAN, MW = 150,000 g/mol, Scientific Polymer Products), polyethylene oxide (PEO, MW = 600,000 g/mol, Dow), N, N dimethylformamide (DMF, Fisher Scientific), and polyvinyl alcohol (PVA, MW = 127,000 g/mol, Dow) were used as received. Fumed silica (FS) particles with different dominant surface groups were Aerosil A200 (silanol) and R805 (octyl) obtained from Degussa Corp. Prior to preparing solutions,

fumed silica particles were dried in a vacuum oven for 5 days at 120°C, to remove any moisture.

Methods

Preparation of Polymer/FS solutions. Polymer solutions were prepared by adding PAN into DMF and stirring with a magnetic stir bar for 1-2 hrs. A separate solution containing fumed silica particles and DMF was mixed at 6000 RPM for 5 min using a High Shear Mixer (SL2, Silverson Machines, Chesham, U.K.) and then added to the polymer solution. The combined solution was shear mixed for 10 min at 6000 RPM. Care was taken to ensure that each solution was homogeneously mixed, since good mixing quality has been linked to the network-forming capabilities of FS. The polymer/FS solution was heated overnight at 60°C while stirring with a magnetic stir bar.

Rheological measurements. Rheological experiments were performed with a TA Instruments AR2000 stress-controlled rheometer with a 40 mm, 2° cone and plate geometry. All samples were measured at 25°C. A steady pre-shear stress (*e.g.*, 200 Pa) was applied for 3 min to each sample to erase any shear history. Dynamic and steady stress shear experiments were conducted on each sample. The stresses applied in the frequency sweeps were selected from the linear viscoelastic (LVE) regime in the stress sweeps. All rheological measurements were repeated on at least two different samples.

Preparation of polymer/FS nanocomposites. The polymer solution was pumped through a syringe with a 22 gauge needle at rates of 0.5 mL/hr. The distance from the end of the needle to the collector plate was fixed at 15 cm. Details of the electrospinning setup are described

elsewhere.^{7, 25} The voltage was varied until a stable Taylor cone²⁶ was achieved. Spun-cast films were prepared using a spin coater (Laurell Technologies, North Wales, PA). Films were prepared on silicon substrates using a spin speed of 2000 RPM, with a 1000 RPM/s ramp rate.

Carbonization. Fiber mats and spun-cast films of PAN/FS were heated in a furnace in a series of steps. First, they were stabilized in air at 280°C for 2 hrs. Next, nitrogen was introduced and the temperature was increased at a rate of 5°C/min. The final temperature of 900°C was maintained for 2 hrs.

Characterization of Polymer/FS Nanocomposites. Fiber mats and spun-cast films were analyzed with electron microscopy. A FEI XL30 field emission SEM was used at the following settings: 6 mm working distance, 5 kV accelerating voltage, spot size 3, and ultrahigh resolution mode. Cross sections fibers were prepared by freeze fracturing, in which fiber mats were submerged in liquid nitrogen and cut with a razor blade. All samples, except of those carbonized, were gold sputter-coated prior to analysis. Fiber diameters of 50 fibers per sample were measured using Adobe Photoshop CS3. For TEM analysis, fiber samples were electrospun directly onto carbon-coated grids, and characterized using a FEI Tecnai G2 Twin. Example operating conditions were: 160 kV accelerating voltage and spot size of 3. Contact angle measurements were made using a goniometer (model 200, Ramé-Hart Instrument, Co., Netcong, NJ) with Drop Image software. Prior to the measurement, electrospun mats were heated at 80°C in a vacuum oven for 12 hrs in order to remove any residual solvents (*i.e.*, DMF) from the electrospinning process. Contact angles were

determined from the profiles of DI water droplets ($\sim 5 \mu\text{L}$) on the electrospun mats, within ~ 1 min of deposition. Each sample was evaluated with >5 droplets (10 measurements/droplet).

2.3. Results and Discussions

2.3.1. Nanocomposites of PAN and FS with Different Surface Chemistries

Prior to electrospinning, the rheology of the solutions containing PAN, DMF, and either hydrophobically- (R805) or hydrophilically-modified (A200) fumed silica was characterized. Dynamic rheology reveals that both PAN/FS (7.9:2.0 wt %) solutions behaved as weak gels, with the elastic modulus (G') dominating viscous modulus (G'') across all frequencies. (Figure 2.1a.) In addition, the elastic modulus of PAN/R805 solution is up to 2-3 times greater at low frequencies than the solution with A200. A similar relationship was also observed with in the steady shear rheology. Both PAN/FS solutions show shear thinning behavior across all shear rates, which indicates weak interactions between the components (*i.e.*, FS) in the solution. (Figure 2.1b.) Furthermore, the PAN/R805 solution has a greater yield stress than the PAN/A200, ~ 2.0 and ~ 0.5 Pa, respectively. (Figure 2.1c.) Based on this rheological data, the hydrophobic FS creates stronger networks within the PAN solutions, which may be the result of particle-particle and/or particle-polymer interactions.

The interactions within the PAN/FS solutions and their corresponding rheological behavior were further investigated by varying the fumed silica composition. Figure 2.2 shows steady shear rheology of PAN solutions containing 5 wt % FS, and with the absence

of FS. The additional fumed silica intensifies the shear thinning appearance, as compared to the previous experiment. Furthermore, the yield stress (at 0.1 s^{-1}) in the PAN/R805 solution is ~ 4 times the PAN/A200 stress. Thus, the hydrophobic particle raises the modulus of the polymer-particle/particle-particle structures, as compared to the more hydrophilic FS.

The changes in solution properties caused by fumed silica are apparent when comparing the rheological behavior of the filled and unfilled solutions. PAN solutions (7.9 and 10.0 wt %) have Newtonian behavior at low shear rates, lacking a yield stress. The 7.9 wt % PAN solution has the same polymer content of the fumed silica solutions. However, at the highest shear rates ($\sim 300 \text{ s}^{-1}$), the apparent viscosities of the filled solutions are still more than 5 times those of the polymer solution. Interestingly, the high shear, apparent viscosities of the FS solutions more closely match the 10 wt % PAN values.

The rheological behavior of FS solutions without PAN was evaluated in order to decouple the particle-particle and particle-polymer interactions. The fumed silica content was increased to 9 wt % to achieve moduli in the same ranges as the polymer solutions, for consistency in the rheological experiments. The associative nature of both fumed silica led to formation of gels. The elastic moduli dominate the viscous moduli across all frequencies. (Figure 2.3a.) Additionally, R805 forms a stronger gel network than A200, as G' is parallel and an order of magnitude greater than G'' . The solution moduli progressively decline with increasing steady shear stresses, revealing shear thinning behavior. (Figure 2.3b.) In the absence of polymer, A200 and R805 fumed silica solutions have low yield stresses (~ 0.4 ,

~ 0.8 Pa at 0.1 s^{-1}) and apparent viscosities at high shear rates (~ 0.05 , ~ 0.01 Pa·s at 1000 s^{-1}), respectively.

Comparing all of the rheological experiments (Figure 2.1, Figure 2.2, Figure 2.3.) provides insight on the particle-particle and particle-polymer interactions within the solutions. Solutions with R805, the hydrophobic FS, consistently have greater moduli than A200, with and without PAN. Since DMF is a polar, aprotic solvent, the octyl groups on R805 associate with neighboring particles with the same chemistry, resulting in networked structures in the solution. A similar finding on the interactions between these same two silica particles and another polar solvent, polyethylene glycol was previously reported.¹⁴ The authors attributed the propensity of R805 to form more rigid gels than A200 to a reverse steric stabilization between the octyl surface groups. Relating their explanation to our study, the interactions between the FS surface groups dominate the interactions between the surface groups and the polymer. Even though PAN is hydrophobic, the octyl groups on the R805 have a greater affinity for themselves, than the carbon-carbon bonds in the polymer backbone.

2.3.2. Films of PAN/FS

To complement the solution rheology, we examined morphology of the spun cast films of the PAN/FS solutions. (Figure 2.4.) The dispersion of a filler within the polymer matrix can affect the properties (*i.e.*, modulus) of the composite.(*e.g.*, ²⁷) Based on the

rheological results, R805 led to solution structures with greater moduli than A200, due to particle-particle associations. Analysis by TEM was consistent with the rheology. Aggregates of R805 fumed silica particles, up to $\sim 2 \mu\text{m}$ in their largest dimension, are present within the films. The existence of these fumed silica networks indicates the origin of the gel-like solution behavior. A series of connected fumed silica structures can span distances on the order of the rheometer gap size, creating a gel.

2.3.3. Electrospun Fibers of PAN/FS

The FS stability in solution was monitored when electrospinning the PAN/FS solutions. Repeat rheological experiments (data not shown) up to 24 hours apart were consistent within experimental error. Thus, the network structures of both the hydrophilic (A200) and hydrophobic (R805) maintain their stability in solution throughout the electrospinning experiments (up to 5 hrs). In addition, aggregates of precipitated FS particles were *not* visible on the bottom of the solution vials up to ~ 48 hrs after preparation, indicating particle loading within the electrospun fibers was not limited by the FS stability.

The addition of fumed silica affected the morphology of the electrospun PAN fibers. PAN fibers without the filler have uniform diameters (361 ± 74 nm), without bead defects. (Figure 2.5a, b.) In comparison, the composite PAN fibers containing A200 and R805 FS have larger diameters and distributions, 1030 ± 300 and 820 ± 270 nm, respectively, more than two times the pure polymer. (Figure 2.5c-f.) The increase in fiber diameter is attributed to

the differences in the rheological behavior between the filled and unfilled solutions. During electrospinning, the jet is stretched as a result of whipping instabilities that occur within the electric field, which influence the fiber diameter and morphology. The viscoelastic forces within the jet resist this elongation. Thus, the fumed silica increases the solution viscosities and relaxation times, leading to larger fiber diameters. This relationship has been widely reported in many polymer solutions (Reviewed by Li and Xia²⁸). However, raising the solution zero viscosity and relaxation times has also been used as a method to effectively suppress bead defects, leading to fibers with more uniform diameters.^{20, 21} Observations of the PAN/FS fibers do not match this trend.

The collection of the rheological and morphological solution data may help to decipher the appearance the electrospun fibers. The PAN/FS solutions have yield stresses, which resist the flow and elongation of the solution. However, the elongational forces at the formation of the electrospun jet (near the Taylor cone), have been estimated to be 10-100 kPa, which are well beyond the PAN/FS yield stresses.²⁹ Hence, a macro-scale network of fumed silica was effectively sheared or broken down at the start of electrospinning. Yet the distribution of sizes of the remaining associations of particles is non-uniform within the sheared solution. From the TEM analysis of the polymer films, which underwent shearing during spin casting, particle sizes vary from individual particles (~10 nm) to large aggregates (~2 μm). (Figure 2.4.) As a result, aggregates of fumed silica particles, varying in size, travel in the electrospun jet, toward the collector plate. After extended from the Taylor cone, the jet takes on a coiled appearance as it thins and the solvent rapidly evaporates. In this

region, capillary instabilities in the partially solidified jet can lead to bead defects in the deposited fibers.³⁰ We speculate that the non-uniform distribution of fumed silica within the jet, led to localized regions of disproportionate levels of moduli, which make it more susceptible to these instabilities. Despite the ability of fumed silica to associate within the solution at low shear conditions, its breakdown, and resulting non-uniform distribution, from high stresses may be lead to defects in the resulting electrospun fibers.

In addition to the fiber diameter and morphology, fumed silica also contributed to differences in the fiber surfaces. At a high magnification, PAN fibers without FS have complex surface textures, which we attribute to the ambient conditions during electrospinning. Hydrophobic polymers, including PAN, can experience localized-phase separations at their outer surfaces that are influenced by the relative humidity.³¹ The textured surface appearance on the fibers became more pronounced with PAN/FS fibers. Fumed silica particles are distributed on the surface of the PAN fibers. (Silica appears whiter than the polymer fibers, due its higher electron density.) Holes or pits (up to ~100 nm wide) are also present in the fiber surfaces, which may be the result of voids from weakly-bound silica particles, or poor coverage by the polymer.

The composite fiber interiors were also investigated by SEM and TEM. A cross sectioned fiber, prepared by freeze facture, contains fumed silica particles within its interiors. (Figure 2.6a.) Shown in Figure 2.6b-d, TEM also confirms the presence on FS aggregates below the fiber surfaces. (Particles are not present in the PAN-only fibers.) Thus, the electrospinning process distributes the fumed silica within the fibers, as well as on the outer

surfaces. Unlike the rheological differences between the two fumed silica solutions, composite fibers exhibit similar appearances. The surface functionality of the FS particles appears to have minor effects on the particle distribution within the fiber.

2.3.4. Electrospun PEO and PVA Solutions Containing Fumed Silica

In light of this finding, we sought to further examine the factors that affect the silica particle distribution on and within the PAN fibers. Previous findings have reported that particles stabilized in the polymer solution become distributed within the electrospun polymer.^{9, 32} On the other hand, silica microspheres were driven to the surface of PAN fibers, and embedded within polyacrylamide, which was attributed to the compatibility differences between the silica and each polymer.²² Since both hydrophobic and hydrophilic FS particles covered the PAN fiber outer surfaces, we evaluated other polymers to determine if the particle distribution is affected by polymer-particle compatibility and/or the electrospinning process.

PEO and polyvinyl alcohol (PVA) were blended with fumed silica and DMF by the same procedure used with PAN solutions, and electrospun. Even though PEO and PVA are hydrophilic polymers, both A200 and R805 FS particles covered the outer surfaces of the electrospun fibers. Fumed silica particle aggregate sizes range from ~30 – 500 nm. (Figure 2.7.) Since the hydrophilic A200 FS was not completely encapsulated with PEO and PVA

fibers, and was distributed on the fiber surfaces similar to R805, we concluded that FS particle location is not determined completely by polymer-particle chemical compatibility.

Thus, we hypothesize that another force (*i.e.*, the electric field) contributes to the particle distribution. Valverde *et al* reported that fumed silica experiences charging in an electric field, which can lead particle motion in the field direction.³³ Furthermore, the applied electric field in electrospinning has also been shown to preferentially populate the surface of polymer blends with the more polarizable species, which may occur within the field gradients at the Taylor cone surface.^{34, 35} Thus, the electric field contributes to the distribution of fumed silica on the electrospun fiber surfaces.

2.3.5. Wet Spun PAN fibers

PAN/FS fibers were prepared by wet spinning to evaluate the particle distribution in the absence of an electric field. Solutions were injected into a coagulation bath containing water, an anti-solvent for PAN, and formed coarse fibers (diameters ~30 μm). As seen with electrospun fibers, SEM analysis of the wet spun composite fibers reveals that FS is present within the fiber cross sections, as well as on the surface. (Figure 2.8a-b.) Furthermore, pits/holes (~50 nm) are present in the vicinity of the fumed silica on the fiber surface, and not visible on the surfaces of the PAN fiber control. (Figure 2.8b, e.) The distribution of FS on/near the fiber surfaces is attributed to its greater surface energy than most polymers, including PAN.^{36, 37} When applying an electric field (as in electrospinning), we hypothesis

that the combination of the electric field and surface activity cause the FS to populate the polymer fiber outer surfaces. The effects of these properties should be considered when tailoring composite electrospun fibers for specific applications, such as water-absorbing/repealing fabric and battery electrodes.

2.3.6. Tailored Hydrophobic Surfaces of Electrospun PAN Fibers with Fumed Silica

Adding fumed silica to the outer surfaces of fibers is a convenient strategy for manipulating their surface properties. As a result of the electrospinning process, the fumed silica particles distributed on the top surfaces of the fibers effectively modified the water repellency of the mats. Droplets of water added onto electrospun PAN fibers containing A200 or R805 fumed silica show significantly different profiles. (Figure 2.9a, b.) A droplet remained on the top surface of a PAN/R805 mat with an average contact angle of $128 \pm 10^\circ$, and maintained its profile well beyond the duration of the measurement (>1 min). In contrast, a droplet of water wet the surface of the mat containing A200. The rapid spreading of the water across the mat made the attempts at contact angle measurement futile. The surface groups on the fumed silica particles, which are accessible on the fiber surfaces, effectively influence the interactions between the mat and liquid. The vastly different responses to water demonstrate the versatility of fumed silica in surface treatments, especially in sub-micron fibrous mats.

2.3.7. Carbonization of PAN/FS Composite Fibers

Filled fibrous carbon mats have many applications (*e.g.*, battery electrodes³⁸) We converted the PAN/FS fibers to carbon composites through a series of thermal treatments to explore another extension of the material. The first heat treatment, known as the stabilization, (280°C in air) crosslinked PAN, as a result of dehydrogenation and cyclization reactions.³⁹ The second heat step (900°C in nitrogen) caused the release of non-carbon component as gases (*e.g.*, ammonia) and the carbonization of PAN.³ After which, two obvious changes are observed with electron microscopy. Firstly, the carbon fibers are conductive and can be analyzed with the SEM without the need for gold sputter coating. The fumed silica particles are more apparent without the gold coating and can be easily seen on and below the surface of the carbon fiber. (Figure 2.10.) As reported above with the polymer fiber, cross sections reveal fumed silica in the fiber interiors. The second change as a result of the carbonization is the reduction in fiber size; fiber diameters decreased by >40%. The evolution of gases and weight loss from the fiber material contributed to the diameter change.³ Despite the fiber shrinkage, silica particles are on the outer surfaces and interiors of the fibers. (Figure 2.10.) While silica does not form an alloy with lithium, the distribution of the particles on and within the carbon fibers can serve as a model material for other more reactive particles (*i.e.*, Si), which have been used as battery electrodes.³⁸ As a direct result of a findings related to the surface groups on the particles, we speculate that stabilized silica/silicon particles, regardless of a hydrophobic or hydrophilic functionalities, can be incorporated on/within the electrospun fibers.

2.4. Conclusion

We found that hydrophobically- and hydrophilically-modified fumed silica particle fillers create rheological differences in PAN/DMF solutions. Specifically, the hydrophobic FS (R805) self associates within the polar solvent, leading to stronger moduli and yield stresses, compared to the hydrophilic FS (A200). However, despite the rheological differences between the PAN/FS solutions, the electrospun fibers had similar fiber size and particle distributions. In particular, fumed silica particles were present on the outer surfaces of the fibers. After finding FS present on hydrophilic (PEO, PVA) electrospun polymer fibers and a wet spun PAN (without an applied electric field), we concluded that the electric field and the surface energy of the silica particles contribute to their locations on the fibers. Thus, the colloidal particle-particle and particle-polymer interactions have less significant roles in the particle distribution. Furthermore, the presence of FS on the electrospun PAN fiber surfaces is an effective way to manipulate the wettability of the fiber mats. Contact angle measurements of water droplets varied by $>100^\circ$ between the two types of composite fibers. Finally, carbon-silica fibers were prepared by series of heat treatments, which can be compared as model composites to other reactive materials, such as silicon, if used as lithium ion battery anodes.

2.5. Acknowledgements

This work was supported by National Science Foundation GOALI Program (#0555959) and a Department of Education GAANN Fellowship (CAB). The authors thank Prof. Jan Genzer for helpful discussions on surface energy.

2.6. References

1. Paul, D. R., Diffusion During the Coagulation Step of Wet-Spinning. *Journal of Applied Polymer Science* **1968**, 12, 383-402.
2. Wang, T.; Kumar, S., Electrospinning of Polyacrylonitrile Nanofibers. *Journal of Applied Polymer Science* **2006**, 102, 1023–1029.
3. Rahaman, M. S. A.; Ismail, A. F.; Mustafa, A., A review of heat treatment on polyacrylonitrile fiber. *Polymer Degradation and Stability* **2007**, 92, (8), 1421-1432.
4. Chun, I.; Reneker, D. H.; Fong, H.; Fang, X. Y.; Dietzel, J.; Tan, N. B.; Kearns, K., Carbon nanofibers from polyacrylonitrile and mesophase pitch. *Journal of Advanced Materials* **1999**, 31, (1), 36-41.
5. Kim, C.; Yang, K. S.; Kojima, M.; Yoshida, K.; Kim, Y. J.; Kim, Y. A.; Endo, M., Fabrication of electrospinning-derived carbon nanofiber webs for the anode material of lithium-ion secondary batteries. *Advanced Functional Materials* **2006**, 16, (18), 2393-2397.
6. Hou, H. Q.; Ge, J. J.; Zeng, J.; Li, Q.; Reneker, D. H.; Greiner, A.; Cheng, S. Z. D., Electrospun polyacrylonitrile nanofibers containing a high concentration of well-aligned multiwall carbon nanotubes. *Chemistry of Materials* **2005**, 17, (5), 967-973.

7. Bonino, C. A.; Ji, L.; Lin, Z.; Toprakci, O.; Zhang, X.; Khan, S. A., Electrospun Carbon-Tin Oxide Composite Fibers for Use as Lithium Ion Battery Anodes. *Chemistry of Materials* **Submitted**.
8. Wang, Y. Z.; Yang, Q. B.; Shan, G. Y.; Wang, C.; Du, J. S.; Wang, S. G.; Li, Y. X.; Chen, X. S.; Jing, X. B.; Wei, Y., Preparation of silver nanoparticles dispersed in polyacrylonitrile nanofiber film spun by electrospinning. *Materials Letters* **2005**, *59*, (24-25), 3046-3049.
9. Kim, G.; Wutzler, A.; Radusch, H.; Michler, G.; Simon, P.; Sperling, R.; Parak, W., One-Dimensional Arrangement of Gold Nanoparticles by Electrospinning. *Chemistry of Materials* **2005**, *17*, (20), 4949-4957.
10. Hiemenz, P. C.; Rajagopalan, R., *Principles of colloid and surface chemistry*. 3rd ed.; Marcel Dekker: NY, 1997.
11. Rossi, L. M.; Shi, L. F.; Quina, F. H.; Rosenzweig, Z., Stober synthesis of monodispersed luminescent silica nanoparticles for bioanalytical assays. *Langmuir* **2005**, *21*, (10), 4277-4280.
12. Nakamura, M.; Ishimura, K., One-pot synthesis and characterization of three kinds of thiol-organosilica nanoparticles. *Langmuir* **2008**, *24*, (9), 5099-5108.

13. Zhou, J. A.; van Duijneveldt, J. S.; Vincent, B., The Phase Behavior of Dispersions of Silica Particles in Mixtures of Polystyrene and Dimethylformamide. *Langmuir* **2010**, 26, (12), 9397-9402.
14. Raghavan, S. R.; Hou, J.; Baker, G. L.; Khan, S. A., Colloidal interactions between particles with tethered nonpolar chains dispersed in polar media: Direct correlation between dynamic rheology and interaction parameters. *Langmuir* **2000**, 16, (3), 1066-1077.
15. Walls, H. J.; Zhou, J.; Yerian, J. A.; Fedkiw, P. S.; Khan, S. A.; Stowe, M. K.; Baker, G. L., Fumed silica-based composite polymer electrolytes: synthesis, rheology, and electrochemistry. *Journal of Power Sources* **2000**, 89, (2), 156-162.
16. Kashiwagi, T.; Gilman, J. W.; Butler, K. M.; Harris, R. H.; Shields, J. R.; Asano, A., Flame retardant mechanism of silica gel/silica. *Fire and Materials* **2000**, 24, (6), 277-289.
17. Raghavan, S. R.; Walls, H. J.; Khan, S. A., Rheology of silica dispersions in organic liquids: New evidence for solvation forces dictated by hydrogen bonding. *Langmuir* **2000**, 16, (21), 7920-7930.
18. Sanchez, A. Colloidal Gels of Fumed Silica: Microstructure, Surface Interactions and Temperature Effects. North Carolina State University, Raleigh, NC, 2006.

19. Kawaguchi, M.; Mizutani, A.; Matsushita, Y.; Kato, T., Molecular weight dependence of structures and rheological properties for fumed silica suspensions in polystyrene solutions. *Langmuir* **1996**, 12, (26), 6179-6183.
20. Fong, H.; Chun, I.; Reneker, D. H., Beaded nanofibers formed during electrospinning. *Polymer* **1999**, 40, (16), 4585-4592.
21. Yu, J. H.; Fridrikh, S. V.; Rutledge, G. C., The role of elasticity in the formation of electrospun fibers. *Polymer* **2006**, 47, (13), 4789-4797.
22. Lim, J.-M.; Moon, J. H.; Yi, G.-R.; Heo, C.-J.; Yang, S.-M., Fabrication of One-Dimensional Colloidal Assemblies from Electrospun Nanofibers. *Langmuir* **2006**, 22, (8), 3445-3449.
23. Ji, L. W.; Saquing, C.; Khan, S. A.; Zhang, X. W., Preparation and characterization of silica nanoparticulate-polyacrylonitrile composite and porous nanofibers. *Nanotechnology* **2008**, 19, (8).
24. Jung, H. R.; Ju, D. H.; Lee, W. J.; Zhang, X. W.; Kotek, R., Electrospun hydrophilic fumed silica/polyacrylonitrile nanofiber-based composite electrolyte membranes. *Electrochimica Acta* **2009**, 54, (13), 3630-3637.
25. Bonino, C. A.; Krebs, M. D.; Saquing, C. D.; Jeong, S. I.; Shearer, K. L.; Alsberg, E.; Khan, S. A., Electrospinning alginate-based nanofibers: From blends to crosslinked low molecular weight alginate-only systems. *Carbohydrate Polymers* **In press**.

26. Taylor, G., Disintegration of Water Drops in Electric Field. *Proceedings of the Royal Society of London Series a-Mathematical and Physical Sciences* **1964**, 280, (138), 383-&.
27. Krishnamoorti, R.; Vaia, R. A.; Giannelis, E. P., Structure and dynamics of polymer-layered silicate nanocomposites. *Chemistry of Materials* **1996**, 8, (8), 1728-1734.
28. Li, D.; Xia, Y. N., Electrospinning of nanofibers: Reinventing the wheel? *Advanced Materials* **2004**, 16, (14), 1151-1170.
29. Han, T.; Yarin, A. L.; Reneker, D. H., Viscoelastic electrospun jets: Initial stresses and elongational rheometry. *Polymer* **2008**, 49, (6), 1651-1658.
30. Reneker, D. H.; Yarin, A. L., Electrospinning jets and polymer nanofibers. *Polymer* **2008**, 49, (10), 2387-2425.
31. Pai, C. L.; Boyce, M. C.; Rutledge, G. C., Morphology of Porous and Wrinkled Fibers of Polystyrene Electrospun from Dimethylformamide. *Macromolecules* **2009**, 42, (6), 2102-2114.
32. Wang, L.; Yu, Y.; Chen, P. C.; Zhang, D. W.; Chen, C. H., Electrospinning synthesis of C/Fe₃O₄ composite nanofibers and their application for high performance lithium-ion batteries. *Journal of Power Sources* **2008**, 183, 717-723.
33. Valverde, J. M.; Quintanilla, M. A. S.; Espin, M. J.; Castellanos, A., Nanofluidization electrostatics. *Physical Review E* **2008**, 77, (3).

34. Sun, X.-Y. Concurrent and Sequential Surface Modification of Electrospun Polymer Micro/Nano Fibers. North Carolina State University, Raleigh, 2008.
35. Sun, X. Y.; Shankar, R.; Borner, H. G.; Ghosh, T. K.; Spontak, R. J., Field-driven biofunctionalization of polymer fiber surfaces during electrospinning. *Advanced Materials* **2007**, 19, (1), 87-+.
36. Chen, Y.; Iroh, J. O., Synthesis and characterization of polyimide silica hybrid composites. *Chemistry of Materials* **1999**, 11, (5), 1218-1222.
37. Brandrup, J.; Immergut, E. H.; Grulke, E. A., *Polymer Handbook*. 4th ed.; Wiley-Interscience: New York, 2005.
38. Ji, L. W.; Zhang, X. W., Fabrication of porous carbon/Si composite nanofibers as high-capacity battery electrodes. *Electrochemistry Communications* **2009**, 11, (6), 1146-1149.
39. Edie, D. D., The Effect of Processing on the Structure and Properties of Carbon Fibers. *Carbon* **1998**, 36, (4), 345-362.

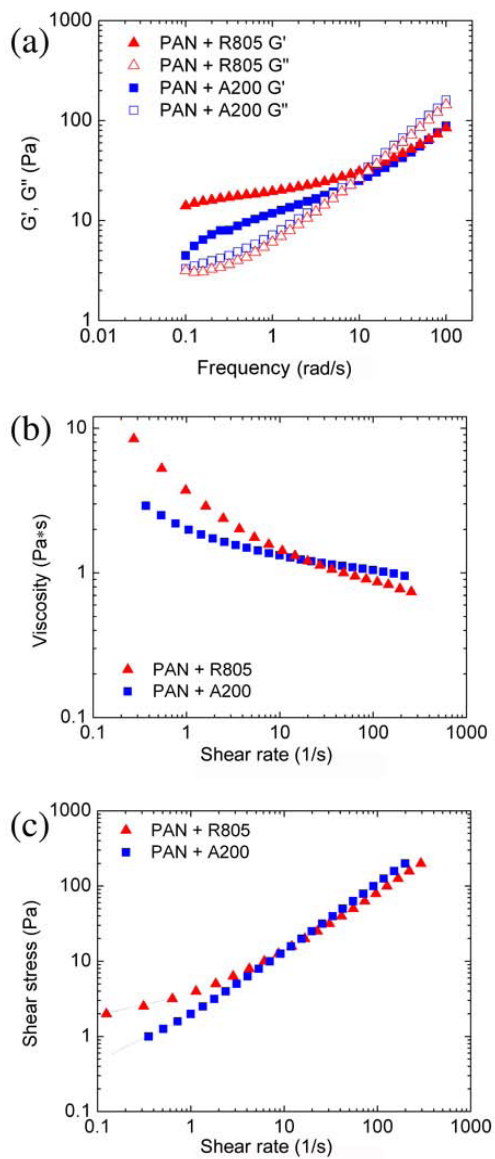


Figure 2.1. Solution rheology of PAN (7.9 %)/DMF with R805 (2.2 %, hydrophobic, \blacktriangle , \triangle) or A200 (2.2 %, hydrophilic, \blacksquare , \square) fumed silica; (a) dynamic frequency sweep, (b) steady shear viscosity, and (c) shear stress/rate plots.

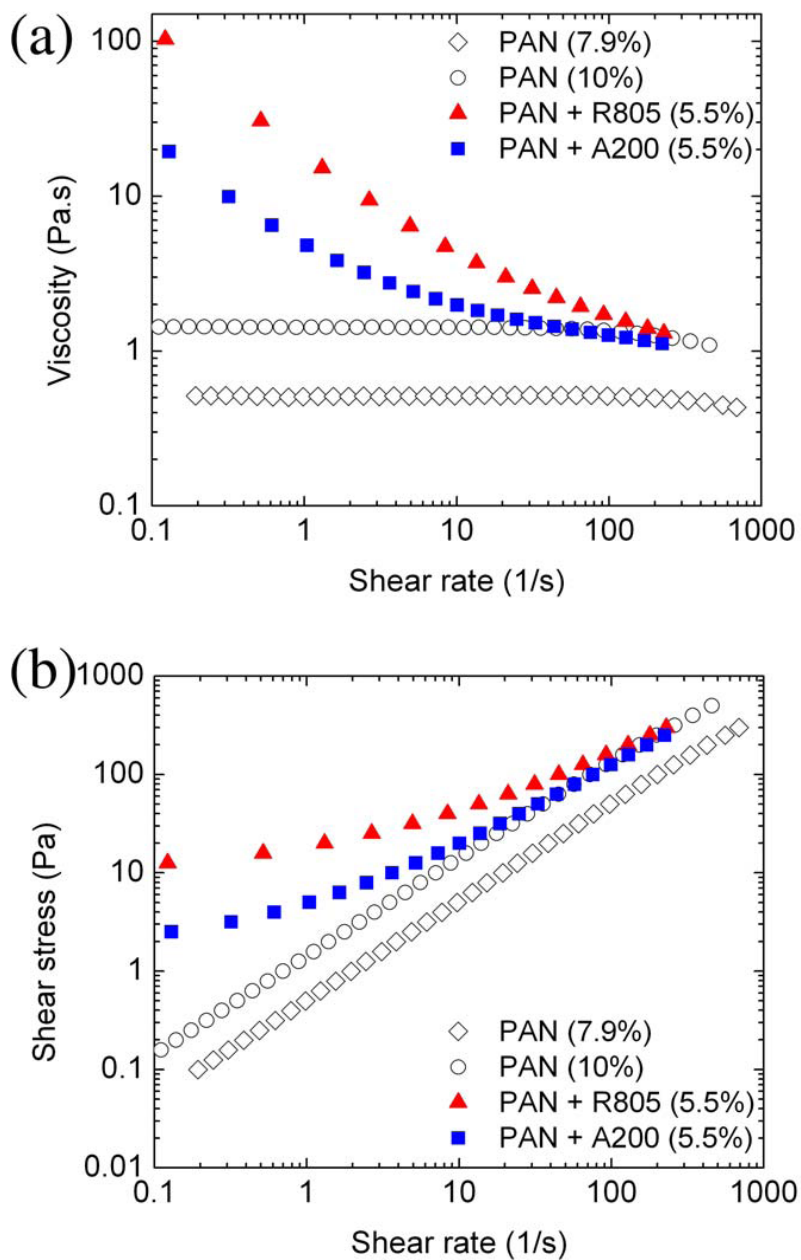


Figure 2.2. Solution rheology of PAN (7.9 %, ◇, 10 %, ○) and PAN with R805 (5.5 %, hydrophobic, ▲) or A200 (5.5 %, hydrophilic, ■) fumed silica; (a) steady shear viscosity and (b) shear stress/rate plots.

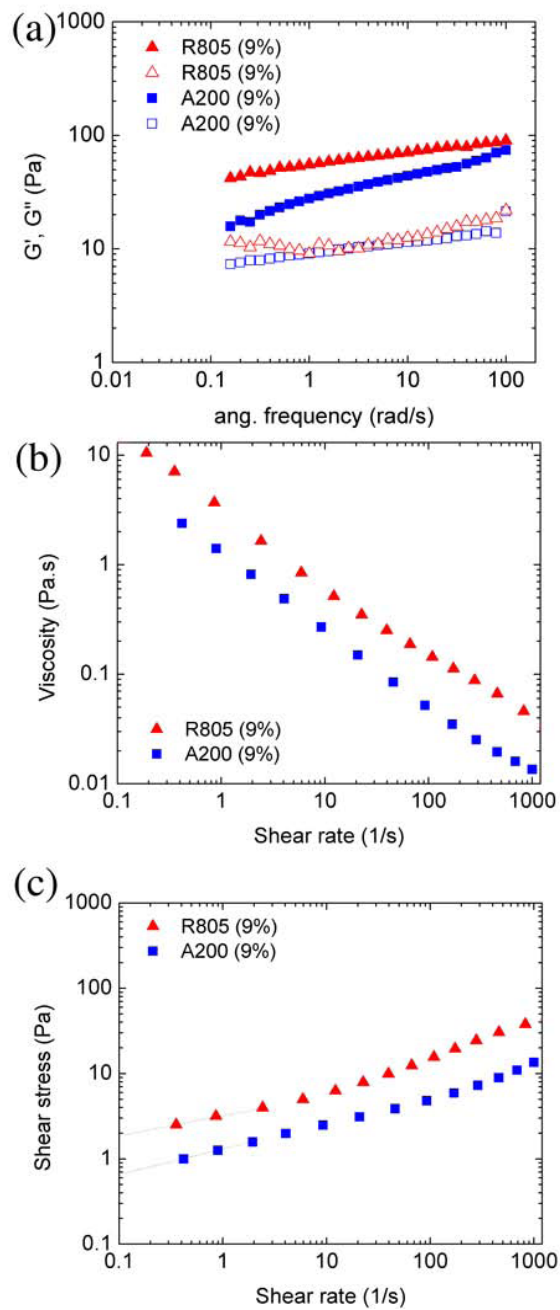


Figure 2.3. Solution rheology of R805 (9 %, hydrophobic, \blacktriangle , \triangle) or A200 (9 %, hydrophilic, \blacksquare , \square) fumed silica; (a) dynamic frequency sweep, (b) steady shear viscosity, and (c) shear stress/rate plots.

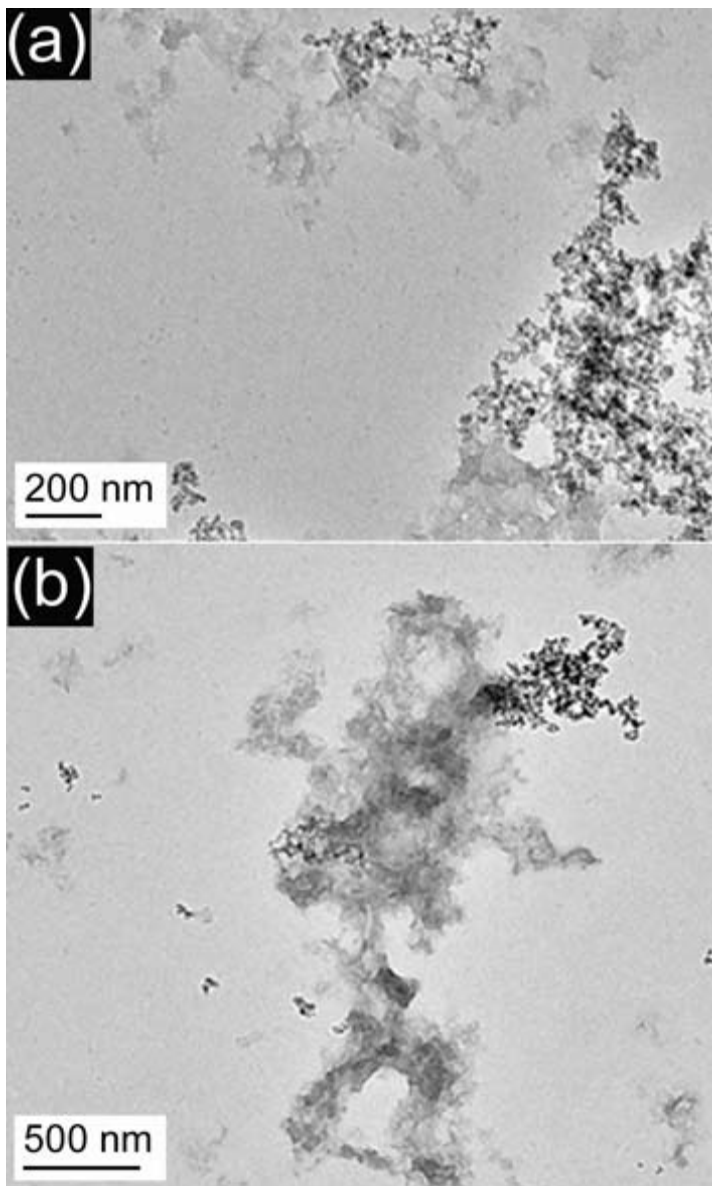


Figure 2.4. Transmission electron micrographs of PAN/R805 (a) and PAN/A200 (b) spun-cast films.

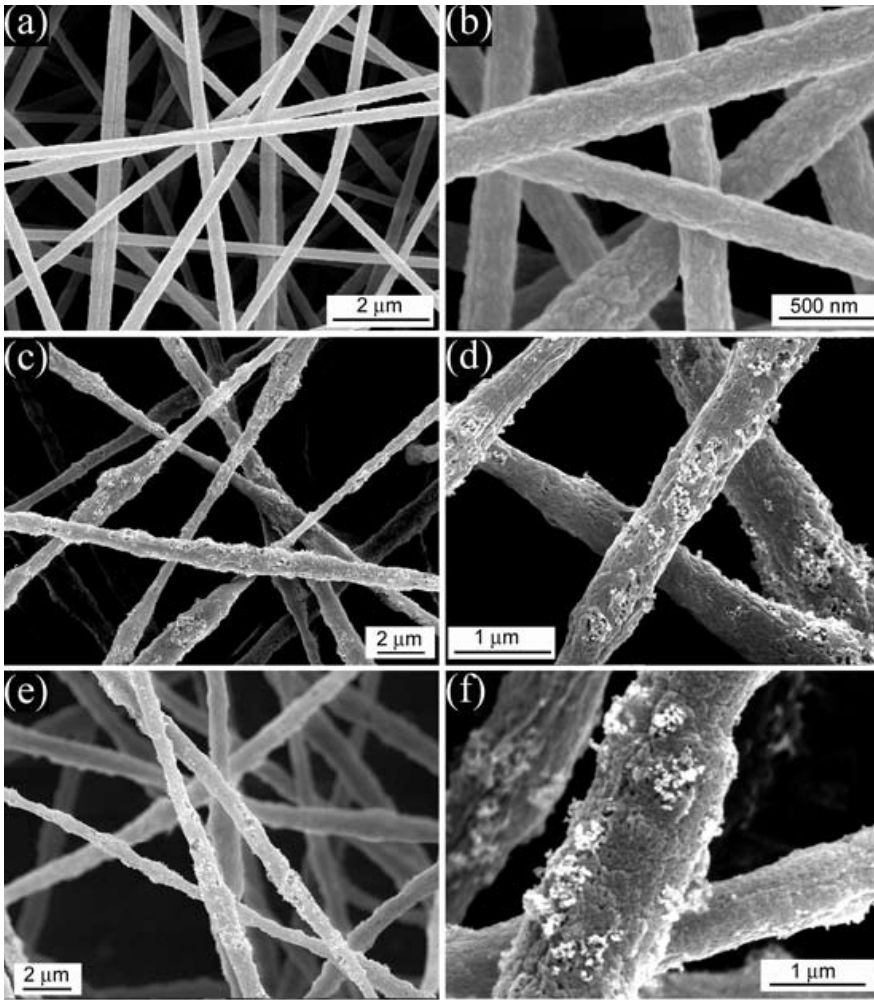


Figure 2.5. Scanning electron micrographs of PAN (a, b), PAN/A200 (c, d), and PAN/R805 (e, f) electrospun fibers.

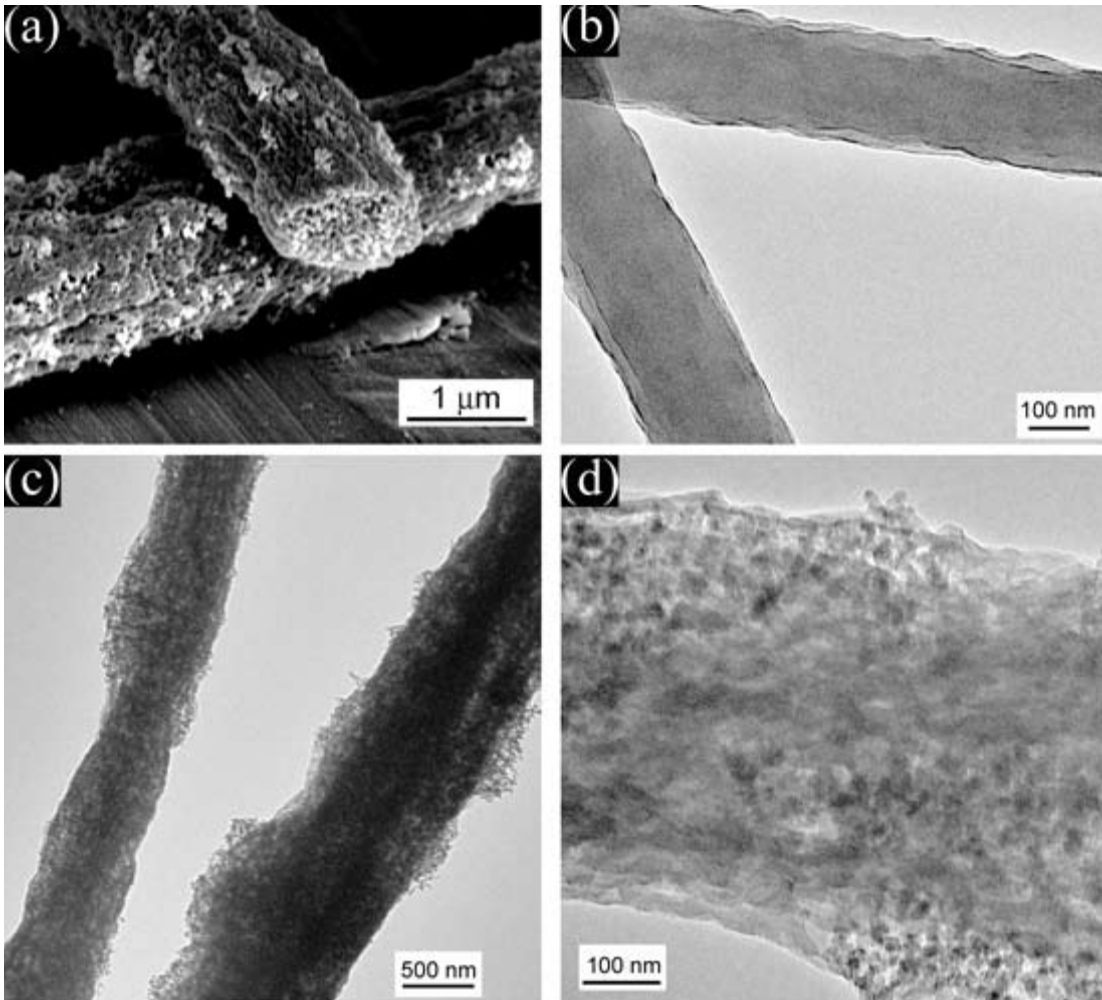


Figure 2.6. Scanning and transmission electron micrographs of PAN with R805 fumed silica (a, c, d) and PAN only (b) electrospun fibers. Fiber cross section (a) was prepared by freeze fracture.

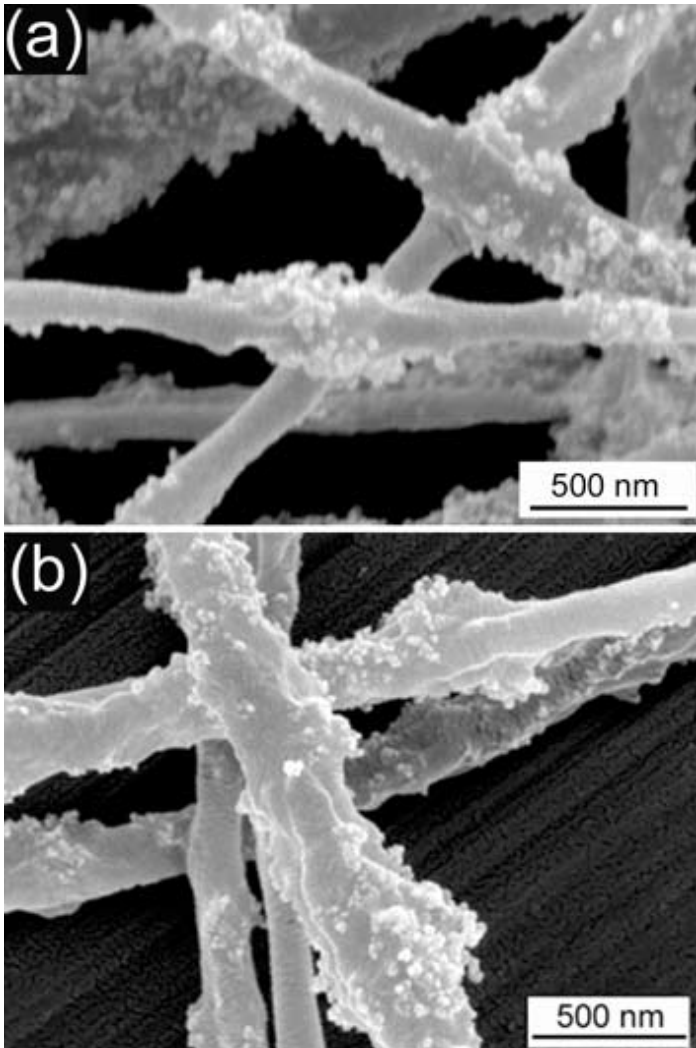


Figure 2.7. Scanning electron micrographs of composite polymer/fumed silica electrospun fibers: PEO/R805 FS (a) and PEO/A200 FS (b).

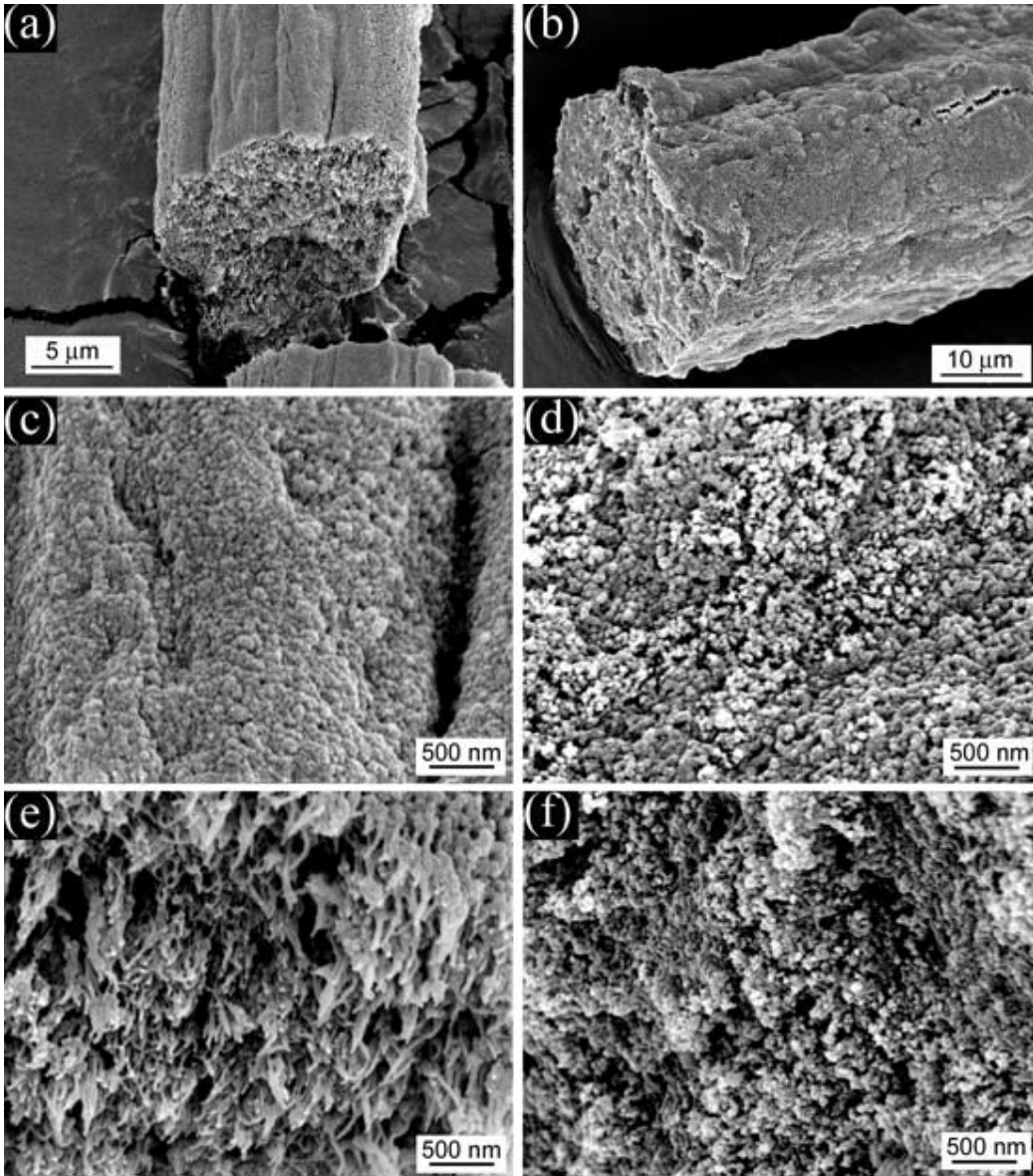


Figure 2.8. SEM images of PAN fiber (a), top surface (c), cross section (e); and PAN/R805 fiber (b), top surface (d), cross section (f) prepared by wet spinning

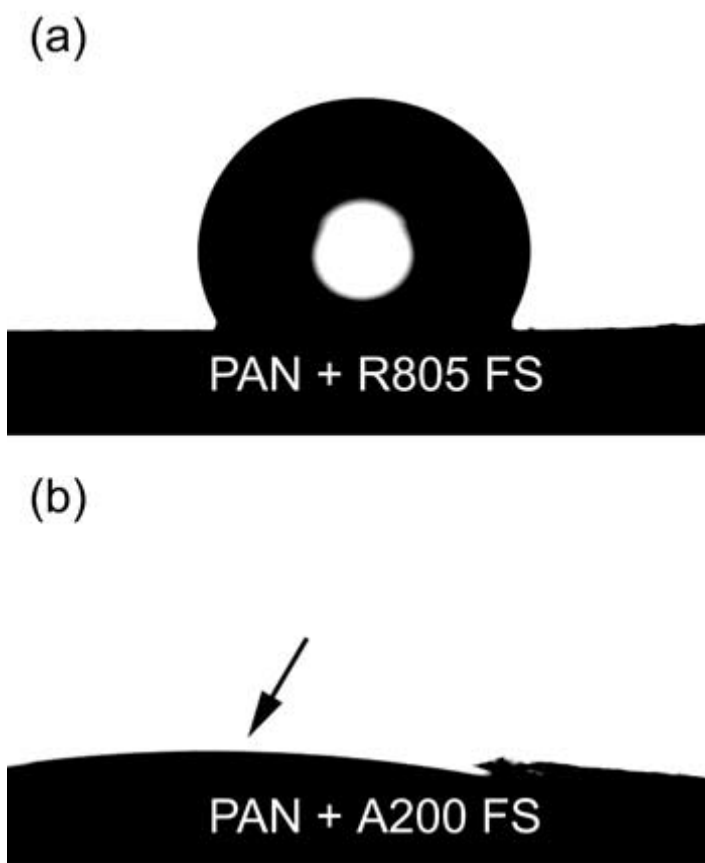


Figure 2.9. Representative contact angle profiles of water on PAN and fumed silica fiber mats. PAN with R805, the hydrophobic FS, has an average contact angle of 128 ± 10 (a), whereas water spreads across PAN with A200, the hydrophilic FS (b). (The arrow indicates the top surface of spreading droplet.)

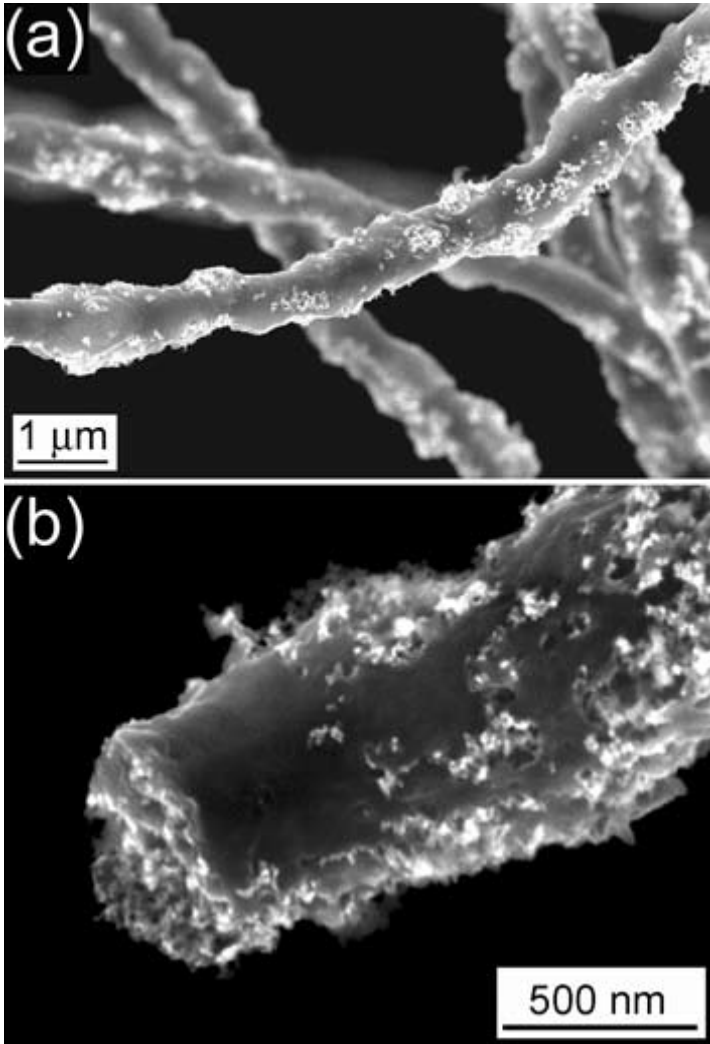


Figure 2.10. SEM images of carbon/fumed silica fibers after carbonization heat treatment.

CHAPTER 3

Electrospun Carbon-Tin Oxide Composite Nanofibers for Use as Lithium Ion Battery Anodes

Chapter 3 is essentially a manuscript by Christopher A. Bonino, Liwen Ji, Zhan Lin, Ozan, Toprakci, Xiangwu Zhang, and Saad A. Khan submitted to *ACS Applied Materials & Interfaces*.

Electrospun Carbon-Tin Oxide Composite Nanofibers for Use as Lithium Ion Battery Anodes

Christopher A. Bonino¹, Liwen Ji², Zhan Lin², Ozan, Toprakci², Xiangwu Zhang², and Saad
A. Khan^{2*}

¹ *Department of Chemical and Biomolecular Engineering, North Carolina State University,
Raleigh, NC 27695-7905*

² *Department of Textiles Engineering, Chemistry, and Science, North Carolina State
University, Raleigh, NC 27695-8301*

Abstract

Composite carbon-tin oxide (C-SnO₂) nanofibers are prepared by two methods and evaluated as anodes in lithium-ion battery half cells. Such an approach complements the long cycle life of carbon with the high lithium storage capacity of tin oxide. In addition, the high surface-to-volume ratio of the nanofibers improves the accessibility for lithium intercalation as compared to graphite-based anodes, while eliminating the need for binders or conductive additives. The composite nanofibrous anodes have 1st discharge capacities of 788 mAh g⁻¹ at 50 mA g⁻¹ current density, which are greater than pure carbon nanofiber anodes,

* corresponding author: khan@eos.ncsu.edu (email); 919-515-4519 (ph)

as well as the theoretical capacity of graphite (372 mAh g^{-1}), the traditional anode material. In the first protocol to fabricate the C-SnO₂ composites, tin sulfate is directly incorporated within polyacrylonitrile (PAN) nanofibers by electrospinning. During a thermal treatment the tin salt is converted to tin oxide and the polymer is carbonized, yielding carbon-SnO₂ nanofibers. In the second approach, we soak the nanofiber mats in tin sulfate solutions prior to the final thermal treatment, thereby loading the outer surfaces with SnO₂ nanoparticles and raising the tin content from 1.9 to 8.6 weight percent. Energy dispersive spectroscopy and X-ray diffraction analyses confirm the formation of conversion of tin sulfate to tin oxide. Furthermore, analysis with Raman spectroscopy reveals that the additional salt soak treatment from the second fabrication approach increases in the disorder of the carbon structure, as compared to the first approach.

3.1. Introduction

Rechargeable lithium ion batteries (LIBs) have the potential to meet the power needs of future technologies, from portable electronics to plug-in electric vehicles (EVs). However, challenges remain that need to be overcome, in particular development of light weight and increased capacity materials for the anode, the negative electrode. One approach in this regard is to use elements that form alloys with lithium, such as tin (Sn) or silicon (Si), which have theoretical specific capacities 2-9 times greater than graphite, the current anode material.¹ However, anodes composed of lithium (Li) alloys may have poor cycle life as a result of large volume changes and pulverization during lithium de/insertion.² An alternative approach is to use blends of nano-scale alloys and carbon, which have complementary properties. Li-alloy nanomaterials are capable of better accommodating the strains from lithium de/alloying as compared to bulk materials and have high lithium capacities, whereas carbon has a good cycle life.^{3,4} A carbon-lithium alloy based anode material that is simple to fabricate and scale-up is therefore an attractive technology for future lithium batteries.

Electrospinning is an emerging process with applications for battery components, including separators and electrodes, e.g.⁵⁻⁷ Electrospun fibers can be made with sub-micron diameters, with different functionalities and having high surface-to-volume ratios.⁸⁻¹⁴ Battery electrodes with nano-scale features can have improved performance due to “short path lengths for electronic and Li ion transport.” (Reviewed by¹⁵) Work by our group and others have shown that carbonized electrospun fibers with lithium alloys, including MnO_x , Fe_3O_4

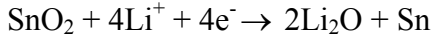
and Si, can be used as LIB anodes.¹⁶⁻²¹ Recently, tin salts have been electrospun with polymer fibers and converted to composite Sn-carbon anodes.^{22, 23} However, these approaches involved complicated fabrication steps, such as a coaxial electrospinning or heat treatment with a reducing atmosphere (i.e., hydrogen gas) that may be cumbersome for scalability. In addition, no attempt has been made to examine ways to enhance tin content in these systems.

We present two different approaches for fabricating electrospun carbon-tin oxide composite nanofibers, which are facile, tailor easily scalable and allows for incorporating additional tin-oxide on nanofiber surface. One method offers an *in situ* protocol to incorporate tin into the nanofibers, whereas the other scheme allows for enhancing tin content in the nanofibrous matrix via a simple post-treatment. In our first approach, solutions containing precursors to carbon fibers and tin oxide particles, PAN and tin sulfate, respectively, are electrospun. Following a series of thermal treatments in inert atmospheres, PAN is carbonized and the tin salt is converted to tin oxide by the following reaction:



The *in-situ* incorporation of tin salts with the electrospinning process, and subsequent conversion by thermal treatment is a straightforward method to fabricate functional composite nanofibers. The composite carbon-tin oxide (C-SnO₂) fiber mats are then used directly as lithium-ion battery anodes. The mechanical stability and good conductivity of the carbon nanofibers allow the elimination of polymer binders and conductive fillers, reducing non-active material in the electrode. The addition of SnO₂ raises the storage capacity of the

nanofibrous anode. Lithium can react with tin oxide to form an alloy by the following scheme:



For the second approach, we modified our fabrication strategy to enhance the loading of tin oxide particles. The electrospun PAN/SnSO₄ nanofibers were thermally treated in air to stabilize the polymer, after which, the nanofibers mats were infiltrated with tin sulfate by an aqueous soaking treatment. The samples were then thermally treated to carbonize the polymer and convert the salt to SnO₂. The salt-soak treatment in this study results in composite nanofibers with their outer surfaces loaded with SnO₂ nanoparticles. Having lithium alloys accessible at the fiber surface is advantageous for Li-ion anodes, since the lithium can be stored at the electrode surfaces. After fabrication, we evaluated the anode performance of the solution-soaked carbon mats. In a previous study by Lee, *et al.*, SnO₂ coated, colloidal sphere-templated structures were prepared from a tin sulfate solution soak and decomposition heat treatment.²⁶ However, when evaluated as LIB anodes, the specific capacities were fairly low (<300 mAh g⁻¹ at 25 mA g⁻¹ current density). Our composite C-SnO₂ nanofibers require fewer process steps, and have higher capacities. To our knowledge, we are the first to use a salt-soaking treatment to fabricate composite electrospun mats used as LIB anodes.

3.2. Experimental Section

Materials. Polyacrylonitrile (PAN, $M_w = 150,000$ g/mol, Scientific Polymer Products), N, N dimethylformamide (DMF, Fisher Scientific), and tin sulfate (Gelest) were used as received.

Methods. *Preparation of PAN/tin salt solutions.* Polymer solutions were prepared by adding tin sulfate (2 wt %) and PAN (7.5 wt %) into DMF and stirring with a magnetic stir bar overnight at 60°C. The solution was sonicated for 10-15 minutes prior to electrospinning.

Solution Characterization. Steady shear rheology experiments were performed at 25°C using a stress-controlled rheometer (AR2000, TA Instruments) with a 40 cm, 2° cone and plate geometry and applying stresses ranging from 0.01–100 Pa (10 points per decade). Zero shear viscosities were estimated by averaging the first 10 points of the Newtonian regime. Ionic conductivity was determined using a potentiostat (Gamry Instruments) and correlating with a standard (1 mS/cm) potassium chloride (Fisher Scientific). Surface tension was measured from a pendant drop analyzer from SEO Co. Ltd (model Phoenix 300).

Preparation of carbon-tin oxide nanofibers. Polymer nanofibers were prepared by electrospinning. PAN solutions were pumped through a 10 mL syringe fitted with a 22 gauge needle at a flow rate of 0.5 mL/hr. The distance between the collector plate and needle was fixed at 15 cm with a 7-8 kV applied voltage. Details of the set-up are described elsewhere.⁸⁻¹² Approximately 50 micron thick mats were prepared by electrospinning for ~18 hrs in an ambient environment with 40-55% relative humidity. As-spun fiber mats were

heated in a furnace in air at 2°C/min up to 280°C, and held constant for 6 hrs to stabilize the PAN. Subsequently, the furnace was purged with nitrogen and heated at a rate of 2°C/min. The final temperature of 600°C was maintained for 8 hrs for the carbonization.

Characterization of polymer and carbon composite fibers. Polymer and heat-treated fibers were characterized using a field emission scanning electron microscope (FE SEM, FEI XL30). Prior to analysis, polymer fiber mats were sputter-coated with gold. The diameters and standard deviations of 50 fibers per sample, without bead defects, were measured using Adobe Photoshop CS3. Carbon fiber mats that were not evaluated for diameter measurements, were not sputter coated. Quantitative elemental analysis was characterized using a SEM (Hitachi S-3200N) with energy dispersive spectroscopy (EDS) system.

Fibers were also electrospun directly onto grids and analyzed with a transmission electron microscope (TEM, Hitachi HF2000 with EDS). Fiber crystalline structure was measured using an X-Ray Diffractometer (Philips X'Pert PRO MRD HR) and a Raman spectrometer (Horiba, 633 nm laser). Lorentzian distribution curves were fit to Raman spectra using Origin 8. Peak intensities and ratios were averages from three spectra for each sample.

Evaluation of fiber mats as Li-ion battery anodes. Carbonized mats were punched out to the appropriate dimensions for 2032 coin-type cells. Battery cells contained fiber mats attached to copper foil (Lyon industries) as the working electrode and lithium ribbon (Aldrich) as the counter electrode. The separator and electrolyte were Separion S240 P25 (Degussa) and 1 M lithium hexafluorophosphate (LiPF₆) in 1:1 (v/v) ethylene carbonate/ethyl

methyl carbonate (Ferro Corporation), respectively. After assembly, the half cells were cycled between 2.80 and 0.02 V using an automatic battery cycler (Arbin). Cycling current densities included 50, 100, 200, 300, or 500 mA g⁻¹.

3.3. Results and Discussions

3.3.1. Carbon-SnO₂ Nanofibers by *In-situ* Electrospinning

In our first approach, solutions containing PAN and SnSO₄ were electrospun into nanofibers. C-SnO₂ composites were then prepared by heating the polymer-salt nanofibers in a controlled-atmosphere furnace. As a first step, we examined properties of nanofibers prior to carbonization. Salt-free PAN nanofibers were used as a control. Figure 3.1b-d reveal that nanofibers obtained from both solutions (with and without salt) have similar-sized diameters, 293±67 nm and 298±57 nm, respectively. However, the addition of SnSO₄ to the PAN solution causes more bead defects. Analysis with TEM reveals what may be salt particles on and beneath the surface of the PAN fibers containing SnSO₄; no particles are observed on the pure PAN fibers. (Figure 3.1e, f.)

The properties of electrospinning solutions can be related to the morphology of electrospun fibers. In particular, solution viscosity, ionic conductivity, and surface tension affect the ability of a solution to be electrospun. (e.g. ²⁷) Table 3.1 shows that PAN solutions containing SnSO₄ have a greater ionic conductivity than pure PAN solutions, which can be attributed to the dissociation of the salt. Both solutions have surface tensions ~33mN/m,

which indicates that PAN has a greater affinity for the air-DMF interface than SnSO₄. In addition, zero shear viscosities are comparable, indicating that salt has minimal effects on the stability of PAN in DMF, unlike what has been seen with other salts (e.g. AlCl₃).²⁸

C-SnO₂ composites were prepared by heating the polymer-salt nanofibers in a controlled-atmosphere furnace. Fibers mats were stabilized at 280°C in air, which crosslinked the PAN chains through dehydrogenation and cyclization reactions.²⁹ The next thermal treatment was performed in a nitrogen atmosphere at 600°C, during which, two conversion reactions occurred. First, the polymer precursor was carbonized, resulting in the release of the non-carbon elements in the forms of methane, hydrogen, hydrogen cyanide, water, carbon dioxide, and/or ammonia.³⁰ During this treatment, the mat color changes to black. The second outcome of the heat treatment is that the tin sulfate salt was converted to tin oxide, following the reaction in Equation 3.1.

3.3.2. Characterization of Stabilized & Carbonized Nanofibers

The C-SnO₂ and carbon fibers were characterized to identify structural changes from their conversion. SEM analysis reveals that the C-SnO₂ and carbon fibers have smaller diameters (176±36 and 223±38 nm, respectively) than the polymer fibers due to the release of gases (e.g. NH₃) and resulting fiber mass reduction during the carbonization process.^{5, 31} In order to examine the presence of SnO₂, the carbonized fibers were observed without a conductive coating because the absence of gold-coating allows for a better contrast and ease

in identifying more electron dense materials (i.e., SnO₂ particles) on the carbon fiber surfaces. (Figure 3.2) The outer surfaces and cross sections of carbon fibers with and without the tin salt have similar appearances; SnO₂ particles are not apparent in the scanning electron micrographs. However, TEM analysis reveals that aggregates of particles with 15-20 nm diameters are present within the fibers after the stabilization and carbonization heat treatments. (Figure 3.3) Using Energy Dispersive Spectroscopy (EDS) we found that the particle aggregates contained tin with and without sulfur, before and after the carbonization heat treatment, respectively. The absence of sulfur after the final thermal treatment indicates that tin sulfate was converted to tin oxide. The peak near 2.7 eV is an artifact of the strong Si peak from a silicon nitride TEM grid.

XRD analysis confirmed the TEM/EDS results on the formation of tin oxide during the final heat treatment. Figure 3.4a and b show X-Ray diffractograms of the fiber mats after the stabilization and carbonization treatments, respectively. Stabilized PAN/SnSO₄ nanofibers have characteristic peaks that can be assigned to tin sulfate (JCPDS no. 16-0252), whereas no tin oxide peaks are found. This result confirms that tin sulfate is not converted to tin oxide during the stabilization heating condition (280°C in air). After the carbonization, the composite fiber patterns contained prominent peaks at near 26°, 33°, and 52°, which were indexed to the (110), (101), and (211) planes of SnO₂ (JCPDS no. 41-1445). Additionally, a broad peak was present at 2θ= 25° on both the C-SnO₂ and carbon samples, corresponding to the (002) diffraction peak of graphite, which indicates the formation of carbon.

The microstructure of the carbon fibers changed throughout the heat treatments, as revealed by Raman spectroscopy. Shown in Figure 3.5a and b are representative Raman spectra of stabilized composite and pure fibers that exhibit two broad peaks. The peaks centered at ~ 1340 and ~ 1580 cm^{-1} correspond to D and G bands of disordered carbon, respectively.³² The presence of these two peaks indicates that the PAN polymer chains reacted to form ring structures with sp^2 and sp^3 bonding. Because the fibers were not yet heated under nitrogen at elevated temperatures for carbonization, the stabilized fibers contain nitrogen, hydrogen, and oxygen, in addition to carbon, as reviewed by Rahaman et al.³⁰ The presence of non-carbon bonds may disrupt ordering of the aromatic rings, leading to disordered carbon structures with small ring clusters. In order to characterize the fiber microstructure, two Lorentzian curves were fit to the spectra. The ratio of the peak intensities I_D/I_G , known as R , characterizes the extent of structural disorder within carbon and is inversely proportional to cluster size of the aromatic rings in non-crystalline graphite materials ($R \sim 1/L_c$).³² Peak ratios of the stabilized fibers were 2.1, verifying the highly disordered structure. R values were the same for stabilized fibers with and without salt. Thus, the SnSO_4 incorporated within the fibers during electrospinning did not affect the hydrocarbon fiber microstructure.

The carbonization heat treatment increased the ordering and cluster sizes of the fiber mats. By our estimates, both samples of carbonized nanofibers had comparable R values, 1.5 – 1.6, which indicate a disordered graphitic structure with small cluster domains. Previous work by Zussman, *et al.* has reported $R < 1.0$ in carbonized PAN nanofibers.³³ However,

differences in methodologies between our studies may explain the discrepancies. For example, the carbonization temperature in our study was 100°C lower, which likely contributed to the more disordered structure.³⁴

3.3.3. Performance of C-SnO₂ Nanofiber Mats as Li-Ion Battery Anodes

The nanofiber mats were evaluated as anodes in Li-ion battery half cells. The conductive nanofiber mat provided ample mechanical structure, eliminating the need for conductive additives (e.g., carbon black) or binders. Mats containing tin oxide achieved higher performances as compared to the pure carbon nanofibers. Shown in Figure 3.6a and b are representative charge-discharge curves for pure carbon and tin oxide-carbon nanofiber anodes. The initial rapid reduction in voltages from 2.8 to ~0.6 V during the first charge cycles (C1) are due to the formation of a solid electrolyte interface (SEI) film on the anode.³⁵ C1 curves of the carbon and tin oxide-carbon have plateaus 0.55 and 0.70 V, respectively, which are attributed to the formation of carbon- and/or tin-lithium alloys.¹ The C-SnO₂ anode has a greater 1st discharge potential than the carbon fiber anode, 700 versus 620 mAh g⁻¹, respectively, because tin alloys can accommodate more lithium than carbon sheets. Both anodes materials have comparable Columbic efficiencies (70%) in their 1st cycles, which were attributed to the formation of the SEI film on the fiber surfaces.³⁵ After subsequent cycles at a constant current density of 50 mA g⁻¹, the capacity of the composite anode approaches the capacity of the pure carbon, which may be the result of damage to tin oxide

from volume changes during lithium insertion.³⁶ (Figure 3.6c) However, the 40th cycle capacity of both anode materials are $\sim 470 \text{ mA h g}^{-1}$, which exceed the theoretical capacity of graphite by 100 mA h g^{-1} .

The benefit of adding tin oxide to carbon nanofibers is more evident at charge densities greater than 50 mA g^{-1} (Figure 3.6d). The 10th cycle discharge capacity of the C-SnO₂ composite is greater than the pure carbon fibers by as much as 150 mAh g^{-1} . At higher charge rates, lithium insertion may be diffusion limited. Thus, the tin oxide-carbon fibers can accommodate more lithium atoms at outer surfaces of the fibers than for pure carbon, which allow for greater accessibility of the lithium during rapid rates of charging.

After cycling, mats were removed from the batteries and rinsed with acetone to remove any residual electrolyte. Micrographs shown in Figure 3.7a and b reveal that the structures of C-SnO₂ and carbon fibers were maintained despite lithium intercalation. Contrary to what has been previously reported with other nanofiber mats, fibers were not damaged and did not show signs of powderization.¹⁷ The ability of the fibrous mats to remain intact during cycling confirms that binders are not needed with the composite and pure carbon nanofibrous anodes.

3.3.4. Nanofibers Surface-loaded with SnO₂ Nanoparticles *via* Soak Treatment

The goal for this part of the study was to enhance the tin oxide content incorporated within the nanofibers during electrospinning with a surface enrichment soaking method.

While the benefits of the first approach included minimal process steps, the content of tin within the fibers was limited by the solubility of tin sulfate in electrospinning solutions and conversion of tin oxide from heat treatments. In our second approach, nanofiber mats were soaked in aqueous tin salt solutions. The PAN-based mats were thermally treated in air prior to the salt infiltration, which oxidized the nanofiber outer surfaces.³⁰ Compared to PAN, the stabilized polymer is more hydrophilic, which enhances coverage and penetration of disassociated salt particles on the nanofiber exteriors. Furthermore, the stabilized mats are more feasible to handle and soak compared to the more flexible, electrospun PAN mat, which can fold over on itself in solution.

3.3.5. Characterization of Stabilized, and Salt-Soaked, & Carbonized Nanofibers

The benefits of the soaking treatment are evident from SEM and TEM analysis on the carbonized fibers (Figure 3.8). PAN/SnSO₄ nanofibers that had been soaked in the tin salt solution and carbonized were covered with particles. Individual particles (~15 nm diameter) and particle aggregates (up to ~200 nm) were present on fibers throughout the mat, which confirmed the efficacy of the soak treatment. (Figure 3.8a, e, f.) Prior to SEM and TEM analysis, the particle-loaded mats were rinsed with ethanol or soaked in water in order to verify particle attachment onto the fibers. In comparison to the salt-soaked fibers, particles were not seen on the surfaces of the control, PAN nanofibers soaked in water prior to carbonization. In order to characterize the elemental content of each type of mat, the fibers were evaluated quantitatively by SEM-EDS. (Figure 3.8d) The tin soak treatment increased

the tin content in the C-SnO₂ fibers by more than 4 times, up from 1.9 to 8.6 wt%, compared to the composite mats in the first study. No tin was present in the control carbon mats from either study.

In addition to analysis by electron microscopy, the crystal structures of the solution-soaked nanofibers were characterized with XRD. Nanofiber mats were analyzed after soaking in solutions and carbonization. Figure 3.9a reveals that the XRD pattern of the composite mats had prominent peaks matching tin oxide reflections (JCPDS no. 41-1445), which is consistent with the results of the first approach. In addition, the heat-treated nanofiber mats have peaks at $2\theta = 25^\circ$, corresponding to the (002) reflection of disordered carbon.

Raman analysis revealed structural differences between the solution-soaked carbon and C-SnO₂ nanofibers. As seen in the first approach, the D and G peaks are present in the spectra of the carbonized fibers at ~ 1335 and ~ 1580 cm⁻¹, respectively. (Figure 3.9b and c) In addition, the pure carbon nanofibers had the same height ratio (R=1.5) as the carbon nanofibers in the first approach, despite the soak treatment and different heating conditions. However, one difference between the carbon nanofibers was the D peak width. The soaked carbon nanofibers had a narrower average width (141 ± 45 cm⁻¹) than the carbon nanofibers without the soak (215 ± 32 cm⁻¹) from the first approach. A broader peak may indicate a greater distribution of aromatic cluster sizes and/or aromatic rings without six carbons.³² These structural differences may account for differences in anode performance, which will be discussed in the next section.

The tin salt solution soaking treatment significantly affected the carbon microstructure of the composite nanofibers. Most notably, the peak ratio was 1.9, which is the greatest of any of the carbonized samples studied. We hypothesize that the infiltration of the tin salt and subsequent formation of tin oxide particles on and within the nanofibers disrupted the formation of carbon ring clusters. The salt soaking treatment increases the tin content in the composite fiber, which can explain the difference in Raman analyses between the two approaches.

3.3.6. Performance of Soaked Carbon-SnO₂ Nanofiber Mats as Lithium Ion Battery

Anodes

The nanofiber mats surface-loaded with tin oxide nanoparticles were evaluated as Li-ion battery anodes. The salt soaking treatment enhances the anode performance, relative to the water-soaked carbon nanofiber control. As observed from Figure 3.10 a and b, the composite fiber mat achieves a 1st discharge capacity of 788 mAh g⁻¹, which is a 200 mAh g⁻¹ improvement over the carbon nanofibers. The added tin content from the salt soak treatment contributed to the enhanced capacity. Both materials have similar 1st cycle Columbic efficiencies (70%), which can be attributed to the formation of the SEI film on the nanofiber surfaces. For C-SnO₂ fibers, lithium was also lost during the reaction with SnO₂ to form Sn (Equation 3.2). The advantages of the salt soak are also apparent in the cycle life performance (Figure 3.10c.). With a current density of 50 mA g⁻¹, the composite SnO₂-

carbon fiber mats maintains a higher capacity than the pure carbon fiber mats for the duration of the test. At the 40th cycle, the capacity of the composite mat is 50 mAh g⁻¹ greater than the control mat.

While the benefits of the added tin oxide to the nanofiber anodes are evident in this study, the capacities are reduced, as compared to the mats in the first study. Most notably, the 10th cycle capacities of pure carbon fiber mat that were soaked in water are more than 100 mAh g⁻¹ lower than the pure carbon fiber mats from the 1st study. We hypothesize that changes to the thermal treatment, from one continuous to two separate cycles (to accommodate the soak treatment), altered the carbon microstructures and caused the reduction in capacities. Structural differences between the carbon nanofibers in the two studies are evident in the Raman analysis. Specifically, the carbon nanofibers in the second study had a smaller size distribution of carbon-ring clusters. We speculate the process of separating the heat steps in the second study (25°C → 280°C + soak + 25°C → 600°C) exposes the mats to a longer combined thermal treatment than the continuous process in the first study (25°C → 280°C → 600°C). Thus, the carbon structure in the nanofibers in the second study may have more order compared to the first study, and in turn, a lower storage capacity for lithium.³⁴ We are pursuing further studies to investigate the role of continuous and separated thermal treatments on the carbon structure in PAN-based nanofibers and their performance as anodes.

While the heat treatment process conditions may require further optimization to maximize anode performance (not the goal of this study), the benefits of the salt soak

treatment compared to the control are evident. The infiltration of tin salts into fiber mats by soak treatments is a facile route to loading tin oxide particles onto nanofiber surfaces. We conceive that this technique can be combined with the incorporation of other nanoparticles that form lithium alloys during electrospinning to further enhance the performance of these materials as Li-ion battery anodes.

3.4. Conclusions

We found that tin oxide can be incorporated into carbon nanofibers, which improves their performance when evaluated as lithium ion battery anodes. The addition of tin sulfate to polymer nanofibers (1) during and (2) after electrospinning, followed by heat treatments, were two facile methods to prepare the C-SnO₂ composites. The latter approach yielded a greater concentration of tin, since tin sulfate has a higher solubility in the soaking solution (water) than the electrospinning solution (DMF). X-ray diffraction and energy dispersive spectroscopy confirmed the formation of tin oxide after the heat treatments. In addition, Raman analysis revealed that the addition of the soaking treatment (Approach #2) led to a more disordered carbon structure than the first approach with one continuous heat treatment.

3.5. Acknowledgements

This work was supported by National Science Foundation GOALI Program (#0555959) and a Department of Education GAANN Fellowship (CAB). The authors thank Professor Peter S. Fediw and Andrew Loebel for helpful discussions.

3.6. References

- (1) Winter, M.; Besenhard, J. O.; Spahr, M. E.; Novak, P. *Advanced Materials* **1998**, *10*, 725-763.
- (2) Besenhard, J. O.; Yang, J.; Winter, M. *Journal of Power Sources* **1997**, *1*, 87-90.
- (3) Wilson, A. M.; Dahn, J. R. *Journal of the Electrochemical Society* **1995**, *2*, 326-332.
- (4) Tarascon, J. M.; Armand, M. *Nature* **2001**, *6861*, 359-367.
- (5) Kim, C.; Yang, K. S.; Kojima, M.; Yoshida, K.; Kim, Y. J.; Kim, Y. A.; Endo, M. *Advanced Functional Materials* **2006**, *18*, 2393-2397.
- (6) Ding, Y. H.; Zhang, P.; Long, Z. L.; Jiang, Y.; Xu, F.; Di, W. *Science and Technology of Advanced Materials* **2008**, *1*.
- (7) Cho, T. H.; Sakai, T.; Tanase, S.; Kimura, K.; Kondo, Y.; Tarao, T.; Tanaka, M. *Electrochemical and Solid State Letters* **2007**, *7*, A159-A162.
- (8) Saquing, C. D.; Manasco, J. L.; Khan, S. A. *Small* **2009**, *8*, 944-951.
- (9) Bonino, C. A.; Krebs, M. D.; Saquing, C. D.; Jeong, S. I.; Shearer, K. L.; Alsberg, E.; Khan, S. A. *Carbohydrate Polymers* **In press**.
- (10) Talwar, S.; Hinestroza, J.; Pourdeyhimi, B.; Khan, S. A. *Macromolecules* **2008**, *12*, 4275-4283.
- (11) Talwar, S.; Krishnan, A. S.; Hinestroza, J. P.; Pourdeyhimi, B.; Khan, S. A. *Macromolecules* **2010**, *18*, 7650-7656.

- (12) Tang, C.; Saquing, C. D.; Harding, J. R.; Khan, S. A. *Macromolecules* **2010**, *2*, 630-637.
- (13) Huang, Z. M.; Zhang, Y. Z.; Kotaki, M.; Ramakrishna, S. *Composites Science and Technology* **2003**, *15*, 2223-2253.
- (14) Li, D.; Xia, Y. N. *Advanced Materials* **2004**, *14*, 1151-1170.
- (15) Arico, A. S.; Bruce, P.; Scrosati, B.; Tarascon, J. M.; Van Schalkwijk, W. *Nature Materials* **2005**, *5*, 366-377.
- (16) Ji, L. W.; Zhang, X. W. *Electrochemistry Communications* **2009**, *4*, 795-798.
- (17) Wang, L.; Yu, Y.; Chen, P. C.; Zhang, D. W.; Chen, C. H. *Journal of Power Sources* **2008**, 717-723.
- (18) Ji, L. W.; Zhang, X. W. *Electrochemistry Communications* **2009**, *6*, 1146-1149.
- (19) Ji, L. W.; Lin, Z.; Medford, A. J.; Zhang, X. W. *Chemistry-a European Journal* **2009**, *41*, 10718-10722.
- (20) Ji, L. W.; Jung, K. H.; Medford, A. J.; Zhang, X. W. *Journal of Materials Chemistry* **2009**, *28*, 4992-4997.
- (21) Ji, L. W.; Lin, Z.; Guo, B. K.; Medford, A. J.; Zhang, X. W. *Chemistry-a European Journal* **2010**, *38*, 11543-11548.
- (22) Yu, Y.; Gu, L.; Wang, C. L.; Dhanabalan, A.; van Aken, P. A.; Maier, J. *Angewandte Chemie-International Edition* **2009**, *35*, 6485-6489.
- (23) Zou, L.; Gan, L.; Kang, F.; Wang, M.; Shen, W.; Huang, Z. *Journal of Power Sources* **2010**, 1216-1210.

- (24) Cueilleron, J.; Hartmanshenn, O. *Bulletin of the Chemistry Society of France* **1959**, *1*, 168-172.
- (25) Courtney, I. A.; Dahn, J. R. *Journal of the Electrochemical Society* **1997**, *6*, 2045-2052.
- (26) Lee, K. T.; Lytle, J. C.; Ergang, N. S.; Oh, S. M.; Stein, A. *Advanced Functional Materials* **2005**, *4*, 547-556.
- (27) Fong, H.; Chun, I.; Reneker, D. H. *Polymer* **1999**, *16*, 4585-4592.
- (28) Phadke, M. A.; Musale, D. A.; Kulkarni, S. S.; Karode, S. K. *Journal of Polymer Science Part B-Polymer Physics* **2005**, *15*, 2061-2073.
- (29) Edie, D. D. *Carbon* **1998**, *4*, 345-362.
- (30) Rahaman, M. S. A.; Ismail, A. F.; Mustafa, A. *Polymer Degradation and Stability* **2007**, *8*, 1421-1432.
- (31) Mittal, J.; Bahl, O. P.; Mathur, R. B. *Carbon* **1997**, *8*, 1196-1197.
- (32) Ferrari, A. C.; Robertson, J. *Physical Review B* **2000**, *20*, 14095-14107.
- (33) Zussman, E.; Chen, X.; Ding, W.; Calabri, L.; Dikin, D. A.; Quintana, J. P.; Ruoff, R. S. *Carbon* **2005**, *10*, 2175-2185.
- (34) Kim, C.; Park, S. H.; Cho, J. K.; Lee, D. Y.; Park, T. J.; Lee, W. J.; Yang, K. S. *Journal of Raman Spectroscopy* **2004**, *11*, 928-933.
- (35) Arora, P.; White, R. E.; Doyle, M. *Journal of the Electrochemical Society* **1998**, *10*, 3647-3667.
- (36) Winter, M.; Besenhard, J. O. *Electrochimica Acta* **1999**, *1-2*, 31-50.

Table 3.1. Properties of Electrospun Solutions.

	PAN solution	PAN + SnSO ₄ solution
Zero Shear Viscosity (Pa·s)	0.47	0.50
Conductivity (mS/cm) ^a	0.03± 0.01	0.11± 0.01
Surface Tension (mN/m) ^a	33± 3	33± 2

^a Means ± standard deviations are reported using a sample size of 5 measurements.

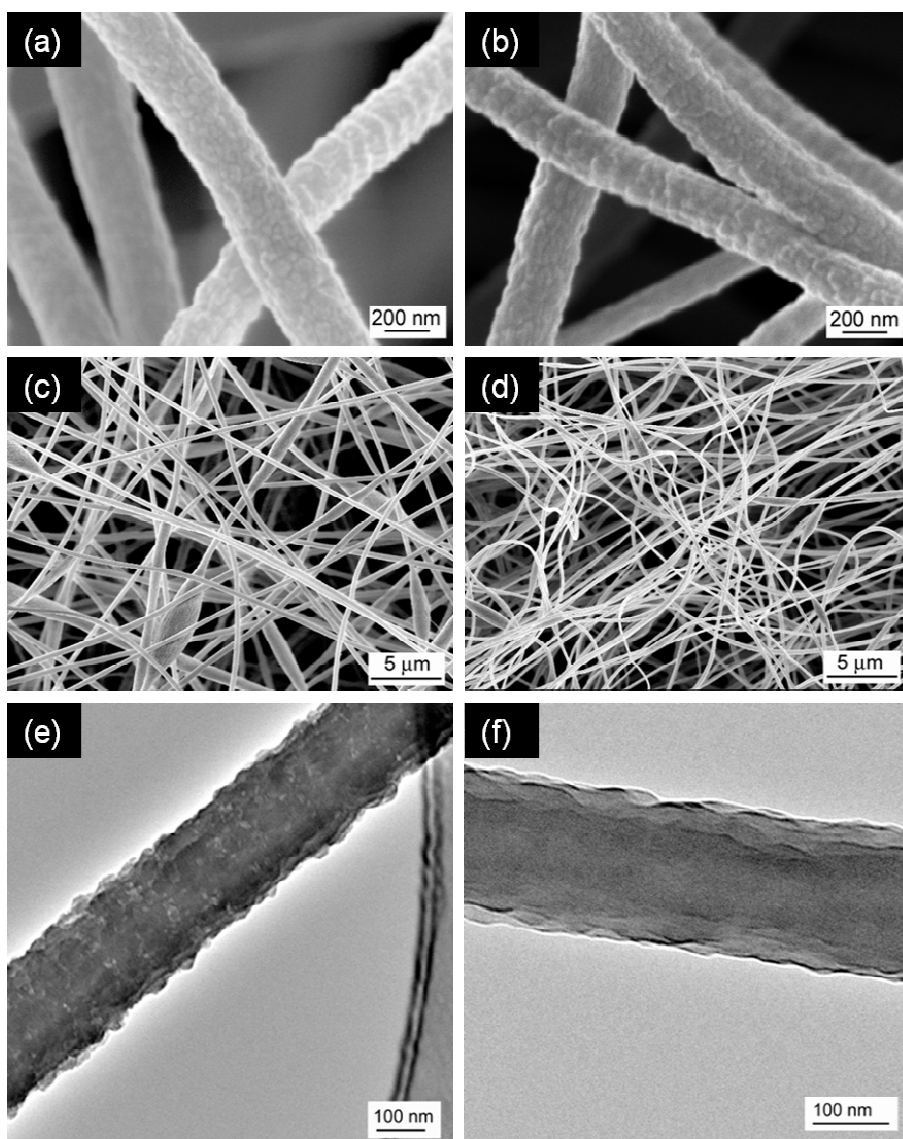


Figure 3.1. Electron micrographs of electrospun PAN nanofibers with (a, c, e) and without (b, d, f) tin sulfate. Figures a-d were captured with SEM and e, f with TEM. Average fiber diameters were 293 ± 67 and 298 ± 57 nm, respectively.

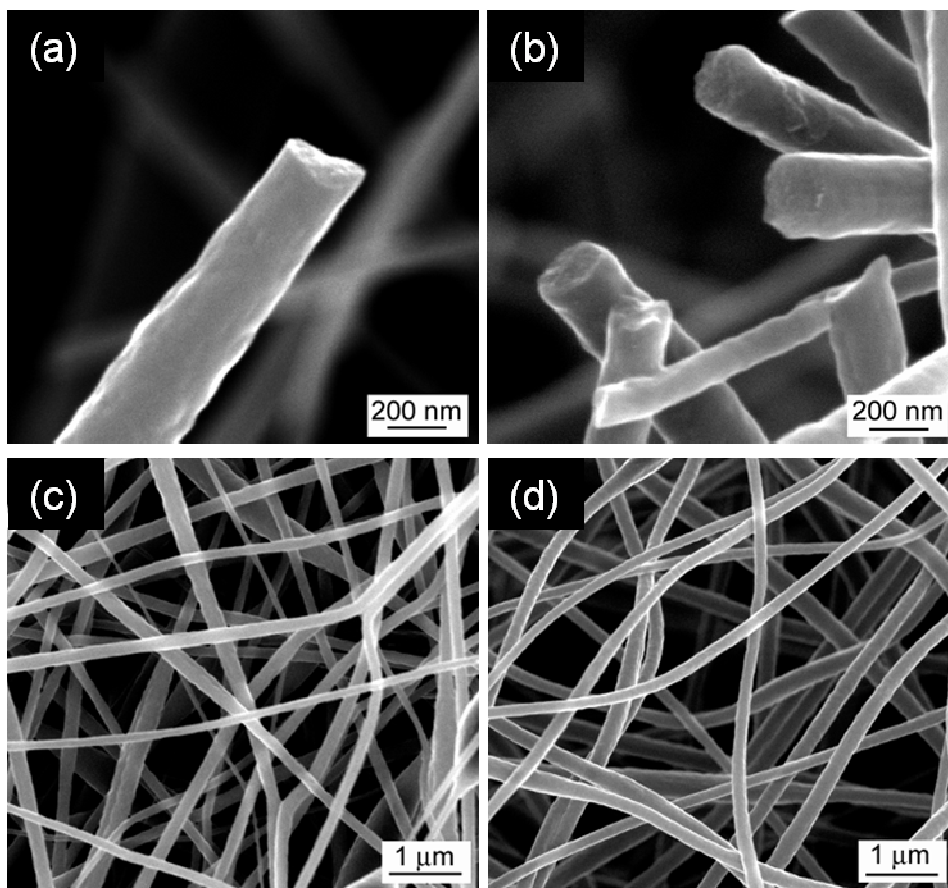


Figure 3.2. Scanning electron micrographs of carbonized nanofibers with (a, c) and without (b, d) tin oxide. Average fibers diameters were 176 ± 36 and 223 ± 38 nm, respectively.

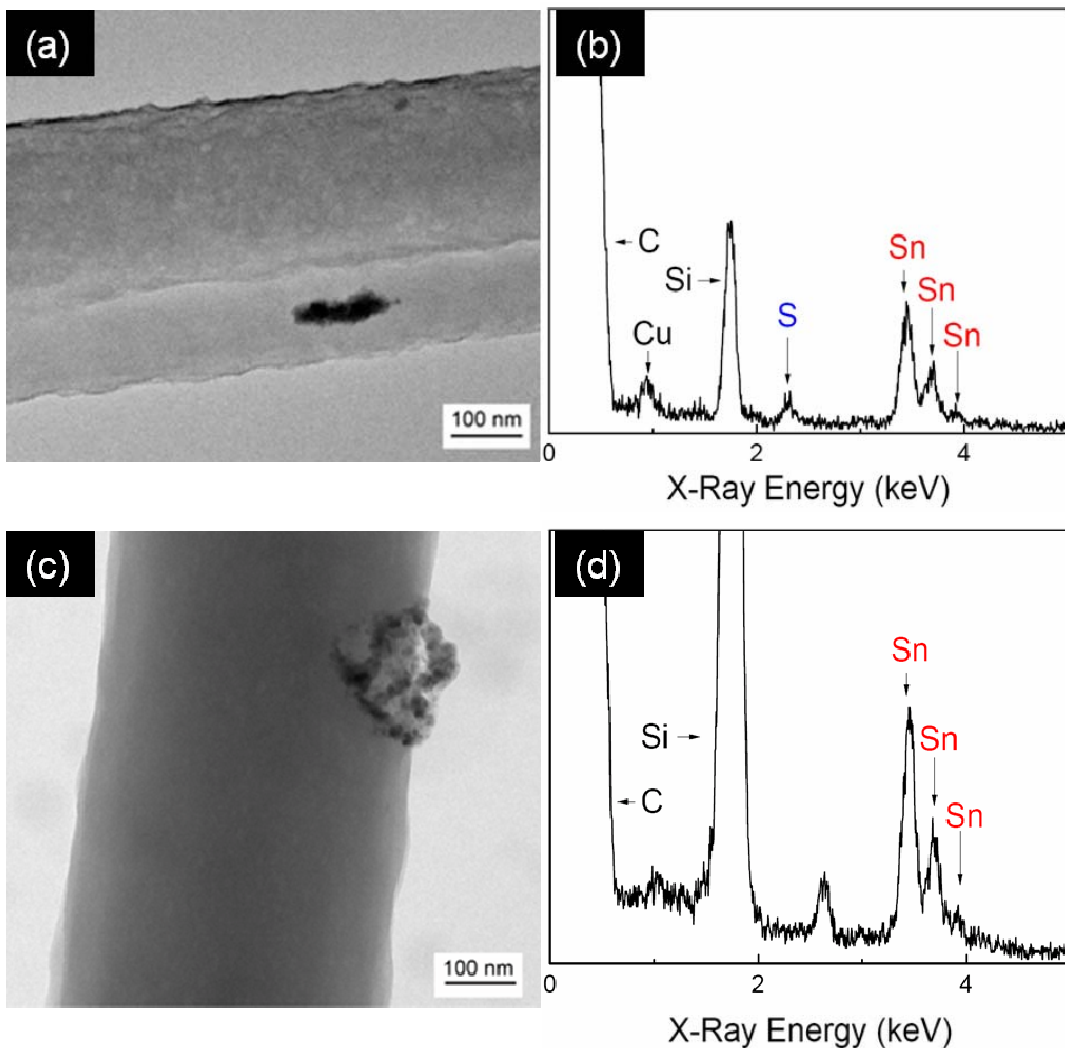


Figure 3.3. Transmission electron micrographs of composite fibers after stabilization (a) and carbonization (c) heat treatments, and corresponding energy dispersive spectra (b, d, respectively). The presence of Sn and S in spectrum (b) indicates that tin sulfate has not been converted to tin oxide during the stabilization. In comparison, the absence of S in spectrum (d) indicates that SnO_2 has formed. The peak near 2.7 eV is an artifact of the strong Si peak from the TEM grid.

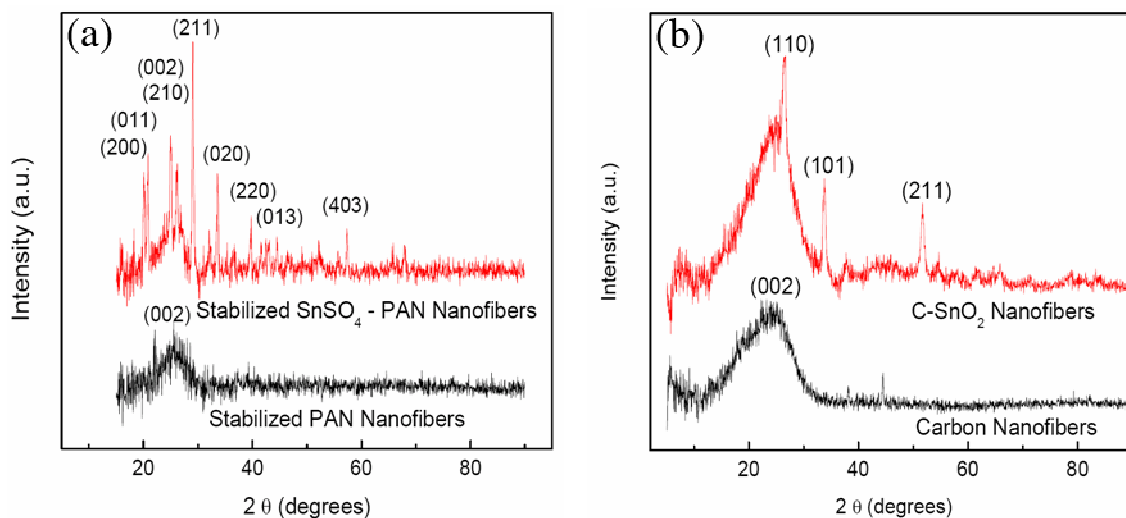


Figure 3.4. X-ray diffraction patterns of fibers after (a) stabilization heat treatment and (b) carbonization heat treatments. Fibers containing the tin salt show a change in crystal structure from SnSO₄ (JCPDS no. 16-0252) to SnO₂ (JCPDS no. 41-1445).

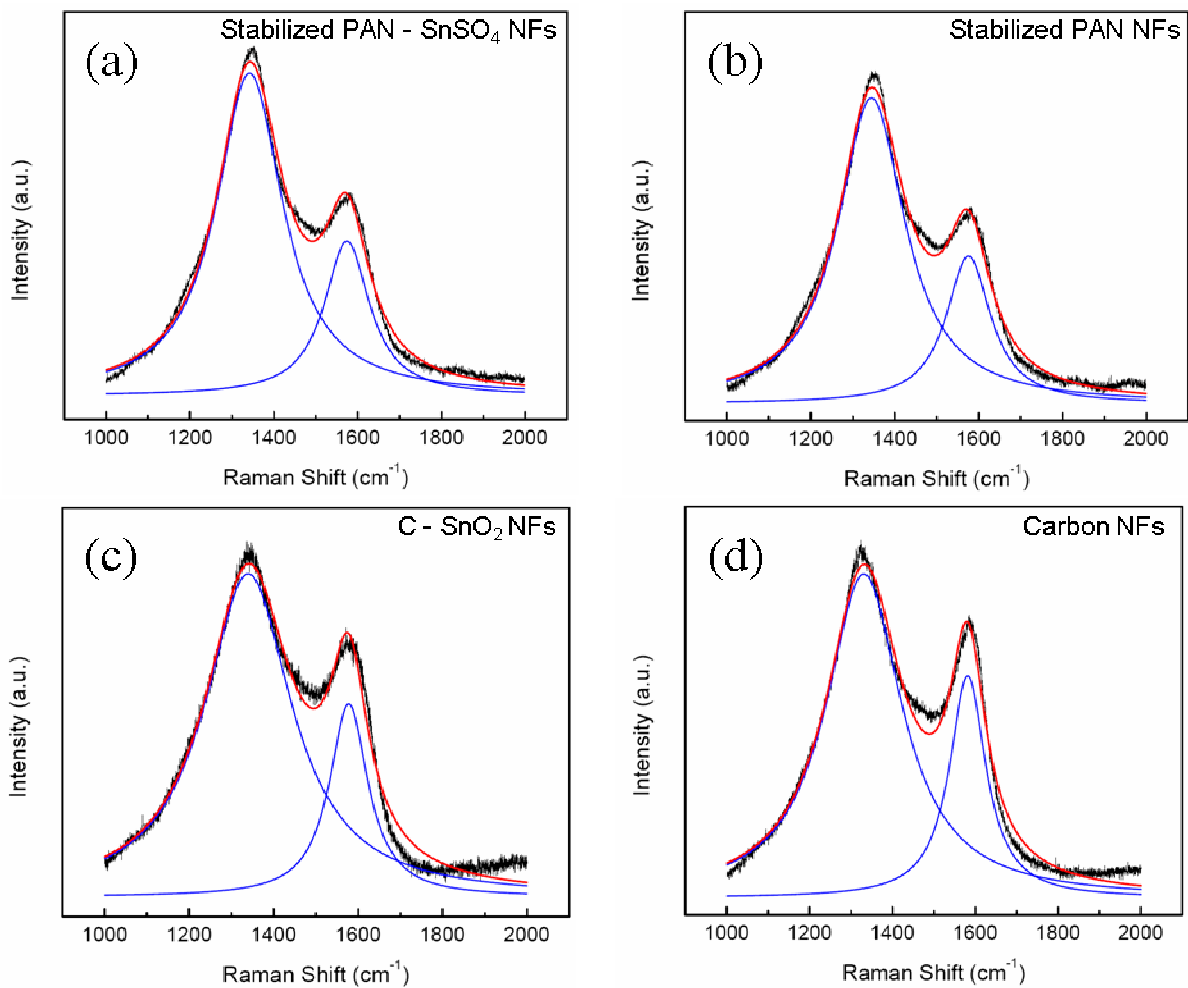


Figure 3.5. Raman spectra of stabilized PAN/SnSO₄ (a), stabilized PAN (b), carbonized PAN/SnSO₄ (c) and carbonized PAN (d) fiber mats. The disordered (D) and graphitic (G) peaks centered at ~1340 and ~1580 cm⁻¹ were fit to the spectra using Lorentzian distributions. Height ratios, $I(D)/I(G)$ are 2.1 ± 0.1 , 2.1 ± 0.1 , 1.6 ± 0.1 and 1.5 ± 0.2 , respectively.

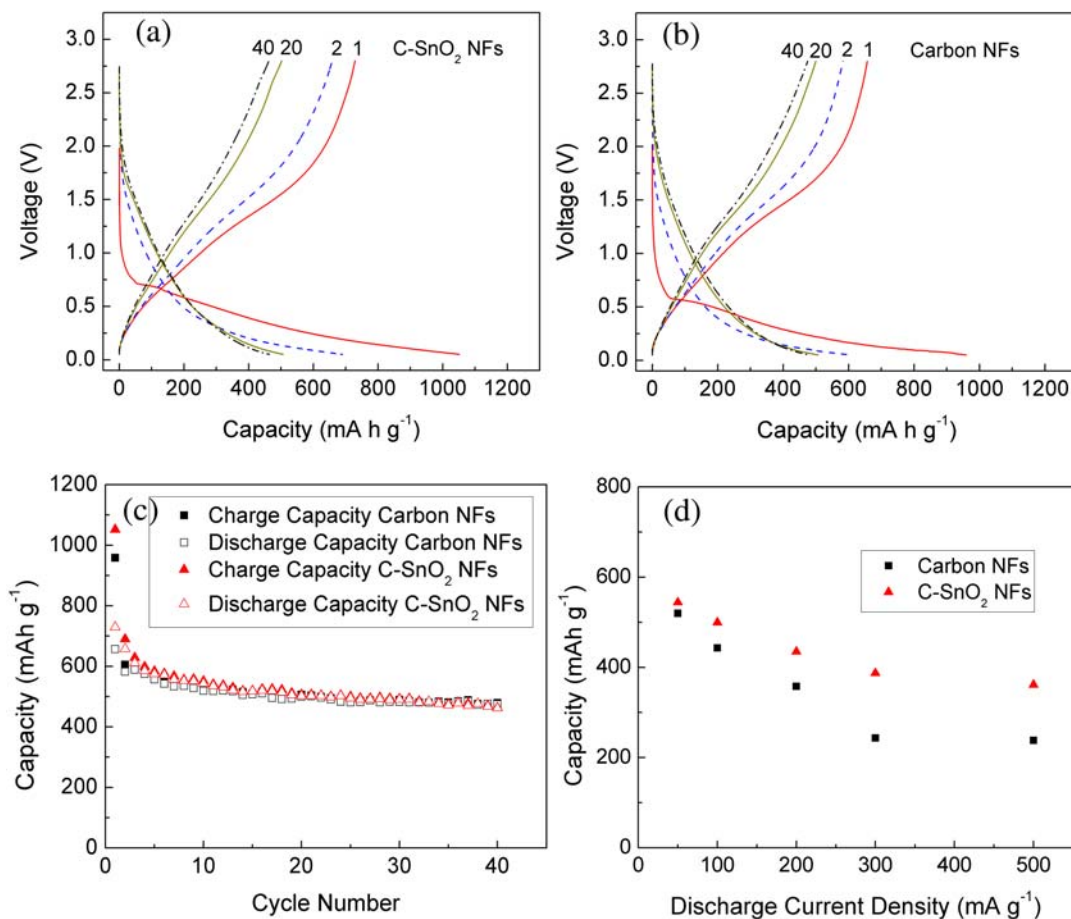


Figure 3.6. Performance of composite and carbon nanofiber mats as anodes in lithium ion battery half cells. Charge-discharge curves for C-SnO₂ (a) and carbon (b) nanofiber anodes cycled between 0.05 and 2.80 V (vs Li/Li⁺) at the rate of 50 mA/g. Curves at 1st, 2nd, 20th, and 40th cycles are shown. Cycle performance at 50 mA g⁻¹ current density (c) and rate capability at 10th cycles (d) for C-SnO₂ composite anodes in Li-ion battery half cells.

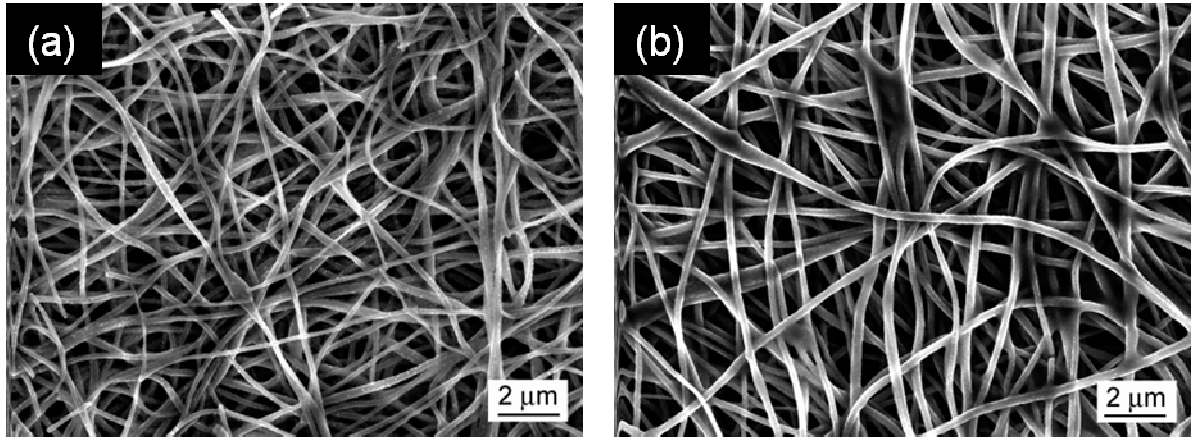


Figure 3.7. Micrographs of C-SnO₂ (a) and carbon (b) fiber anodes after 40 cycles, verifying the mats maintain their structure during lithium de/insertion.

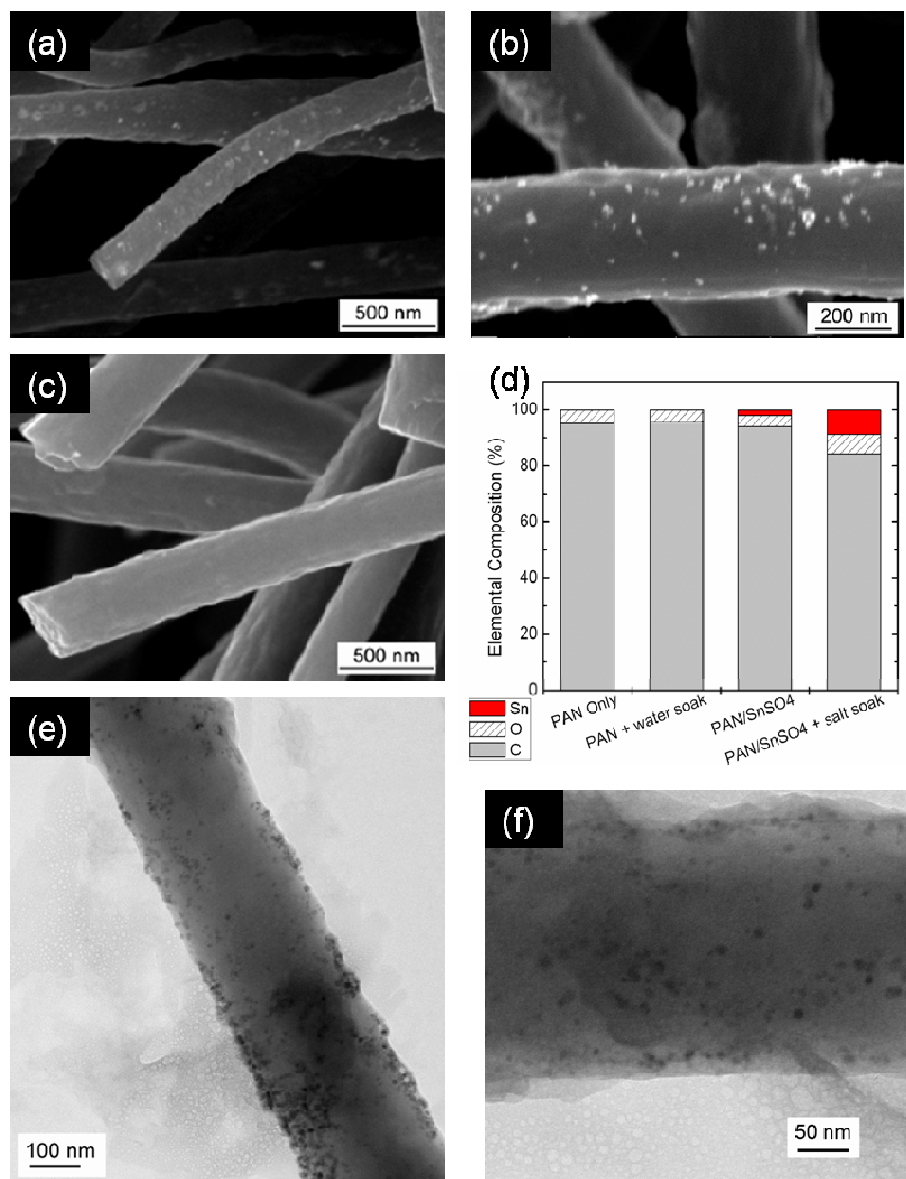


Figure 3.8. Scanning and Transmission Electron Micrographs of PAN/SnSO₄ (a, b, e, f) nanofibers that have been stabilized, soaked in aqueous tin sulfate, and then carbonized to form C-SnO₂ composites. Micrograph (c) is PAN nanofibers that have been stabilized, soaked in water, and then carbonized. The corresponding elemental composition of the anode mats as measured by EDS is shown in (d).

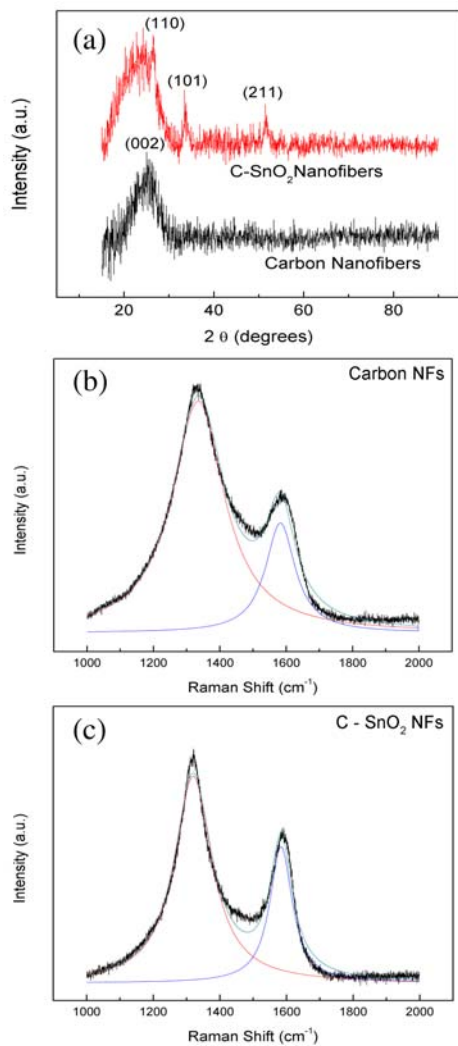
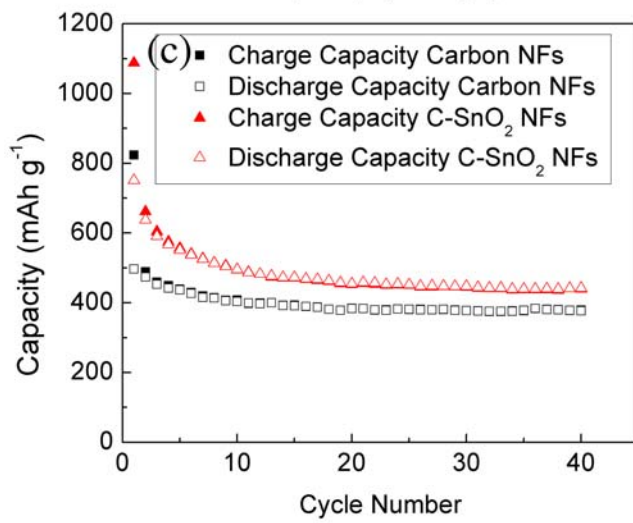
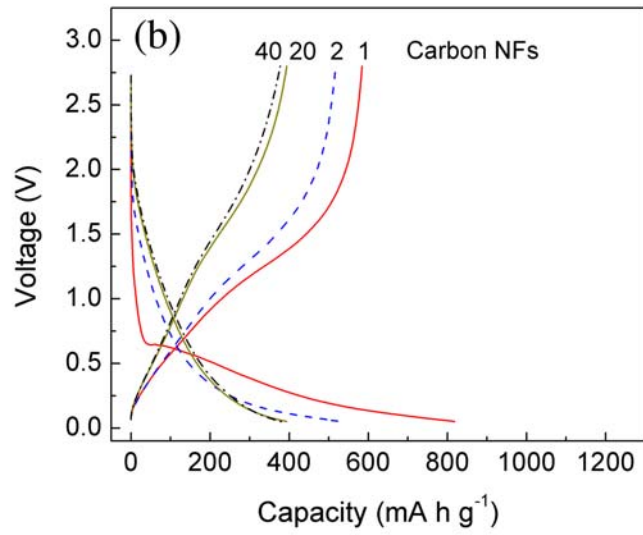
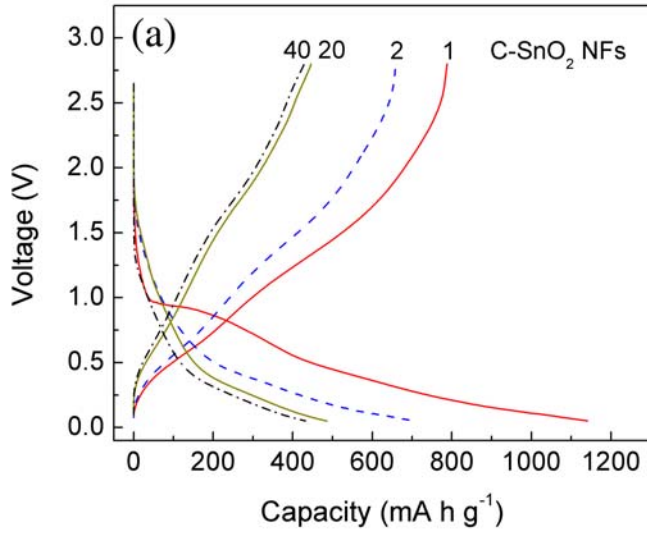


Figure 3.9. X-ray diffraction patterns (a) of fibers after soak and carbonization heat treatments. Peaks in the composite fiber mats correspond to SnO₂ (JCPDS no. 41-1445). Raman spectra of soaked and carbonized PAN/SnSO₄ (b) and PAN (c) nanofiber mats. Height ratios I(D)/I(G) are 1.9±0.1 and 1.5±0.1, respectively. The formation of the tin oxide nanoparticles during the heat treatment may disrupt the carbon microstructure, causing more disorder as indicated by the peak ratio.

Figure 3.10. Charge-discharge curves for (a) pure carbon nanofibers, soaked in water prior to carbonization, and (b) SnO₂-carbon nanofibers, soaked in salt solution prior to carbonization. Cycle life (c) of carbon-tin oxide and carbon nanofiber mats with solution soak treatments. The anodes were cycled with a constant 50 mA g⁻¹ current density.



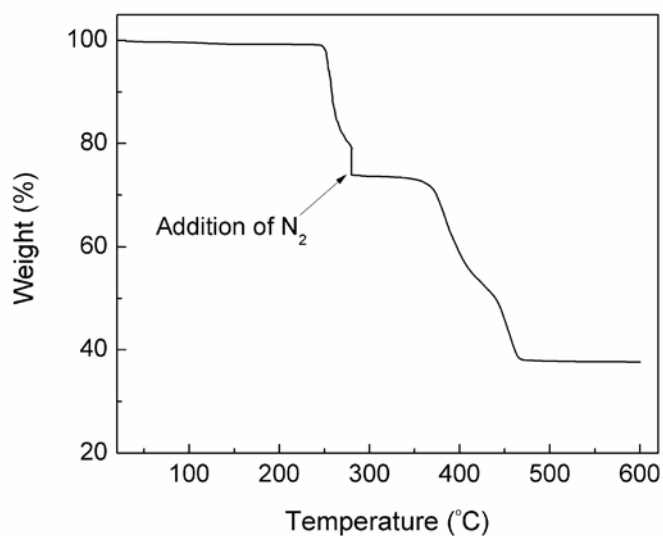


Figure 3.11. Thermal gravimetric analysis (TGA) of tin sulfate decomposition during stabilization and carbonization heat treatments. SnSO_4 was heated in air at $2^\circ\text{C}/\text{min}$ up until 280°C , held constant for 6 hours, and then it was heated in nitrogen up to 600°C . The remaining 37 wt % is SnO_2 . Mass loss is attributed to the conversion of tin sulfate to tin oxide and the release of sulfur dioxide.

CHAPTER 4

Electrospinning alginate-based nanofibers: From blends to crosslinked low molecular weight alginate-only systems

Chapter 4 is essentially a manuscript by Christopher A. Bonino, Melissa D. Krebs, Carl D. Saquing, Sung In Jeong, Kimberly L. Shearer, Eben Alsberg, and Saad A. Khan accepted for publication in *Carbohydrate Polymers*, in press ([doi:10.1016/j.carbpol.2011.02.002](https://doi.org/10.1016/j.carbpol.2011.02.002)).

Electrospinning alginate-based nanofibers: From blends to crosslinked low molecular weight alginate-only systems

Christopher A. Bonino¹, Melissa D. Krebs², Carl D. Saquing¹, Sung In Jeong², Kimberly L.
Shearer¹, Eben Alsberg^{2,3}, Saad A. Khan^{3*}

¹*Department of Chemical & Biomolecular Engineering, North Carolina State University, Raleigh, North Carolina*

²*Department of Biomedical Engineering, Case Western Reserve University, Cleveland, Ohio*

³*Department of Orthopaedic Surgery, Case Western Reserve University, Cleveland, Ohio*

Abstract

We report here preparation of nanofibers containing alginate using two different molecular weights (MWs): 37 kDa and 196 kDa. Low MW alginates are attractive for *in vivo* tissue scaffolds where degradation and clearance from the body are desirable, whereas higher MW alginates are amenable for topical use as wound coverage because of its better mechanical properties. We use polyethylene oxide (PEO) as a carrier material to aid in

* corresponding author: khan@eos.ncsu.edu (email); 919-515-4519 (ph)

electrospinning, and relate the solution properties, including entanglement concentration, relaxation time, conductivity, and surface tension, to their ability to be electrospun. In addition, we examine an FDA-approved, nonionic surfactant as a route to enhancing the alginate-PEO ratio (>80:20), and less toxic alternative to Triton X-100. Finally, alginate-only nanofibers that are also water-insoluble are obtained by crosslinking the electrospun fibers with calcium and subsequently removing the PEO and surfactants by soaking the nanofibers in water.

4.1. Introduction

Electrospun nanofibers are promising materials for biomedical applications, such as drug delivery, wound dressings, and tissue scaffolds. Nanofibrous mats have high surface areas and tunable morphologies, which can influence cell proliferation and behavior (Chew, Wen, Dzenis, & Leong, 2006). Additionally, the abundance of polymers and polymer blends that can be electrospun provide researchers many options for tailoring the mechanical and biological properties for their desired application. Several synthetic polymers, such as poly(ϵ -caprolactone), polylactide, and polyglycolide, have been electrospun for use as tissue scaffolds (Liang, Hsiao, & Chu, 2007). However, one drawback of fibers made from these polymers is the use of cytotoxic organic solvents during fabrication, which would require thorough washing and/or solvent evaporation treatments on the mats prior to use with cells. Natural, water-soluble polymers are an attractive alternative, as they are readily soluble in aqueous media because of their hydrophilic nature, and have low immunogenicity (Lee et al., 2009).

Sodium alginate is a water-soluble, biocompatible polysaccharide that is used in drug delivery (Augst, Kong, & Mooney, 2006), wound dressings (Hashimoto et al., 2004), and tissue engineering (Alsberg et al., 2002). Ionically crosslinked alginate gels are biodegradable, a property which can be tuned by changing the composition and MW of the polymer chains. Alginate is composed of blocks of β -D-mannuronic acid (M) and α -L-guluronic acid (G). Only the G blocks in alginate can be crosslinked with divalent cations

(e.g., Ca^{2+}) (Smidsrod & Skjakbraek, 1990). When used *in vivo*, ionically crosslinked alginate degrades when the calcium ions are exchanged with other ions in the body, such as Na^+ (Shoichet, Li, White, & Winn, 1996). As such, the variation in the M to G ratio, based on the alginate source, can provide one avenue to control the degradation. However, compared to the composition of alginate, modification of the polymer MW is a more exploitable route to controlling *in vivo* degradation. Alginate chains can be shortened to lower MWs by exposure to gamma-irradiation. Low radiation doses (< 8 Mrad) create chain scissions of the glycosidic bonds between the M and G blocks, with minimal effects on the block content and length (Alsberg et al., 2003). When used as tissue scaffolds, ionically crosslinked low MW alginate (< 50 kDa) degrades more quickly than higher MW. Shorter degradation times may be more optimal for some tissue regeneration applications that want to match tissue formation with polymer degradation rate (Alsberg et al., 2003). One significant advantage of low MW polymer chains is that polymers with MW less than 50 kDa can be passed by the kidneys when used *in vivo* (Al-Shamkhani & Duncan, 1995). Thus, nanofibers composed of low MW alginate are attractive for *in vivo* biomedical applications where degradation and clearance from the body are desirable.

The use of low MW polymers has important implications when developing material fabrication methods. In particular, electrospinning is influenced by polymer chain length, among many other variables (Shenoy, Bates, Frisch, & Wnek, 2005). Polymer chain entanglements in solution are essential to the formation of a continuous jet, leading to uniform, nonwoven fibers. Therefore, polymer solutions with inadequate entanglements,

such as those in dilute concentrations or with low viscoelasticity or MW, may form only beaded fibers or droplets (McKee, Wilkes, Colby, & Long, 2004; Yu, Fridrikh, & Rutledge, 2006). These added challenges have likely prevented the widespread usage of low MW polymers in electrospinning. In addition, ionic conductivity and surface tension have significant effects on the electrospinning process (Fong, Chun, & Reneker, 1999; McKee, Wilkes, Colby, & Long, 2004; Yu, Fridrikh, & Rutledge, 2006). The ability of a polymer solution to form uniform nanofibers can be linked directly to its solution properties.

Nanofibrous mats of alginate can be fabricated by electrospinning. Even though attempts to electrospin pure alginate in water have been unsuccessful, alginate solutions have been blended with a second material (i.e. glycerol, polyvinyl alcohol (PVA), polyethylene oxide (PEO)) to successfully form nanofibers (Bhattacharai, Li, Edmondson, & Zhang, 2006; Lu et al., 2006; Safi, Morshed, Ravandi, & Ghiaci, 2007; Nie et al., 2008; Nie et al., 2009; Jeong et al., 2010). The second co-solvent/polymer is believed to mitigate the charge repulsions between the alginate chains, improve chain flexibility, and create hydrogen bonds (Caykara, Demirci, Eroglu, & Guven, 2005; Nie et al., 2008). Blends of alginate with PEO have shown promise among the alginate-based solutions electrospun. The ratio of alginate to PEO in the electrospun fiber has been maximized to 80:20 with the addition of Triton X-100, a PEO-based non-ionic surfactant, and dimethyl sulfoxide (DMSO) (Bhattacharai, Li, Edmondson, & Zhang, 2006; Bhattacharai & Zhang, 2007). The addition of the surfactant and organic solvent resulted in bead-free fibers, most likely from a reduction in surface tension. However, the study did not fully investigate the role of solution properties on electrospinnability. In fact,

many studies that have electrospun alginate-PEO blends focused extensively on the morphology and properties of the nanofiber mats, whereas little work has been done to relate the pre-electrospinning alginate properties to the resultant nanofibers. The ability to relate solution properties to nanofiber formation will aid in the understanding of electrospinning alginate nanofibers, and can be extended to other polymer blends containing polyelectrolytes. One of the objectives of our study is to characterize the rheological and solution properties of blends containing high (196 kDa) or low (37 kDa) MW alginate and PEO, and relate these to the electrospun fiber morphology. While Bhattarai and Zhang reported to have electrospun different molecular weights of alginate that were obtained by sample degradation at room temperature, their study focused on solution viscosities and did not characterize MWs (Bhattarai & Zhang, 2007). Polymer chain lengths of the low MW alginate in our study were shortened by gamma-irradiation, which is a more controlled method than sample degradation. To the best of our knowledge, we are also the first to demonstrate the fabrication of nanofibers composed entirely of low MW alginate.

In addition to the MW of alginate, we also report methods to minimize the cytotoxicity involved in preparing the electrospun mats through the use solely of biocompatible materials. While some groups have previously shown the potential for alginate-based fibers as cell scaffolds, they used Triton X-100 and/or DMSO, which have possible cytotoxicity issues (Rubin, 1975; Dayeh et al., 2004; Bhattarai, Li, Edmondson, & Zhang, 2006; Saquing, Manasco, Bonino, & Khan, 2008). In this study, we compare alginate-PEO blends containing Triton X-100 (without DMSO) to those containing Pluronic

F127, an FDA-approved surfactant. Both Triton X-100 and F127 have hydrophilic PEO blocks. However, the hydrophobic polypropylene oxide (PPO) block is less toxic than the alkyl benzene block on Triton, one reason that Pluronic F127 is a viable material for biomedical applications (Sluzky, Klibanov, & Langer, 1992; Ren, Marquardt, & Lech, 1997; Khattak, Bhatia, & Roberts, 2005). After electrospinning, the alginate-based nanofibers are ionically crosslinked in a calcium solution, without the need for cytotoxic chemical crosslinkers (Birnbaum, Pendleton, Larsson, & Mosbach, 1981; Huanglee, Cheung, & Nimni, 1990). Subsequent removal of PEO via soaking in water leads to alginate-only nanofibers that retain their morphological integrity. An alginate variety with a high ratio (66%) of G blocks was selected to maximize crosslink density. The use of such biocompatible polymers, solvents, and crosslinkers therefore readily permits the fabrication of nanofibrous mats as scaffolds for potential use in regenerative medicine or drug delivery applications.

4.2. Materials and Methods

Materials.

Sodium alginate was obtained from FMC Biopolymers (Princeton, NJ) ($M_w = 196$ kDa, $M_w/M_n = 1.6$, 66:34 G:M blocks) and used as received. Low MW alginate ($M_w = 37$ kDa, $M_w/M_n = 1.5$) was prepared from the high MW by gamma irradiation. Dry alginate

was irradiated with a 5 Mrad dose at 25°C (Phoenix Laboratory, University of Michigan, Ann Arbor, MI), following a previously reported procedure(Alsberg et al., 2003). Additionally, polyethylene oxide (Polysciences, Warrington, PA, PEO, $M_w = 600$ kDa), polyethylene glycol (Polysciences, Warrington, PA, PEG, $M_w = 35$ kDa), Triton X-100 (Sigma Aldrich, St. Louis, MO), and Pluronic F127 (Sigma Aldrich, St. Louis, MO) were also used. Solutions were prepared by making separate solutions of PEO (4 wt%) or PEG (40 wt%) and 196 kDa (4 wt%) or 37 kDa (13.5 wt%) alginate in deionized water, and then combining with the surfactant. Solution ratios of up to 2.8:1.2:2.0 (196 kDa alginate:PEO:surfactant) and 8.0:1.6:2.0 (37 kDa alginate:PEO:surfactant) were investigated. Solutions were mixed overnight at room temperature with a magnetic stir bar. Crosslinking treatment of electrospun fibers used ethanol (reagent grade, Sigma Aldrich, St. Louis, MO) and calcium chloride (Sigma Aldrich, St. Louis, MO)

Solution characterization.

Rheological experiments were performed with a TA Instruments (New Castle, DE) AR2000 stress-controlled rheometer with a 40 cm, 2° cone and plate geometry. All samples were measured at 25°C. Dynamic and steady state shear experiments were conducted on each sample. The stresses applied in the frequency sweeps were selected from the linear viscoelastic (LVE) regime in the stress sweeps. All rheological measurements were repeated on at least two different samples to ensure repeatability within $\pm 5\%$. Ionic conductivity measurements were made using a potentiostat from Gamry Instruments (Warminster, PA).

Surface tensions were determined using a pendant drop analyzer from SEO Co. Ltd (model Phoenix 300, Lathes, South Korea).

Preparation of alginate nanofibers.

The electrospinning setup consisted of a syringe pump (model NE-1010, New Era Pump Systems, Inc., Wantagh, NY), high voltage power supply (model AU-60P0.5, Matsusada Precision, Inc. Kusatsu-City Japan), and collector plate covered in Reynolds Wrap non-stick aluminum foil for easy removal of mats. The polymer solution was pumped through a syringe with a 22 gauge needle at rates of 0.50-0.75 mL/hr. The distance from the end of the needle to the collector plate was fixed at 15 cm. The voltage was varied from 10-15 kV until a stable Taylor cone was achieved, and then maintained at a constant level (Taylor, 1964). All nanofibers were made at room temperature (21-24°C) and relative humidity 40-55%.

Crosslinking of alginate nanofibers.

After electrospinning, nanofiber mats were removed from the collector plate and ionically crosslinked. Mats were soaked in ethanol (1 min), followed by a calcium chloride solution (2 wt%) in 1:5 ethanol:water (10 sec). Finally, the mats were rinsed in water (1 min). The crosslinked fibers were submerged in water for up to four days, without agitation, at room temperature to confirm their stability. After soaking, mats were dried in a lyophilizer (VirTis 10-324 lyophilizer, Gardiner, NY) overnight.

Characterization of nanofibers.

Nanofiber mats were analyzed with a scanning electron microscope (SEM). A FEI XL30 field emission SEM was used at the following settings: 6 mm working distance, 5 kV accelerating voltage, spot size 3, and ultrahigh resolution mode. Fiber diameters and standard deviations on 50 fibers per sample were measured using Adobe Photoshop C3. Spectra of stand alone fiber mats without salt windows were collected from 4000-400 cm^{-1} with 4 cm^{-1} resolution and 512 scans using a Fourier Transform Infrared (FTIR) Spectrometer (model Nicolet 6700, Thermo Electron Corp.) in the transmission mode.

4.3. Results and Discussion

4.3.1. Solution rheology and electrospinning alginate

Our initial attempt at electrospinning pure alginate nanofibers focused on solutions containing alginate concentrations spanning two decades (0.04-5.0 wt.% for 196 kDa alginate, and 0.15-15 wt% for 37 kDa alginate). Attempts to electrospin either MW resulted in beads or droplets but no nanofibers as shown in Figure 4.1 for two representative samples. Other groups have also reported similar results when attempting to electrospin aqueous alginate solutions (Bhattarai, Li, Edmondson, & Zhang, 2006; Safi, Morshed, Ravandi, & Ghiaci, 2007; Nie et al., 2008; Nie et al., 2009). An explanation proposed by these groups has been the inability of alginate to form chain entanglements.

Solution rheology has been suggested to be a good indicator of the range of polymer concentration appropriate for electrospinning as well as determining the entanglement concentration. McKee, *et al.* reported that neutral and charged polymer solutions could be electrospun into uniform fibers at concentrations 2-8 times above the entanglement concentration (McKee, Wilkes, Colby, & Long, 2004; McKee, Hunley, Layman, & Long, 2006). To estimate the entanglement concentrations of our sample, the viscosity-shear stress behavior was measured for polymer concentrations that spanned two decades. Figure 4.2 shows the specific viscosity ($\eta_{sp} = (\eta_o - \eta_s)/\eta_s$, where η_o is the solution zero shear viscosity and η_s the solvent viscosity) of these samples as a function of concentration (C). Several pieces of information can be obtained from these plots. First, there are two distinct changes in slope, corresponding to the overlap (C^*) and entanglement (C_e) concentrations. Alginates with MW 37 (Figure 4.2a) and 196 (Figure 4.2b) kDa were found to have entanglement concentrations (C_e) of approximately 4.0 and 0.6 weight percent in water solutions, respectively. Entanglement concentrations decrease with increasing polymer MW, as a result of the longer polymer chain lengths (Rubinstein & Colby, 2003). We also find that the entanglement concentrations of alginate solutions occur at zero shear viscosities ~ 0.05 Pa·s, or $\sim 50 \times \eta_s$ which is consistent with theoretical predictions (Dobrynin, Colby, & Rubinstein, 1995). In addition, the slopes of the curves match well with scaling predictions of neutral polymers in good solvent: $\eta_{sp} \sim C^{1.0}$ for the dilute regime ($C < C^*$), $\eta_{sp} \sim C^{1.25}$ for the semidilute unentangled regime ($C^* < C < C_e$), and, $\eta_{sp} \sim C^{3.75}$ for the semidilute entanglement regime ($C_e < C < C^{**}$) (Dobrynin, Colby, & Rubinstein, 1995). (C^{**} is the concentrated

regime.) We speculate that the alginate solutions act as neutral polymers, instead of charged polyelectrolytes, due to counterions (e.g., Na^+) that effectively screen the carboxylic acid groups on alginate (Krause, Bellomo, & Colby, 2001). Purification of the alginate may be necessary to reduce counterions and cause alginate solutions to follow the scaling predictions of polyelectrolytes (Rubinstein, Colby, & Dobrynin, 1994). However, Nie *et al.* recently reported that concentration plots of unpurified alginate solutions matched charged polymer models (Nie et al., 2009). We hypothesize that the concentration of counterions varies with the source and distributor of alginate. Variations in the solution behavior of alginate based on its source is an important finding to consider for future materials research with the biopolymer.

In addition to solution behavior predictions from the concentration curves, we also found that alginate does in fact have an entanglement concentration well below the solution concentrations attempted for electrospinning. Our efforts to electrospin aqueous alginate solutions in concentrations up to 5.5% or $\sim 9 \times C_{\text{ent}}$ were unsuccessful, suggesting that chain entanglement is not the dictating factor for alginate solutions to electrospin (Figure 4.1). It should be noted that strain rates at the transition between the Taylor cone and jet during the electrospinning process are high (Han, Yarin, & Reneker, 2008); however, the zero shear viscosity provides information on chain entanglement of a system.

The inability of a polymer solution to be electrospun can often be overcome by blending it with another polymer. PEO has been blended with charged biopolymers, such as

chitosan, or low MW polymers, such as polyethylene glycol (PEG), that are incapable of being electrospun alone to generate nanofibers (Yu, Fridrikh, & Rutledge, 2006; Klossner, Queen, Coughlin, & Krause, 2008). Recently, blends of sodium alginate and PEO have been electrospun (Bhattacharai, Li, Edmondson, & Zhang, 2006; Lu et al., 2006; Safi, Morshed, Ravandi, & Ghiaci, 2007; Jeong et al., 2010). PEO and alginate chains can interact by hydrogen bonding, which contributes to their compatibility in solution (He, Zhu, & Inoue, 2004; Caykara, Demirci, Eroglu, & Guven, 2005). However, hydrogen bonding between alginate and its carrier polymer alone does not allow for a blend to be electrospun. To demonstrate this, attempts were made to electrospin blends of alginate and 35 kDa PEG (2.0:20.0). The solutions electrospayed, but did not form continuous fibers (Figure 4.3a, b). We hypothesize that the chain length of the carrier polymer also plays a role in the electrospinning of alginate.

4.3.2. Effect of Triton X-100 surfactant on alginate/PEO blends

While blended nanofibers can be formed from electrospinning alginate and PEO, the amount of alginate in the blend can be increased with the addition of small amounts of surfactants (Bhattacharai & Zhang, 2007). Initially, the effects of the nonionic surfactant Triton X-100 on the solution properties of alginate-PEO blends and on the morphology of the resultant nanofibers were investigated. Alginate-PEO solutions were maintained at a total concentration of 4 wt%, because PEO (600 kDa) can be electrospun at this concentration

(data not shown). We find that alginate-PEO blends at a ratio of 70:30 by weight produces beaded nanofibers (Figures 3c, d). However, the addition of small amounts (1 wt%) of Triton X-100 to the sample, generates bead-free fibers (Figure 4.3e, f). Surfactants lower the surface tension of the polymer solution, which suppresses bead defects (Fong, Chun, & Reneker, 1999). Table 4.1 shows the various properties of polymer solutions containing alginate and PEO. Alginate and PEO have limited surface activities and reduce the surface tension of water to 55 mN/m. The addition of Triton X-100 causes the surface tension of the polymer blend to decrease to 29 mN/m, which possibly contributes to the morphological transition from beaded to uniform fibers. However, it is important to note that reducing the surface tension of alginate solutions with surfactants did not lead to uniform fibers (Figure 4.1b). Alginate solutions, regardless of added surfactants, that were not blended with PEO formed droplets (Saquing, Manasco, Bonino, & Khan, 2008). Thus, reducing surface tension enhances the electrospinnability of alginate solutions for systems that have reached the onset of fiber formation.

The roles of other solution properties that could impact the electrospinnability of the alginate/PEO solutions were also examined. Rheological properties, such as zero shear viscosity and relaxation time have been known to affect fiber morphology (Yu, Fridrikh, & Rutledge, 2006; Talwar, Hinstroza, Pourdeyhimi, & Khan, 2008). However, we found that the addition of PEO did not have a significant effect on the solution relaxation time, as determined by dynamic oscillatory measurements. Solutions of alginate and alginate/PEO/triton blends with similar zero shear viscosities also have similar moduli and

relaxation times (Figure 4.4). Additionally, the ionic conductivity of the alginate-only solutions was reduced after blending with PEO, thereby diluting its total solution concentration, showing that alginate is the greatest contributor of the solution conductivity due to its anionic nature in water. As expected, the addition of a nonionic surfactant did not affect the conductivity. These results (Figure 4.3, Figure 4.4; Table 4.1) taken together indicate that the surface tension is the most important factor in electrospinning these polymers and that the additions of both PEO and Triton X-100 are necessary to generate nanofibers with up to 70% (relative to PEO) or 2.8 wt% alginate.

4.3.3. Role of biocompatible F127 nonionic surfactant

With the potential uses for alginate-based nanofibers in biomedical applications, there is strong interest in using only non-cytotoxic materials. Therefore, Triton X-100 was replaced with an FDA-approved surfactant, Pluronic F127. Using the same procedure as discussed in the previous section, alginate-PEO blended solutions were characterized and electrospun. As shown before with Triton X-100, the addition of Pluronic F127 effectively suppressed bead defects (Figure 4.5). Blends of alginate and PEO were electrospun with minimal beads at weight ratios up to 60:40 (2.4:1.6 wt%). The formation of fibers with minimal bead defects were primarily due to the decrease in surface tension, since the rheology and ionic conductivity of blends with and without surfactant were similar. As shown in Table 4.2, the addition of F127 could not match the same maximum amount of

alginate for bead-free fibers as with Triton X-100 (70% by weight). This is because the surface tension of F127 solutions are 35-36 mN/m compared to 29 for Triton solutions. Pluronic is a triblock copolymer (PEO-PPO-PEO) and is expected to have lower packing density at the water-air interface compared to Triton X-100 (Hiemenz & Rajagopalan, 1997). However, the use of an FDA-approved surfactant in electrospun solutions as a method to enhance the alginate loading fiber morphology is an attractive option.

4.3.4. Electrospinning low MW alginate

From a materials perspective, low MW polymer chains are less desirable to use in electrospinning due to limited entanglements. However, from a tissue engineering perspective, small polymer chain lengths have a faster rate of *in vivo* degradation than high MW chains and can be cleared by the kidneys (Al-Shamkhani & Duncan, 1995; Alsberg et al., 2003). In this study, we attempted to electrospin irradiated alginate ($M_w = 37$ kDa). As observed previously with the high MW alginate, solutions containing only low MW alginate in concentrations $>3 \times C_e$ did not electrospin.

The inability to electrospin low MW alginate was overcome by blending it with PEO and Pluronic F127 surfactant, using the same approach as with the high MW alginate. However, compared to the high MW alginate case, the alginate content was raised from 2.8:1.2 to 8.0:1.6 (by polymer wt% relative to PEO) using the low MW polymer. A shorter

chain length polymer requires a greater concentration to achieve comparable solution viscosities to a high MW polymer. Despite a greater concentration of alginate (8 wt%) for the low MW solution, the zero shear viscosity was less than the high MW alginate solution (2.8 wt%) (2.3 vs. 14.5 Pa·s, Figure 4.6). In addition, the longest relaxation time of the low MW solution was an order of magnitude less than the high MW solution. Polymers with short chain lengths have fewer entanglements than high MW chains, and relax sooner (Rubinstein & Colby, 2003).

Uniform nanofibers containing low MW alginate, PEO, and F127 surfactant were obtained (Figure 4.7a, b). To our knowledge, we are the first to prepare alginate-based nanofibers from a low MW alginate. The average fiber diameters were ~150 nm, the same size as fibers with high MW alginate. Thus, the final fiber diameter was not dependent on solution composition of the concentrations investigated, despite using a solution with a low MW polymer as the majority species in the blend. We speculate the consistency in the solution and processing conditions (solution viscosity, temperature, humidity) contributed to similarities in the fiber sizes between the two different MW solutions (Yu, Fridrikh, & Rutledge, 2006; Tripatanasuwan, Zhong, & Reneker, 2007). Electrospinning blends containing low MW alginate reduced the amount of PEO as the inert, carrier polymer, thereby allowing for a greater polysaccharide component, which is of greater interest when these nanofibers are used as tissue scaffolds. In our case, we achieved nanofibers with alginate/PEO ratio of 8.0/16, i.e., with over 83% alginate in the blend. In addition, the

complete removal of PEO (M_w 600 kDa) from the nanofibers would leave only the low MW material, which would be capable of renal clearance if used *in vivo*.

4.3.5. Crosslinked alginate-only nanofibers

Prior to use as tissue engineering scaffolds, alginate-based materials need to be crosslinked to preserve their structure in an aqueous environment. Ionic crosslinking with divalent ions (e.g. Ca^{2+}) avoids potentially toxic materials used in chemical crosslinking reactions (Birnbaum, Pendleton, Larsson, & Mosbach, 1981; Huanglee, Cheung, & Nimni, 1990; Smidsrod & Skjakbraek, 1990). The alginate used throughout these studies has a high G-M block ratio (66-34) to increase ionic crosslinking sites. We determined that the fiber morphology could be best maintained using ethanol in a pre-crosslinking treatment and as part of the crosslinking solution. Mats were soaked in ethanol first, followed by a calcium chloride solution (2 wt%) in 1:5 ethanol:water, as delineated in the methods section. PEO is soluble in ethanol, but alginate is not, which prevents the alginate from being dissolved into solution before it is effectively crosslinked. After crosslinking, the nanofiber mats were soaked in water to test their structural and durability. The nanofibers composed of both high and low MW alginates were shown to remain intact after exposure to water (Figure 4.7c-f).

Soaking fibers in water to remove PEO reduced fiber diameters, which was dependent on fiber composition. Diameters of fibers containing blends of high MW alginate

(2.4-2.8 wt %) and PEO (1.2-1.6 wt%) shrunk by ~34% (Figure 4.8a). In comparison, fiber blends containing the low MW alginate (8.0 wt%) and PEO (1.6 wt%) decreased by only ~9%, due to the smaller concentration of PEO. Minimal changes in fiber diameter after PEO removal may help maintain the fiber mat integrity, which is another advantage of using the low MW blend. Future work with mechanical testing will evaluate fiber strength after crosslinking and PEO removal.

FTIR analysis of the fibers was conducted in order to determine if PEO was completely removed in the soaking step. Figure 4.8b shows the spectrum for fibers prior to and following soaking. Peaks that correspond to C-O-C bond stretching in PEO located at 844, 1103 cm^{-1} , and $-\text{CH}_2$ bond stretching at 1343 cm^{-1} , disappear after soaking (Ji et al., 2006). Our results reveal that PEO is removed during the soak treatment, which is important because the remaining mat is pure alginate; as our group has previously shown, pure alginate can be modified with cell adhesion ligands to be interactive with cells, whereas PEO is inert and does not contribute to cellular interactions (Jeong et al., 2010). In addition, nanofibrous mats containing low MW alginate are of particular interest for *in vivo* studies after the high MW PEO is removed. It is worth noting that, despite the effective removal of PEO, the outer surfaces do not appear to be highly porous (Zhang et al., 2006). We speculate that the PEO was present in small domains within the fiber, which could not be detected with SEM analysis. Blends of PEO and alginate are miscible, which explains the smooth surface appearance of the soaked fibers (Caykara, Demirci, Eroglu, & Guven, 2005).

4.4. Conclusions

The addition of small amounts of surfactants can enhance the concentration of alginate and morphology of electrospun fibers from alginate/PEO blends. We found this concept to hold true for low molecular alginates and an FDA approved Pluronic surfactant, both of which holds great promise for *in vivo* applications.. In particular, nanofibers of alginate blends with compositions greater than 80/20 for alginate-to-PEO ratio were obtained in such systems. Alginate-only fibers, evidenced from FTIR, were also achieved by crosslinking the nanofibers and removing the PEO and surfactant. Finally, compared to the rheological properties and ionic conductivity, we found surface tension of the solutions had the greatest effect on whether the solution blends could be electrospun. Reducing the surface tension could thus be an effective method to tune the fiber morphology while maximizing the amount of alginate.

4.5. Acknowledgments

This work was supported by U.S. Department of Education Graduate Assistance in Areas of National Need (GAANN) Fellowship Program at North Carolina State University (CAB), and a National Science Foundation Graduate Research Fellowship (MDK). We also thank Professor Ralph Colby (Penn. State) for helpful discussions related to the specific viscosity plots.

4.6. References

- Al-Shamkhani, A., & Duncan, R. (1995). Radioiodination of Alginate Via Covalently-Bound Tyrosinamide Allows Monitoring of Its Fate in-Vivo. *Journal of Bioactive and Compatible Polymers*, *10*, 4-13.
- Alsberg, E., Anderson, K. W., Albeiruti, A., Rowley, J. A., & Mooney, D. J. (2002). Engineering growing tissues. *Proceedings of the National Academy of Sciences of the United States of America*, *99*, 12025-12030.
- Alsberg, E., Kong, H. J., Hirano, Y., Smith, M. K., Albeiruti, A., & Mooney, D. J. (2003). Regulating bone formation via controlled scaffold degradation. *Journal of Dental Research*, *82*, 903-908.
- Augst, A. D., Kong, H. J., & Mooney, D. J. (2006). Alginate hydrogels as biomaterials. *Macromolecular Bioscience*, *6*, 623-633.
- Bhattacharai, N., Li, Z. S., Edmondson, D., & Zhang, M. Q. (2006). Alginate-based nanofibrous scaffolds: Structural, mechanical, and biological properties. *Advanced Materials*, *18*, 1463-1467.
- Bhattacharai, N., & Zhang, M. (2007). Controlled Synthesis and Structural Stability of Alginate-based Nanofibers. *Nanotechnology*, *18*, 10.

- Birnbaum, S., Pendleton, R., Larsson, P. O., & Mosbach, K. (1981). Covalent Stabilization of Alginate Gel for the Entrapment of Living Whole Cells. *Biotechnology Letters*, 3, 393-400.
- Caykara, T., Demirci, S., Eroglu, M. S., & Guven, O. (2005). Poly(ethylene oxide) and its blends with sodium alginate. *Polymer*, 46, 10750-10757.
- Chew, S. Y., Wen, Y., Dzenis, Y., & Leong, K. W. (2006). The role of electrospinning in the emerging field of nanomedicine. *Current Pharmaceutical Design*, 12, 4751-4770.
- Dayeh, V. R., Chow, S. L., Schirmer, K., Lynn, D. H., & Bols, N. C. (2004). Evaluating the toxicity of Triton X-100 to protozoan, fish, and mammalian cells using fluorescent dyes as indicators of cell viability. *Ecotoxicology and Environmental Safety*, 57, 375-382.
- Dobrynin, A. V., Colby, R. H., & Rubinstein, M. (1995). Scaling Theory of Polyelectrolyte Solutions. *Macromolecules*, 28, 1859-1871.
- Fong, H., Chun, I., & Reneker, D. H. (1999). Beaded nanofibers formed during electrospinning. *Polymer*, 40, 4585-4592.
- Han, T., Yarin, A. L., & Reneker, D. H. (2008). Viscoelastic electrospun jets: Initial stresses and elongational rheometry. *Polymer*, 49, 1651-1658.

- Hashimoto, T., Suzuki, Y., Tanihara, M., Kakimaru, Y., & Suzuki, K. (2004). Development of alginate wound dressings linked with hybrid peptides derived from laminin and elastin. *Biomaterials*, *25*, 1407-1414.
- He, Y., Zhu, B., & Inoue, Y. (2004). Hydrogen bonds in polymer blends. *Progress in Polymer Science*, *29*, 1021-1051.
- Hiemenz, P. C., & Rajagopalan, R. (1997). *Principles of colloid and surface chemistry*. NY, Marcel Dekker.
- Huanglee, L. L. H., Cheung, D. T., & Nimni, M. E. (1990). Biochemical-Changes and Cytotoxicity Associated with the Degradation of Polymeric Glutaraldehyde Derived Cross-Links. *Journal of Biomedical Materials Research*, *24*, 1185-1201.
- Jeong, S. I., Krebs, M. D., Bonino, C. A., Khan, S. A., & Alsberg, E. (2010). Electrospun alginate nanofibers with controlled cell adhesion for tissue engineering. *Macromolecular Bioscience*, DOI: 10.1002/mabi.201000046.
- Ji, Y., Ghosh, K., Shu, X. Z., Li, B. Q., Sokolov, J. C., Prestwich, G. D., et al. (2006). Electrospun three-dimensional hyaluronic acid nanofibrous scaffolds. *Biomaterials*, *27*, 3782-3792.
- Khattak, S. F., Bhatia, S. R., & Roberts, S. C. (2005). Pluronic F127 as a cell encapsulation material: Utilization of membrane-stabilizing agents. *Tissue Engineering*, *11*, 974-983.

- Klossner, R. R., Queen, H. A., Coughlin, A. J., & Krause, W. E. (2008). Correlation of Chitosan's Rheological Properties and Its Ability to Electrospin. *Biomacromolecules*, *9*, 2947-2953.
- Krause, W. E., Bellomo, E. G., & Colby, R. H. (2001). Rheology of sodium hyaluronate under physiological conditions. *Biomacromolecules*, *2*, 65-69.
- Lee, K. Y., Jeong, L., Kang, Y. O., Lee, S. J., & Park, W. H. (2009). Electrospinning of polysaccharides for regenerative medicine. *Advanced Drug Delivery Reviews*, *61*, 1020-1032.
- Liang, D., Hsiao, B. S., & Chu, B. (2007). Functional electrospun nanofibrous scaffolds for biomedical applications. *Advanced Drug Delivery Reviews*, *59*, 1392-1412.
- Lu, J.-W., Zhu, Y.-L., Guo, Z.-X., Hu, P., & Yu, J. (2006). Electrospinning of sodium alginate with poly(ethylene oxide). *Polymer*, *47*, 8026-8031.
- McKee, M. G., Hunley, M. T., Layman, J. M., & Long, T. E. (2006). Solution rheological behavior and electrospinning of cationic polyelectrolytes. *Macromolecules*, *39*, 575-583.
- McKee, M. G., Wilkes, G. L., Colby, R. H., & Long, T. E. (2004). Correlations of solution rheology with electrospun fiber formation of linear and branched polyesters. *Macromolecules*, *37*, 1760-1767.

- Nie, H., He, A., Zheng, J., Xu, S., Li, J., & Han, C. C. (2008). Effects of Chain Conformation and Entanglement on the Electrospinning of Pure Alginate. *Biomacromolecules*, *9*, 1362-1365.
- Nie, H. R., He, A. H., Wu, W. L., Zheng, J. F., Xu, S. S., Li, J. X., et al. (2009). Effect of poly(ethylene oxide) with different molecular weights on the electrospinnability of sodium alginate. *Polymer*, *50*, 4926-4934.
- Ren, L. F., Marquardt, M. A., & Lech, J. J. (1997). Estrogenic effects of nonylphenol on pS2, ER and MUC1 gene expression in human breast cancer cells-MCF-7. *Chemico-Biological Interactions*, *104*, 55-64.
- Rubin, L. F. (1975). Toxicity of Dimethyl-Sulfoxide, Alone and in Combination. *Annals of the New York Academy of Sciences*, *243*, 98-103.
- Rubinstein, M., & Colby, R. H. (2003). *Polymer Physics*. New York, Oxford University Press.
- Rubinstein, M., Colby, R. H., & Dobrynin, A. V. (1994). Dynamics of Semidilute Polyelectrolyte Solutions. *Physical Review Letters*, *73*, 2776-2779.
- Safi, S., Morshed, M., Ravandi, S. A. H., & Ghiaci, M. (2007). Study of electrospinning of sodium alginate, blended solutions of sodium alginate/poly(vinyl alcohol) and sodium alginate/poly(ethylene oxide). *Journal of Applied Polymer Science*, *104*, 3245-3255.

- Saquin, C. D., Manasco, J. L., Bonino, C. A., & Khan, S. A. (2008). *Electrospun metal nanoparticle-alginate based polymer blend nanofiber composites for biomedical applications. American Chemical Society National Meeting, New Orleans, LA.*
- Shenoy, S. L., Bates, W. D., Frisch, H. L., & Wnek, G. E. (2005). Role of chain entanglements on fiber formation during electrospinning of polymer solutions: good solvent, non-specific polymer-polymer interaction limit. *Polymer*, *46*, 3372-3384.
- Shoichet, M. S., Li, R. H., White, M. L., & Winn, S. R. (1996). Stability of hydrogels used in cell encapsulation: An in vitro comparison of alginate and agarose. *Biotechnology and Bioengineering*, *50*, 374-381.
- Sluzky, V., Klivanov, A. M., & Langer, R. (1992). Mechanism of Insulin Aggregation and Stabilization in Agitated Aqueous-Solutions. *Biotechnology and Bioengineering*, *40*, 895-903.
- Smidsrod, O., & Skjakbraek, G. (1990). Alginate as Immobilization Matrix for Cells. *Trends in Biotechnology*, *8*, 71-78.
- Talwar, S., Hinestroza, J., Pourdeyhimi, B., & Khan, S. A. (2008). Associative polymer facilitated electrospinning of nanofibers. *Macromolecules*, *41*, 4275-4283.
- Taylor, G. (1964). Disintegration of Water Drops in Electric Field. *Proceedings of the Royal Society of London Series a-Mathematical and Physical Sciences*, *280*, 383-&.

Tripatanasuwan, S., Zhong, Z. X., & Reneker, D. H. (2007). Effect of evaporation and solidification of the charged jet in electrospinning of poly(ethylene oxide) aqueous solution. *Polymer*, *48*, 5742-5746.

Yu, J. H., Fridrikh, S. V., & Rutledge, G. C. (2006). The role of elasticity in the formation of electrospun fibers. *Polymer*, *47*, 4789-4797.

Zhang, Y. Z., Feng, Y., Huang, Z. M., Ramakrishna, S., & Lim, C. T. (2006). Fabrication of porous electrospun nanofibres. *Nanotechnology*, *17*, 901-908.

Table 4.1. Properties of electrospun solutions and observations of nanofiber morphology

Sample ^a	Alginate	Alginate/ Triton ^b	Alginate/ PEO ^c	Alginate/PEO/ Triton ^{b,c}
Zero shear Visc (Pa·s)	22.0	21.9	14.3	14.3
Relaxation Time (sec)	0.06	0.05	0.05	0.04
Conductivity (mS/cm)	7.15± 0.07	6.80± 0.07	4.79± 0.05	4.62± 0.05
Surface Tension (mN/m)	63± 2	29± 1	55± 2	29± 2
Electrospun Fibers	Droplets	Droplets	Beaded Fibers	Uniform Fibers

^a Total polymer concentration was maintained at 4 wt%.

^b Concentration of Triton X-100 was 1 wt%.

^c Concentrations of alginate and PEO were 2.8 and 1.2 wt% (70:30 by wt), respectively.

(means ± standard deviations are reported)

Table 4.2. Properties of electrospun solutions containing Pluronic F127 and observations of nanofiber morphology

Sample ^a	Alginate	Alginate/ F127 ^b	Alginate/ PEO ^c	Alginate/ PEO/F127 ^{b,c}
Zero shear Visc (Pa·s)	22.0	21.5	14.0	15.5
Relaxation Time (sec)	0.06	0.06	0.05	0.06
Conductivity (mS/cm)	7.15± 0.07	7.04± 0.07	4.10± 0.04	3.53± 0.05
Surface Tension (mN/m)	63± 2	35± 1	57± 1	36± 1
Electrospun Fibers	Droplets	Droplets	Beaded Fibers	Uniform Fibers

^a Total polymer concentration was maintained at 4 wt%.

^b Concentration of Pluronic F127 was 2 wt%.

^c Concentrations of alginate and PEO were 2.4 and 1.6 wt% (60:40 by wt), respectively.

(means ± standard deviations are reported)

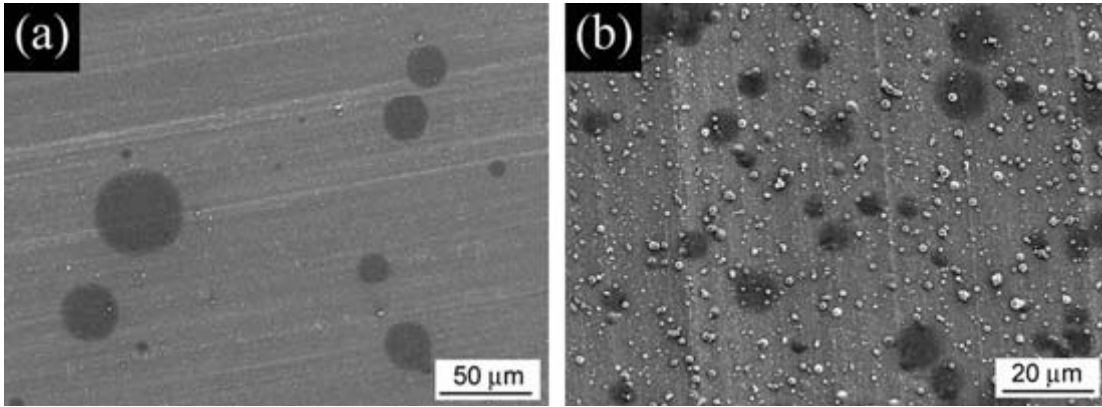


Figure 4.1. Scanning electron micrographs of electrospun droplets of alginate (a) and alginate/Triton X-100 (b), both without PEO. Fibers were not seen with all aqueous alginate solutions investigated, regardless of the addition of a surfactant.

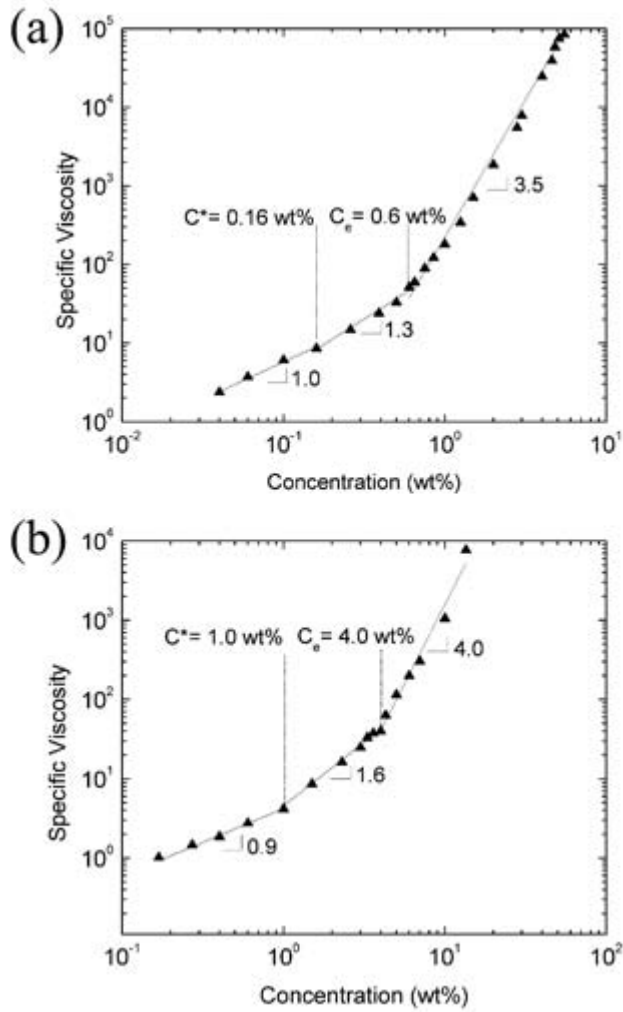


Figure 4.2. Dependence of specific viscosity (η_{sp}) on concentration for (a) 196 kDa and (b) 37 kDa aqueous sodium alginate solutions. The entanglement concentrations (C_e) are 0.6 and 4 wt%, respectively.

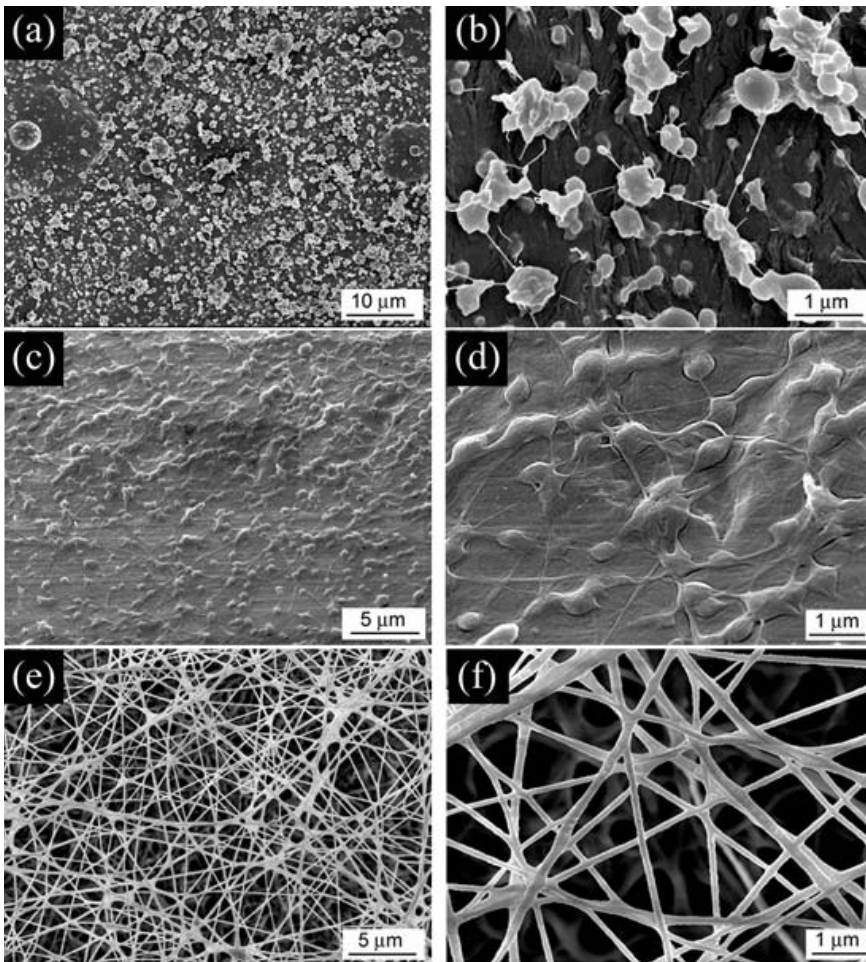


Figure 4.3. Scanning electron micrographs of electrospun droplets of alginate-PEG blended (2.0:20.0 wt%) solution (a, b). PEG (35 kDa) is not an effective carrier polymer for alginate, due to its low MW and inability to be electrospun. Also shown are blended nanofibers prepared from alginate-PEO (600 kDa) (70:30 by wt) solutions. Beaded fibers (c) and (d) were made without surfactant, whereas uniform fibers (e) and (f) contained 1 wt% Triton X-100.

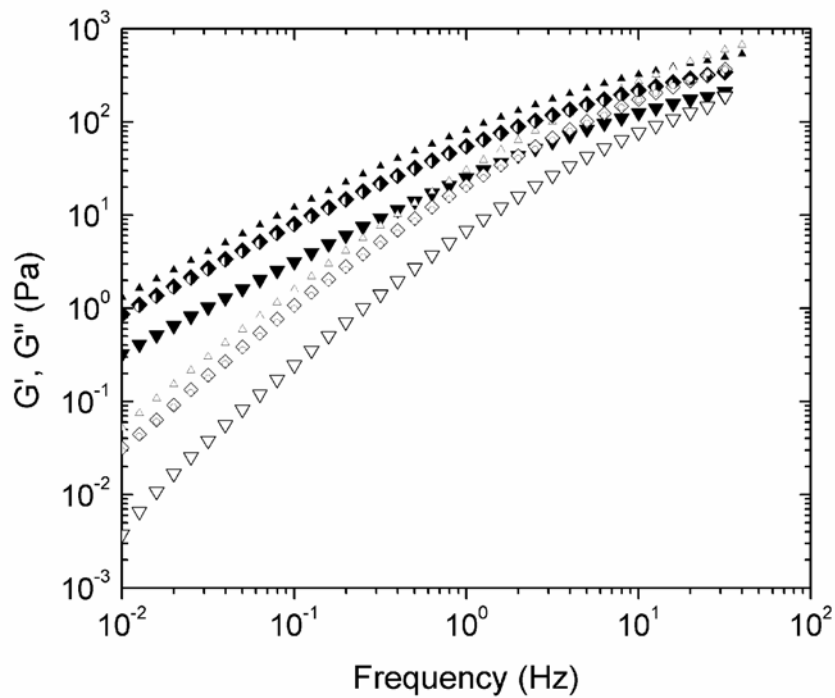


Figure 4.4. Elastic (G') and viscous (G'') moduli as a function of frequency for 2.8 wt% ($\blacktriangledown, \triangledown$) and 4.0 wt% alginate ($\blacktriangle, \triangle$), and blends containing alginate/PEO/Triton X-100 (2.8:1.2:1.0 wt%) (\blacklozenge, \lozenge) and alginate/PEO (2.8:1.2 wt%) (\bullet, \circ).

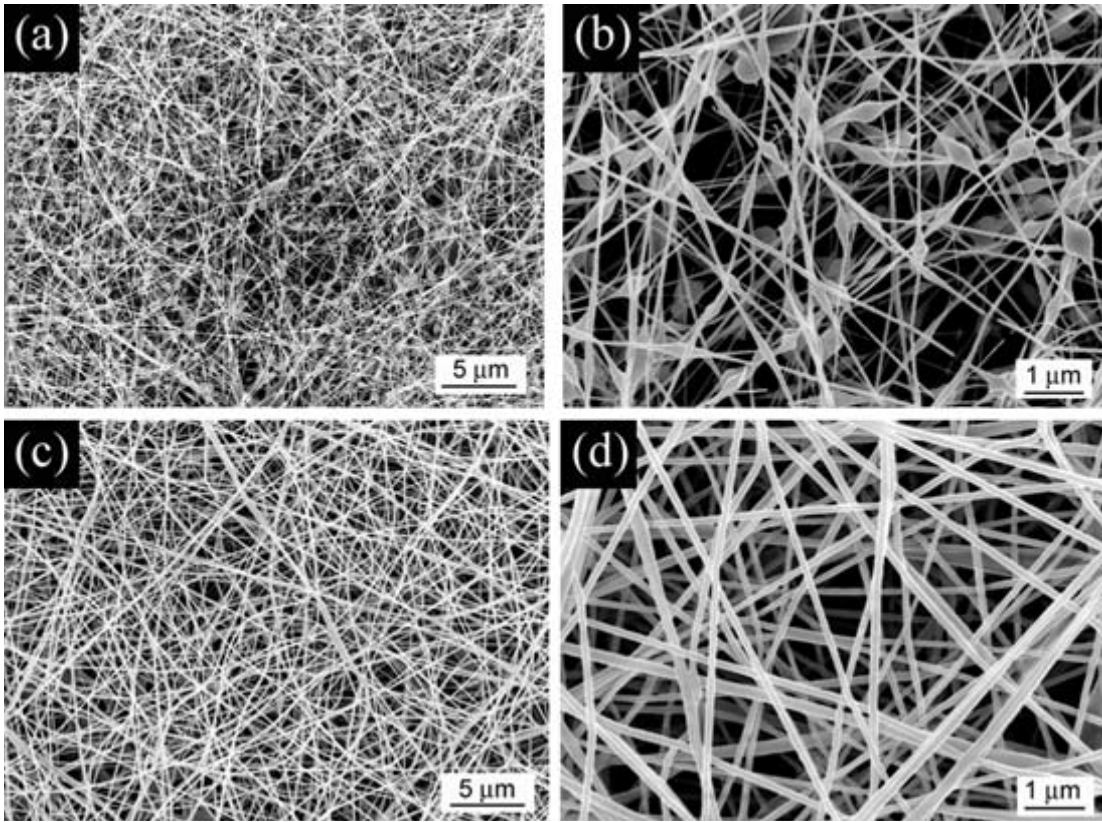


Figure 4.5. Scanning electron micrographs of nanofibers composed of alginate and PEO (2.4:1.6 wt% or 60:40) without (a, b) and with Pluronic F127 (2 wt%) (c, d).

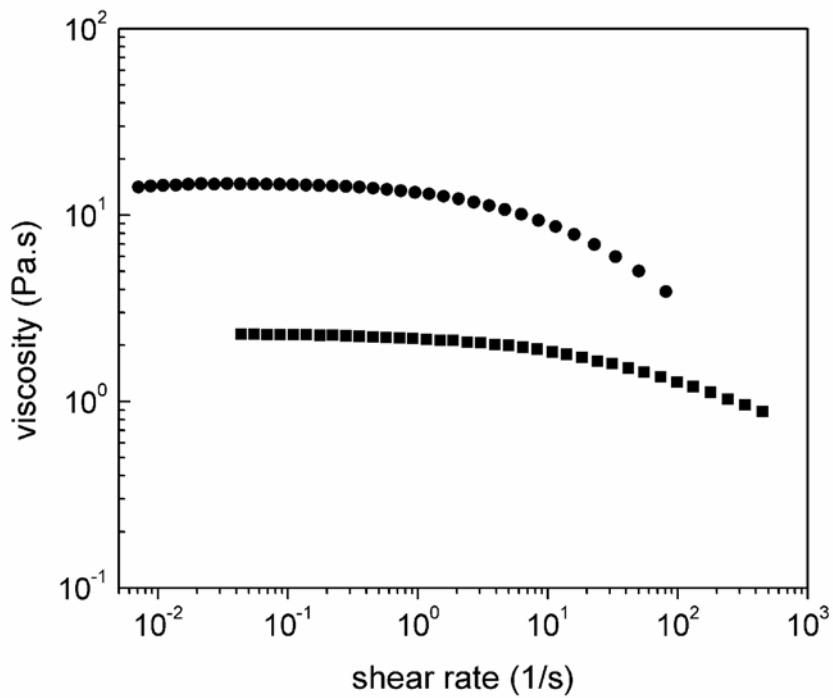


Figure 4.6. Steady shear viscosity curves for electrospun solutions containing blends of PEO with 196 kDa alginate (■) and 37 kDa alginate (●).

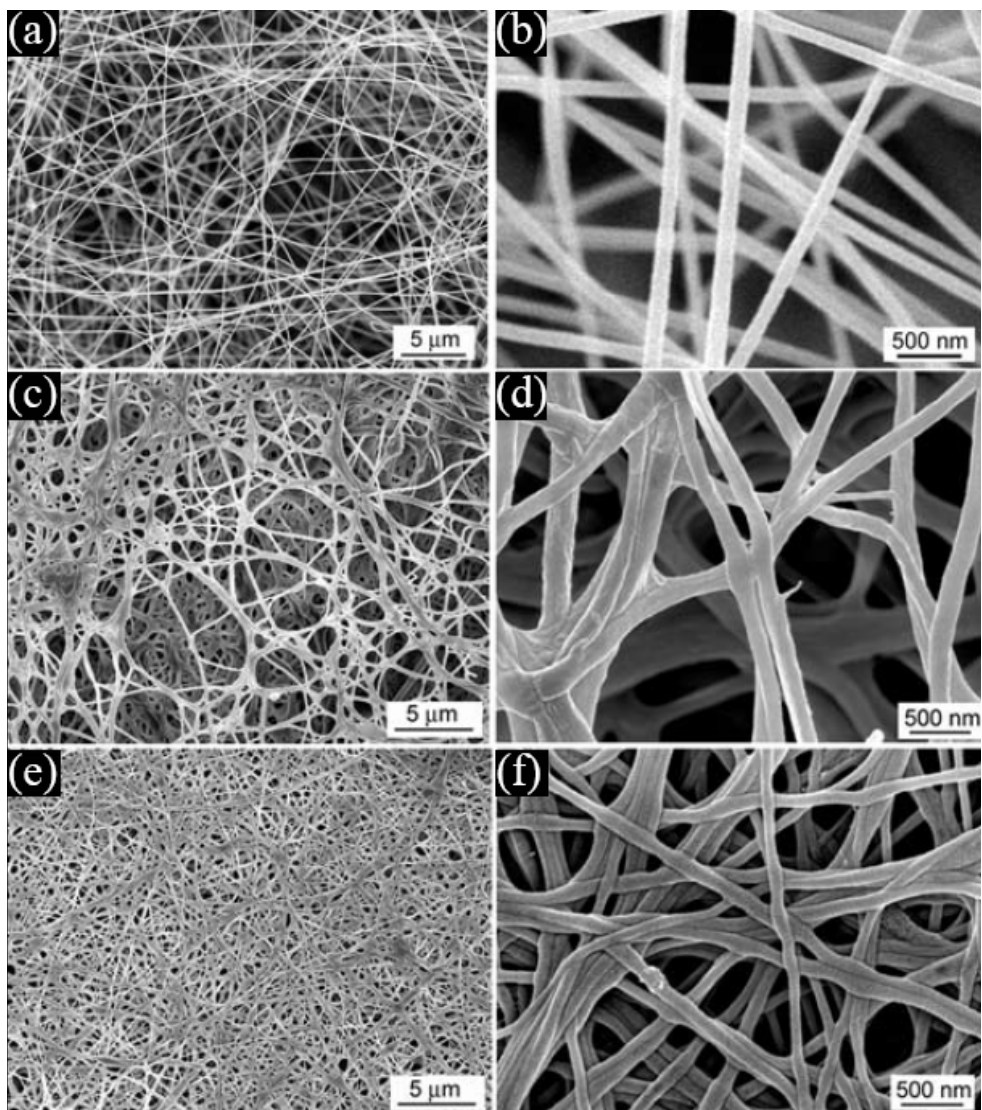


Figure 4.7. Scanning electron micrographs of nanofibers containing 37 kDa alginate/PEO/Pluronic F127 (8.0:1.6:2.0 wt%) (a, b) prior to crosslinking. Nanofibers composed of 196 kDa (c, d) and 37 kDa (e, f) alginate after crosslinking with calcium and soaking in water for 4 days to remove PEO.

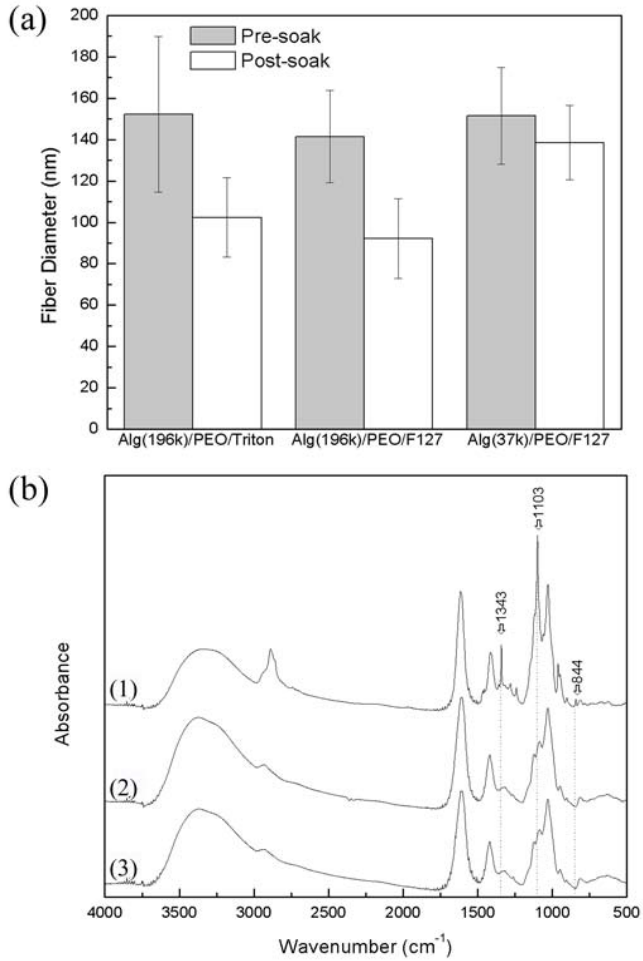


Figure 4.8. Fiber diameters (a) of alginate(196kDa)/PEO/Triton X-100 (2.8:1.2:1.0), alginate(196kDa)/PEO/F127 (2.4:1.6:2.0), and alginate (37kDa)/PEO/F127 (8.0:1.6:2.0) before and after crosslinking and soaking in water. (Error bars = 1 standard deviation.) FTIR spectrographs (b) of nanofibers containing 37 or 196 kDa MW alginate and PEO before (37 kDa (1)) and after (37 kDa (2), 196 kDa (3)) soaking. PEO peaks at 844, 1102, and 1342 cm^{-1} disappear after soaking.

CHAPTER 5

Three Dimensional Electrospun Alginate Mats *via* Tailored Charge Repulsions

Chapter 5 is essentially a manuscript by Christopher A. Bonino, Kirill Efimenko, Sung In Jeong, Melissa Krebs, Eben Alsberg, and Saad A. Khan prepared for submission to *ACS Nano*.

Three-Dimensional Electrospun Alginate Mats *via* Tailored Charge Repulsions

Christopher A. Bonino¹, Kirill Efimenko¹, Sung In Jeong², Melissa D. Krebs², Eben Alsberg^{2,3}, Saad A. Khan^{4*}

¹*Department of Chemical & Biomolecular Engineering, North Carolina State University, Raleigh, North Carolina*

²*Department of Biomedical Engineering, Case Western Reserve University, Cleveland, Ohio*

³*Department of Orthopaedic Surgery, Case Western Reserve University, Cleveland, Ohio*

Abstract

We report on the formation of three-dimensional (3D) electrospun mat structures from alginate – polyethylene oxide (PEO) solution blends. The unique architectures expand the capabilities of traditional electrospun mats for applications such as regenerative medicine, where a scaffold can help to promote tissue growth in three dimensions. The mat structures extend off the surface of the flat collector plate without the need of any modifications in the electrospinning apparatus, are self supporting when the electric field is removed, and are composed of bundles of nanofibers. We propose a mechanism for the unique formations, as

* corresponding author: khan@eos.ncsu.edu (email); 919-515-4519 (ph)

related to the fiber-fiber repulsions from surface charges on the negatively-charged alginate. Furthermore, we discuss the role of the electric field in the distribution of alginate within the nanofibers. X-Ray Photon Spectroscopy is used to analyze the surface composition of the electrospun nanofiber mats and related to cast films made in the absence of the electric field. We discuss techniques to tailor the 3D architecture and nanofiber morphology by changing the relative humidity, solution pH, and surface tension. We also compare other ionic solutions (i.e., PEO with sodium chloride) with similar solution properties (i.e., ionic conductivity) to the alginate solutions and their corresponding 3D mat formations.

5.1. Introduction

Electrospinning is a facile method to fabricate nanofibrous mats, which have a range of applications. The feature sizes of electrospun mats, such as fiber diameters, can be tailored by the solution properties (e.g., viscosity, polymer concentration) and process conditions (e.g., flow rate, electric field).¹ The mat thickness is also affected by the total mass of deposited fibers and size of collector plate. Since the mat thickness is much smaller than the mat diameter, it is commonly used in applications benefiting from two dimensional, porous structures. For example, electrospun mats have been used as filters², battery electrodes³ and separators.⁴ In these applications, a high surface area material with a small thickness (<100 μm) may be desirable, due to the size constraints of the testing media. However, for other applications (i.e., tissue engineering) a two-dimensional mat is less ideal. One role of a tissue scaffold is to mimic the extracellular matrix, a fibrous three dimensional network that provides structural support for developing tissues.⁵ While electrospun mats have shown promise as tissue scaffolds⁶, their feature sizes and topography also have drawbacks. Specifically, electrospun nanofiber mats have relatively flat topography, limited thicknesses, and dense fiber packing. When used as tissue scaffolds, cell infiltration can be restricted to the top layers of the electrospun mat, as a result of the mat feature sizes, (e.g, ⁷). Hence, a traditional electrospun nanofiber mat may have limited uses in regenerative medicine without modification.

Researchers have tailored the electrospun mat formations by a variety approaches in order to expand their capabilities. One such route has been to modify the electrospinning setup. Changes to the collector plate, which vary in complexity from parallel plates⁸ and screws,⁹ to multi-sided columns,¹⁰ have led to controlled alignments of fibers in two (2D) and three dimensional (3D) mat structures. In addition, post treatments of the conventional electrospun mats, such as photomasking¹¹ or stacking layered mats,¹² have been implored to increase the spacing between fibers. While these approaches may be novel, they also add additional process steps and accessories, as well as may create challenges when trying to preserve the mat architecture during removal from the collector.

An alternative approach to making three dimensional mat structures, which has received little attention, focuses on the initial formulation of the electrospun solution. Careful selection of the solution components and properties, may lead to arrangements of electrospun fibers that extend outward from the surface of the collector plate.^{13, 14} The 3D formation can be accomplished by fabricating fibers containing a high charge density material (i.e., polyelectrolyte) that is distributed on or near their outer surfaces, which create repulsive forces between adjacent fibers.

The applied electric field during electrospinning can have significant consequences on the distribution of charged solution components in the formed fibers. The movement of ionic species within a DC electric field is influenced by a variety of forces (e.g., Columbic, electrophoretic).¹⁵ In one predominant outcome, a negatively-charged macro(molecule) can be directed towards the positive polarity electric field source. During electrospinning the

negatively-charged species can be preferentially driven to the Taylor cone and electrospun jet surfaces.¹⁶ This phenomenon can be exploited to prepare electrospun fibers with tailored surface compositions. For example, Sun *et al* electrospun a solution blend containing neutral (i.e., polyethylene oxide) and charged (i.e., peptide-polymer conjugate) components, and observed that the charged peptide populated the outer surfaces, while PEO was within the fiber interiors.¹⁷ Thus, the electrospinning process can produce fibers with charged surfaces, from solutions with ionic components.

Furthermore, compared to neutral solutions, ionic solutions have a higher charge density at the jet surface, which may also affect the morphology of the electrospun fibers. For example, the Reneker group reported the addition of sodium chloride to PEO helped to suppress bead defects.¹⁸ Essentially, the increased charge density in the salt solutions mitigated the capillary instabilities in the jet. Hence, (macro)molecules that dissociate in polar solvents (i.e., salts, polyelectrolytes) have important implications on electrospinning process.

For electrospun fibers containing polyelectrolytes, the dissociation of the ionic species can be manipulated by two methodologies: (1) changing solution pH prior to electrospinning and (2) changing the water content within electrospun jet and fibers by adjusting the relative humidity (RH). The former can be undertaken by dissolving the polyelectrolyte into a solution with an appropriate pH range, relative to its pKa. For example, sodium alginate, a polyelectrolyte and weak acid, contains carboxylic derivatives

(i.e., guluronic acid, mannuronic acid) that can dissociate in solutions with pH >3.4, the highest pKa value.¹⁹

In addition to the solution ionic conductivity, the relative humidity is another variable that has significant effects on electrospinning. Humidity has been linked to the creation/suppression of bead defects, as well as porous surfaces in electrospun fibers.²⁰⁻²² For water-soluble polymers, reducing the humidity raises the rate of solvent evaporation, which causes the electrospun jet to solidify at a closer distance to the source (needle).²³ The solidified jet ceases its viscoelastic behavior and its ability to be elongated or subjected to additional capillary instabilities. Thus, water-soluble fibers electrospun at low humidities (<20%) can have larger diameters and fewer bead defects than at high RH conditions (>40%).²⁰ Despite the implications on fiber morphology, few electrospinning studies typically report RH, much less control ambient experimental conditions. Variations in lab environments may hamper the reproducibility of results caused by the week-to-week variations in the same lab, or between labs at different parts of the world.

In this study, not only do we control the humidity, we also use it to manipulate the formation of three dimensional structures in our fiber mats. Polyelectrolytes forming solid substrates (i.e., films) can be hydrated by water from a humid ambient atmosphere, leading to the solvation and higher mobility of the ions.²⁴ Thus, by changing the humidity of the electrospinning conditions, we alter the concentration of dissociated ions in the fibers, which affect the like-charge repulsions between fibers and the 3D mat formation.

A few studies have reported the occurrence of 3D electrospun mats from solutions containing charged species (e.g., salts, polyelectrolytes).^{13, 14, 25} However, the proposed mechanisms failed to address the influence of the positive-charged electric field at the needle source on negatively-charged solution components. In this work, we prepare electrospun fibers that contain sodium alginate, an anionic polyelectrolyte, which has been shown to display electroresponsive behavior in DC fields.²⁶ We propose that negatively-charged groups on alginate populate the surfaces of the electrospun fibers from the attractive forces in the applied field. The resulting fibers have predominately negatively-charged surfaces, and experience repulsions from other charged, adjacent fibers, causing them to extend off of the collector plate. This phenomenon can be manipulated by the number of disassociated ions within the fiber, which are affected by solution pH and moisture content of the fibers, by way of the relative humidity. To our knowledge, we are the first to methodically alter the formation of 3D electrospun structures by this approach. The 3D mats in this work have fascinating architectures, which have potential uses for applications, such as regenerative medicine. These 3D structures contain alginate, a natural biopolymer, as well as PEO and Pluronic F127 surfactant, both FDA-approved polymers, which make this material a promising biomedical technology.

5.2. Experimental Section

Materials Sodium alginate was obtained from FMC Biopolymers (Princeton, NJ) and its molecular weight (M_w) was reduced from 196 kDa to 37 kDa by 5 Mrad gamma irradiation (Phoenix Laboratory, University of Michigan, Ann Arbor, MI). Additional details on the irradiation procedure have been previously reported.²⁷ Polyethylene oxide ($MW = 600$ kDa, Dow), Pluronic F127 nonionic surfactant (Sigma Aldrich, St. Louis, MO), and sodium chloride (Sigma Aldrich, St. Louis, MO) were used as received. Sodium hydroxide (1 M, Sigma Aldrich, St. Louis, MO) was diluted to with deionized water to achieve a specific solution pH. Solutions containing Alginate-PEO (10.6:0.8 wt %) and Alginate-PEO-F127 (10.6:0.8:1.5 wt %) were prepared following a procedure previously reported.²⁸

Methods

Solution Characterization. Ionic conductivities of the polymer solutions were measured using a potentiostat (Gamry Instruments) that was calibrated with a 1 mS/cm potassium chloride standard (Fisher Scientific). Steady state flow and dynamic rheological experiments were performed on a AR2000 stress-controlled rheometer (4 cm, 2° cone, TA Instruments, New Castle, DE) at 25°C. Surface tensions were measured using a pendant drop analyzer from SEO Co. Ltd (model Phoenix 300, Lathes, South Korea). Solution pH was measured using a pH meter (Compact Twin, Horiba, Kyoto, Japan).

Electrospinning of 3D mats. The electrospinning setup consisted of a syringe pump (model NE-1010, New Era Pump Systems, Inc., Wantagh, NY), high voltage power supply

(model AU-60P0.5, Matsusada Precision, Inc. Kusatsu-City Japan), and ground collector plate covered with aluminum foil. Solutions were pumped through a syringe with a 22 gauge needle at 0.5 mL/hr flowrate. The distance between the needle tip and collector plate was fixed at 12 cm. During electrospinning, the power supply voltage was adjusted in order to maintain the formation Taylor cone on the solution droplet. Timed experiments typically were terminated after 40 minutes. All electrospinning experiments were conducted within a plexiglass glove box to control the ambient conditions. Temperature and relative humidity within the chamber were monitored using a hygrometer (Fisher), and adjusted by flowing dry, compressed air into either an empty or water-filled flask. (Figure 5.1.)

Characterization of electrospun mats. Electrospun mats were photographed using a digital SLR camera (EOS Rebel XS, Canon). High magnification analysis was performed with A FEI XL30 field emission SEM (6 mm working distance, 5 kV accelerating voltage, spot size 3). Fiber diameters were measured with Adobe Photoshop CS3 on 100 fibers per sample. In addition, surface analyses of electrospun mats, dried solutions, and neat materials were made using an X-ray Photon Spectrometer (Kratos Axis Ultra). Each XPS spectra were calibrated to a C-C peak location at 284.5 eV.

5.3. Results and Discussions

5.3.1. Formation of Three-Dimensional Electrospun Mats

We have observed 3D mat structures when electrospinning solutions that contain alginate (M_w 37 kDa) and PEO (M_w 600 kDa), with and without Pluronic F127 nonionic surfactant. We believe that the chemical structure of alginate, which contains carboxylic acid groups that can dissociate into negatively-charged ions, contributes to like-charge Columbic repulsions. As a result, alginate-based fibers are repelled by neighboring fibers and create a 3D mat formation. One example of a 3D structure shown in Figure 5.2a formed by electrospinning an aqueous alginate – PEO – Pluronic F127 blend (10.6:0.8:1.5 wt %) for 40 minutes (0.5 mL/hr) at 30% relative humidity. A cone-like formation extends ~7 cm off the surface of the collector plate towards the needle. Smaller peaks (<1 cm tall) surround the 3-4 cm wide base of the larger cone. Peaks also protrude from the cone tip and along the underside of the cone (near the bottom of photograph). Bundles of fibers span between the peaks and the cone base, which are oriented parallel along the 3D structure, and perpendicular to the collector plate. Interestingly, the cone structure remains fixed in place after removing the electric field. The 3D mat structure supports its own weight, which prevents possible damage to the mat inflicted during removal from a modified collector plate configuration (e.g., screws extending from the plate⁹). To our knowledge, we are the first to report of the occurrence of a self-supporting 3D electrospun mat.

Examination of the 3D mat with scanning electron microscopy reveals that the cone tip has an asymmetrical appearance, consisting of several folds that run along with the direction of its growth. (Figure 5.2b) Furthermore, as shown in Figure 5.2c and d, the cone is composed entirely of layers of nanofibers. Nanofibers located at the base and pinnacle of the cone have the same diameters: 249 ± 45 nm. This result was surprising to us, considering the distance that the electrospun jet travels from the needle to the cone tip or base varies from 5 to 12 cm, corresponding to different amounts of stretching during the whipping instability region. This result suggests that most of the solvent evaporated and the jet solidified within a short distance of the needle, which may have prevented the jet from experiencing further elongations and diameter reductions. Additionally, the fibers shown in Figure 5.2c and d have few bead defects. The occurrence of bead defects is affected by the solution surface tension and ambient relative humidity, and will be addressed in detail later.

The formation of the 3D structure was investigated over time to gain a better understanding of its growth mechanism. The electrospun mat shown in Figure 5.3a formed peaks up to ~ 1 mm tall on the collector plate after 9 minutes. The textured appearance was more prominent in the center of the mat than its outer perimeter. SEM analysis of the mat reveals dense groupings of nanofibers, the largest of which are ~ 150 μm across, and are on top a base layer of fibers. (Figure 5.3d, g.) (Holes or craters in the mat surface are attributed to capillary instabilities, which caused the breakup of the jet into droplets.²⁹)

We hypothesize that, after 9 min of electrospinning, the base layer of fibers prevented surface charges on the topmost fibers from being neutralized by the grounded collector plate.

We further speculate that repulsions from excess negative surface charges between adjacent fibers cause fiber sections to extend off of the surface of the mat. (Figure 5.4a.) Additional layers of fibers that are deposited onto the mat are also repelled from the site of the protrusion, causing a peak to form. As the peak height increases, the electric field changes between the needle and plate. Compared to the flat surface in the traditional electrospun mat, the peaks create differences in topography across the mat, and cause localized regions of a higher electric field. As a result, subsequent layers of fibers are preferentially deposited in the vicinity of the peaks. Several fibers, centered on one peak (left side of micrograph, Figure 5.3d), also extend between other nearby peaks and form lines of parallel fibers. Additional layers of fibers with negatively-charged surfaces are continuously deposited near the peak sites, which causes the peaks to become more pronounced.

After 15 minutes, the largest peaks extend >1 cm off the surface of the collector plate. (Figure 5.3b.) Furthermore, some of the smaller formations have evolved from disordered bundles of fibers ~ 50 μm tall to peaks with defined features ~ 200 μm tall. (Figure 5.3e.) Layers of fibers connect the neighboring peaks creating the ridges around the peak formations. Fibers that are not in position to connect the neighboring peaks are deposited randomly over the ridges. (Figure 5.3h.) The peaks are composed entirely of nanofibers, which suggest that the dynamics of the 3D mat formation occur after the jet has been elongated to its final dimensions. After which, the combination of the electric field and the surface charges on the fibers alter their positions on the mat.

The 3D structure developed into a macro-scale formation after 25 minutes. (Figure 5.3c) Centimeter-sized peaks, connected by layers of fibers made up a base of the structure that is 5-7 cm across. Figure 5.3f shows that the mat has a complicated structure with ridges and valleys (10-100 μm wide). Topography of this size scale may be advantageous if used a tissue scaffold, since cells would be able to move into these spaces.

Based on these experimental observations, we hypothesize that the 3D mechanism is based on the repulsions between neighboring fibers from the charged groups (i.e., carboxylic acid) in alginate. In addition, we believe that the concentration of the negatively-charged groups is disproportionately distributed throughout the fiber, favoring the outer surfaces, as a result of the electric field. As the polymer solution blend passes through the needle that is connected to the power supply, negatively-charged species are attracted to the positively-charged electric field on needle walls, as well as Taylor cone outer surfaces.¹⁶ (Figure 5.4b.) In turn, alginate becomes concentrated near the solution-air interface of the electrospun jet and resulting nanofibers, whereas PEO remains within the interior. (Figure 5.4a.)

X-ray photon spectroscopy confirmed our hypothesis. Scans of pure materials show that alginate and PEO have different atomic compositions of oxygen and carbon, 40.3:53.9 and 31.5:68.0, respectively. (Table 5.1, Figure 5.5) In addition, sodium is unique to alginate. In addition to the neat materials, we also analyzed films and electrospun mats containing alginate – PEO (10.6:0.8 wt %) without the Pluronic surfactant, in order to investigate the surface segregation of the polymer blend. Analysis of a solvent cast film of the alginate-PEO blend reveals the atomic concentration within the 5-10 nm from the top surface matches

PEO. In a thermodynamically stable polymer blend, the more hydrophobic polymer preferentially segregates to the air interface. In contrast, the C and O composition of the outer surface of the electrospun nanofibers matches alginate. (The preference of sodium might be due to ‘bound’ counter ions in the vicinity of the charged polyelectrolyte.³⁰) Thus, the electric field influenced the spatial composition within the fibers, resulting in the negatively-charged polyelectrolyte to dominate the surface concentration.

5.3.2. Effects of Relative Humidity on 3D Electrospun Mat Formation

Humidity has a significant effect on fibers formed during electrospinning. As stated above, aqueous polymer solutions transition from uniform to beaded fibers as the humidity is increased.²⁰ Moreover, the effects of humidity are further complicated when electrospinning a polyelectrolyte solution. While high humidities (>40%) can cause beaded fibers to form, the retained water in the fiber also causes the polyelectrolyte to dissociate into charged groups (R-COO⁻, Na⁺), raising its charge density. As a result, fibers can be reoriented by like-charge repulsions in adjacent fibers, (as well as by the electric field,) and can lead to a 3D mat structure. Thus, relative humidity is a crucial variable to manipulate the 3D structures in the electrospun mats.

Beginning at the low humidity condition (~10%), only a small texture was visible by the naked eye on the surface of the mat. Analysis with SEM revealed that mats contained uniform, bead-free fibers with average diameters 299±40 nm. (Figure 5.6a, b.) Increasing

the humidity beyond 10% RH has profound effects on the mat appearance. At 20% RH, a conical structure (2 cm tall, 2 cm diameter) was limited to a small region of the collector plate, whereas regions surrounding regions lacked a 3D appearance (<1 mm peaks). (Figure 5.6c, d; Table 5.2.) The cone formed relatively slowly, as the first signs of peaks appeared after 30 min. With less water retained within the fiber in the dry environment, there are fewer dissociated carboxylic acid groups and charges on the outer surfaces of the fibers. Thus, neighboring fibers are repelled by shorter distances compared to fibers with greater concentrations of surface charges, and the 3D formation is a compact, slow-forming structure.

The 3D formation becomes much larger in diameter and height at 30% RH. (Figure 5.6e, f) The structure forms faster than compared the dryer conditions (1 cm tall in 10 min) because with more retained water, the alginate-based fibers have more surface charges and repulsions. Despite the unique shape of the mat, the fibers are bead-free, with diameters 237 ± 33 nm. Of the conditions evaluated, the 3D mats prepared at 30% RH have the combination of uniformly-sized fibers and large structural formation.

At 40-50% RH, the electrospun mat transitions to a new 3D formation. (Figure 5.6g-j) Instead of a self-supporting cone, 0.5 – 2 cm wide strands form on the collector plate and align with the electric field. A similar observation was reported previously with other charged polymers (e.g., Poly(p-xylenetetrahydrothiophenium chloride¹⁴), which was attributed to the accumulation of excess charges on the sections of the electrospun fibers. Each strand starts from the pinnacle of a peak on the collector plate. As we discovered with

the cone structures, the strands are also composed of sub-micron diameter fibers. (Figure 5.7a.) One noticeable difference is that the strands contain clusters of fibers oriented perpendicular to the collector plate (or parallel to the electric field). (Figure 5.7b.) We hypothesize that increasing the humidity leads to an increase in the density of charges on the fiber surfaces. The like-charge repulsions between fibers result in parallel alignments, in order to minimize the electrostatic forces. The strands of fibers that are anchored to the mat surface at one point extend outward along the field lines. Subsequent layers of fibers are deposited on top of the aligned fiber clusters, which increase the size of the strand. In addition, bead defects are present on these fibers, which are consistent with water-soluble polymers electrospun in 40-50% RH.²⁰ Compared to the 3D structure at 30%, the strands formed 40 and 50% RH are taller (up to 7 cm), and spread over a larger area on the mat ($6 \times 10 \text{ cm}^2$). However, the strands took longer to form than the cone structure, 16-18 and 10 min, respectively. (Table 5.2.) We speculate that the 3D formation in the high humidity conditions was distributed over a vast area on the collector plate as a result the fibers' high surface charge densities, as compared to dry conditions. In addition, the size of the mat may be the result of large regions of whipping instabilities that occur in a partially-solidified jet.¹⁸ Thus, the 3D structure was distributed over a vast area, leading to a slower rate of formation compared to the 30% RH condition. Furthermore, the greater regions of whipping instabilities in the jet contributed to the formation of bead defects, as well as smaller fiber diameters.

As seen at low RH, the 3D structure at 60% RH did not form within 40 minutes of electrospinning. The 2D mat was composed of heavily beaded fibers, due to the whipping instabilities in the jet. (Figure 5.6k, l) While humid conditions contribute to a high concentration of dissociated carboxylic groups at the fiber outer surfaces, the water vapor in the air may also cause screening, as well as a breakdown of the electric field.

The variety of 3D mat structures prepared through the range of humidity conditions can be customized for the desired use. The driest conditions are most suitable for uniform fiber diameters and relatively flat mat topographies, whereas cone and strand structures form at moderate humidity levels. Finally, high humidity levels are appropriate if alginate beads/spheres are preferred to fibers.

5.3.3. Effects of Solution pH on 3D Electrospun Mat Formation

Raising the pH had profound effects on the 3D mat formations from the alginate – PEO solutions. In order to increase the solution pH, alginate was dissolved in dilute NaOH solutions before blending with PEO. The combined solution blend (pH 7.9) led to faster and larger 3D structure formations, compared to solutions prepared by dissolving alginate in DI water (pH 7.0). At 20% RH, the cone is more than 3 times taller than the cone made from the pH 7.0 solution. (Figure 5.8.) As discussed above, when sodium alginate is dissolved in a basic solution, a greater concentration of carboxylic acid groups dissociate as compared to a neutral pH. Thus, more charges are generated on/below the fiber surfaces in the pH 7.9

solution, leading to Columbic repulsions between fibers, which explain the appearance differences from the pH 7.0 electrospun mat. In addition to the differences in electrospun mat structures, increasing the pH also led to larger fiber diameters (385 ± 53 , 294 ± 44 nm). Reasons for the difference in diameters are under investigation.

5.3.4. Effects of Surface Tension on 3D Electrospun Mat Formation

The connection between reducing the surface tension in electrospinning solutions and the suppression of bead defects are well documented (e.g.,^{18, 31}). We recently showed that a PEO-based nonionic surfactant, Pluronic F127, helped mitigate the formation of beads in alginate-PEO blends.³² In this study, Pluronic F127 also aids in the 3D mat formation. Electrospun mats prepared from alginate – PEO (10.6:0.8 wt %) solutions have minimal 3D topography as compared to mats from solutions containing 1.5 wt % F127 in the same conditions, as shown in Figure 5.9a and Figure 5.6g, respectively. However, SEM analysis reveals that small peaks 20-50 μm across are present on the mats without the surfactant, which still validates our central hypothesis about like-charge repulsions. (Figure 5.9b) Furthermore, the addition of Pluronic F127 lowers the surface tension of the alginate-PEO solution from 57 to 35 mN/m. (Table 5.5.) We speculate that the reduction in surface tension allows for more alginate to migrate to the air-water interface with the applied electric field, as compared to the solution without the surfactant. XPS analysis of drops and electrospun mats from solutions containing Pluronic F127 differ from the solutions without

surfactant (Table 5.4 and Table 5.1, respectively). Specifically, the surface concentration of the electrospun mats does not match the atomic composition of alginate (O:C 40.3:53.9). Since Pluronic contains a PPO block that is more hydrophobic than the other materials in the solution, it is present at the surface of both the drop and the electrospun fibers. However, because the XPS scan penetrates within top 5-10 nm of the sample, it is likely that the atomic composition measurement also include other components. Based on the XPS results from the surfactant-free solutions, we believe that the film and electrospun surface compositions include Pluronic F127 with PEO, and Pluronic F127 with alginate, respectively.

5.3.5. 3D Mat Formation in Solutions Without Alginate

We investigated the electrospun 3D formation in another ionic solution, by replacing alginate with sodium chloride. We closely matched the zero shear viscosity, ionic conductivity, and surface tension of PEO – NaCl – F127 (5.0:1.0:1.5 wt %) solutions with the alginate blend properties. (Table 5.5) The PEO solution formed a 3D structure that was significantly different from the alginate solutions. Specifically, a thin webbing of fibers extended from the collector plate (~8 cm) toward the needle. (Figure 5.10.) As observed with the “strands” that formed from alginate solutions, the webbing could not support its own weight when the electric field was removed. SEM analysis of the 3D mats revealed that the thin webbing is composed of only a few layers of fibers. Individual fibers vary in diameter from 200 nm to 2 μ m and have “Y”-like appearances, possibly from the result of the jet

splitting in multiple directions. A similar appearance was reported with other electrospun polymers (e.g., poly vinyl alcohol/NaCl²⁵ and poly-hydroxyethylmethacrylate (HEMA)³³), and was attributed to regions with excess surface charges that split from the main jet to form smaller branches.

We concluded from the web formation, that the PEO-salt solutions are likely not capable of matching the appearance of the 3D structures observed alginate blends. One reason may be due to the size of the charged species in the two solutions. Compared to Cl⁻, the carboxylic acid groups are less mobile in solution because they are bonded to a larger molecule ($M_w = 37$ kDa): alginate. Thus, when passing through the positive polarity electric field during electrospinning, chlorine ions migrate to the solution-air interface more quickly and become more concentrated than negatively-charged alginate polymer chains. (Figure 5.11.) As a result, the PEO-salt fibers have a greater surface charge density compared to alginate, leading to a greater number of like-charge repulsions between the fibers, which cause the formation of a less dense 3D structure.

This explanation can also be applied to describe the results for another charged solution that created a 3D electrospun structure. Poly(p-xylene-tetrahydrothiophenium chloride), a cationic polyelectrolyte and precursor to poly(p-phenylene vinylene) (PVP), formed narrow strands that extended from the collector plate during electrospinning.¹⁴ Unlike the alginate solutions, the chlorine anion is much smaller than the cationic polyelectrolyte. Electrospinning with a positive polarity at the needle creates an electrospun jet with the chlorine loaded on the outer surfaces, much like with the PEO – salt solutions,

and forms a low density mat of strands. Hence, the charge mobility of the anionic materials in electrospun solutions influences the 3D structural formation.

5.4. Conclusion

The formation of three dimensional alginate nanofibrous structures is caused by the polyelectrolytic nature of alginate and the electrospinning conditions. Blends of alginate and PEO, with and without Pluronic F127 surfactant, were electrospun into 3D formations composed of nanofibers. We explained the 3D structure is a result of repulsions between neighboring fibers, due to surface charges. We showed by XPS analysis that alginate, a negatively-charged polyelectrolyte, is preferentially distributed on the outer surfaces of the electrospun fibers, whereas PEO preferentially surface-segregates in the absence of the electric field. The relative humidity changes the 3D structure, which we attribute to a greater number of surface charges from the dissociated alginate chains. We observed that increasing the solution pH enhanced the size of the mat formations, which we also attributed to the dissociation of alginate. Ionic solutions prepared without alginate (PEO and salt) resulted in a different 3D formation, which may be due to the mobility of free charges. This approach to making 3D nanofibrous architectures from solutions containing charged components is a strategy to expand the capabilities of electrospinning beyond traditional 2D mat structures, and have potential uses as tissue scaffolds. Furthermore, this work substantiates the importance of controlling relative humidity during electrospinning.

5.5. Acknowledgements

This work was supported by U.S. Department of Education Graduate Assistance in Areas of National Need (GAANN) Fellowship Program at North Carolina State University (CAB), and a National Science Foundation Graduate Research Fellowship (MDK).

5.6. References

1. Li, D.; Xia, Y. N., Electrospinning of nanofibers: Reinventing the wheel? *Advanced Materials* 2004, 16, (14), 1151-1170.
2. Yoon, K.; Kim, K.; Wang, X. F.; Fang, D. F.; Hsiao, B. S.; Chu, B., High flux ultrafiltration membranes based on electrospun nanofibrous PAN scaffolds and chitosan coating. *Polymer* 2006, 47, (7), 2434-2441.
3. Ji, L. W.; Zhang, X. W., Fabrication of porous carbon/Si composite nanofibers as high-capacity battery electrodes. *Electrochemistry Communications* 2009, 11, (6), 1146-1149.
4. Cho, T. H.; Sakai, T.; Tanase, S.; Kimura, K.; Kondo, Y.; Tarao, T.; Tanaka, M., Electrochemical performances of polyacrylonitrile nanofiber-based nonwoven separator for lithium-ion battery. *Electrochemical and Solid State Letters* 2007, 10, (7), A159-A162.
5. Lee, J.; Cuddihy, M. J.; Kotov, N. A., Three-dimensional cell culture matrices: State of the art. *Tissue Engineering Part B-Reviews* 2008, 14, (1), 61-86.
6. Liang, D.; Hsiao, B. S.; Chu, B., Functional electrospun nanofibrous scaffolds for biomedical applications. *Advanced Drug Delivery Reviews* 2007, 59, (14), 1392-1412.

7. Jeong, S. I.; Krebs, M. D.; Bonino, C. A.; Khan, S. A.; Alsborg, E., Electrospun alginate nanofibers with controlled cell adhesion for tissue engineering. *Macromolecular Bioscience* 2010, (10), 934-943.
8. Li, D.; Wang, Y.; Xia, Y., Electrospinning Nanofibers as Uniaxially Aligned Arrays and Layer-by-Layer Stacked Films. *Advanced Materials* 2004, 16, (4), 361.
9. Wang, Y.; Li, H.; Wang, G.; Yin, T.; Wang, B.; Yu, Q., Electrospinning of Polymer Nanofibers with Ordered Patterns and Architectures *Journal of Nanoscience and Nanotechnology* 2010, 10, (3), 1699-1706.
10. Zhang, D. M.; Chang, J., Electrospinning of Three-Dimensional Nanofibrous Tubes with Controllable Architectures. *Nano Letters* 2008, 8, (10), 3283-3287.
11. Sundararaghavan, H. G.; Metter, R. B.; Burdick, J. A., Electrospun Fibrous Scaffolds with Multiscale and Photopatterned Porosity. *Macromolecular Bioscience* 2010, 10, (3), 265-270.
12. Srouji, S.; Kizhner, T.; Suss-Tobi, E.; Livne, E.; Zussman, E., 3-D Nanofibrous electrospun multilayered construct is an alternative ECM mimicking scaffold. *Journal of Materials Science-Materials in Medicine* 2008, 19, (3), 1249-1255.
13. Kim, T. G.; Chung, H. J.; Park, T. G., Macroporous and nanofibrous hyaluronic acid/collagen hybrid scaffold fabricated by concurrent electrospinning and deposition/leaching of salt particles. *Acta Biomaterialia* 2008, 4, (6), 1611-1619.

14. Okuzaki, H.; Takahashi, T.; Miyajima, N.; Suzuki, Y.; Kuwabara, T., Spontaneous formation of poly(p-phenylenevinylene) nanofiber yarns through electrospinning of a precursor. *Macromolecules* 2006, 39, (13), 4276-4278.
15. Hiemenz, P. C.; Rajagopalan, R., *Principles of colloid and surface chemistry*. 3rd ed.; Marcel Dekker: NY, 1997.
16. Sun, X.-Y. Concurrent and Sequential Surface Modification of Electrospun Polymer Micro/Nano Fibers. North Carolina State University, Raleigh, 2008.
17. Sun, X. Y.; Shankar, R.; Borner, H. G.; Ghosh, T. K.; Spontak, R. J., Field-driven biofunctionalization of polymer fiber surfaces during electrospinning. *Advanced Materials* 2007, 19, (1), 87-+.
18. Fong, H.; Chun, I.; Reneker, D. H., Beaded nanofibers formed during electrospinning. *Polymer* 1999, 40, (16), 4585-4592.
19. Martinsen, A.; Storro, I.; Skjakbraek, G., Alginate as Immobilization Material .3. Diffusional Properties. *Biotechnology and Bioengineering* 1992, 39, (2), 186-194.
20. Tripatanasuwan, S.; Zhong, Z. X.; Reneker, D. H., Effect of evaporation and solidification of the charged jet in electrospinning of poly(ethylene oxide) aqueous solution. *Polymer* 2007, 48, (19), 5742-5746.
21. Pai, C. L.; Boyce, M. C.; Rutledge, G. C., Morphology of Porous and Wrinkled Fibers of Polystyrene Electrospun from Dimethylformamide. *Macromolecules* 2009, 42, (6), 2102-2114.

22. Casper, C. L.; Stephens, J. S.; Tassi, N. G.; Chase, D. B.; Rabolt, J. F., Controlling surface morphology of electrospun polystyrene fibers: Effect of humidity and molecular weight in the electrospinning process. *Macromolecules* 2004, 37, (2), 573-578.
23. Yarin, A. L.; Koombhongse, S.; Reneker, D. H., Bending instability in electrospinning of nanofibers. *Journal of Applied Physics* 2001, 89, (5), 3018-3026.
24. Durstock, M. F.; Rubner, M. F., Dielectric properties of polyelectrolyte multilayers. *Langmuir* 2001, 17, (25), 7865-7872.
25. Barakat, N. A. M.; Kanjwal, M. A.; Sheikh, F. A.; Kim, H. Y., Spider-net within the N6, PVA and PU electrospun nanofiber mats using salt addition: Novel strategy in the electrospinning process. *Polymer* 2009, 50, (18), 4389-4396.
26. Kim, S. J.; Yoon, S. G.; Lee, Y. H.; Kim, S. I., Bending behavior of hydrogels composed of poly(methacrylic acid) and alginate by electrical stimulus. *Polymer International* 2004, 53, (10), 1456-1460.
27. Alsberg, E.; Kong, H. J.; Hirano, Y.; Smith, M. K.; Albeiruti, A.; Mooney, D. J., Regulating bone formation via controlled scaffold degradation. *Journal of Dental Research* 2003, 82, (11), 903-908.
28. Bonino, C. A.; Krebs, M. D.; Saquing, C. D.; Jeong, S. I.; Shearer, K. L.; Alsberg, E.; Khan, S. A., Electrospinning alginate-based nanofibers: From blends to crosslinked low molecular weight alginate-only systems. *Carbohydrate Polymers* In press.

29. Reneker, D. H.; Yarin, A. L., Electrospinning jets and polymer nanofibers. *Polymer* 2008, 49, (10), 2387-2425.
30. Bordi, F.; Cametti, C.; Colby, R. H., Dielectric spectroscopy and conductivity of polyelectrolyte solutions. *Journal of Physics-Condensed Matter* 2004, 16, (49), R1423-R1463.
31. Bhattarai, N.; Li, Z. S.; Edmondson, D.; Zhang, M. Q., Alginate-based nanofibrous scaffolds: Structural, mechanical, and biological properties. *Advanced Materials* 2006, 18, (11), 1463-1467.
32. Bonino, C. A.; Krebs, M. D.; Saquing, C. D.; Jeong, S. I.; Shearer, K. L.; Alsberg, E.; Khan, S. A., Electrospinning alginate-based nanofibers: From blends to crosslinked low molecular weight alginate-only systems. *Carbohydrate Polymers* In press.
33. Koombhongse, S.; Liu, W. X.; Reneker, D. H., Flat polymer ribbons and other shapes by electrospinning. *Journal of Polymer Science Part B-Polymer Physics* 2001, 39, (21), 2598-2606.

Table 5.1. Surface atomic composition measured by XPS

	Peak position	PEO	Alginate	Alginate-PEO^d	Alginate-PEO^d
	(eV)	(%)^{a, b}	(%)^{a, c}	Film^b	Electrospun Mat
				(%)^a	(%)^a
O	532	31.5	40.3	29.6	38.7
C	286	68.0	53.9	64.8	56.9
Na	1070	0	5.8	2.8	4.2
Si^e	151	0.4	0	2.8	0.2

^a Atomic percent is average of at least two runs, standard deviation <2.5%.

^b Solvent cast film.

^c Neat material.

^d Solution blend 10.6:0.8 wt% (93:7%).

^e Silica is present in PEO in the form of fumed silica.

Table 5.2. Observations of electrospun formations at various relative humidities

Relative Humidity	10%	20%	30%	40%	50%	60%
Time for 1 mm tall formation (min)^a	--	30	5	12	17	--
Time for 1 cm tall formation (min)^a	--	35	10	16	18	--
2D mat diameter (cm)	14	14	17	17	16	16
3D mat diameter (cm)^b	--	2	6	7-10	6-10	--
3D mat height (cm)	<0.1	2	5	7	7	<0.1
Average fiber diameter (nm)^c	300±40	294±44	237±33	239±41	171±40	80±23
Comments on mat	textured appearance	small cone	wide cone	strands	strands	textured appearance
Comments on fibers	uniform diameters	uniform diameters	uniform diameters	a few bead defects	bead defects	heavily beaded fibers

^a Maximum dimensions of 3D structure off of collector plate, monitored up to 40 min.

^b For 3D regions >1 mm in height off of collector plate.

^c Average ± standard deviation (100 fibers/sample)

Table 5.3. Observations of electrospun formations at different solution pH

pH	7.0^a	7.9^{a, b}
Time for 1 mm tall formation (min)^a	30	8
Time for 1 cm tall formation (min)^a	35	10
2D mat diameter (cm)	14	10
3D mat diameter (cm)^b	2	3-4
3D mat height (cm)	2	7
Average fiber diameter (nm)^c	294±44	385±53
Comments	small cone	tall cone

^a Solution composition is alginate-PEO-F127 (10.6:0.8:1.5 wt %)

^b Alginate was dissolved in 0.005 M NaOH solution, prior to blending with PEO and F127.

^c Average ± standard deviation (100 fibers/sample)

Table 5.4. Surface atomic composition measured by XPS, with Pluronic F127 surfactant

	Peak position	PEO	Alginate	Pluronic F127	Alginate-PEO-F127^d Film^b	Alginate-PEO-F127^d Electrospun Mat
	(eV)	(%)^{a, b}	(%)^{a, c}	(%)^{a, c}	(%)^a	(%)^a
O	532	31.5	40.3	20.7	28.0	32.5
C	286	68.0	53.9	79.3	69.0	65.4
Na	1070	0	5.8	0	2.5	1.7
Si^e	151	0.4	0	0	0.6	0.5

^a Atomic percent is average of at least two runs, standard deviation <2.5%.

^b Solvent cast film.

^c Neat material.

^d Solution blend 10.6:0.8:1.5 wt %.

^e Silica is present in PEO in the form of fumed silica.

Table 5.5. Properties of electrospinning solutions evaluated for 3D mats

	Alginate-PEO- F127^a	Alginate- PEO^b	PEO-NaCl-F127^c
Zero Shear Viscosity (Pa s)	4.3	4.2	4.6
Conductivity (mS/cm)^d	13.2±1.3	14.1±1.4	12.7±1.5
Surface Tension (mN/m)^d	35±1	57±1	37±1
Electrospinning Comments	3D mat	2D mat	webbing

^a Solution blend 10.6:0.8:1.5 wt %.

^b Solution blend 10.6:0.8 wt %.

^c Solution blend 5.0:1.0:1.5 wt %.

^d Values are averages±standard deviations of five measurements

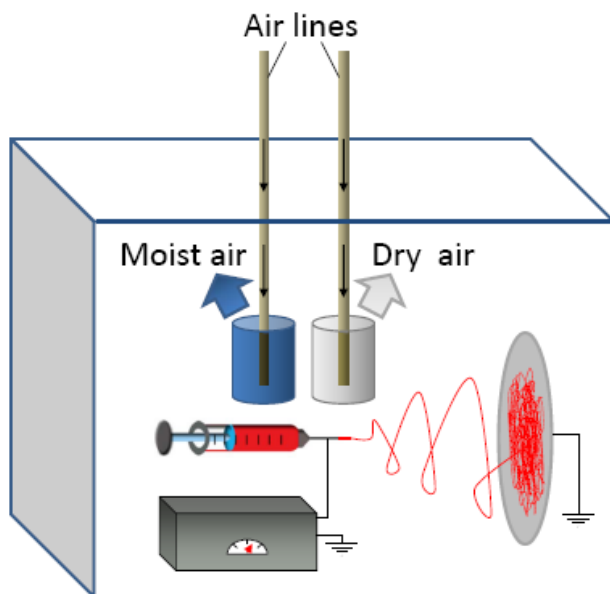


Figure 5.1. Electrospinning setup with controlled humidity environment

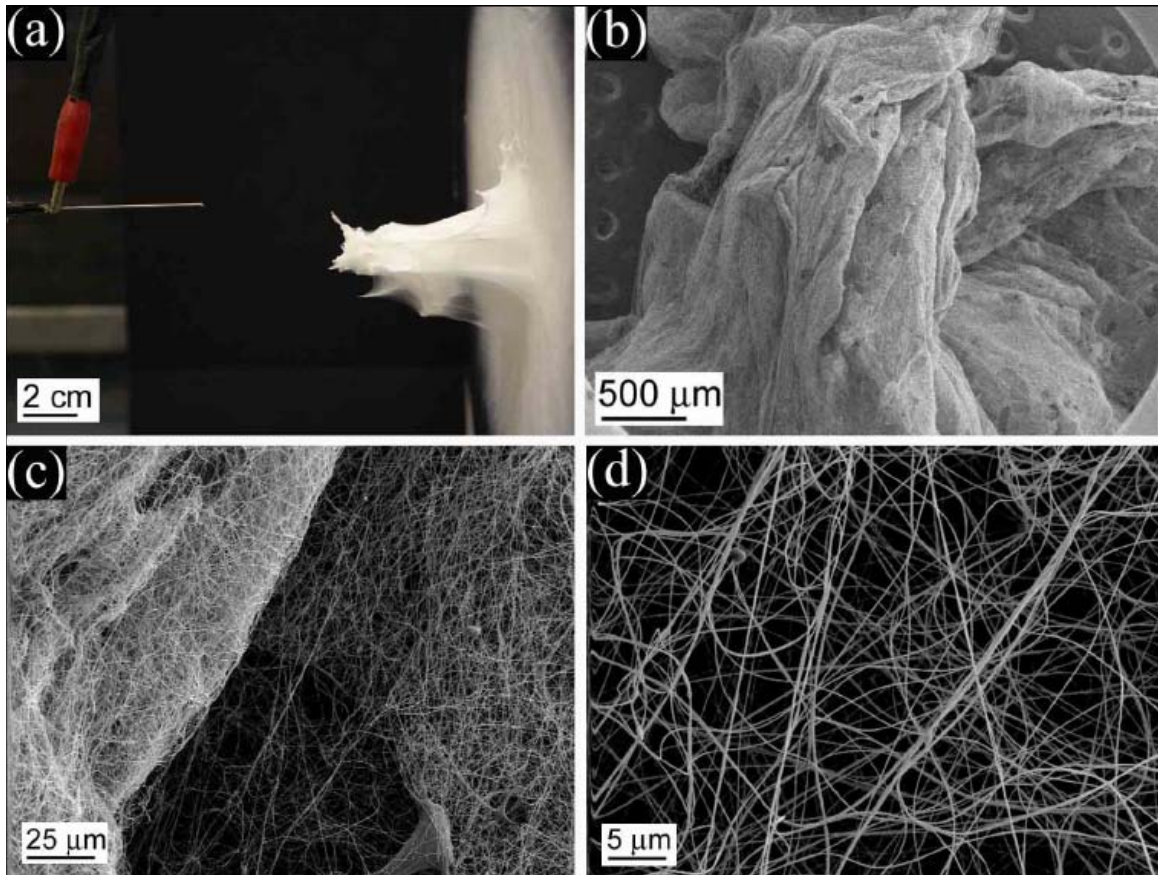


Figure 5.2. Photograph (a) and SEM micrographs (b, c, d) of electrospun cone formation, composed of layers of nanofibers. The electrospinning solution contained: alginate – PEO – F127 (10.6:0.8:1.5 wt %) in water (30% RH).

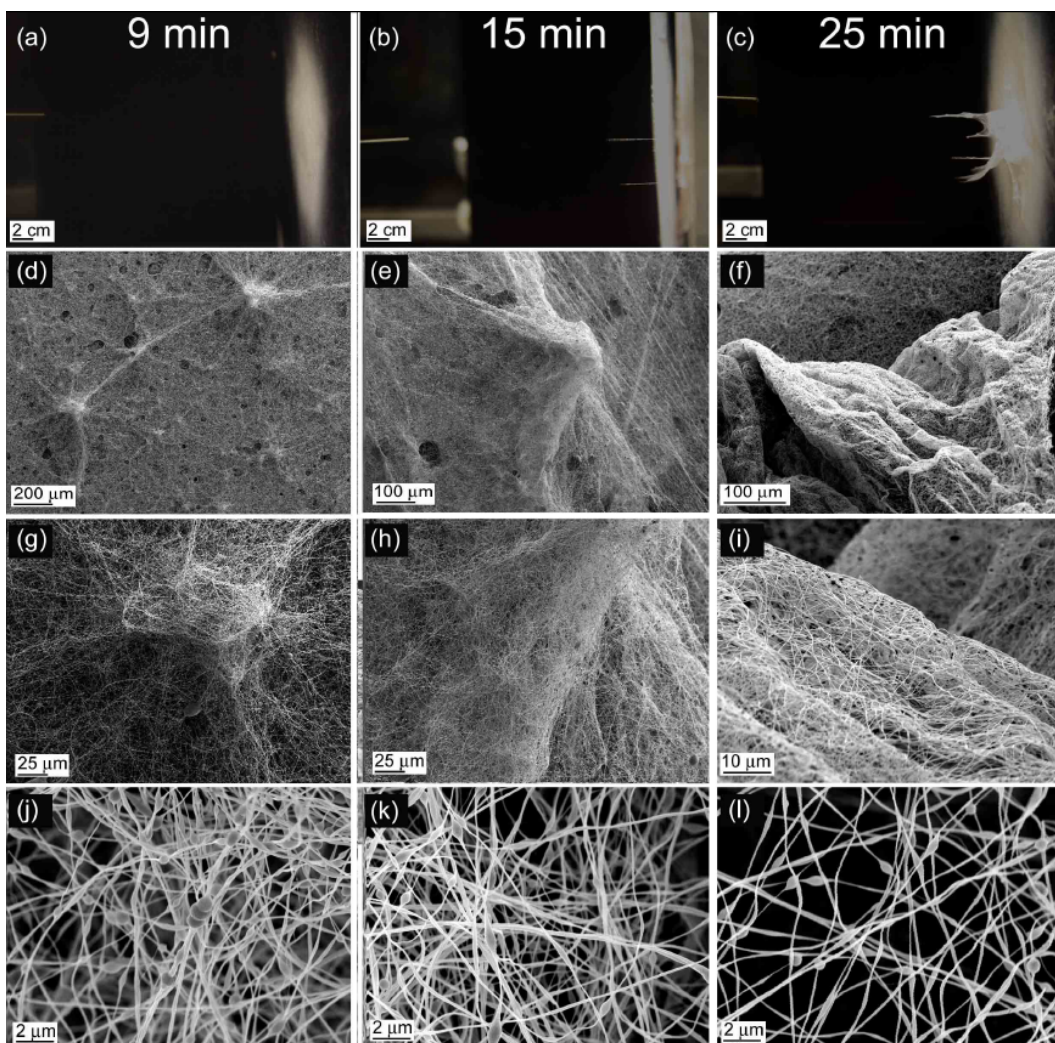
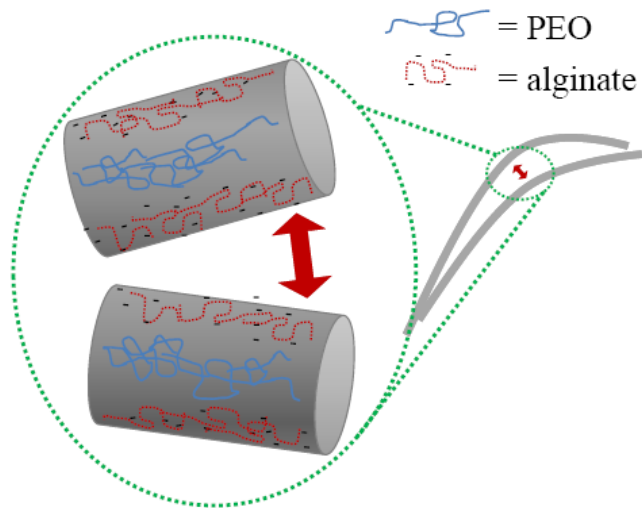


Figure 5.3. Photographs and SEM micrographs of formation of 3D mat structure after 9 (a, d, g, j), 15 (b, e, h, k), and 25 min (c, f, i, l) of electrospinning an aqueous alginate – PEO – F127 (10.6:0.8:1.5 wt %) solution (40% RH).

(a)



(b)

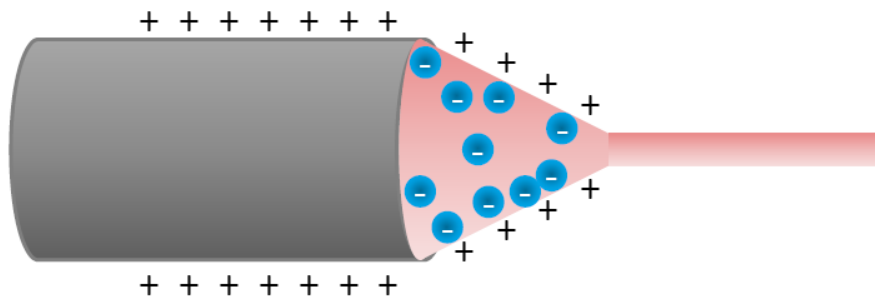


Figure 5.4. Diagrams depicting fiber-to-fiber repulsions that lead to the formation of 3D structures (a) and the effects of the electric field on negatively-charged species (i.e., alginate) in solution within the Taylor cone (b).

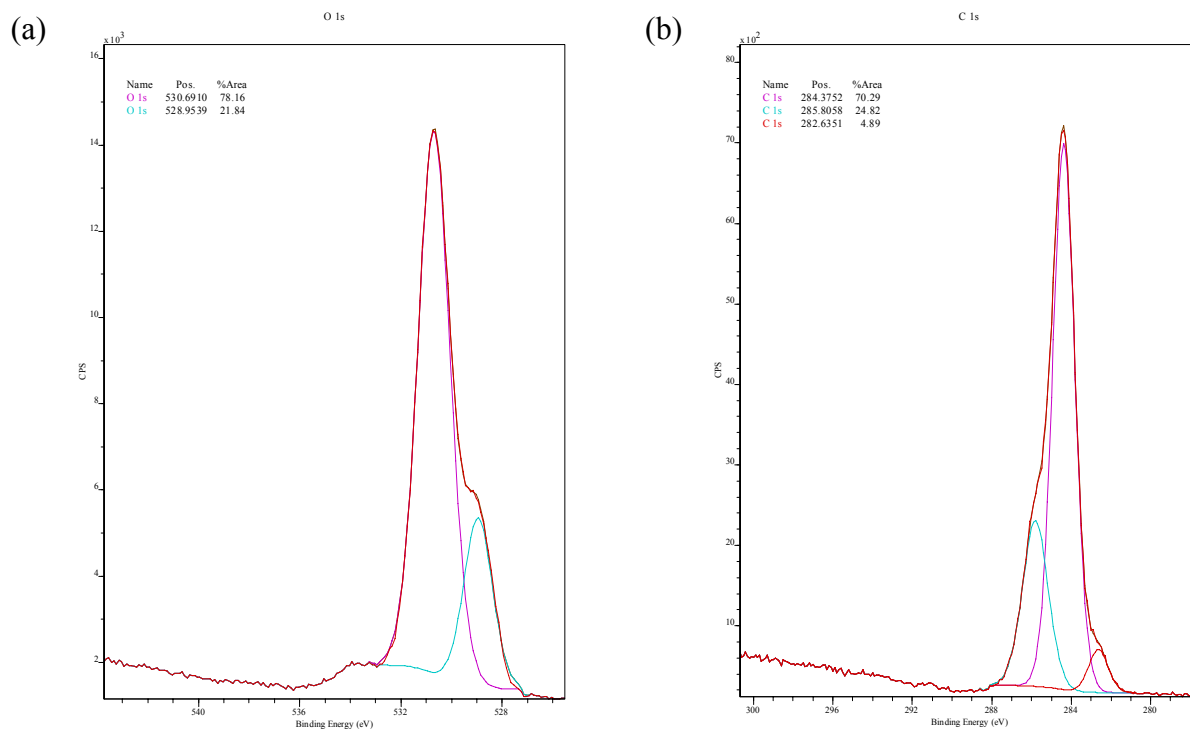


Figure 5.5. Representative high resolution XPS scans of oxygen (a) and carbon (b) spectra on electrospun alginate – PEO (10.6-0.8 wt %) 3D mats.

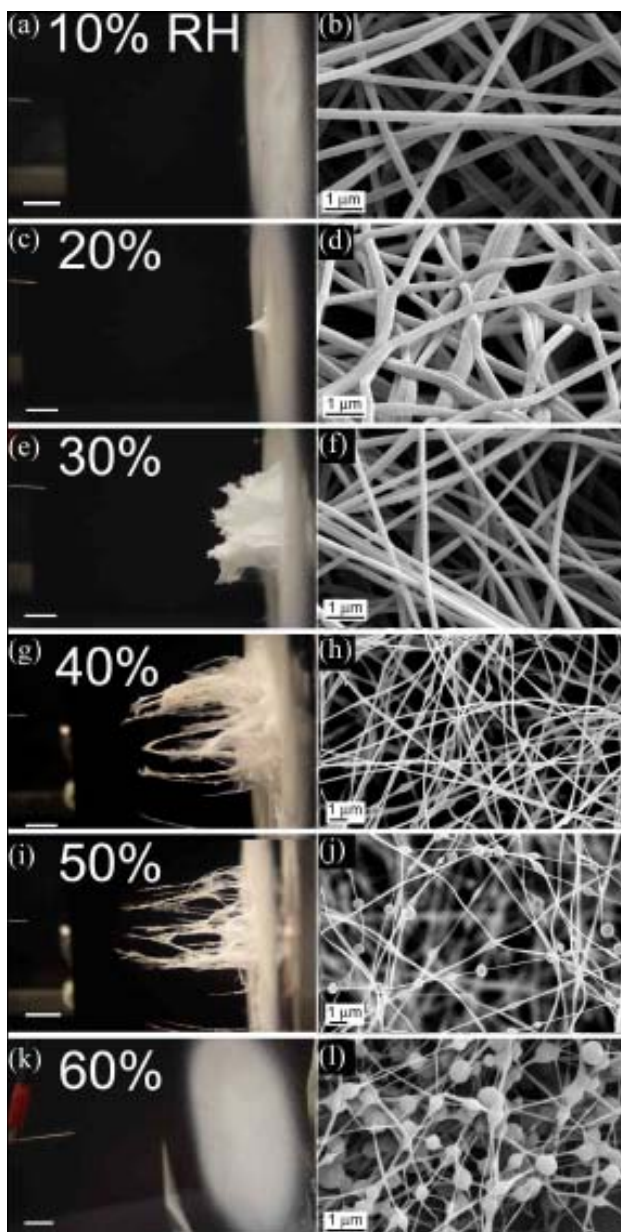


Figure 5.6. Photographs (a, c, e, g, i, k) and SEM micrographs (b, d, f, h, j, l) of electrospun mat structures and nanofibers, respectively, prepared at six different relative humidity conditions by electrospinning an alginate – PEO – F127 (10.6:0.8:1.5 wt %) solution. Scale bars on photographs are 2 cm.

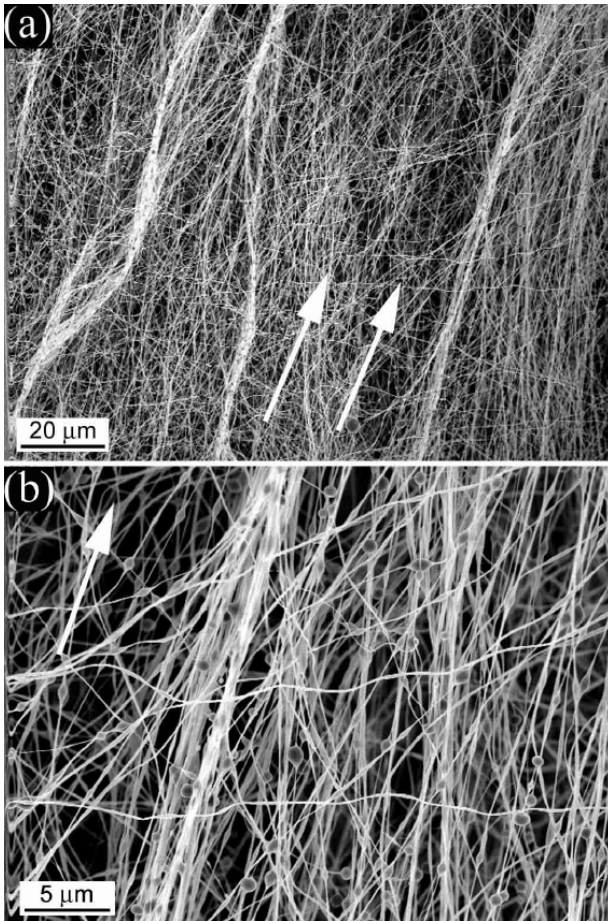


Figure 5.7. SEM micrograph of section of horizontal ‘strand’ on 3D electrospun mat (from Figure 5.4g), prepared by electrospinning alginate – PEO – F127 (10.6:0.8:1.5 wt %) at 40% RH. Arrows indicate the direction of the applied electric field.

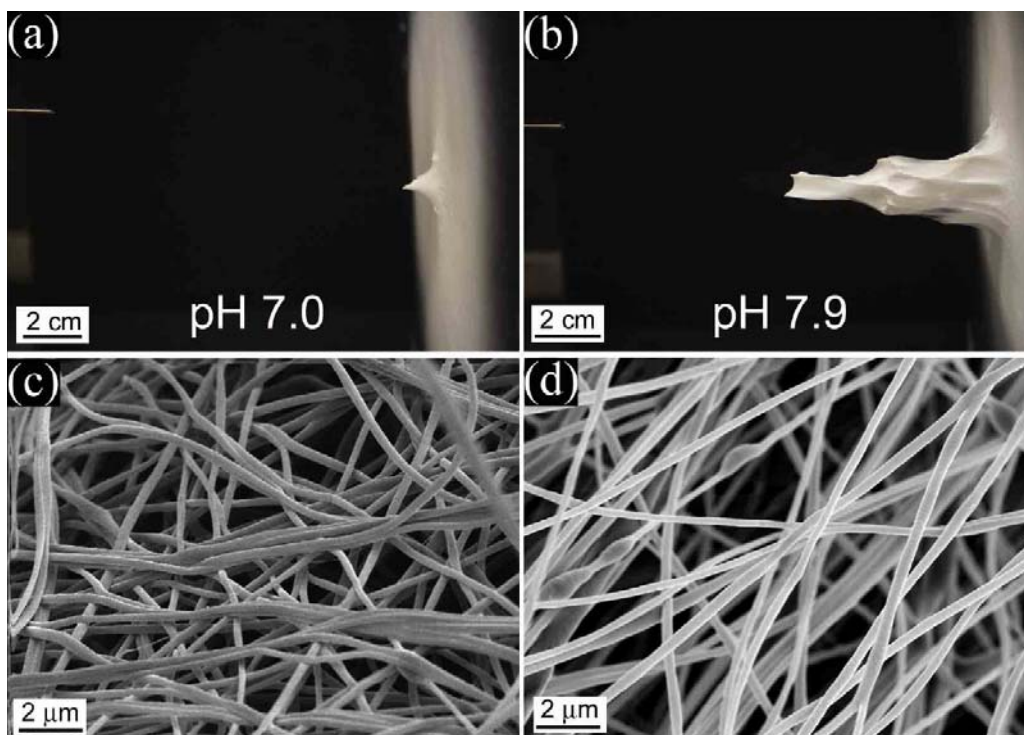


Figure 5.8. Photographs and SEM micrographs of mat and fibers electrospun from solutions containing alginate – PEO – F127 (10.6:0.8:1.5 wt %) at pH 7.0 (a, c) and pH 7.9 (b, d). (20% RH)

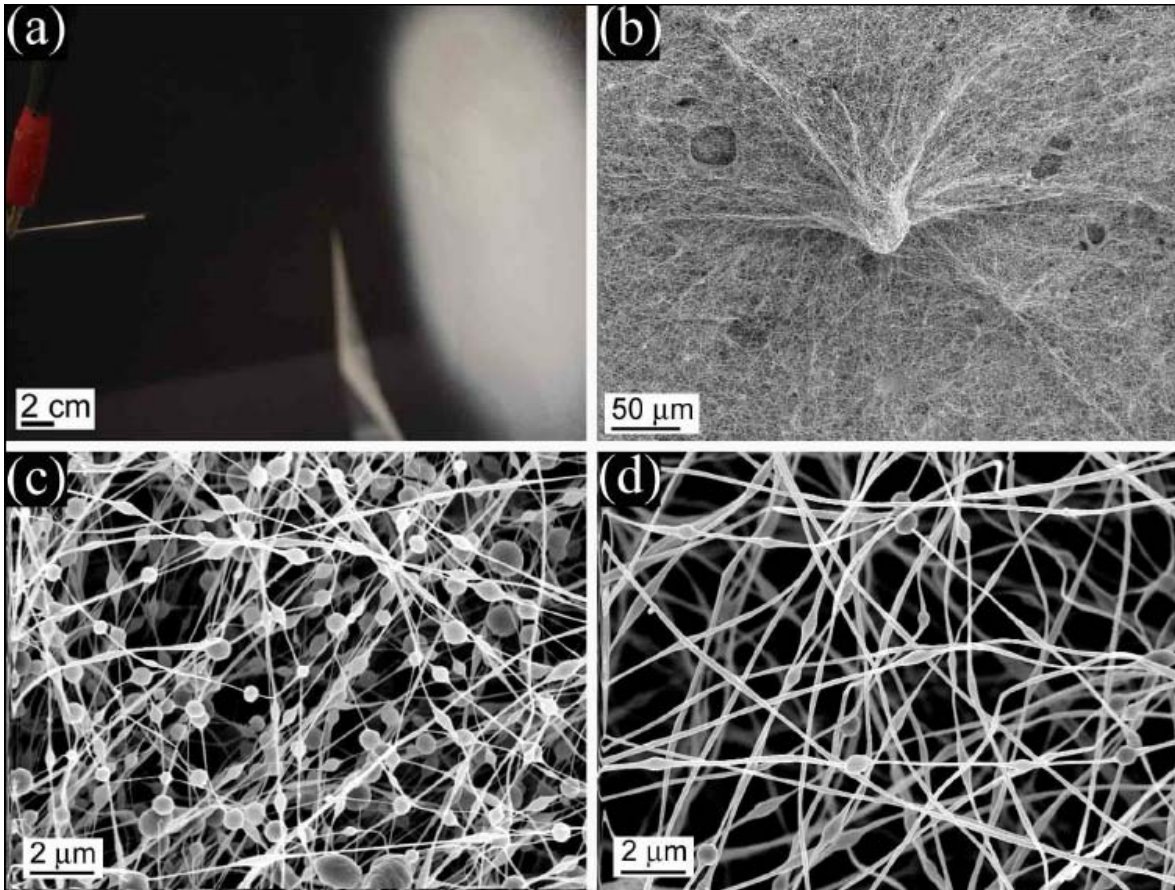


Figure 5.9. Photograph (a) of electrospun mat with 2D visual appearance prepared from surfactant-free solution containing alginate – PEO (10.6:0.8 wt %) at 40% RH. SEM micrographs of peaks on mat surface (b) and beaded nanofibers (c) prepared from the surfactant-free solution. SEM micrograph of nanofibers (d) prepared from the alginate – PEO solution containing Pluronic F127 surfactant (1.5 wt %).

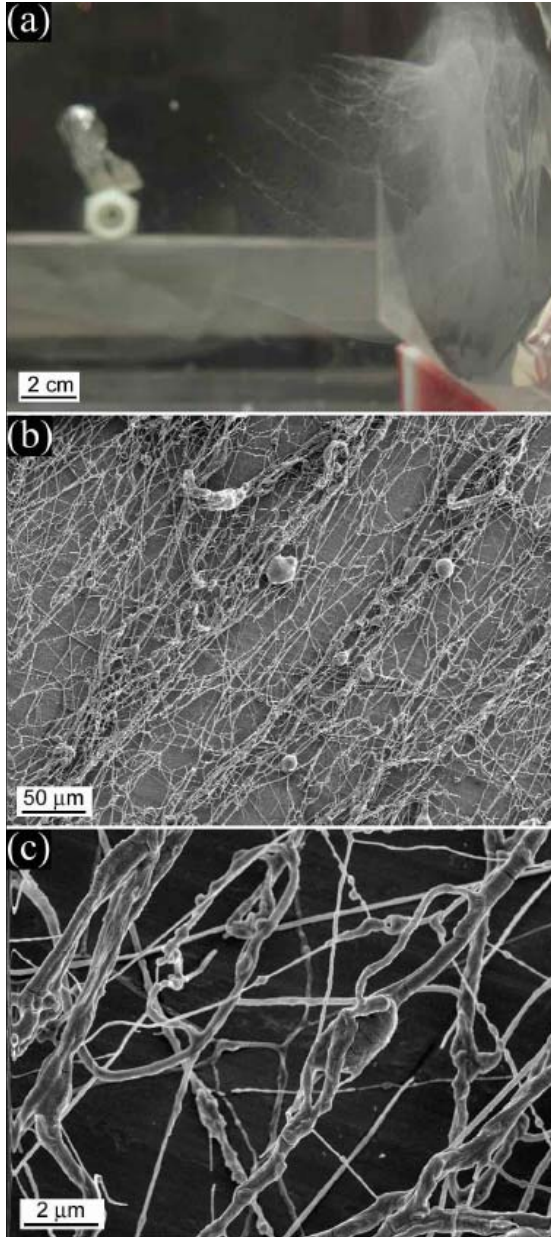


Figure 5.10. Photographs and SEM micrographs of web-like mat and fibers electrospun from PEO – NaCl – F127 solutions (5.0:1.0:1.5 wt %).

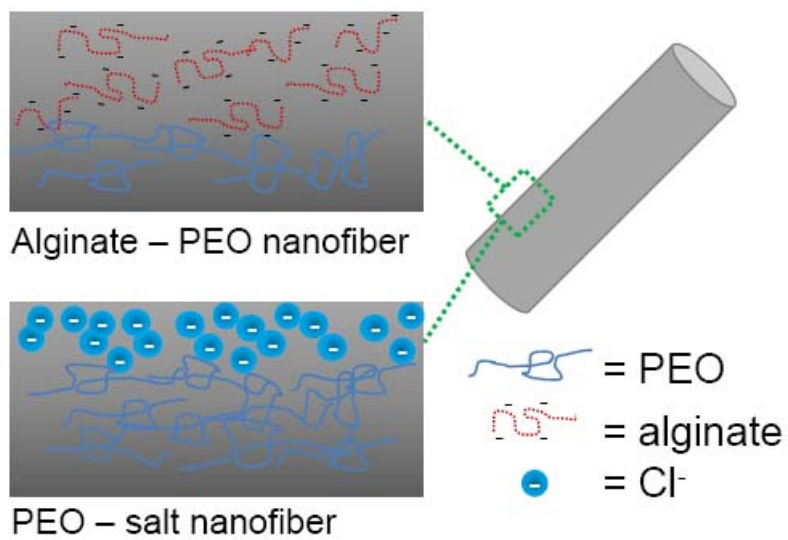


Figure 5.11. Diagram depicting distribution of negatively-charged polymers (alginate) and salts (Cl⁻) below surface of electrospun nanofibers.

CHAPTER 6

Real-time *in-situ* Rheology of Alginate Hydrogel

Photocrosslinking

Chapter 6 is essentially a manuscript by Christopher A. Bonino, Julia E. Samorezov, Oju Jeon , Eben Alsberg, and Saad A. Khan prepared for submission to *Soft Matter*.

Real-time *in-situ* Rheology of Alginate Hydrogel Photocrosslinking

Christopher A. Bonino¹, Julia E. Samorezov², Oju Jeon², Eben Alsberg^{2,3}, and Saad A. Khan^{5*}

¹*Department of Chemical & Biomolecular Engineering, North Carolina State University, Raleigh, North Carolina*

²*Department of Biomedical Engineering, Case Western Reserve University, Cleveland, Ohio*

³*Department of Orthopaedic Surgery, Case Western Reserve University, Cleveland, Ohio*

Abstract

The reaction dynamics of biodegradable, photocrosslinkable sodium alginate hydrogels are studied by *in-situ*, dynamic rheology. Alginate, chemically-modified with methacrylate groups, crosslinks by ultraviolet (UV) light exposure in the presence of a photoinitiator. The gel formation is monitored during UV irradiation from a light emitting diode (LED) bottom plate fixture on the rheometer. Material properties of the hydrogels, including gel points and relaxation exponent, are evaluated using the Winter-Chambon criteria. We also report a new, complementary method for determining the gel point from the reduction in sample strain at the onset of gelation, and inflection point of the strain curve. In

* corresponding author: khan@eos.ncsu.edu (email); 919-515-4519 (ph)

addition, the crosslinking dynamics and hydrogel moduli are altered by changing the UV irradiation intensities (3-15 mW/cm^2) and degree of methacrylation (5-25%). Dynamic rheological measurements of hydrogels as described in this paper are a potentially powerful tool to elucidate the dynamics of gelation and predict (optimal?) mechanical properties. This technique may aid in the design of polymer formulations with light-reactive chemical species, which have tunable properties that can be matched to a range of applications, including regenerative medicine.

6.1. Introduction

In the rapidly evolving field of biomedical engineering, hydrogels have exciting possibilities as functional biomaterials. Hydrogels are insoluble, three dimensional (3D) networks of crosslinked polymers that can be swelled by aqueous solutions and have customizable shapes, mechanical stability, and rate of degradation, making them promising materials for drug delivery and regenerative medicine.¹ Drugs and cells can be incorporated within hydrogels and released or delivered *in vivo* to specific targeted areas.² Of particular interest for *in vivo* applications are hydrogels made from naturally occurring polymers, due to their low toxicity and biodegradability.

Hydrogels of sodium alginate, a polysaccharide derived from brown algae have been used as tissue engineering scaffolds.³ Alginate hydrogels can form by crosslinking the biopolymer ionically with divalent cations (e.g. Ca^{2+})⁴ or chemically (e.g. glutaldehyde)⁵. While alginate hydrogels made by these two methods have shown promise, both crosslinking approaches also have drawbacks. Ionically-crosslinked alginate hydrogels are limited by their range of mechanical stability and uncontrolled rate of degradation.⁶ In addition, reagents used to chemically-crosslinked alginate hydrogels may have cytotoxicity concerns.⁷

An alternative crosslinking approach uses UV to initiate free radical polymerization, which is especially useful for biomedical applications. Hydrogels that are photocrosslinkable can be injected *in vivo* with cells⁸ and/or bioactive factors^{9, 10} to a target region (e.g. damaged tissue) and then crosslinked with brief exposure to UV light in the presence of a

photoinitiator. Furthermore, by varying the number of reactive groups, the degree of crosslinking of the hydrogels can be tailored to yield specific mechanical properties and degradation rates that resemble natural tissues and match desired cell proliferation rates, respectively.² Since tissues have a broad range of moduli (~1 kPa, liver to ~40 GPa, bone)¹¹, a material that can achieve a wide range of stiffness without significantly changing its chemistry will be useful to study effects of scaffold modulus on cell behavior. Further, such a material would be versatile enough for use as a tissue engineering scaffold for a variety of applications. Recently, light crosslinkable alginate hydrogels with customizable mechanical and degradation properties have been synthesized.¹² Alginate was made photocrosslinkable by coupling methacrylate groups to carboxylic acid moieties in the material backbone using carbodiimide chemistry. Hydrogels from methacrylated alginate (MAALG) are biodegradable and cells encapsulated in these hydrogels show good viability.¹²

While previous work has evaluated the mechanical properties of crosslinked MAALG hydrogels formed from alginate with a range of methacrylation, a systematic characterization of these properties during hydrogel formation has not been performed. This analysis is important because of the interplay between kinetics of crosslinking reactions and mechanical properties of the developing hydrogel. For example, as a solution gels and becomes more viscous, the reaction becomes limited by the diffusion of unreacted chemical species.¹³ In turn, identical solutions that form hydrogels with remaining unreacted crosslinking groups at the completion of UV exposure will have lower moduli than highly crosslinked gels. In this study, the alginate gelation reaction kinetics involve of a series of chemical reactions. The

reaction begins with the formation of free radicals by a photoinitiator that has been irradiated with UV light. The free radicals attack the methacrylate groups on the alginate and also form radicals.¹⁴ The alginate becomes crosslinked when two free radical methacrylate groups react to form a bond. (Figure 6.1.)

Dynamic rheology is an established technique for monitoring the kinetics of a photocrosslinking reaction. Changes in the rheological properties of the material reflect the formation and density of crosslinks.¹⁵ Material properties, such as the elastic (G') and viscous (G'') moduli, can be detected using small amplitude oscillatory shear, with minimal disruptions to the chemical reaction. In addition, the evolution of a photocrosslinking reaction can be monitored *in situ* using a specialized UV source fixture.¹⁶ With this fixture, sample rheology can be measured while the material is irradiated, which captures the transition from sol to gel. The dynamic moduli of the curing material can accurately predict the gel point, signifying the time at which networks span between the plates of the rheometer.¹⁵ The precise time when the onset of gelation occurs can be predicted using the Winter-Chambon criteria, shown by the following equations:¹⁷

$$G'(\omega) = S\Gamma(1-n)\cos\left(\frac{n\pi}{2}\right)\omega^n \quad (6.1)$$

$$G''(\omega) = S\Gamma(1-n)\cos\left(\frac{n\pi}{2}\right)\tan\left(\frac{n\pi}{2}\right)\omega^n \quad (6.2)$$

$$0 < n < 1 \quad (6.3)$$

$$0 < \omega < \frac{1}{\lambda_0} \quad (6.4)$$

$$\tan \delta = \frac{G''}{G'} = \tan\left(\frac{n\pi}{2}\right) \quad (6.5)$$

S is the gel stiffness, Γ is Euler's gamma function, n is the relaxation exponent, and ω is the oscillation frequency. Equation 4 denotes limits zero and $1/\lambda_0$, the inverse of the characteristic time of prepolymers at the onset of glassy behavior, where the power-law behavior is valid.¹⁸ At the gel point, the loss tangent, $\tan \delta$, is independent of frequency. Thus, curves of $\tan \delta$ for a material undergoing crosslinking measured at different frequencies will intersect at one point, corresponding to the gel point. For a polymer gel with relaxation exponent of 0.5, the gel point will correspond by the G'/G'' crossover on a time sweep.¹⁹

In this study we use dynamic rheology to study the crosslinking reaction of UV light crosslinkable, methacrylated alginate. MAALG macromers were reconstituted in cell culture media containing a water soluble photoinitiator, allowing for incorporation of cells and ready use as tissue scaffolds. The evolution of rheological material properties were monitored *in situ* using a UV photocuring bottom plate fixture with a light emitting diode (LED) radiation source. With this setup, the sample was irradiated uniformly while experiencing a constant oscillatory small-amplitude stress. To our knowledge, we are the first to report an *in-situ* rheological study on a photocrosslinkable polysaccharide. Rheological material properties, including G' , G'' , $\tan \delta$, and the complex viscosity, η^* , of MAALG were characterized during gelation. Gel points were determined from frequency sweeps at discrete times during the reaction, as well as using the intersection of $\tan \delta$ curves at different oscillatory

frequencies. The relaxation exponent, n , was estimated from the slope of the elastic modulus versus frequency curve near the gel point. In addition to the Winter-Chambon criteria, we report an alternative method for determining the gel point using sample strain. Making use of stress-controlled experiments, we can monitor the rapid reduction in sample strain that occurs near the gel point. While this method is not as precise as Winter-Chambon approach, it is useful for crosslinking systems with fast gelation kinetics with rapid increases in G' and poor G'' signals beyond the crossover. In addition, we study the effects of the degree of methacrylation on alginate gel points and moduli. Alginates with 5-25% methacrylation, corresponding to the percent of alginate monomers subunits with methylacrylate groups, were evaluated. Also, UV intensity was varied from 3 to 15 mW/cm² to explore its effect on gelation kinetics. This is important because UV light sources vary from lab to lab, which may lead to variations in hydrogel moduli and mechanical stability if gelation time is kept constant, regardless of actual UV intensity. Furthermore, we selected relatively low UV intensities in ranges that would be appropriate for hydrogels used to encapsulate cells and temperature-sensitive materials such as bioactive factors. UV intensities much greater than 15 mW/cm² may lead to detrimental temperatures for cells due to the exothermic effects of the polymerization.²⁰ Changing the degree of methacrylation, and UV intensity and exposure time are methods to manipulate the rate of gelation and gel moduli, and tailor the hydrogel mechanical stability and rate of degradation. Thus, these are important parameters to consider when forming hydrogel tissue scaffolds for biomedical applications.

6.2. Experimental Section

Materials. Photocrosslinkable alginate (5-25% (actual) methacrylation, (10-45%, theoretical)) was prepared by a reaction scheme as described previously.¹² Irgacure D2959 photoinitiator and Dulbecco's Modified Eagle Medium with low glucose (DMEM) were used as received from Sigma Aldrich (St. Louis, MO).

Methods. *Preparation of solutions.* Solutions of the photocrosslinkable alginates were prepared by dissolving the photoinitiator Irgacure D2959 (0.05% w/v) and methacrylated alginate (2% w/v) in DMEM. Solutions were kept at 4°C in the dark to prevent sample degradation and/or reaction prior to measurements.

Rheological measurements. Rheological experiments were performed with a TA Instruments (New Castle, DE) G2 stress-controlled rheometer with UV photocuring bottom plate fixture with temperature controlled bath. Light emitting diodes (LEDs) within the fixture emitted UV radiation at 365 nm wavelength through a clear acrylic, UV transparent window. Radiation intensity was fixed throughout each experiment and values of 3-15 mW/m² were investigated, which was calibrated using a radiometer. A 20 mm aluminum parallel plate was used for the top geometry and the gap was maintained at 0.5 mm. All measurements were made at 25°C, at least three hours and less than 24 hours after preparing solutions. Solution gelling behavior was monitored using dynamic oscillatory time and frequencies sweep experiments. Samples were exposed to UV radiation the start (t=0) of each time sweep. Throughout the time sweep, constant oscillations were applied at a fixed frequency (1, 5, or 10 rad/s) with a stress of 0.05 Pa, which was in the linear viscoelastic

(LVE) regime of the material. UV exposure was terminated at the completion of each time sweep, after which frequency sweep experiments were performed. Rheological measurements were duplicated to ensure repeatability within $\pm 5\%$ error.

6.3. Results and Discussions

6.3.1. Evolution of Crosslinking Reaction

Steady state and dynamic rheology was employed to study alginate gelation kinetics. Prior to UV exposure, the solutions were liquid-like, with a zero shear viscosity on the order of magnitude of the solvent, $\sim 0.007 \text{ Pa}\cdot\text{s}$. (Figure 6.2.) However, the solution viscosity increased by several orders of magnitude after UV photocrosslinking. Because steady shear rheology can break down the structure of a sample, small amplitude oscillatory experiments were used to monitor the crosslinking reaction *in situ*. The evolution of the elastic (G') and viscous (G'') moduli for alginate with 11% methacrylation are shown in

Figure 6.3. The moduli were measured as a function of frequency after exposure with 5 mW/cm^2 UV radiation. G'' was an order of magnitude greater than G' at low frequencies after exposure for 900 s (15 min) and both moduli were frequency dependent, indicating a pregel. After 1200 s (20 min) the sample was past the gel point, with G' and G'' near parallel and on the same order of magnitude. The value of n , the relaxation exponent for the gel, is ~ 0.5 , which was approximated from a power law relationship ($G', G'' \sim \omega^n$) on the data

beyond the gel point. After 1800 s (30 min) the sample was highly crosslinked, as G' became independent of frequency and more than two orders of magnitude greater than G'' .

The transition from sol-to-gel can also be shown from plots of η^* versus frequency. The appearance of the η^* curves changed as the crosslinking reaction evolved. (Figure 6.4) After 900 s, the slope was zero at low frequencies and then became shear thinning. In comparison, the η^* curves were shear thinning in all frequencies after 1200 and 1800 s exposure time, with slopes of -0.52 and -1.01, respectively. A decrease in dynamic viscosity can indicate the material is a postgel or solid, which confirms the onset of gelation as predicted by G' and G'' in Figure 6.3.²¹ In addition, the relaxation exponent of the gel can be estimated from the slope of the complex viscosity at the gel point, $\eta^* \sim \omega^{n-1}$. The η^* curve after 1200 s of exposure and within 100 s of the G'/G'' crossover has a slope of -0.52, and relaxation exponent ~ 0.5 , which is consistent with the value obtained from the frequency plots near the gel point in Figure 6.3. The relaxation exponent is indicative of the gelation with large, linear flexible molecules.¹⁵

Another representation of the crosslinking reaction is shown as a function of time with a constant oscillation frequency (1 rad/s). (Figure 6.5.) The sample was irradiated over the duration of the experiment ($t \geq 0$). G'' exceeded G' at the early stages of the free radical polymerization, as the sample was a pregel. However, G' surpassed G'' after 1100 s (18.3 min), near the gel point, and the elastic behavior of the sample was dominant for the duration of the experiment. Near this time point, a network of crosslinks formed between the two parallel plates on the rheometer. The G'' signal falls off after the gel point, indicating the

sample behaved like a highly elastic solid and viscous liquid character of the sample was difficult to detect. As the crosslinking reaction progressed, the reaction rate decreased, as indicated by the decrease in slope of the G' curve (~ 1300 s). The decrease in reaction rate was attributed to autodeceleration, caused by diffusion limitations of the unreacted groups in the increasingly viscous media.¹³ The elastic modulus increased by four orders of magnitude over the course of the reaction, revealing the complex and morphological nature of the material. The formation of methacrylate bonds in crosslinked alginate hydrogels resulting from UV irradiation was verified by ^1H NMR and reported previously.¹²

6.3.2. Gel Point

The versatile dynamic rheological characterization produced additional information about the crosslinking reaction and gel material properties. The sample gel point is determined using the Winter-Chambon criteria by evaluating time sweeps at different frequencies. Figure 6.6 shows time sweeps for alginate with 11% methacrylation (MAALG-11) with 5 mW/cm^2 radiation intensity; $\tan \delta$ curves for frequencies 1, 5, and 10 rad/s intersect ~ 1100 s, which corresponds to the gel point. The FTMS method was not used since the stress was controlled instead of the strain. The apparent relaxation exponent of the gel is approximately 0.5, which was estimated from Equation 5 using $\tan \delta$ value at the gel point. When evaluating the collective efforts for obtaining n at the gel point, including dynamic moduli, complex viscosity, and $\tan \delta$ methods, we estimate that the n value is ~ 0.5 ,

which is indicative of linear, flexible polymers, such as the methylacrylated alginate from our study.¹⁵ The gel point for polymer gels with $n \sim 0.5$ can be conveniently approximated from G'/G'' crossover in time sweeps.

We identified another method to characterize the onset of gelation. The sample strain was monitored over the evolution of the crosslinking reaction, exploiting the fixed stress dynamic experiment. This new approach is advantageous for reaction systems, such as ours, with a narrow window for the $\tan \delta$ curves from a rapid change in modulus and poor G'' signal beyond the gel point. Curves of % strain versus time are plotted at the same three frequencies from the previous section (1, 5, 10 *rad/s*). (Figure 6.7a, b.) Near the onset of gelation, the sample strain rapidly decreases due to an increase in modulus. Interestingly, the inflection point of the strain plot at 1 *rad/s* corresponds to the gel point (~ 1100 s). (Figure 6.7b.) We believe that the occurrence of the minimum slope for the strain is related to the spike in zero shear viscosity at the gel point.¹⁵ While our inflection point method can predict the gel point at 1 *rad/s*, this is not viable for higher frequencies. At 5 and 10 *rad/s*, the strain curve reaches a maximum before decreasing, and display inflection points beyond the gel point. Further studies to investigate the peak strain appearance are ongoing. While the inflection point method was limited at 2 of 3 frequencies for this sample, we find that the method accurately predicts gel points for the majority of the samples and conditions investigated that were evaluated at 1 *rad/s*. (See next sections.) Although this method cannot predict the gel point to the accuracy and versatility of the $\tan \delta$ method, we believe

that this is an interesting, complementary approach that can be applied to indicate the crosslinking reaction dynamics using a stress-controlled rheometer.

6.3.3. Varying UV Intensity

The kinetics of gelation for photocrosslinkable alginate can be manipulated with UV intensity. The rate of gelation can affect the gel mechanical properties. In turn, the gel properties influence cell proliferation, migration, and differentiation on gels used as tissue scaffolds.^{8, 22, 23} Furthermore, past studies (e.g.⁸) with UV curable systems commonly report time to gelation at one UV dosage. However, variability in UV sources between laboratories may cause repeatability concerns over the extent of the crosslinking. In our study, the rheometer's bottom plate with built-in UV light source is capable of easily altering the irradiation level and is ideal for evaluating the effects of changing UV intensity. Figure 6.8 a shows time sweeps for MAALG-25 as a function of UV intensity. The gel point varies from 354 to 1470 s by reducing radiation levels from 15 to 3 mW/cm^2 . The relationship between UV intensity and crossover time is plotted in Figure 6.8b. A line fit to the experimental data shows a power law dependence, $I \sim t_c^{-0.85}$, which is in agreement with a relationship previously reported with a different crosslinking reaction (i.e., urethane-based thiols).¹⁶ Decreasing UV intensity reduces the number of free radicals formed by the photoinitiator, which also reduces rate of photocrosslinking. The effect of UV intensity on gelation is also apparent when comparing the shape of the elastic moduli curves. In samples with 10 and 15 mW/cm^2

exposure, G' increases by two orders of magnitude within ~ 200 s after the gel point. The rapid change suggests that there is a surplus of reactive species dispersed throughout the sample at the onset of gelation that continue to react as the material transitions to a highly crosslinked gel. In comparison, the elastic moduli of the samples with 3 and 5 mW/cm^2 of exposure increased at a slower rate, and did not approach the same modulus (~ 5000 Pa) after 1800 s of monitoring the samples. When scaled with the crossover time, the curves collapse to one master curve at the early stages of gelation. (Figure 6.8a inset.) However, beyond the gel point ($t/t_c \sim 1$), the data deviate from one master curve, which indicates that the hydrogel formation mechanism is intensity dependent. While UV intensities less than 5 mW/cm^2 were capable of initiating the crosslinking reaction in MAALG-25, the concentration of available free methacrylate radicals at the onset of gelation was not adequate to maintain the crosslinking reaction to the same degree as the higher UV intensities. Crosslinking increases the sample viscosity and reduces the mobility of free radicals in solution. Thus, the reactive species that form in the advance stages of the reaction may become trapped within the gel structure and unable to react.²⁴ This may explain why the growth rate of the moduli in samples exposed to lower UV intensities is less than, despite having identical concentrations of methacrylate groups and photoinitiator, as the samples with higher UV exposure.

As we discussed in the previous section, the inflection point ($\delta(\log strain)/\delta t = 0$) or the minimum slope in the strain plotted versus time can be used to identify the gel point. Shown in Figure 6.9, strain decreases at the onset of gelation for each UV intensity. The highest UV intensities (10, 15 mW/cm^2) yielded the greatest reduction in strain. As expected,

highly-crosslinked hydrogels will have smaller strains than weaker networks that were inducted by low UV intensities ($>10 \text{ mW/cm}^2$). As observed previously for a sample evaluated at 1 rad/s , the inflection points of the each strain curve matches t_c . Thus, the inflection point method is valid for alginate hydrogels with a range of crosslinking dynamics.

6.3.4. Varying Degree of Methacrylation

In addition to UV intensity, the degree of methacrylation is essential to material properties of photocrosslinkable alginate hydrogels, affecting their performance as tissue scaffolds. We have previously shown that degree of methacrylation correlates with the swelling and rate of degradation of the hydrogel.¹² In regenerative medicine, scaffold modulus and rate of degradation affect the formation of new tissues.³ In our study, we characterized the evolution of gelation for photocrosslinkable alginate with 5, 7, 11, 19, and 25% methacrylation. Compared to hydrogels made with varying UV intensity, hydrogels with differing degrees of methacrylation do not approach the same terminal moduli. (Figure 6.10a.) As expected, reducing the crosslink density of the hydrogel results in a lower modulus.

Since the elastic moduli did not reach to the plateau moduli in the time frames evaluated in this study, curve fits were applied to estimate the terminal moduli. The time sweeps were scaled by crossover times and fit using an empirical model developed by Cao et al.²⁵

$$G' = G'_{\infty} (1 - \exp[-\alpha (\frac{t}{t_c} - 1)^{\beta}]) \quad (6.6)$$

G'_{∞} is the plateau modulus, and α and β are fitting parameters. Shown in Figure 6.10b, model curves match well with the experimental data for time beyond the gel point ($t > t_c$). The plateau moduli estimates vary by three orders of magnitude with degrees of magnitude with 5-25% degree of methacrylation. If used as scaffolds, the moduli of the alginate hydrogels could match the stiffness of a wide range of tissue types, including liver, breast, or arterial wall tissues.¹¹

When comparing individual samples, the effects of methacrylation on rheological behavior vary. Two important properties of gels, the gel points and terminal moduli of each sample, are shown in Figure 6.10c.. The terminal moduli of the samples with the highest degree of methacrylation, MAALG-19 and 25, were at least one order larger than the other (MAALG-5, 7, 11) samples. Increasing the concentration of available reactive groups corresponds to a higher reaction rate and crosslink density in the termination of experiment. While the effects of degree of methacrylation on gel rheology were apparent when comparing MAALG-19 and 25 to other samples, the rheological behavior of these two samples has similarities. Specifically, they had similar gel points (530, 524 s) and comparable plateau moduli (6860, 4859 Pa), respectively.

The gelation times do not necessarily indicate the moduli of the fully crosslinked hydrogels, when comparing MAALG-5, 7, and 11. Gel points differ by up to 60 s between the samples, whereas the plateau moduli vary significantly. (Figure 6.10c.) The predicted

terminal moduli of MAALG-7 is half that of MAALG-11 (410, 846 Pa, respectively). Additionally, despite having the closest degrees of methacrylation of the samples investigated, MAALG-5 and 7 have stark differences. Specifically, the elastic and viscous moduli of MAALG-5 are much smaller than MAALG-7 (~ 7 Pa), and remain on the same order of magnitude after the gel point. Furthermore, MAALG-5 shows a clear G'' signal >50 s beyond the gel point. As a result of the low methacrylate concentration, the MAALG-5 forms a weak gel, displaying viscoelastic tendencies beyond the gel point. A weakly crosslinked hydrogel can be advantageous in biomedical applications when more rapid degradation would be beneficial.²⁶

As in the previous section, the inflection point method was applied to the alginates with differing degrees of methacrylation. (Figure 6.11.) Strain decreases at the onset of gelation for MAALG-7, 11, 19, and 25, and the inflection points, or minimum slope values, matches t_c . The one exception is MAALG-5, which reaches maximum strain prior to decreases, and is similar to strain curves at frequencies greater than 1 *rad/s* reported above. MAALG-5 formed a weak gel, which may have contributed to the deviation from the other samples.

6.4. Conclusion

In-situ, small amplitude oscillatory shear rheology is an effective tool for monitoring the crosslinking reaction of photocrosslinkable, methacrylated alginate hydrogels. The gel point was estimated using the Winter-Chambon criteria, which approximately matched the G'/G'' crossover. In addition, we identified an alternative approach to approximate gel points using the change in sample strain. For the majority of the samples we investigated, the minimum slope, or inflection point, of log strain as a function of time corresponded to the gel point. Studies that investigate the strain in other polymers undergoing crosslinking are ongoing. Furthermore, this study evaluated the crosslinking reactions of alginates with differing UV irradiation exposure intensities and differing degrees of methacrylation. UV intensity varied with gelation time by a power law relationship. The elastic moduli of alginates with varying degrees methacrylation were fit with an empirical model, which estimates the terminal moduli.

6.5. Acknowledgements

This work was supported by U.S. Department of Education Graduate Assistance in Areas of National Need (GAANN) Fellowship Program at North Carolina State University (CAB) and a National Science Foundation Graduate Fellowship (JES). We thank TA Instruments for the use of the UV-curing bottom plate fixture. We also thank Prof. Robert Prud'homme (Princeton) for helpful discussions.

6.6. References

1. Jagur-Grodzinski, J., Polymeric gels and hydrogels for biomedical and pharmaceutical applications. *Polymers for Advanced Technologies* **2009**, 21, (1), 27-47.
2. Peppas, N. A.; Hilt, J. Z.; Khademhosseini, A.; Langer, R., Hydrogels in biology and medicine: From molecular principles to bionanotechnology. *Advanced Materials* **2006**, 18, (11), 1345-1360.
3. Alsberg, E.; Hill, E. E.; Mooney, D. J., Craniofacial tissue engineering. *Critical Reviews in Oral Biology & Medicine* **2001**, 12, (1), 64-75.
4. Smidsrod, O.; Skjakbraek, G., Alginate as Immobilization Matrix for Cells. *Trends in Biotechnology* **1990**, 8, (3), 71-78.
5. Yeom, C. K.; Lee, K. H., Characterization of sodium alginate membrane crosslinked with glutaraldehyde in pervaporation separation. *Journal of Applied Polymer Science* **1998**, 67, (2), 209-219.
6. Lee, K. Y.; Alsberg, E.; Mooney, D. J., Degradable and injectable poly(aldehyde guluronate) hydrogels for bone tissue engineering. *Journal of Biomedical Materials Research* **2001**, 56, (2), 228-233.
7. Huanglee, L. L. H.; Cheung, D. T.; Nimni, M. E., Biochemical-Changes and Cytotoxicity Associated with the Degradation of Polymeric Glutaraldehyde Derived Cross-Links. *Journal of Biomedical Materials Research* **1990**, 24, (9), 1185-1201.

8. Schmedlen, K. H.; Masters, K. S.; West, J. L., Photocrosslinkable polyvinyl alcohol hydrogels that can be modified with cell adhesion peptides for use in tissue engineering. *Biomaterials* **2002**, 23, (22), 4325-4332.
9. Krebs, M. D.; Jeon, O.; Alsberg, E., Localized and Sustained Delivery of Silencing RNA from Macroscopic Biopolymer Hydrogels. *Journal of the American Chemical Society* **2009**, 131, (26), 9204-+.
10. Ifkovits, J. L.; Burdick, J. A., Review: Photopolymerizable and degradable biomaterials for tissue engineering applications. *Tissue Engineering* **2007**, 13, (10), 2369-2385.
11. Nemir, S.; West, J. L., Synthetic Materials in the Study of Cell Response to Substrate Rigidity. *Annals of Biomedical Engineering* **2010**, 38, (1), 2-20.
12. Jeon, O.; Bouhadir, K. H.; Mansour, J. M.; Alsberg, E., Photocrosslinked alginate hydrogels with tunable biodegradation rates and mechanical properties. *Biomaterials* **2009**, 30, (14), 2724-2734.
13. Bowman, C. N.; Kloxin, C. J., Toward an Enhanced Understanding and Implementation of Photopolymerization Reactions. *Aiche Journal* **2008**, 54, (11), 2775-2795.
14. Fisher, J. P.; Dean, D.; Engel, P. S.; Mikos, A. G., Photoinitiated polymerization of biomaterials. *Annual Review of Materials Research* **2001**, 31, 171-181.
15. Winter, H. H., *Physical and Chemical Gelation*. Elsevier: New York, 2001; Vol. 5, p 6991-6999.

16. Khan, S. A.; Plitz, I. M.; Frantz, R. A., Insitu Technique for Monitoring the Gelation of Uv Curable Polymers. *Rheologica Acta* **1992**, 31, (2), 151-160.
17. Winter, H. H.; Chambon, F., Analysis of Linear Viscoelasticity of a Cross-Linking Polymer at the Gel Point. *Journal of Rheology* **1986**, 30, (2), 367-382.
18. Derosa, M. E.; Winter, H. H., The Effect of Entanglements on the Rheological Behavior of Polybutadiene Critical Gels. *Rheologica Acta* **1994**, 33, (3), 220-237.
19. Winter, H. H., Can the Gel Point of a Cross-Linking Polymer Be Detected by the G' - G'' Crossover. *Polymer Engineering and Science* **1987**, 27, (22), 1698-1702.
20. Burdick, J. A.; Peterson, A. J.; Anseth, K. S., Conversion and temperature profiles during the photoinitiated polymerization of thick orthopaedic biomaterials. *Biomaterials* **2001**, 22, (13), 1779-1786.
21. Winter, H. H., Transient Networks: Evolution of rheology during chemical gelation. *Progress in Colloid & Polymer Science* **1987**, 75, 104-110.
22. Khatiwala, C. B.; Peyton, S. R.; Putnam, A. J., Intrinsic mechanical properties of the extracellular matrix affect the behavior of pre-osteoblastic MC3T3-E1 cells. *American Journal of Physiology-Cell Physiology* **2006**, 290, (6), C1640-C1650.
23. Pelham, R. J.; Wang, Y. L., Cell locomotion and focal adhesions are regulated by substrate flexibility. *Proceedings of the National Academy of Sciences of the United States of America* **1997**, 94, (25), 13661-13665.
24. Khan, S. A., Effect of Shear on the Gelation of Uv-Curable Polymers. *Journal of Rheology* **1992**, 36, (4), 573-587.

25. Cao, X. J.; Cummins, H. Z.; Morris, J. F., Structural and rheological evolution of silica nanoparticle gels. *Soft Matter* **2010**, 6, 5425-5433.
26. Alsberg, E.; Kong, H. J.; Hirano, Y.; Smith, M. K.; Albeiruti, A.; Mooney, D. J., Regulating bone formation via controlled scaffold degradation. *Journal of Dental Research* **2003**, 82, (11), 903-908.

Table 6.1. Properties of Alginate Hydrogel with Different UV Irradiation Levels

Intensity ^a (mW/cm ²)	t _c (s)	G', G''(t _c) (Pa)	t ₁₀₀ ^b (s)	t ₁₀₀ - t _c (s)
3	1470.5	1.8	2169.0	689.5
5	954.4	2.5	1350.7	396.3
10	523.8	5.8	735.0	211.2
15	353.8	4.7	503.5	149.7

^a Alginate with 25% methacrylation

^b t₁₀₀ is the time point at which the modulus is 100× greater than the modulus at the gel point

Table 6.2. Properties of Alginate Hydrogels with Varying Degree of Methacrylation

Degree of Methacrylation ^a	t_c (s)	G', G'' (Pa)	G'_∞ (Pa)
25%	524	5.8	6860
19%	530	4.6	4859
11%	719	6.3	846
7%	741	3.9	410
5%	775	0.3	7.3

^a UV intensity 10 mW/cm²

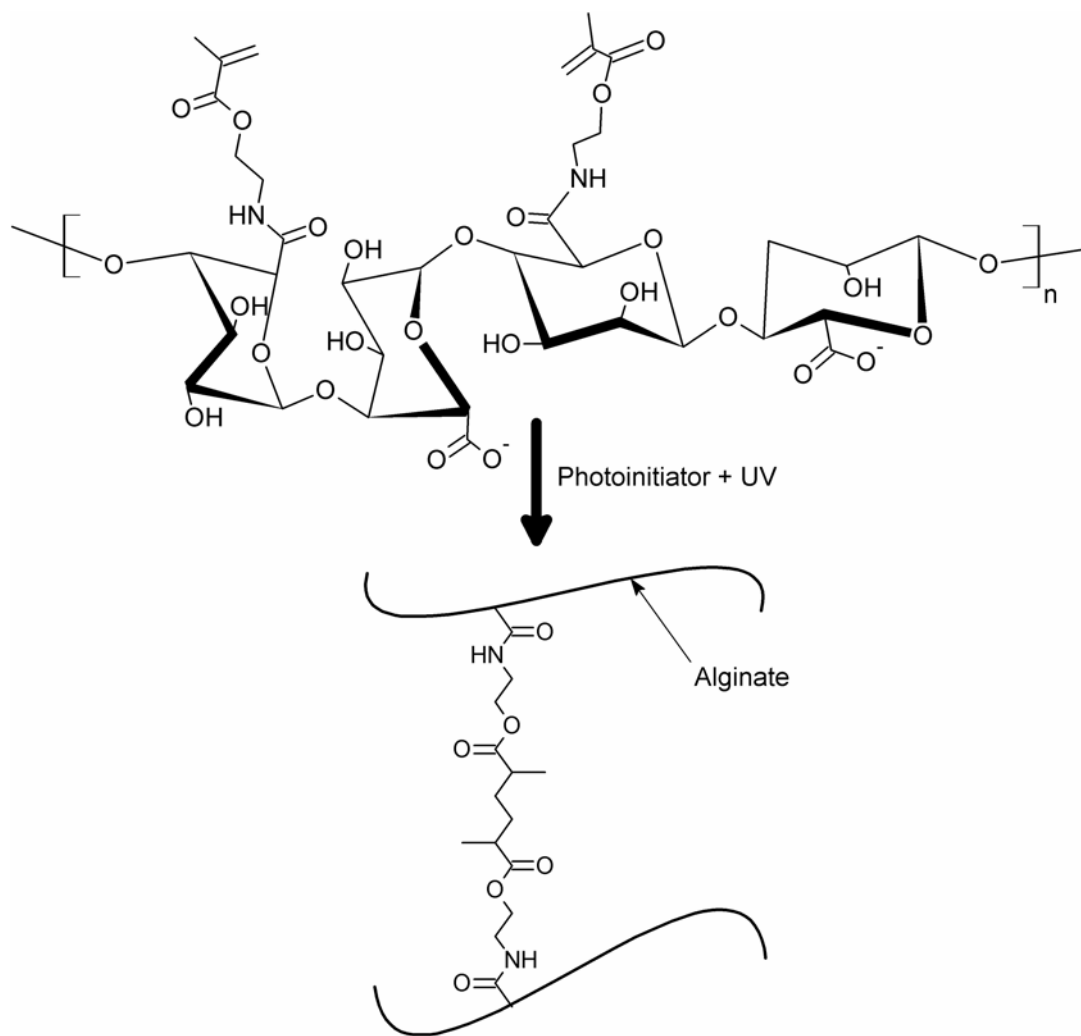


Figure 6.1. Scheme for photocrosslinking reaction of methacrylated alginate.

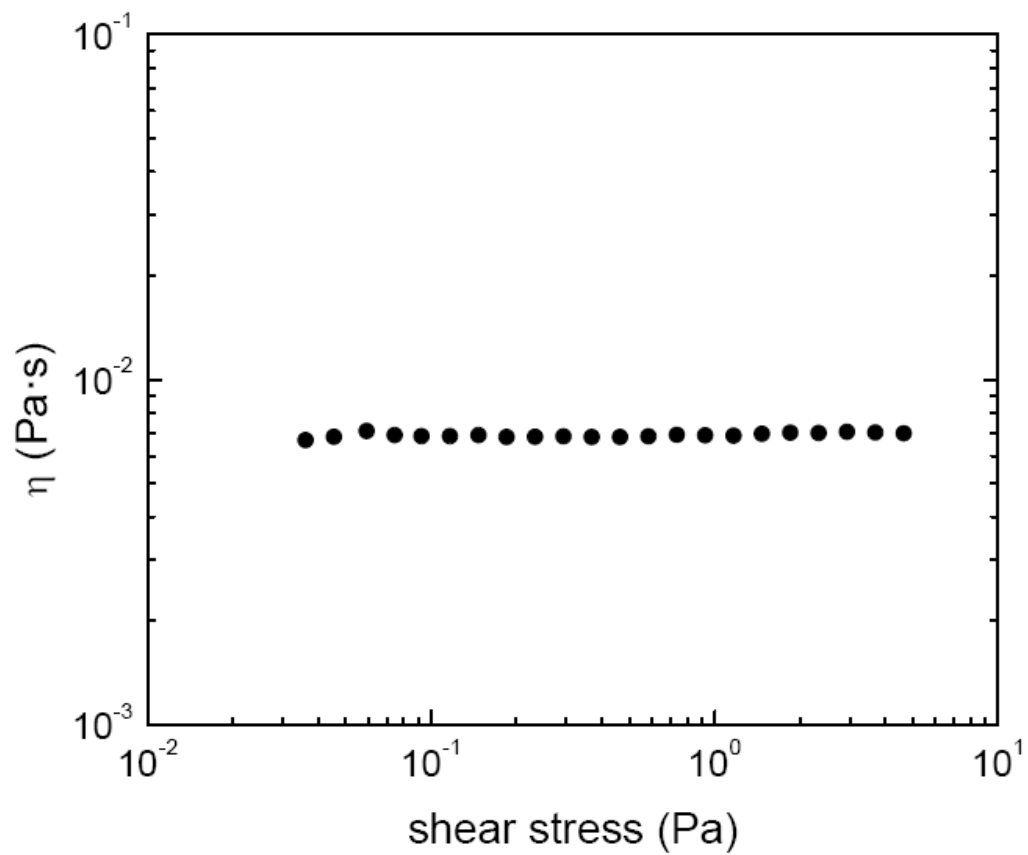


Figure 6.2. Steady shear viscosity profile of alginate solution prior to UV exposure. Zero shear viscosity is $0.007 \pm 0.0004 \text{ Pa}\cdot\text{s}$, obtained from averaging the first 10 data points in the Newtonian region.

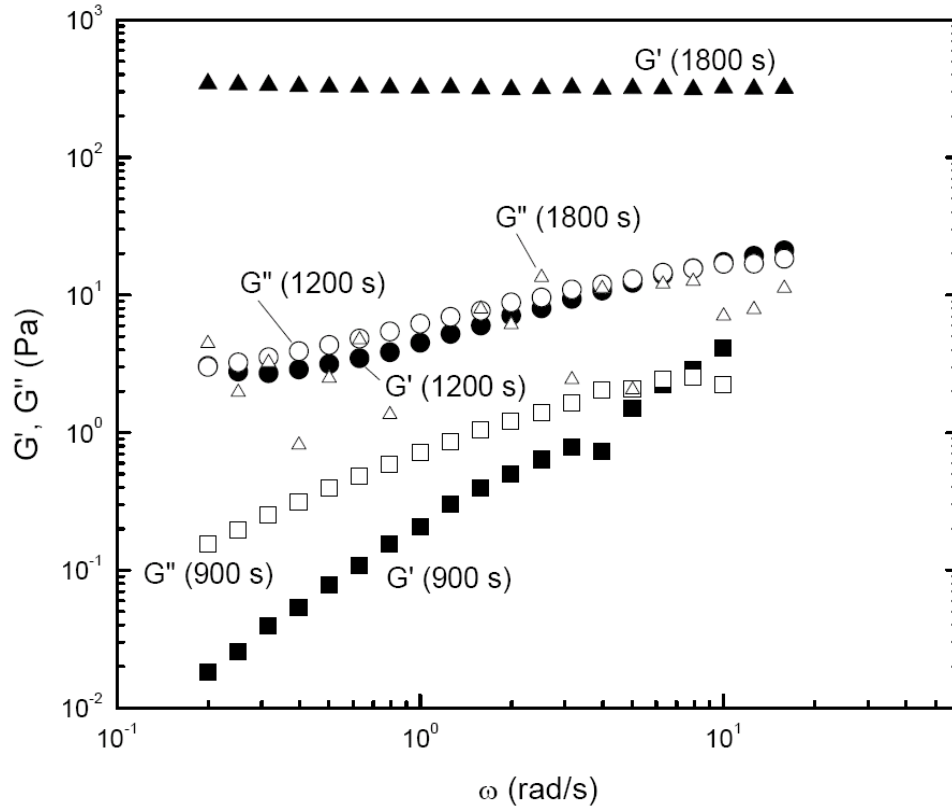


Figure 6.3. Elastic (G') and viscous (G'') moduli of photocrosslinkable alginate (11% methacrylation) as a function of frequency plotted after different exposure times with 5 mW/cm^2 UV radiation. At 900 s the solution is a pregel, with G'' is greater than G' at low frequencies and both moduli are frequency dependent. At 1200 s G' and G'' are parallel and have similar values across most frequencies, indicating the material is a postgel. After 1800 s G' is frequency independent and more than two orders of magnitude greater than G'' , indicating a highly crosslinked sample.

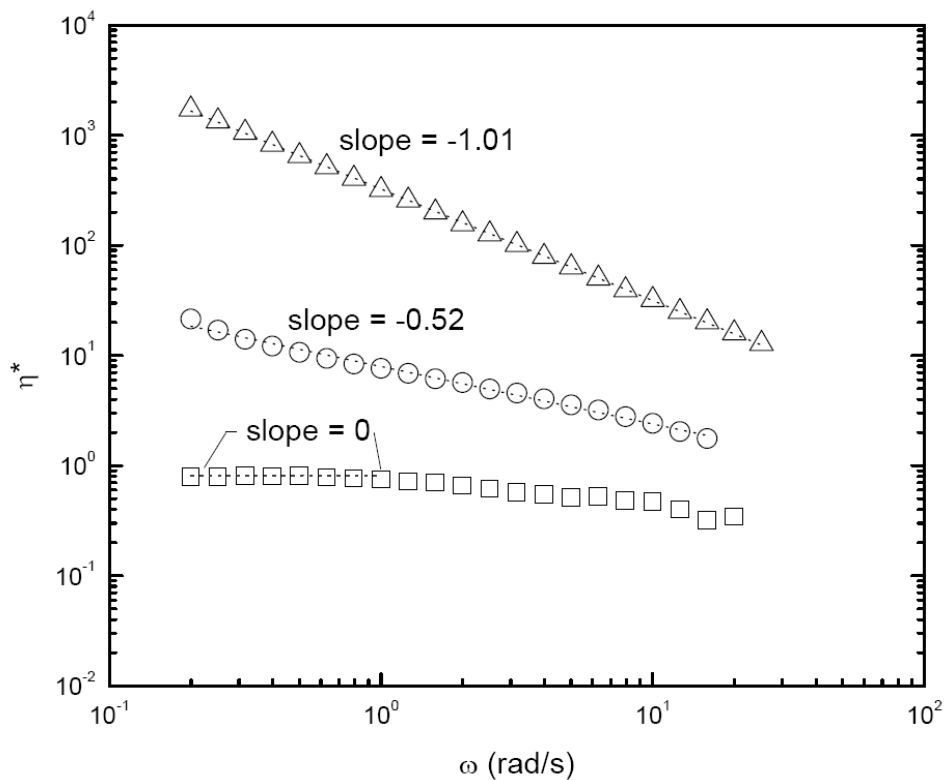


Figure 6.4. Dynamic viscosity of photocrosslinkable alginate as a function of frequency plotted after 900 (\square), 1200 (\circ), and 1800 (Δ) s of UV exposure with 5 mW/cm^2 UV radiation. Slopes at low frequencies decrease from 0 to -1, indicating the evolution of sol to gel.

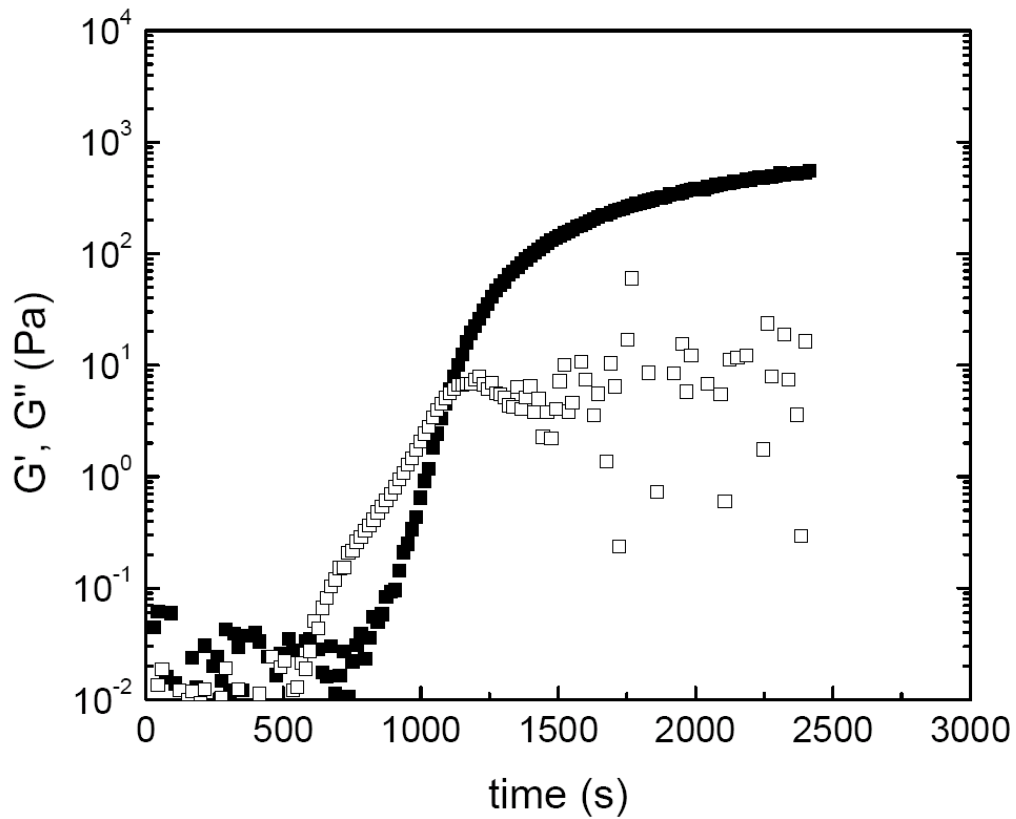


Figure 6.5. Time dependent rheology of alginate with 11% methacrylation. Beginning at $t=0$, sample was exposed to UV radiation with 5 mW/cm^2 intensity and 1 rad/s oscillation with 0.05 Pa stress. The elastic (G' , \blacksquare) and viscous (G'' , \square) moduli are plotted as a function of time. The gel point time (t_c) is $1080.8 \pm 32.2 \text{ s}$, estimated by the G'/G'' crossover, and the corresponding modulus is $11.2 \pm 4.0 \text{ Pa}$. (Means \pm standard deviations are reported, sample size = 6.)

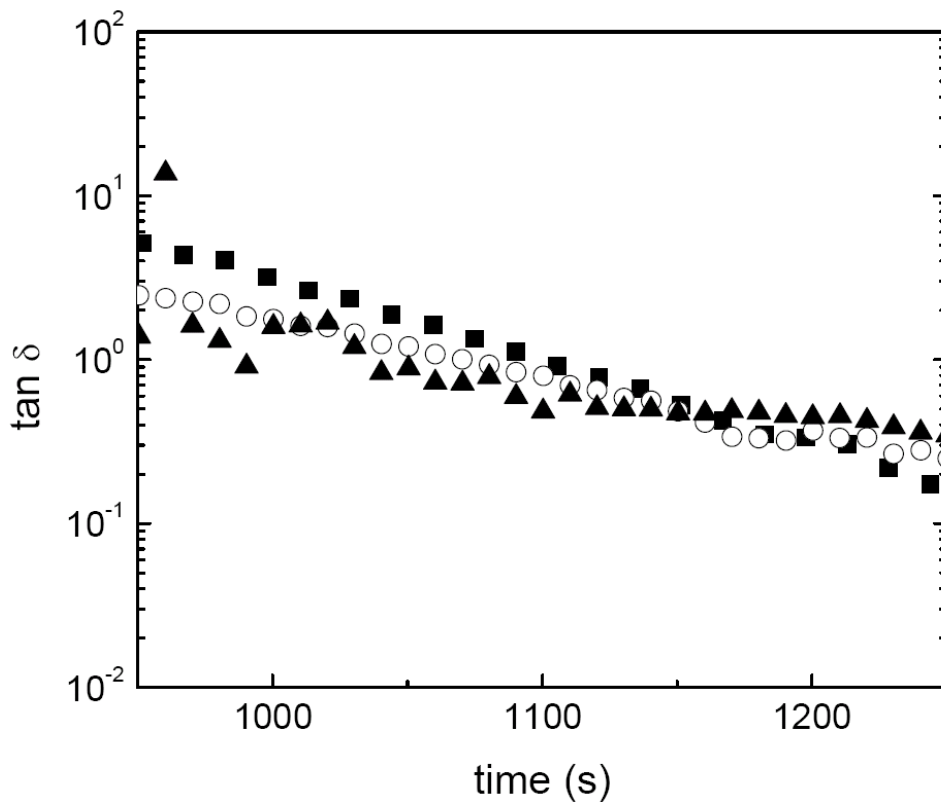


Figure 6.6. Evolution of tan delta for 11% methacrylated alginate solution with 5 mW/cm^2 UV irradiation using 1 (■), 5 (○), and 10 rad/s (▲) frequencies. The intersection point of the curves at $\sim 1100 \text{ s}$ indicates the gel point.

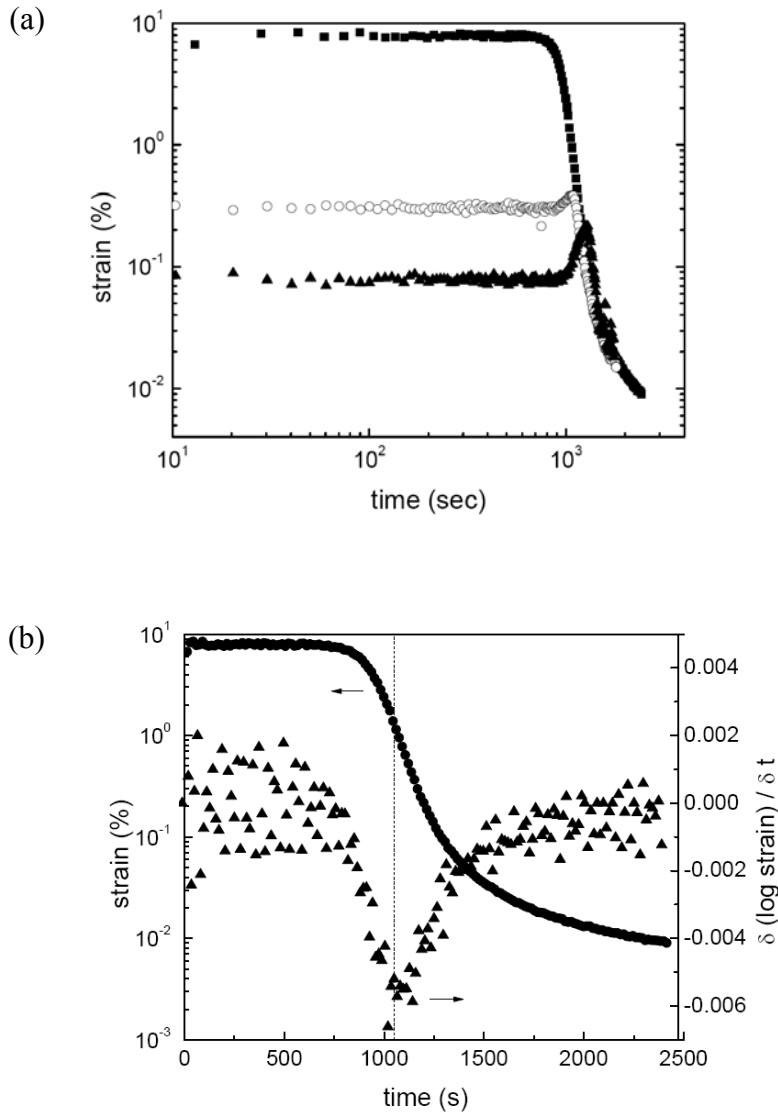


Figure 6.7 (a) Strain on MAALG-11 throughout the crosslinking reaction, shown at 1 (■), 5 (○), and 10 rad/s (▲) and a 0.05 Pa constant stress. Strain reduces at onset of gelation. (b) Strain (●) and derivative of log strain (▲) at 1 rad/s plotted as functions of time. The dashed line marks the inflection point of the strain curve, the minimum of the derivative, and corresponds to the gel point.

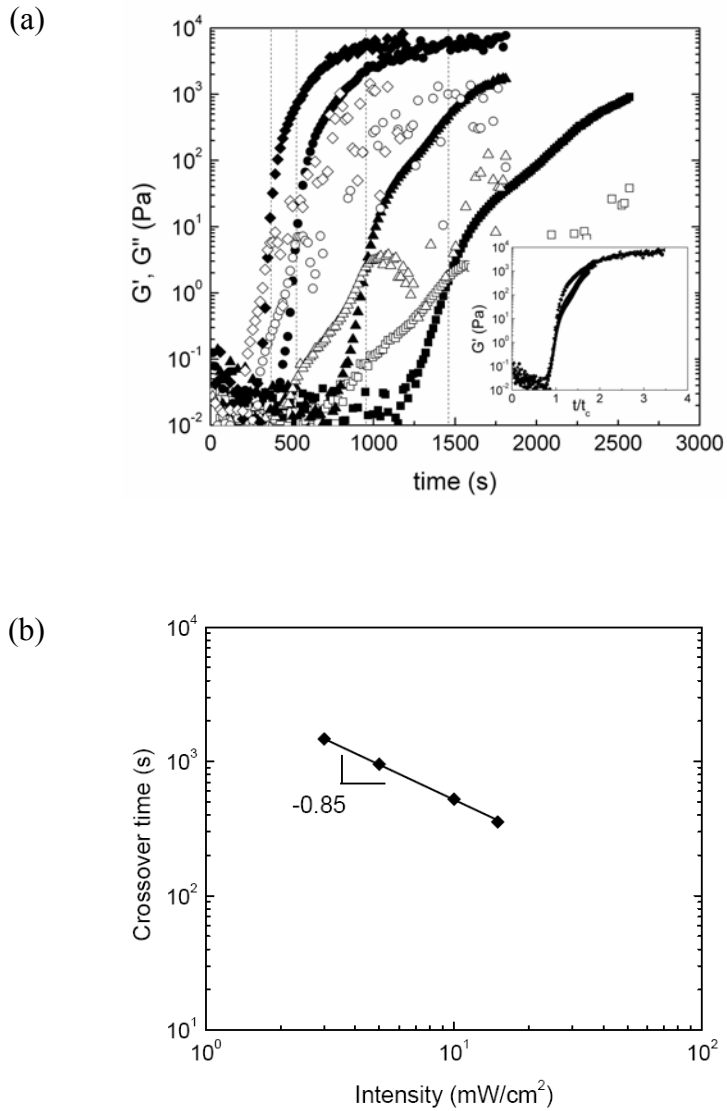


Figure 6.8 (a) Evolution of elastic and viscous moduli of alginate with 25% methacrylation at 3 (■□), 5 (▲△), 10 (●○), and 15 (◆◇) mW/cm² doses of UV irradiation. Dashed lines indicate G' , G'' crossover and gel points. Inset graph: the elastic moduli collapse when the dependent variable is scaled by the crossover time, as t/t_c . (b) Crossover times plotted versus UV intensity. The line is a power law curve fit.

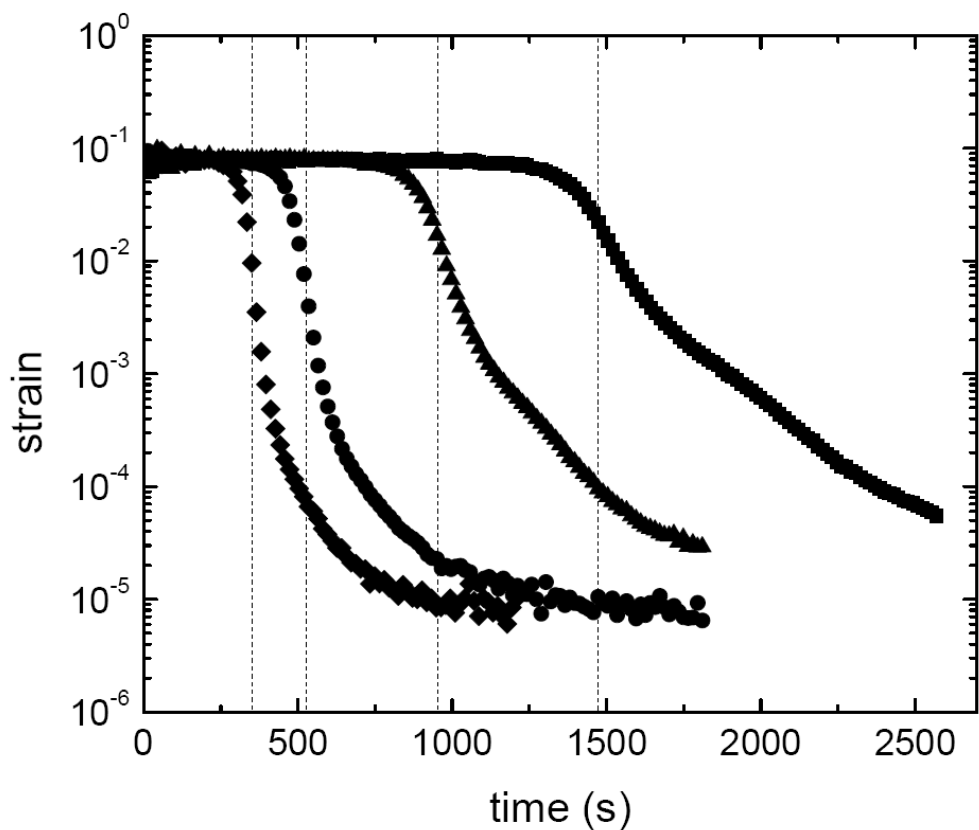
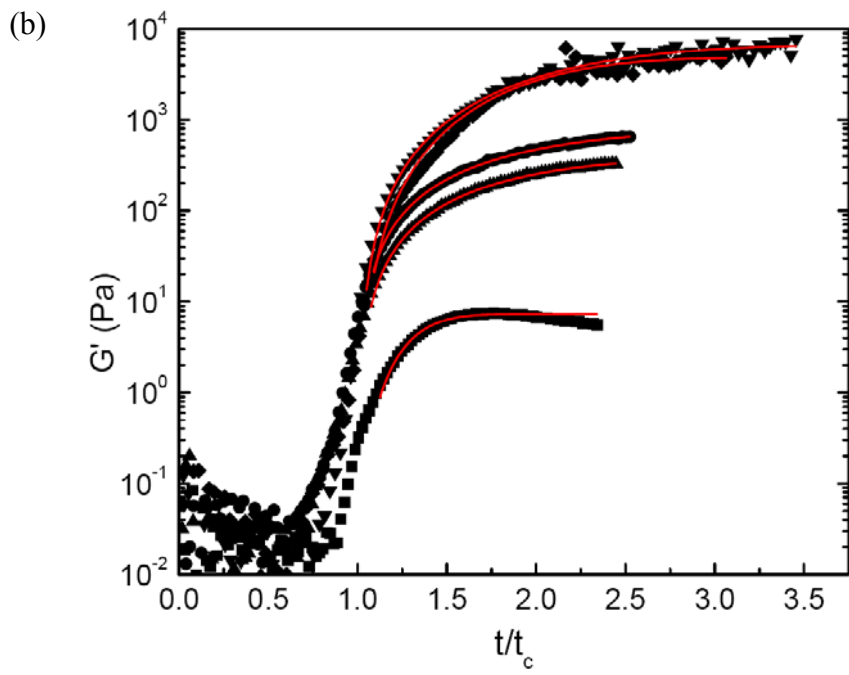
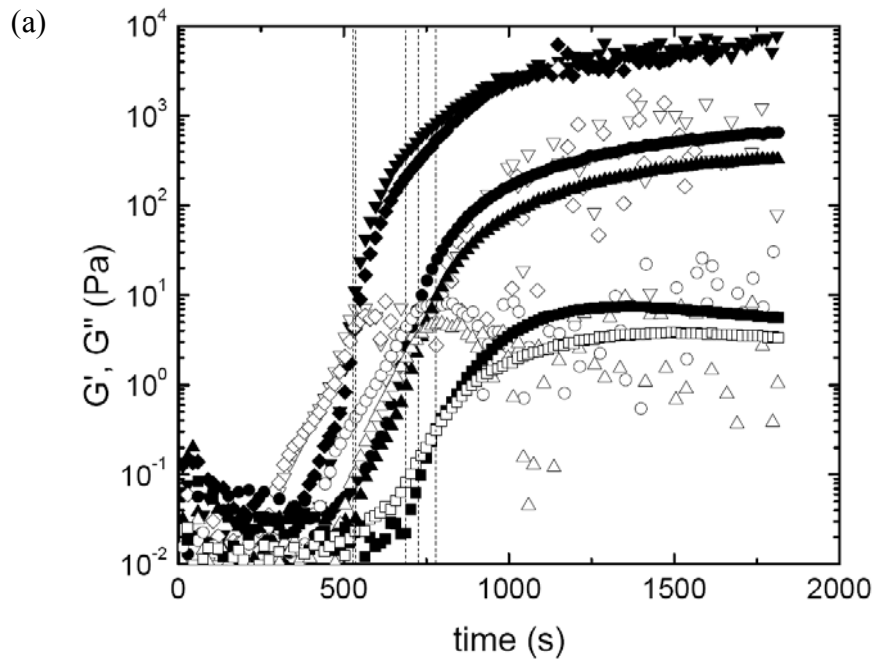
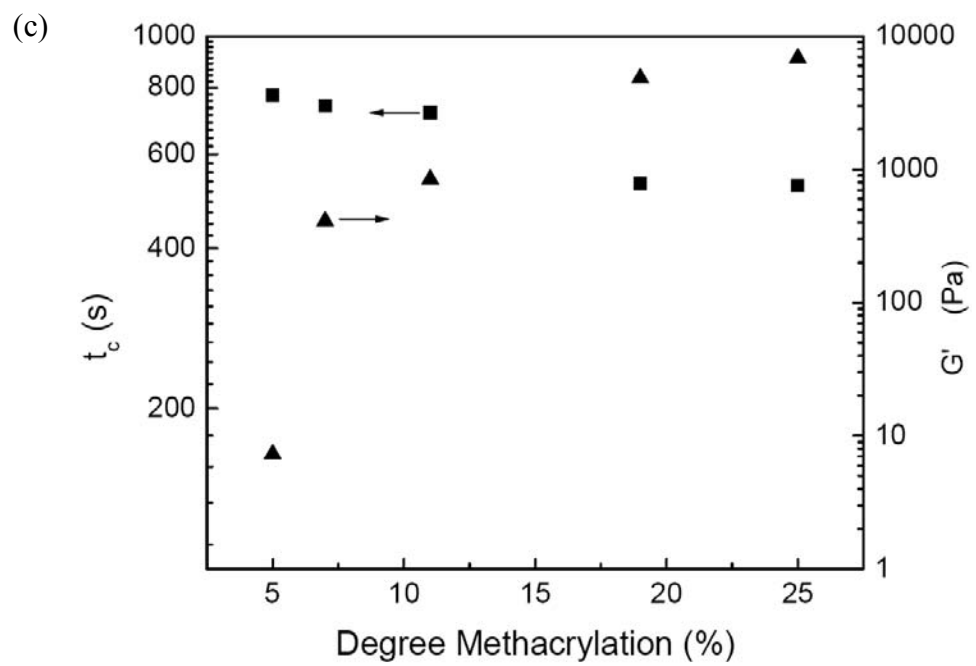


Figure 6.9. Sample strain as a function of time for 3(■), 5(▲), 10(●), and 15(◆) mW/cm^2 intensities. Dashed lines indicate gel points, which match with the inflection points of the experimental data.

Figure 6.10. (a) Elastic and viscous moduli as a function of time for photocrosslinkable alginate with 5(■□), 7(▲△), 11(●○), 19(◆◇), and 25% (▼, ▼) degrees of methacrylation. UV irradiation with 10 mW/cm² intensity was applied for t ≥ 0. Dashed lines mark crossover times, which are approximately the gel points. (b) Time sweeps scaled with crossover times and fitted. Solid red lines are curve fits from: $G' = G'_{\infty} \left(1 - \exp \left[-\alpha \left(t/t_c - 1 \right)^{\beta} \right] \right)$. For 5, 7, 11, 19, and 25% degrees of methacrylation, $G'_{\infty} = 7.3, 410, 846, 4859, 6860$ Pa; $\alpha = 8.1, 1.0, 0.8, 0.8, 0.6$; $\beta = 2.0, 1.5, 1.4, 2.2, 1.9$, respectively. (c) Crossover times and plateau moduli for alginate hydrogels with different degrees of methacrylation. Plateau modulus was estimated from curve fit.





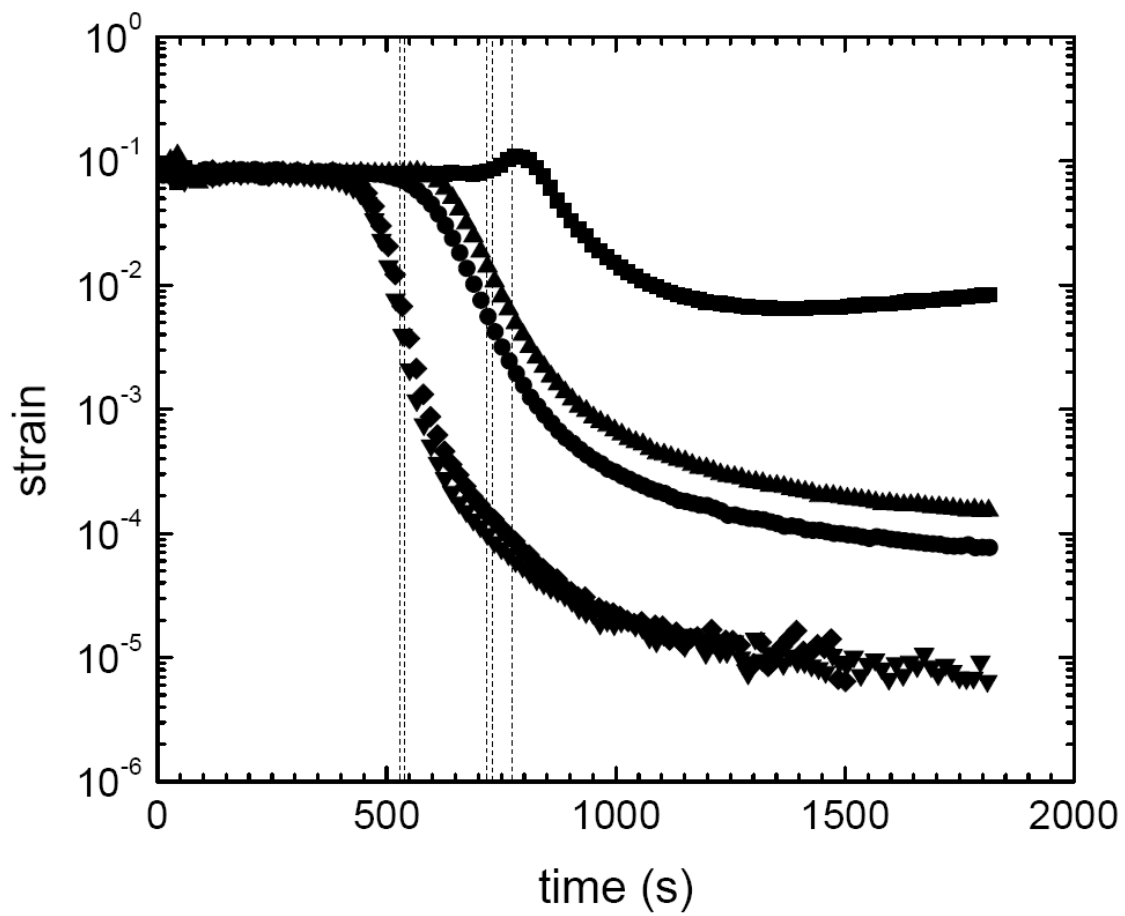


Figure 6.11. Strain as a function of time for photocrosslinkable alginate with 5 (■), 7 (▲), 11 (●), 19 (◆), and 25% (▼) degree of methacrylation. Dashed lines indicate gel points, which match the inflection points for 7, 11, 19, and 25%.

CHAPTER 7

Conclusions and Recommendations

Conclusions & Recommendations

7.1. Conclusions

In the preceding chapters we attempted to address two underlying themes:

- (3) To examine the interactions between the polymers and (nano)particles, surfactants, or salts.
- (4) To identify possible underlying mechanisms responsible for changes in the functional material when solution properties and/or process conditions are manipulated during fabrication.

In pursuit of these research themes, we investigated systems with electrospun nanofibers and hydrogels. Some of the major findings are summarized below.

Chapter 2: The surface groups on fumed silica particles contributed to rheological differences in solutions containing the particles and a polymer (*i.e.*, PAN). However, these differences had little effect on the electrospun fiber morphology or particle distribution. Furthermore, the electric field contributes to the particle distribution on the fiber surfaces. The surface distribution of the particles is an effective means to modify the wettability of the polymer fibers.

Chapter 3: Of the two methods to create composite tin oxide-carbon nanofibers that were investigated, a post-electrospinning soak treatment resulted in the highest tin loading. This was attributed to the higher solubility of the tin salt (tin sulfate) in the aqueous post-treat solution, than in the electrospinning solution with DMF. When evaluated as lithium ion battery anodes, nanofibrous mats containing tin oxide achieved better performances (*i.e.*, specific capacities) than carbon-only mats.

Chapter 4: Blending alginate with PEO and an ionic surfactant was an effective strategy to fabricate alginate-based nanofibers. In particular, the surfactant leads to a reduction in bead defects in the electrospun nanofibers, by reducing the surface tension. Furthermore, while PEO (M_w 600 kDa) is required for alginate to electrospin, the carrier polymer can be subsequently removed to yield alginate-only nanofibers following a soak and crosslinking treatment.

Chapter 5: Alginate-based nanofibers were electrospun into mats with three dimensional architectures. The 3D structures can be manipulated by changing the solution pH and relative humidity during electrospinning. The 3D formation is a product of like-charge repulsions between fibers, which have surfaces loaded with the charged polyelectrolyte, alginate. While the surface charges can lead to a self-supporting 3D structure, their distribution near the surface also has a significant role in the formation.

Chapter 6: The crosslinking reaction of photocrosslinkable alginate hydrogels was characterized using *in-situ* rheology. Gel properties, such as the gel point, were identified by applying the Winter-Chambon criteria. Furthermore, a new approach to monitor the change in sample strain was identified as another approach to monitor the gelation. The final hydrogel properties (*i.e.*, modulus) were tailored by manipulating the crosslinking density and UV exposure conditions.

7.2. Recommendations

In this thesis, we discussed the solution properties and process parameters that affected composite and blended electrospun nanofibers, and hydrogels. The scope of this research can be continued with extensions of the works discussed, as well as expanded into other similar systems.

7.2.1. Distribution of nanoparticles and/or other solution components within composite/blended nanofibers by manipulating particle conductivity, charged components, and electrical field

Electrospun composite fibers containing conductive particles are of interest in applications such as wound dressings.¹ For example, silver nanoparticles on or underneath the surfaces of nanofibers have antimicrobial qualities.² However, the distribution of conductive particles within/on the nanofibers may be affected by the electric field. Kim *et al* reported aligned chains of gold nanoparticles within PEO nanofibers, which they attributed to the electric field.³ Additionally, Sun *et al* previously showed that the distribution of a polarizable polymer conjugate was preferentially distributed on PEO espun fiber surfaces, as a result of the applied electric field.⁴ Despite these finding, the literature lacks a thorough investigation of the effects of nanoparticle conductivity and charged solution components on distribution within electrospun nanofibers. Nanofibers electrospun from blended solutions

containing polymers (neutral or polyelectrolytes), surfactants (nonionic or ionic), nanoparticles (conductive, semi-conductive, or insulator) may have a variety of component distributions. The polarity of the electric field may also influence the nanofiber composition, as a function of its radial position. Thus, investigating how to fabricate composite electrospun nanofibers with distributions (surface or interior) tailored for specific applications would be interesting.

The above study would be appropriate for aqueous polymer solutions. However, another area of interest includes nanoparticle and polymer systems with non-water solvents (*e.g.*, DMF, toluene). This is because there are many applications for water-insoluble polymers (*e.g.*, PAN-based nanofibers as battery electrodes.) Recently a limited variety of nanoparticles that are stabilized in DMF solutions have been commercially available.⁵ Direct use of these nanoparticle solutions in electrospun solutions would eliminate additional process steps (*e.g.*, dialysis⁶) that are part of transferring nanoparticles from other solvents, such as water. Hence, a study that compares the distribution of conductive (*e.g.*, gold) and non-conductive (*e.g.*, silica) nanoparticles within a water-insoluble polymer (*e.g.*, PAN, polystyrene) would be worthwhile to investigate.

7.2.2. Composite graphitic carbon nanofibers containing nanoparticles by infiltration methods

Carbon nanofiber mats used as Li-ion battery anodes reported in this thesis (Chapter 3) and other works (*e.g.*, ^{7, 8}) have potential benefits, as well as limitations, which can be related to their carbon structures. In most cases, PAN is converted to carbon by a series of heat treatments, typically 600-1100°C in inert atmosphere. The carbon formed in these conditions has a disordered structure.⁹ One advantage of using disordered carbons as lithium ion battery anodes is their high specific capacity, as compared to graphitic carbons (the traditional anode material in commercial batteries). While mechanism for the improved capacities in disordered carbon is not fully understood, researchers have proposed that cavities within carbon structures can occupy lithium, in addition to the lithium intercalated between graphene plates (as reviewed by Kaskhedikar and Maier¹⁰). However, this disordered structure may have drawbacks during lithium deinsertion from the material. (Figure 7.1) During a discharge cycle, the profile of a disordered carbon curve can have a gradual slope with increasing applied voltage towards its final discharge capacity. A deviation of the discharge curve profile from the charge curve can be referred as “hysteresis.”¹¹ In comparison, a discharge curve of a graphitic anode has a more rapid increase in capacity at lower voltages, before reaching a plateau, and less hysteresis.¹² The difference in the two curve appearances can be related the structural differences between the two materials. Intercalated lithium can efficiently deinsert from the ordered arrangement of

graphene layers within graphitic carbon at low voltage potentials. In contrast, higher potentials are required for lithium to deintercalate from a disordered carbon structure. Researchers have proposed that lithium may bind to carbon atoms within the disordered structure.¹¹ Thus, PAN-based carbon prepared in heat treatments <1100°C may have some limitations in their performance as anodes, due to the disordered carbon structures.

Converting PAN to more ordered or graphitic structures is one solution to reduce the hysteresis between charge-discharge cycles. PAN can undergo heat treatments up to 3000°C to yield graphitic structures.¹³ However, conversion at elevated temperatures is not appropriate for nanoparticle-filled carbon composites. Materials capable of forming lithium alloys, such as Si and SnO₂, melt below 1700°C.¹⁴ Thus, adding these nanoparticles prior to the heat treatment (*i.e.*, during electrospinning) would be futile.

One advantage of the electrospun mat soak treatment described in this thesis (Chapter 3) is that nanoparticles or their precursors can be incorporated within the fibers at any point after electrospinning, including after the carbonization of polymer fibers. Thus, an extension of this work is related to the infiltration of nanoparticles within carbon nanofibers. In essence, electrospun PAN nanofibers can be converted into a range of carbon structures, based on their heat treatment conditions. Of particular interest would be the infiltration of graphitic carbon nanofibers with lithium-alloy particles, and subsequent evaluation as Li-ion battery anodes. The ordered structure of graphitic carbon (as discussed above) would be complemented by the high storage capacity of the alloys. The infiltration of the alloy

particles (or their precursors) may be enhanced by acid oxidation¹⁵ or elevated pressures.¹⁶⁻¹⁸ Furthermore, carbon nanotubes might offer an alternative carbon material to the electrospun nanofibers.^{19, 20}

7.2.3. 3D Electrospun *In situ* Crosslinked Nanofibers

A natural extension of Chapters 5 and 6 would combine crosslinking and electrospinning alginate-based fibers into 3D structures. A few recent studies have electrospun materials undergoing a crosslinking reaction.²¹⁻²⁶ One advantage of this technique would be elimination of a separate crosslinking step. *In-situ* crosslinking would be desirable for the 3D mat structures, which may experience structure collapse during a separate solution crosslinking treatment. Furthermore, materials that cannot electrospun in their pure state (*e.g.*, alginate) may benefit from crosslinking. Increasing increases solution viscosity and chain entanglements have been used as strategies to enhance electrospinning.²⁷⁻

29

Preliminary results of electrospinning photocrosslinkable alginate have led to the following observations. Firstly, 3D structures form more slowly with the UV curable polymer, compared to non-modified alginate. This is likely because the UV curable alginate has fewer carboxylic acid groups as a result of the methacrylate modification, and fewer charge repulsions between fibers, as compared to unmodified alginate. Secondly, the time

from which the alginate solution exits the needle to when it deposited onto the collector plate is likely not sufficient for the UV crosslinking reaction. (This observation is consistent with the crosslinking dynamics discussed in Chapter 6.) However, modification of the electrospinning apparatus to allow for UV exposure within the syringe or needle is a possible means to initiate the reaction in the solution.

7.2.4. Rheology of alginate hydrogels containing cells

Cells have been encapsulated within hydrogels in regenerative medicine studies(*e.g.*, Krebs *et al*³⁰). One benefit of hydrogels is related to their high water content, which allows for cell movement within the scaffold. Recent work by the Mooney group has shown that cells may increase the modulus of a forming hydrogel by forming attachments to between peptide-modified polymer chains.³¹ However, the literature lacks a study that the mechanical properties of UV-curable hydrogels containing cells. This study would be interesting because the photocurable hydrogels that contain cells are becoming a promising technology for *in vivo* tissue engineering.³²

7.3. References

1. Huang, Z. M.; Zhang, Y. Z.; Kotaki, M.; Ramakrishna, S., A review on polymer nanofibers by electrospinning and their applications in nanocomposites. *Composites Science and Technology* **2003**, 63, (15), 2223-2253.
2. Rujitanaroj, P. O.; Pimpha, N.; Supaphol, P., Wound-dressing materials with antibacterial activity from electrospun gelatin fiber mats containing silver nanoparticles. *Polymer* **2008**, 49, (21), 4723-4732.
3. Kim, G.; Wutzler, A.; Radusch, H.; Michler, G.; Simon, P.; Sperling, R.; Parak, W., One-Dimensional Arrangement of Gold Nanoparticles by Electrospinning. *Chemistry of Materials* **2005**, 17, (20), 4949-4957.
4. Sun, X. Y.; Shankar, R.; Borner, H. G.; Ghosh, T. K.; Spontak, R. J., Field-driven biofunctionalization of polymer fiber surfaces during electrospinning. *Advanced Materials* **2007**, 19, (1), 87-+.
5. Sigma-Aldrich, In *February 1, 2010*, 2010, Ed. www.sigmaaldrich.com.
6. Zhou, J. A.; van Duijneveldt, J. S.; Vincent, B., The Phase Behavior of Dispersions of Silica Particles in Mixtures of Polystyrene and Dimethylformamide. *Langmuir* **2010**, 26, (12), 9397-9402.

7. Wang, L.; Yu, Y.; Chen, P. C.; Zhang, D. W.; Chen, C. H., Electrospinning synthesis of C/Fe₃O₄ composite nanofibers and their application for high performance lithium-ion batteries. *Journal of Power Sources* **2008**, 183, 717-723.
8. Ji, L. W.; Zhang, X. W., Fabrication of porous carbon/Si composite nanofibers as high-capacity battery electrodes. *Electrochemistry Communications* **2009**, 11, (6), 1146-1149.
9. Rahaman, M. S. A.; Ismail, A. F.; Mustafa, A., A review of heat treatment on polyacrylonitrile fiber. *Polymer Degradation and Stability* **2007**, 92, (8), 1421-1432.
10. Kaskhedikar, N. A.; Maier, J., Lithium Storage ion Carbon Nanostructures. *Advanced Materials* **2009**, 21, (25-26), 2664-2680.
11. Zheng, T.; McKinnon, W. R.; Dahn, J. R., Hysteresis during lithium insertion in hydrogen-containing carbons. *Journal of the Electrochemical Society* **1996**, 143, (7), 2137-2145.
12. Linden, D.; Reddy, T. B., *Handbook of Batteries*. 3rd ed.; McGraw-Hill: New York, 2002.
13. Sittig, M., *Carbon and Graphite Fibers Manufacture and Applications*. Noyes Data Corporation: Park Ridge, NJ, 1980; p 422.
14. Haynes, W. M., *CRC handbook of chemistry and physics*. 91st ed.; Taylor & Francis: Boca Raton, 2010.

15. Hou, H. Q.; Ge, J. J.; Zeng, J.; Li, Q.; Reneker, D. H.; Greiner, A.; Cheng, S. Z. D., Electrospun polyacrylonitrile nanofibers containing a high concentration of well-aligned multiwall carbon nanotubes. *Chemistry of Materials* **2005**, 17, (5), 967-973.
16. Rodriguez-Guerrero, A.; Molina, J. M.; Rodriguez-Reinoso, F.; Narciso, J.; Louis, E., Pore filling in graphite particle compacts infiltrated with Al-12 wt.%Si and Al-12 wt.%Si-1 wt.%Cu alloys. *Materials Science and Engineering a-Structural Materials Properties Microstructure and Processing* **2008**, 495, (1-2), 276-281.
17. Rodriguez-Guerrero, A.; Sanchez, S. A.; Narciso, J.; Louis, E.; Rodriguez-Reinoso, F., Pressure infiltration of Al-12 wt.% Si-X (X = Cu, Ti, Mg) alloys into graphite particle preforms. *Acta Materialia* **2006**, 54, (7), 1821-1831.
18. Etter, T.; Papakyriacou, A.; Schulz, P.; Uggowitzer, P. J., Physical properties of graphite/aluminium composites produced by gas pressure infiltration method. *Carbon* **2003**, 41, (5), 1017-1024.
19. Lee, S. W.; Kim, J.; Chen, S.; Hammond, P. T.; Shao-Horn, Y., Carbon Nanotube/Manganese Oxide Ultrathin Film Electrodes for Electrochemical Capacitors. *Acs Nano* **2010**, 4, (7), 3889-3896.
20. Lee, S. W.; Yabuuchi, N.; Gallant, B. M.; Chen, S.; Kim, B. S.; Hammond, P. T.; Shao-Horn, Y., High-power lithium batteries from functionalized carbon-nanotube electrodes. *Nature Nanotechnology* **2010**, 5, (7), 531-537.

21. Tang, C.; Saquing, C. D.; Harding, J. R.; Khan, S. A., In Situ Cross-Linking of Electrospun Poly(vinyl alcohol) Nanofibers. *Macromolecules* **2010**, 43, (2), 630-637.
22. Xu, X. M.; Zhang, J. F.; Fan, Y. W., Fabrication of Cross-Linked Polyethyleneimine Microfibers by Reactive Electrospinning with In Situ Photo-Cross-Linking by UV Radiation. *Biomacromolecules* **2010**, 11, (9), 2283-2289.
23. Schiffman, J. D.; Schauer, C. L., One-step electrospinning of cross-linked chitosan fibers. *Biomacromolecules* **2007**, 8, (9), 2665-2667.
24. Kim, S. H.; Nair, S.; Moore, E., Reactive electrospinning of cross-linked poly(2-hydroxyethyl methacrylate) nanofibers and elastic properties of individual hydrogel nanofibers in aqueous solutions. *Macromolecules* **2005**, 38, (9), 3719-3723.
25. Gupta, P.; Trenor, S. R.; Long, T. E.; Wilkes, G. L., In situ photo-cross-linking of cinnamate functionalized poly(methyl methacrylate-co-2-hydroxyethyl acrylate) fibers during electrospinning. *Macromolecules* **2004**, 37, (24), 9211-9218.
26. Jeong, S. I.; Krebs, M. D.; Bonino, C. A.; Samorezov, J. E.; Khan, S. A.; Alsberg, E., Electrospun Chitosan–Alginate Nanofibers with In Situ Polyelectrolyte Complexation for Use as Tissue Engineering Scaffolds. *TISSUE ENGINEERING: Part A* **2011**, 17, (1&2), 59-70.

27. McKee, M. G.; Hunley, M. T.; Layman, J. M.; Long, T. E., Solution rheological behavior and electrospinning of cationic polyelectrolytes. *Macromolecules* **2006**, *39*, (2), 575-583.
28. McKee, M. G.; Wilkes, G. L.; Colby, R. H.; Long, T. E., Correlations of solution rheology with electrospun fiber formation of linear and branched polyesters. *Macromolecules* **2004**, *37*, (5), 1760-1767.
29. Fong, H.; Chun, I.; Reneker, D. H., Beaded nanofibers formed during electrospinning. *Polymer* **1999**, *40*, (16), 4585-4592.
30. Krebs, M. D.; Jeon, O.; Alsberg, E., Localized and Sustained Delivery of Silencing RNA from Macroscopic Biopolymer Hydrogels. *Journal of the American Chemical Society* **2009**, *131*, (26), 9204-+.
31. Park, H.; Kang, S. W.; Kim, B. S.; Mooney, D. J.; Lee, K. Y., Shear-reversibly Crosslinked Alginate Hydrogels for Tissue Engineering. *Macromolecular Bioscience* **2009**, *9*, (9), 895-901.
32. Peppas, N. A.; Hilt, J. Z.; Khademhosseini, A.; Langer, R., Hydrogels in biology and medicine: From molecular principles to bionanotechnology. *Advanced Materials* **2006**, *18*, (11), 1345-1360.

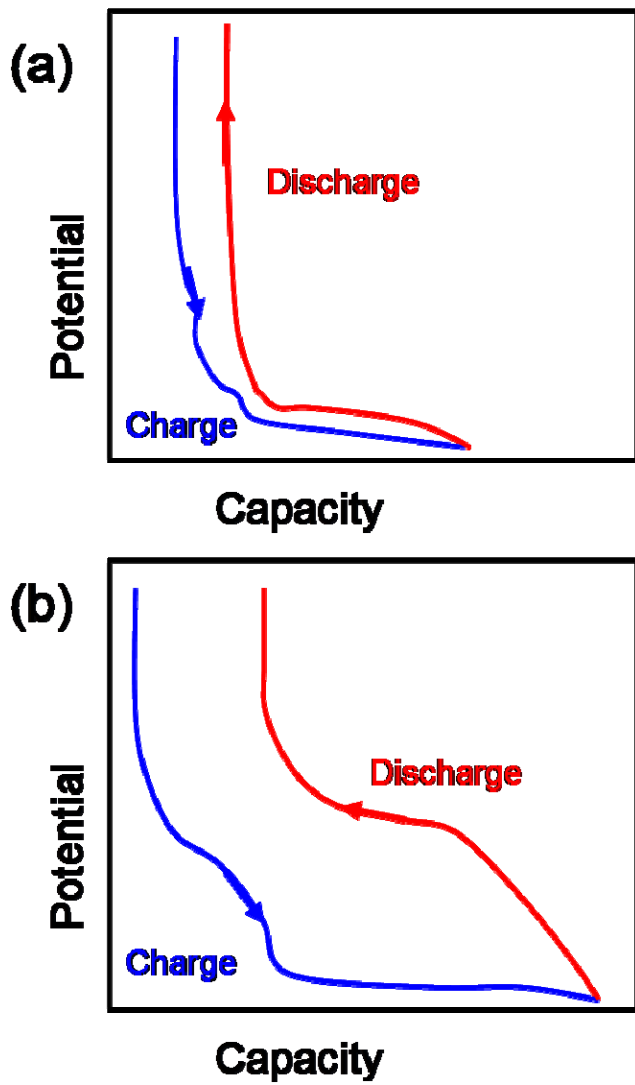


Figure 7.1. Diagram depicting appearance of charge-discharge curves for graphite-like (a) and disordered carbon-like (b) anodes.